

A Quarter Century of *Wind* Spacecraft Discoveries

Lynn B. Wilson III¹, Alexandra L. Brosius^{1,2}, Natchimuthuk Gopalswamy¹,
Teresa Nieves-Chinchilla¹, Adam Szabo¹, Kevin Hurley³, Tai Phan³, Justin C.
Kasper⁴, Noé Lugaz^{5,6}, Ian G. Richardson^{7,1}, Christopher H.K. Chen⁸, Daniel
Verscharen^{9,5}, Robert T. Wicks¹⁰, Jason M. TenBarge^{11,12}

¹NASA Goddard Space Flight Center, Heliophysics Science Division, Greenbelt, MD 20771, USA.

²The Pennsylvania State University, Department of Meteorology and Atmospheric Science, University
Park, PA 16802, USA.

³Space Sciences Laboratory, University of California, Berkeley, CA 94720-7450, USA.

⁴University of Michigan, Ann Arbor, School of Climate and Space Sciences and Engineering, Ann Arbor,
MI 48109, USA.

⁵Space Science Center, Institute for the Study of Earth, Oceans, and Space, University of New
Hampshire, Durham, NH, USA.

⁶Department of Physics, University of New Hampshire, Durham, NH, USA.

⁷Department of Astronomy, University of Maryland, College Park 20742, USA.

⁸School of Physics and Astronomy, Queen Mary University of London, London E1 4NS, UK.

⁹Mullard Space Science Laboratory, University College London, Holmbury St. Mary, Surrey RH5 6NT,
UK.

¹⁰Department: Mathematics, Physics and Electrical Engineering, Northumbria University: Newcastle
upon Tyne, Tyne and Wear, NE1 8ST, UK.

¹¹IREAP, University of Maryland, College Park, MD 20742, USA.

¹²Princeton University, Princeton, NJ 08544, USA.

Key Points:

- *Wind* has made seminal advances to the fields of astrophysics, turbulence, kinetic physics, magnetic reconnection, and the radiation belts
- *Wind* pioneered the study of the source and evolution of solar radio emissions below 15 MHz
- *Wind* revolutionized our understanding of coronal mass ejections, their internal magnetic structure, and evolution

Abstract

The *Wind* spacecraft, launched on November 1, 1994, is a critical element in NASA's Heliophysics System Observatory (HSO) – a fleet of spacecraft created to understand the dynamics of the sun-Earth system. The combination of its longevity (>25 years in service), its diverse complement of instrumentation, and high resolution and accurate measurements has led to it becoming the “standard candle” of solar wind measurements. *Wind* has over 55 selectable public data products with over ~1100 total data variables (including OMNI data products) on SPDF/CDAWeb alone. These data have led to paradigm shifting results in studies of statistical solar wind trends, magnetic reconnection, large-scale solar wind structures, kinetic physics, electromagnetic turbulence, the Van Allen radiation belts, coronal mass ejection topology, interplanetary and interstellar dust, the lunar wake, solar radio bursts, solar energetic particles, and extreme astrophysical phenomena such as gamma-ray bursts. This review introduces the mission and instrument suites then discusses examples of the contributions by *Wind* to these scientific topics that emphasize its importance to both the fields of heliophysics and astrophysics.

Plain Language Summary

The *Wind* spacecraft is a south ecliptic pointed spinning spacecraft that was launched on November 1, 1994. It is equipped with an array of instrument suites that measure electric and magnetic fields, electrons from thermal to relativistic energies, protons and alpha-particles from thermal to suprathermal energies, and energetic ions from hydrogen to trans-iron elements. *Wind* can also observe remote sources of electromagnetic radiation in the radio and gamma-ray frequency ranges. This diverse array of instrumentation and numerous near-Earth environments explored has allowed researchers to examine such a broad range of research topics including astrophysics, turbulence, kinetic physics, magnetic reconnection, interplanetary and interstellar dust, transient solar phenomena, and the radiation belts. Examples of the contributions of *Wind* to the fields of heliophysics and astrophysics are reviewed.

1 The *Wind* Mission

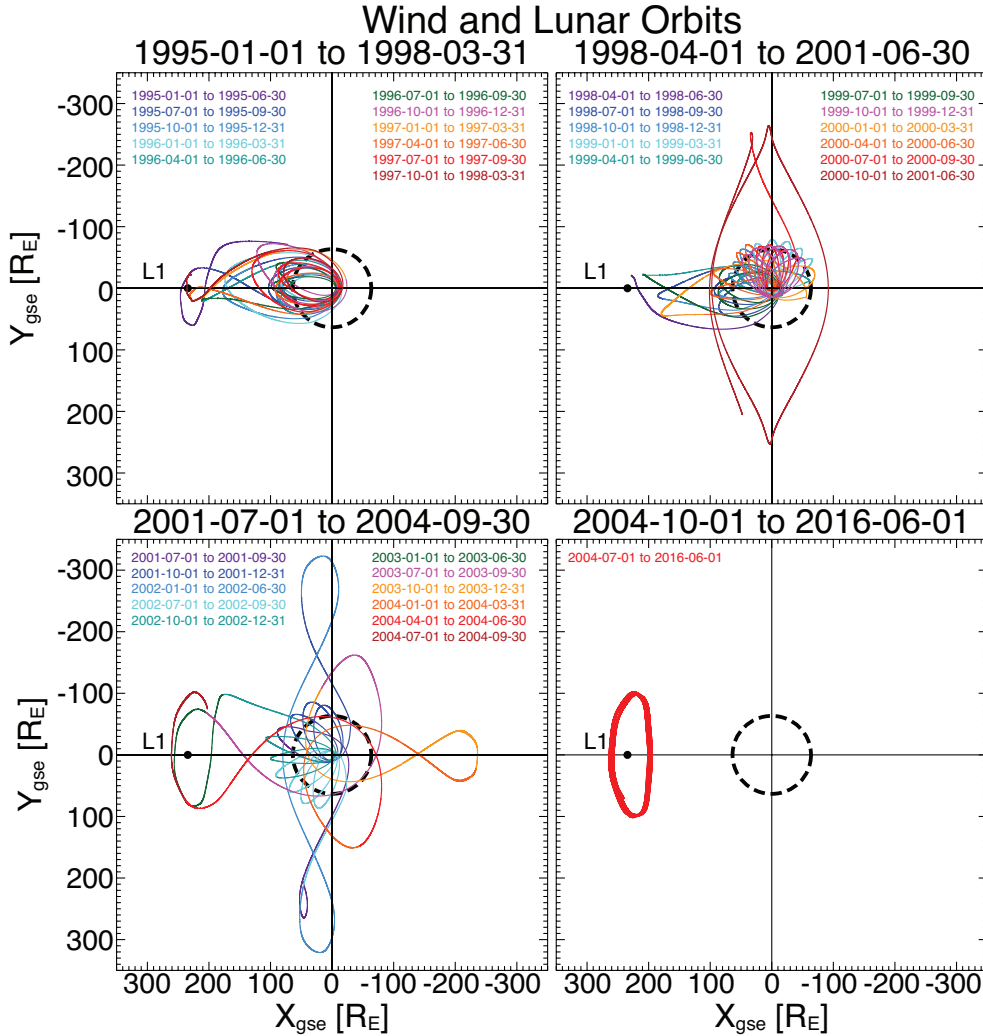


Figure 1: Orbital trajectories of the *Wind* spacecraft in the GSE XY plane from 1 November 1994 to 1 June 2016. Colors denote time ranges as indicated. The dashed black circle indicates the Moon’s orbit (Adapted from Figure 1 in Malaspina & Wilson III, 2016). Note that the orbit has not noticeably changed since 1 June 2016.

58 NASA launched the *Wind* spacecraft on November 1, 1994. *Wind* and *Polar* (Harten
 59 & Clark, 1995) were part of the stand-alone Global Geospace Science (GGS) Program
 60 (Acuña et al., 1995), a subset of the International Solar Terrestrial Physics (ISTP) Program
 61 (Whipple & Lancaster, 1995). The ISTP Program included the additional missions
 62 *Geotail* (Nishida, 1994), the Solar and Heliospheric Observatory or *SoHO* (Domingo et
 63 al., 1995), and *Cluster* (Escoubet et al., 1997). The objective of the ISTP program was
 64 to study the origin of solar variability and activity, the transport of manifestations of that
 65 activity to the Earth via plasma processes, and the cause-and-effect relationships between
 66 that time varying energy transport and the near-earth environment.

67 *Wind* is a spin stabilized spacecraft – spin axis aligned with ecliptic south – with
 68 a spin period of ~ 3 seconds. Prior to May 2004, *Wind* performed a series of orbital ma-
 69 neuvers (H. Franz et al., 1998), as shown in Figure 1, that led to the spacecraft visiting

70 numerous regions of the near-Earth environment. For instance, between launch and late
 71 2002 *Wind* completed ~ 67 petal orbits through the magnetosphere and two lunar rolls
 72 out of the ecliptic in April and May of 1999. Between August 2000 and June 2002 *Wind*
 73 completed four east-west prograde 1:3-Lissajous orbits reaching $\gtrsim 300 R_E$ along the $\pm Y$ -
 74 GSE direction (Fränz & Harper, 2002). From November 2003 to February 2004 *Wind*
 75 performed an excursion to the second Earth-Sun libration point, or Lagrange point, called
 76 L2¹.

77 In May 2004, *Wind* made its final major orbital maneuver using a lunar gravita-
 78 tional assist to insert it into a Lissajous orbit² about the first Earth-Sun libration point,
 79 labeled L1 by late June 2004. On June 26, 2020, the *Wind* flight operations team (FOT)
 80 successfully completed the first halo orbit insertion maneuver and the second was suc-
 81 cessfully completed on August 31, 2020. The third maneuver was successfully completed
 82 on November 9, 2020. This orbital change was necessary to prevent the spacecraft tra-
 83 jectory from entering the solar exclusion zone – around the solar disk where solar radio
 84 emissions cause sufficient interference with spacecraft communications to prevent teleme-
 85 try signal locks. The projection of the orbit in the ecliptic plane will not noticeably change,
 86 however the out-of-ecliptic projection will now be a stationary ellipse centered on the
 87 solar disk. The difference between a halo and Lissajous orbit in this context is the out
 88 of ecliptic position, or z-component. In the latter, the z-component oscillation/orbital
 89 period is decoupled from the in-plane components. The halo orbit forces all three com-
 90 ponents to couple so the orbit becomes an ellipse tilted relative to the ecliptic plane.

91 The mission has amassed >5380 refereed publications using *Wind* data between
 92 launch and December 31, 2019 with a NASA ADS h-index of 145, an i10-index of 3132,
 93 $>153,160$ citations, and $>1,012,890$ reads as of Jan. 11, 2021. Despite being 25+ years
 94 old, the *Wind* mission still remains active and *Wind* data continue to be relevant as ev-
 95 idenced by the >1065 refereed publications between January 1, 2017 and December 31,
 96 2019. Further, *Wind* data access requests were $>10,291,900$ between January 1, 2017
 97 and December 31, 2019 on NASA’s SPDF/CDAWeb or ~ 9400 per day. Thus, *Wind* is
 98 one of the longest running³ and most productive missions in the Heliophysics System Ob-
 99 servatory (HSO).

100 The paper is organized as follows:

- 101 • **Section 2** reviews the instrument suites, their capabilities, current status, and
 102 provides some long-term statistics as an illustration of *Wind*’s capabilities;
- 103 • **Section 3** provides background information and context for the following subsec-
 104 tions that review *Wind*’s scientific advances;
 - 105 – **Section 3.1** reviews *Wind*’s contribution to gamma ray and solar x-ray astron-
 106 omy;
 - 107 – **Section 3.2** reviews *Wind*’s contribution to interstellar and interplanetary dust;
 - 108 – **Section 3.3** reviews *Wind*’s contribution to our understanding of the lunar wake;

¹ Note that L2 is located ~ 233 – $235 R_E$ downstream of Earth and $\sim 500 R_E$ downstream of the Ad-
 vanced Composition Explorer (ACE) (Stone et al., 1998). For reference, ACE launched in 1997 and was
 designed to study energetic particles and their composition. Unlike *Wind*, ACE was not designed to study
 kinetic physics or remote solar and astrophysical phenomena using electric fields.

² Note that *Wind*’s L1 orbit has a $\pm Y$ -GSE($\pm X$ -GSE) displacement about the sun-Earth line of ~ 100
 R_E ($\sim 35 R_E$), much larger than the other NASA mission at L1 ACE. Note that the $\pm Z$ -GSE displacement
 from the ecliptic plane is $\lesssim 30 R_E$ for both ACE and *Wind*. For more details, see the *Wind* Senior Review
 reports provided at: <https://wind.nasa.gov>.

³ The only NASA run mission currently operating that is older is the *Voyager* mission at >43 years,
 but both spacecraft have significantly reduced capabilities from their original design. Some other missions
 have been operating >19 years and are still active but operating at limited/reduced capacity. *Wind* is
 still fully functional and yielding new data products due to hardware redundancy and large fuel supplies.

- 109 – **Section 3.4** reviews *Wind*'s contribution to magnetic reconnection in Earth's
110 magnetotail;
- 111 – **Section 3.5** reviews *Wind*'s contribution to our understanding of the Earth's
112 radiation belts;
- 113 – **Section 3.6** reviews *Wind*'s contribution to our understanding of the terres-
114 trial foreshock;
- 115 – **Section 3.7** includes multiple subsections focused on work in the solar wind;
116 * **Section 3.7.1** reviews *Wind*'s contribution to our understanding of large
117 scale structures and magnetic reconnection in the solar wind;
- 118 * **Section 3.7.2** reviews *Wind*'s contribution to our understanding of kinetic
119 instabilities and waves in the solar wind;
- 120 * **Section 3.7.3** reviews *Wind*'s contribution to our understanding of tur-
121 bulence in the solar wind; and
- 122 * **Section 3.7.4** reviews some long-term statistical studies performed by *Wind*
123 in the solar wind;
- 124 – **Section 3.8** includes multiple subsections focused on transient, large-scale, mag-
125 netic phenomena;
126 * **Section 3.8.1** reviews *Wind*'s contribution to our understanding of inter-
127 planetary shocks;
- 128 * **Section 3.8.2** reviews *Wind*'s contribution to our understanding of inter-
129 planetary coronal mass ejections; and
- 130 * **Section 3.8.3** reviews *Wind*'s contribution to our understanding of stream
131 interaction regions and corotating interaction regions;
- 132 – **Section 3.9** reviews *Wind*'s contribution to our understanding of solar ener-
133 getic particles;
- 134 – **Section 3.10** starts by introducing solar radio bursts and how *Wind* has made
135 major advances then goes into several subsections including;
136 * **Section 3.10.1** reviews *Wind*'s contribution to our understanding of type
137 II radio bursts;
- 138 * **Section 3.10.2** reviews *Wind*'s contribution to our understanding of type
139 III radio bursts;
- 140 * **Section 3.10.3** reviews *Wind*'s contribution to our understanding of type
141 III storms; and
- 142 * **Section 3.10.4** reviews *Wind*'s contribution to our understanding of type
143 VI radio bursts;
- 144 – **Section 3.11** discusses *Wind*'s relationship to the HSO with a focus on *Parker*
145 *Solar Probe* and *Solar Orbiter*;
- 146 • **Section 4** provides a summary and review of the highlights contained within this
147 review paper.
- 148 • **Appendix A** provides definitions of symbols/parameters used in the text;
- 149 • **Appendix B** provides a review of several plasma instabilities and their proper-
150 ties, all of which *Wind* data has been used to investigate;
- 151 • **Appendix C** lists some of the databases relying upon or created by *Wind* data;
152 and
- 153 • Finally we provide a Glossary and an Acronyms appendix for the reader to help
154 with the jargon and acronyms/initialisms used herein.

155 2 *Wind* Instrument Suites and Long-term Statistics

156 The *Wind* instruments can be divided into two categories: field and particle suites.
157 The field instruments measure γ -rays, radio waves, electric fields, and magnetic fields.
158 The particle instruments measure thermal protons, alpha-particles, and electrons in ad-
159 dition to suprathermal and heavy ions (e.g., carbon-nitrogen-oxygen, iron, trans-iron).
160 All of the thermal particle instruments (and some of the suprathermal) measure parti-
161 cles as functions of energy and solid angle which allows researchers to construct veloc-

162 ity distribution functions (VDFs) – particle probability density functions in velocity space.
 163 The full 3D VDF measurements also allow researchers to calculate velocity moments of
 164 the distribution such as number density, bulk flow velocity, thermal pressure/temperature,
 165 and heat flux. The *Wind* instrument names and acronyms are listed below in Table 1.

Table 1: *Wind* Instrument Names

| Abbrev. | Instrument name | Reference |
|--------------|---|------------------------------|
| TGRS | Transient Gamma-Ray Spectrometer | A. Owens et al. (1995) |
| KONUS | Gamma-Ray Spectrometer | Aptekar et al. (1995) |
| EPACT | Energetic Particles: Acceleration, Composition, and Transport | von Rosenvinge et al. (1995) |
| SMS | Solar Wind and Suprathermal Ion Composition Experiment | Gloeckler et al. (1995) |
| MFI | Magnetic Field Investigation | Lepping et al. (1995) |
| WAVES | The Radio and Plasma Wave Investigation | Bougeret et al. (1995) |
| 3DP | Three-Dimensional Plasma and Energetic Particle Investigation | Lin et al. (1995) |
| SWE | Solar Wind Experiment | Ogilvie et al. (1995) |

166 It is important to note that unlike most other missions, *Wind* was designed with
 167 significant redundancy in its measurements. For instance, there are at least five possi-
 168 ble measurements of the solar wind number density (two from 3DP, two from SWE, one
 169 from WAVES, and one from SMS under certain conditions) and prior to 2000 there were
 170 two different gamma ray instruments. The MFI comprises of two fluxgate magnetome-
 171 ters at different locations on a 12 meter boom (one closer at ~ 8 m, the other at 12 m)
 172 which improves spacecraft noise/artifact removal. There are three separate measurements
 173 of protons with energies >50 keV (one from 3DP, one from SMS, and one from EPACT).
 174 Finally, there are at least three separate measurements of heavy ions (i.e., ions more mas-
 175 sive than alpha-particles). The instrument capabilities and current status are shown in
 176 Table 3 (see the Glossary and Acronyms Appendices for definitions).

177 Most of the instruments continue to be fully functional, aside from temporary data
 178 losses due to a command and attitude processor (CAP) and tape unit anomaly (both
 179 issues were resolved or mitigated). The dates of significant spacecraft and instrumen-
 180 tal issues are listed in Table 2 for reference.

181 In this review, we present *Wind* results for a variety of environments in an effort
 182 to highlight a reasonable fraction of *Wind*'s publications. For a broad overview of *Wind*
 183 particles and field observations, Figure 2 shows 25+ years of observations from MFI and
 184 SWE instruments across more than two solar cycles (late cycle 22–cycle 24) indicated
 185 by the background color. The temporal resolutions for MFI and SWE are ~ 1 minute (av-
 186 erages) and ~ 92 seconds, respectively. A 2D histogram was constructed from one week
 187 bins on the horizontal axis while the vertical axis is split up into 300 bins for each panel.
 188 The data were artificially clipped when creating the 2D histogram to reduce low statis-
 189 tics bins. The range of values used to construct the histograms are $0 \leq B_o \leq 300$ nT,
 190 $0 \leq n_i \leq 300$ cm^{-3} , and $200 \leq V_i \leq 1400$ $km\ s^{-1}$. The range of values shown on the
 191 vertical axis are further restricted to focus on the values most commonly observed over

Table 2: Wind Instrument and Spacecraft Anomalies

| Date | Part Affected | Impact |
|-------------------|----------------------------------|---|
| January 19, 1995 | GTM1 ^a | failure |
| October 1995 | APE-A/APE-B/IT HVPS ^b | suffered a loss of gain |
| April 30, 1997 | CAP1 ^c | Reed-Solomon encoder failure |
| December 13, 1997 | DTR2 ^d | power supply failure |
| January 2000 | TGRS | γ -ray instrument turned off (planned coolant outage) |
| May 2000 | SMS-SWICS | solar wind composition sensor turned off |
| June 2001 | SWE-VEIS | thermal electron detectors HVPS failure |
| August 2002 | SWE-Strahl | reconfigured to recover VEIS functionality |
| June 2009 | SMS DPU | experienced a latch-up reset – MASS acceleration/deceleration |
| 2010 | SMS-MASS | power supply in fixed voltage mode experienced a small degradation in the acceleration/deceleration power supply |
| May 19, 2014 | 3DP-PESA Low | suffered an anomaly that affected only the telemetry HK ^e data |
| October 27, 2014 | CAP1 | anomaly at ~21:59:38 GMT |
| November 7, 2014 | CAP2 | set to primary while recovery starts on CAP1 |
| November 26, 2014 | SWE | full reset due to CAP1 anomaly |
| January 30, 2015 | CAP1 | fully recovered |
| April 11, 2016 | DTR1 TUA | began experiencing read/write errors (~1% bit errors) |
| May 6, 2016 | DTR1 TUB | FOT sets as primary recorder |

^a two GGS telemetry modules, GTM1 and GTM2 ^b high voltage power supply

^c two command and attitude processors, CAP1 and CAP2

^d two digital tape recorders, DTR1 and DTR2, each with independent tape units, TUA and TUB

^e house keeping

192 the total interval. The color bars show the number of counts in each bin where white space
193 represents no counts and red [represents] saturation. These calculations include solar wind
194 and magnetospheric intervals. The fluxgate magnetometer had few data gaps during mag-
195 netospheric passes. The SWE Faraday cups could not track the bulk ion population within
196 the magnetosphere and exhibit sparser coverage than MFI prior to May 2004. Table 4
197 provides some one-variable statistics of the data shown in Figure 2 for reference.

198 These specific data products were chosen primarily for ease of use and that they
199 are some of the most commonly utilized data from *Wind*. Figure 2 shows data taken from
200 every region that *Wind* has visited in its 25+ years of observations from the magneto-
201 sphere, radiation belts, lunar environment, bow shock and foreshock regions, and solar
202 wind. However, as noted above, the SWE Faraday cups cannot track the bulk of the ther-
203 mal ion population while inside the magnetosphere because it is designed to measure a
204 cold, fast beam. Thus, there are multi-hour data gaps in the SWE Faraday cup data dur-
205 ing the >60 perigee passes through the magnetosphere. However, again the magnetome-
206 ter data is perfectly valid. In fact, most of the large B_o values seen prior to 2004 are from

Table 3: Operational Instruments on *Wind*

| Name | Type | Cadence | Range | Status & Notes |
|--------------|--------------------------|---------------------------------------|---|---|
| MFI | $3 B_{o,j}$ ^a | $\sim 11\text{--}22$ sps ^b | $\pm 4 - \pm 65,536$ nT | Nominal $\pm 0.001 - \pm 16$ nT |
| WAVES | | | | Nominal |
| TDS Fast | $2 \delta E_j$ | $1.8\text{--}120$ ksps | $\sim 0.1\text{--}300$ mV/m | ~ 80 μV rms |
| TDS Slow | 1 or $3 \delta E_j$ | $0.1\text{--}7.5$ ksps | $\sim 0.5\text{--}300$ mV/m | ~ 300 μV rms |
| | 1 or $3 \delta B_j$ | $0.1\text{--}7.5$ ksps | $\sim 0.25 - \gtrsim 30$ nT | $\sim 10^{-9}$ nT ² Hz ⁻¹ @ 100 Hz |
| TNR | $1 \delta E_j$ | ~ 1 min | $\sim 4\text{--}256$ kHz | ~ 7 nV Hz ^{-1/2} |
| RAD1 | $2 \delta E_j$ | ~ 1 min | $\sim 20\text{--}1040$ kHz | ~ 7 nV Hz ^{-1/2} |
| RAD2 | $2 \delta E_j$ | ~ 1 min | $\sim 1.1\text{--}14$ MHz | ~ 7 nV Hz ^{-1/2} |
| 3DP | | | | Nominal |
| EESA | e^- | $\sim 3\text{--}22$ s | $\sim 0.003\text{--}30$ keV | $\sim 20\%$ $\Delta E/E^c$, $\sim 5.6\text{--}22.5^\circ$ |
| PESA | H^+, He^{2+} | $\sim 3\text{--}75$ s | $\sim 0.003\text{--}30$ keV | $\sim 20\%$ $\Delta E/E$, $\sim 5.6\text{--}22.5^\circ$ |
| SST Foil | e^- | ~ 12 s | $\sim 25\text{--}400$ keV | $\sim 30\%$ $\Delta E/E$, $\gtrsim 22.5^\circ$ |
| SST Open | H^+ | ~ 12 s | $\sim 25\text{--}6000$ keV | $\sim 30\%$ $\Delta E/E$, $\gtrsim 22.5^\circ$ |
| SWE | | | | VEIS Off, Strahl Reconf. |
| FCs | H^+, He^{2+} | ~ 92 s | $\sim 0.15\text{--}8$ keV | $\sim 6.5\%$ $\Delta E/E$ |
| Strahl | e^- | ~ 12 s | $\sim 0.005\text{--}5$ keV | $\sim 3\%$ $\Delta E/E$ $\sim 3^\circ \times 30^\circ$ |
| SMS | | | | SWICS Off, MASS Reduced |
| STICS | H – Fe | $\gtrsim 3$ min | $\sim 8\text{--}226$ keV/e 1–60 amu/e | $\sim 5\%$ $\Delta E/E$, $\sim 4^\circ \times 150^\circ$ $\sim 12\%$ $\Delta M/M^d$ |
| EPACT | | | | IT off, APE Reduced |
| LEMT | He – Fe | $\gtrsim 5\text{--}60$ min | $\sim 2\text{--}12$ MeV/n $\sim 2\text{--}90$ Z | $\gtrsim 20\%$ $\Delta E/E$ $\gtrsim 2\%$ $\Delta Q/Q^e$ |
| STEP | H – Fe | $\gtrsim 10$ min | $\sim 0.02\text{--}2.56$ MeV/n | $\gtrsim 30\%$ $\Delta E/E$ $\sim 17^\circ \times 44^\circ$ |
| KONUS | photons | $\gtrsim 2$ ms $\gtrsim 3$ s | $\sim 0.02\text{--}15$ MeV $\sim 0.02\text{--}1.5$ MeV | Nominal $\gtrsim 5\%$ $\Delta E/E$ Background Mode |
| TGRS | photons | $\gtrsim 62$ μs | $\sim 0.025\text{--}8.2$ MeV | Off (out of coolant) ~ 3 keV @ 1 MeV eff. $\sim 43\%$ @ 511 keV |

^a three magnetic field vector components ^b samples per second ^c normalized energy resolution
^d normalized mass resolution ^e normalized charge resolution

207 magnetospheric passes. While these data products are not comprehensive of *Wind*'s ca-
208 pabilities, they are useful and illustrative of the longevity and diversity of environments
209 that *Wind* has sampled.

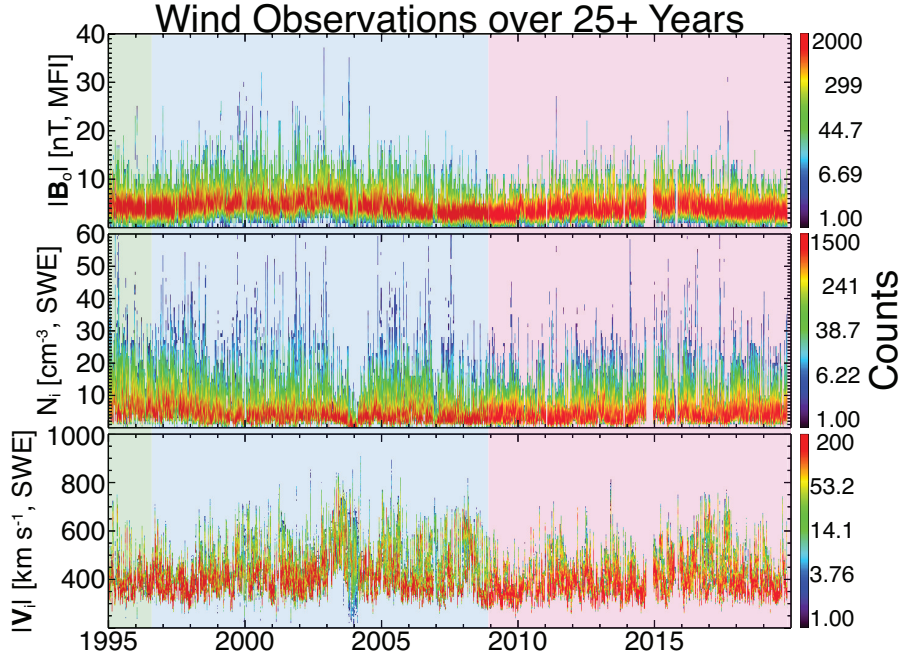


Figure 2: A 2D histogram representation of 25+ years of Wind observations. The panels are as follows from top to bottom: quasi-static magnetic field magnitude [nT], total ion number density [cm⁻³], and total ion bulk flow speed [km/s]. The shading corresponds to solar cycles 22 (green), 23 (blue), and 24 (magenta). The color bars indicate the counts in each bin (see text for details).

Table 4: Solar wind statistics

| Solar Cycle | n_i [cm ⁻³] ^a | V_i [km s ⁻¹] | B_o [nT] |
|----------------------|--|-----------------------------|------------------|
| Overall ^b | 1.70–16.8, ~5.24 | 304–633, ~405 | 2.42–12.0, ~5.04 |
| 22 End | 2.65–20.2, ~7.42 | 310–637, ~398 | 2.45–11.3, ~5.01 |
| 23 All | 1.57–17.0, ~5.11 | 309–652, ~418 | 2.55–13.7, ~5.46 |
| 24 All | 1.75–15.5, ~5.11 | 299–605, ~392 | 2.30–10.2, ~4.62 |

^a $X_{5\%}-X_{95\%}$, \bar{X} (where $X_{y\%}$ is the y^{th} percentile and \bar{X} is the median).

^b Magnetospheric data are not included in the particle stats as SWE cannot measure magnetospheric ions

210 **3 Selected Science Results from *Wind***

211 This section starts by providing the reader with some background and contextual
 212 information that will be assumed in the subsequent subsections. The following subsections
 213 go on to summarize *Wind*'s contributions to numerous subfields within space plasma
 214 physics and astrophysics. The purpose is to illustrate both the breadth and importance
 215 of *Wind* in advancing our understanding of these fields. This section will also illustrate
 216 one of *Wind*'s greatest assets; the redundancies of some of its instruments which greatly
 217 improve the calibration and accuracy of the data products. Note that throughout this
 218 review, we intentionally prioritize *Wind*-centric references when available to help further
 219 illustrate the capabilities and diversity of *Wind*'s accomplishments. These citations are
 220 not meant to imply the reference was the first or seminal work on any given topic but
 221 to keep the focus on accomplishments by the *Wind* mission. We add notes/discussion,

222 where appropriate, to help the reader distinguish between a *Wind*-centric and original/discovery
 223 paper.

224 *Wind* was designed to examine space plasmas. A plasma is an ionized gas exhibit-
 225 ing a collective behavior that is found in nearly all regions of space. Plasmas are medi-
 226 ated by long-range forces (i.e., electromagnetic) as well.

227 The near-Earth environment (see cartoon in Figure 3) is comprised of a neutral at-
 228 mosphere surrounded by a plasma (e.g., see review by Borovsky et al., 2020). The tran-
 229 sition between the two is not abrupt. The neutral atmosphere consists of the troposphere,
 230 the stratosphere, the mesosphere, and a portion of the thermosphere. In the thermosphere,
 231 temperature increases as a function of altitude and as a function of extreme ultraviolet
 232 radiation. The ultraviolet radiation ionizes neutral constituents and gives rise to the iono-
 233 sphere, a collisionally mediated, weakly ionized plasma. Above the ionosphere is the plas-
 234 masphere surrounded by the magnetosphere which is bounded by the magnetopause. Within
 235 the magnetosphere are the Van Allen radiation belts, magnetotail, and several other re-
 236 gions. The magnetosheath separates the magnetopause from the bow shock, one of the
 237 largest features of the near-Earth environment. The bow shock is the outermost bound-
 238 ary between the magnetosphere and the interplanetary medium (IPM) and solar wind.
 239 The magnetopause forms due to the Earth’s magnetic field acting as an obstacle to the
 240 supersonic flow of the solar wind. The plasma compresses on the sunward side, piling
 241 up leading to a nonlinearly steepening fast/magnetosonic wave. Eventually this steep-
 242 ening wave reaches a balance between nonlinear steepening and energy dissipation, at
 243 which point the bow shock forms.

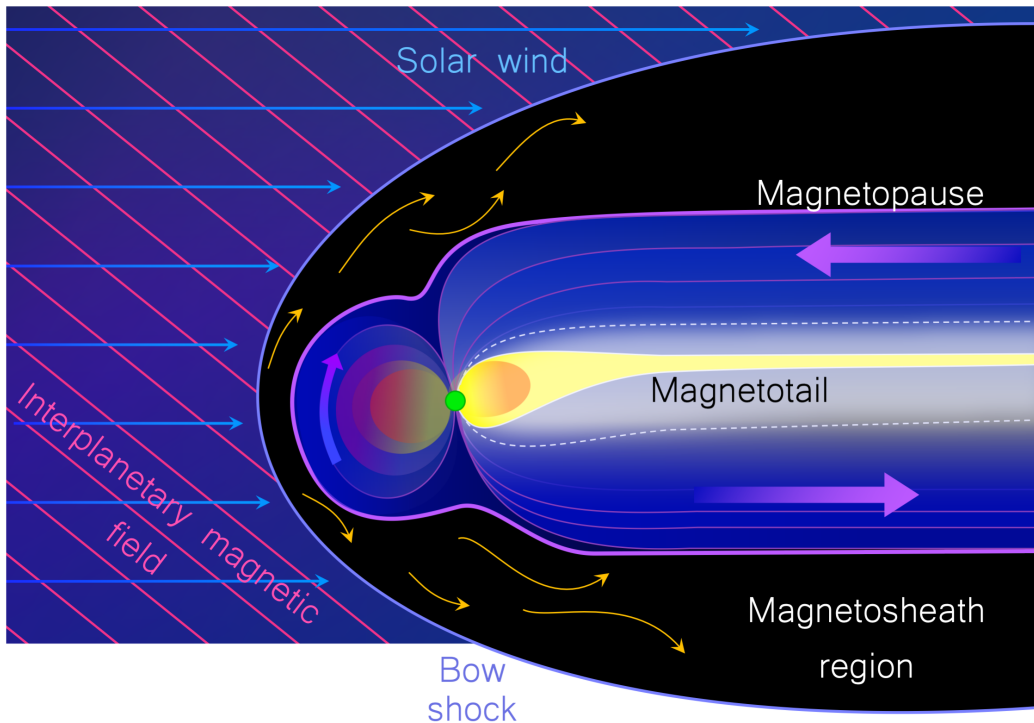


Figure 3: *Cartoon of the Earth’s global geospace environment (not to scale) shown in the plane orthogonal to the ecliptic.*

244 Plasmas are ordered as collisionless, weakly collisional, collisional, and strongly col-
 245 lisional. A weakly collisional system is one in which the collision rate is small but not

246 completely negligible compared to other relevant time scales (e.g., cyclotron frequency).
 247 The solar wind is an example of a weakly collisional, magnetized plasma that is constantly
 248 emitted from the Sun with variable speeds from ~ 280 km/s to >800 km/s (e.g., see Fig-
 249 ure 2) and comprised of $\sim 95\%$ protons, $\gtrsim 4\%$ alpha-particles, and electrons (e.g., see re-
 250 view by Verscharen, Klein, & Maruca, 2019). In the solar wind near Earth, one Debye
 251 length is ~ 9 meters while the scattering cross-sectional radius for neutral particles can
 252 be roughly six orders of magnitude smaller. Further, the transit time from the sun to
 253 the Earth for a typical solar wind parcel is ~ 3 -4 days while the Coulomb collision pe-
 254 riod between particles is typically $\gtrsim 0.5$ -1.0 days (e.g., see discussion in Wilson III et al.,
 255 2018, and references therein). Many plasmas, like that of the solar wind, are not in ther-
 256 modynamic or even thermal equilibrium. That is, the temperatures of species s' and s
 257 are not equal or $(T_{s'}/T_s)_{tot} \neq 1$ for $s' \neq s$ (see Appendix A for symbol definitions) and
 258 there is an ubiquitous presence of finite heat fluxes, i.e., nonequilibrium particle distri-
 259 butions. The former negates thermal equilibrium and both the former and latter negate
 260 thermodynamic equilibrium.

261 The collisionless limit is obviously that which ignores all Coulomb collisions on the
 262 time scales of interest. Shock waves in most space plasma environments are considered
 263 collisionless because the gradient scale length of the ramp tends to fall between the elec-
 264 tron and ion inertial lengths (i.e., ~ 1 -100 km near Earth) while the Coulomb collision
 265 mean free path of protons can be ~ 1 AU⁴ (e.g., Wilson III et al., 2018). Thus they are
 266 called collisionless shocks.

267 A shock is a sudden transition between supersonic and subsonic flows and is char-
 268 acterized by an abrupt change in pressure, temperature, and density in the medium (e.g.,
 269 see discussion in Krasnoselskikh et al., 2002; Shu, 1992; Wilson III, 2016; Wilson III et
 270 al., 2017, and references therein). Shock waves can arise from the nonlinear steepening
 271 of compressional waves when the steepening is balanced by some form of irreversible en-
 272 ergy dissipation (e.g., see discussion in Shu, 1992). Despite their collisionless nature, shock
 273 waves can and do form in the solar wind. This can result either from some magnetic dis-
 274 turbance propagating faster than the supersonic solar wind (e.g., solar transient erup-
 275 tions) or said disturbance standing against the incident solar wind (e.g., planetary bow
 276 shocks). A shock will arise if the difference in speed exceeds the fast magnetosonic speed
 277 (see Appendix A for definitions), i.e., the relevant speed of communication in the medium.

278 Collisionless shock waves are distinguished by their Mach number (M_f), shock nor-
 279 mal angle⁵, θ_{Bn} (e.g., quasi-perpendicular shocks satisfy $\theta_{Bn} \geq 45^\circ$), and upstream av-
 280 eraged plasma beta ($\langle \beta_{tot} \rangle_{up}$). The asymmetric ram pressure/forces due to the super-
 281 sonic solar wind combined with plasma coupling to the fields causes the Earth's mag-
 282 netic dipole field to be “dragged out” into a tail with the appearance of something akin
 283 to a wind sock. On the sunward (upstream) side of the bow shock, this region of the quasi-
 284 parallel portion of the bow shock is called the ion foreshock (see Section 3.6 and Figure
 285 7) and is filled with multiple backstreaming ion populations and energetic electrons (e.g.,
 286 see discussion in Wilson III, 2016; Wilson III et al., 2016, and references therein). The
 287 interplanetary magnetic field (IMF) can be visualized as open solar magnetic field lines
 288 approaching Earth at approximately 45 degrees to the Earth-Sun direction. The radial
 289 Sun-Earth line is along the horizontal in Figure 3 and the plane shown is orthogonal to
 290 the ecliptic.

291 A unique attribute of *Wind* for solar wind studies is that it is the only near-Earth
 292 spacecraft that consistently measures the “plasma line” (also known as the upper hy-
 293 brid line) in the solar wind, which is primarily dependent upon the total electron den-
 294 sity. The upper hybrid line is a thermal emission that occurs at the upper hybrid fre-

⁴ The Coulomb collision mean free path of protons near 1 AU is also on the order of ~ 1 AU.

⁵ the angle between upstream average magnetic field vector and shock normal unit vector

295 quency, f_{uh} (see Appendix A for symbol definitions), and can be measured because the
 296 WAVES antennae are longer than the local Debye length, λ_{De} (see Table 6). The plasma
 297 frequency is so much larger than the cyclotron frequency in the solar wind, i.e., $f_{pe} \gg$
 298 f_{ce} , that the following is almost always satisfied $f_{uh} \sim f_{pe}$. Even without this approx-
 299 imation, the spacecraft accurately measures the magnetic field so one can invert the ob-
 300 served upper hybrid line frequency to solve for the total electron density. This gives the
 301 only unambiguous measurement of the total electron density from any instrument and
 302 is used to calibrate the thermal particle detectors not just on *Wind*, but other spacecraft
 303 as well (e.g., THEMIS plasma instruments McFadden, Phan, et al., 2008; McFadden, Carl-
 304 son, et al., 2008).

305 To understand charged particle motion, free energy, and instabilities we first in-
 306 troduce the concepts of particle VDFs. A VDF is a seven dimensional function of three
 307 spatial components, three velocity (or momentum) components, and one temporal com-
 308 ponent. Generally, spacecraft measure a VDF at a given time and location, so the VDF
 309 reduces to a three dimensional function of the 3-vector velocity (or momentum). Gener-
 310 ically speaking, the VDF is a probability density function of velocity for a particle en-
 311 semble. An example VDF is the well known Maxwell-Boltzmann distribution, or Maxwellian
 312 (for more examples see Wilson III et al., 2019b, and references therein).

313 Free energy in the context of space plasmas refers to non-Maxwellian features in
 314 a VDF such as temperature anisotropies, secondary beams, excess skewness (i.e., heat
 315 flux), etc. In general, any deviation from an isotropic Maxwellian is a form of free en-
 316 ergy but the magnitude of the deviation is critical for determining whether or how that
 317 energy will be transformed. This definition of free energy derives from the assumption
 318 that an isotropic Maxwellian is the global, maximum entropy distribution.

319 A plasma instability⁶ is the mechanism through which a plasma converts some par-
 320 ticle free energy source into electromagnetic fluctuations. All thermal plasmas contain
 321 pre-existing thermal fluctuations at the natural frequencies of the system, often called
 322 normal modes (e.g., see discussion in Gary, 1993; Stix, 1992). The properties of these
 323 normal modes depend on the background plasma parameters (e.g., magnetic field strength,
 324 density, temperature, etc.). The normal modes determine which possible thermal fluc-
 325 tuations can absorb the free energy from the particle populations, if present, and grow
 326 over time above the thermal amplitude level. In some ways, an instability is like a “walkie
 327 talkie” between the source (particle free energy) and receiver (electromagnetic fluctu-
 328 ations). In this analogy, the transmitting walkie talkie channel frequency is analogous
 329 to the pre-existing normal modes of the system while the receiving walkie talkie is anal-
 330 ogous to the electromagnetic modes. For more details and specific examples of instabil-
 331 ities, see Appendix B.

332 Another topic of considerable interest in plasma physics is magnetic reconnection.
 333 Magnetic reconnection is a universal plasma process by which a change in the magnetic
 334 field topology results in the destruction of magnetic flux and the conversion of electro-
 335 magnetic energy to particle kinetic energy (see Hesse & Cassak, 2020, for a detailed re-
 336 view). Magnetic reconnection has been known to be an important particle energization
 337 mechanism in astrophysical plasmas for decades. It occurs in response to the compres-
 338 sion of regions with oppositely directed magnetic fields. As the oppositely directed mag-
 339 netic fields slowly converge, a current sheet begins to form creating a spatially thin re-
 340 gion called the diffusion region (Sonnerup, 1979). Traditionally this is associated with
 341 a so called “X-line” or place where the magnetic field lines trace out an X (e.g., see the
 342 gray boxes in the cartoon in Figure 6). The diffusion region is where magnetic flux is

⁶Note that the use of both kinetic and plasma instability will occur throughout. The former specifically refers to features in the VDFs while the latter also encompasses fluid-like instabilities.

343 destroyed and electromagnetic energy starts to convert to particle kinetic energy forming
 344 two oppositely directed, outflowing jets, called “reconnection exhausts.”

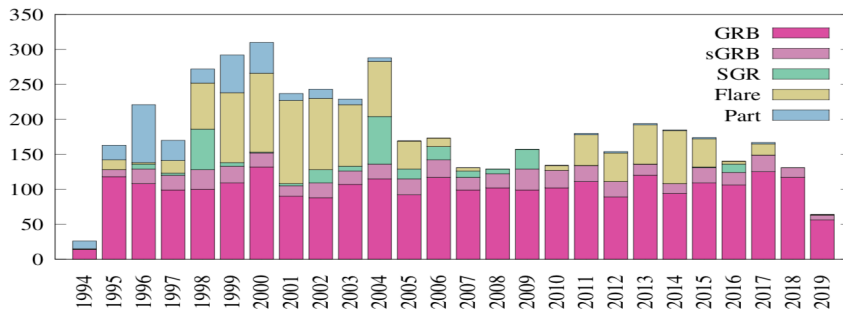
345 When the magnetic field changes on shorter spatial scales than the particles can
 346 respond (i.e., they can no longer follow a single magnetic field line), they are said to be
 347 demagnetized. The magnetic reconnection process starts in the diffusion region, which
 348 is characterized by the presence of dissipative electric fields on small length scales (i.e.,
 349 smaller than the particle gyroradii and/or inertial length). There are in fact two diffusion
 350 regions, one for the electrons and one for the ions. When inside of the ion diffusion
 351 region, thermal ions become demagnetized but electrons can still remain magnetized. How-
 352 ever, inside the electron diffusion region, both particle populations become demagnetized.
 353 The presence of dissipative fields allows changes in magnetic field topology by redistribut-
 354 ing energy between fields and particles resulting in large scale (much larger than ion gy-
 355 roradii and/or inertial lengths) consequences.

356 In the following subsections we highlight selected scientific discoveries and/or ad-
 357 vances made using *Wind* observations.

358 3.1 Remote Astrophysics

359 3.1.1 Gamma Ray Bursts

360 Cosmic gamma ray bursts (GRBs) are the brightest electromagnetic events known
 361 to occur in the universe and are triggered by the collapse of massive stars (long GRBs)
 362 or the coalescence of compact objects (short GRBs). Even though the call for propos-
 363 als to the ISTP program had already taken place, the discovery of gamma ray bursts in
 364 the 1970s by Klebesadel et al. (1973) prompted the addition of two gamma ray detec-
 365 tors to the *Wind* instrument payload, the KONUS (Aptekar et al., 1995) and TGRS (A. Owens
 366 et al., 1995) experiments. The KONUS instrument, also called KONUS-W, is the first
 367 Russian instrument to fly on a US spacecraft.



Statistic of ~4700 KW triggers from November 1994 to mid-2019.

Figure 4: *KONUS* statistics of various astrophysical events emitting gamma rays. The vertical axis is number of events. The color code corresponds to the type of burst trigger for the instrument, which are defined as: GRB is gamma ray burst ($\gtrsim 2740$, magenta); sGRB is short gamma ray burst (~ 500 , purple); SGR is soft gamma repeater (~ 270 , green); Flare is solar flare ($\gtrsim 1040$, yellow); and Part is particle event-induced (taken from Figure 1 in D. Frederiks et al., 2019).

368 By studying GRBs, we can learn about the formation of large-scale structures in
 369 the early universe and present-day processes (Fishman & Meegan, 1995; Fishman, 1995).
 370 GRBs consist of an initial flash of gamma-rays lasting from tens of milliseconds to min-

371 utes followed by a longer duration afterglow at radio and optical wavelengths. KONUS's
 372 combination of broad energy range, longevity, and all-sky coverage make it a unique re-
 373 source for many studies (e.g., Tsvetkova et al., 2017). For a particularly bright short event,
 374 Guiriec et al. (2017) find unique evidence of a photospheric jet by comparing simulta-
 375 neous KONUS^{7,8} and *Fermi* observations. In 2019, the gravitational wave facilities Ad-
 376 vanced LIGO and Virgo provided evidence of short GRBs associated with both binary
 377 neutron star mergers and the emission of gravitational radiation (Abbott et al., 2019)⁹.
 378 As of 2020, 300 bursts per year are detected by KONUS (roughly 6000 to date). Figure
 379 4 shows the number of GRBs detected by KONUS between 1994 and 2019 (D. Frederiks
 380 et al., 2019).

381 **3.1.2 Soft Gamma Repeaters (Magnetars)**

382 Soft gamma repeaters (SGRs), also called magnetars, are strongly magnetized Galac-
 383 tic neutron stars with surface magnetic fields up to 10^{14} G. Magnetars emit large bursts
 384 of X-rays and gamma-rays at irregular intervals (Aptekar et al., 2002; Kouveliotou et al.,
 385 1999). Approximately thirty magnetars have been identified. When these sources become
 386 active, they emit several up to several hundreds of bursts within a timeframe of days to
 387 months.

388 Magnetar giant flares (GFs) are of greater apparent intensity than GRBs with an
 389 average occurrence rate of once per decade (D. D. Frederiks et al., 2007; Hurley et al.,
 390 2010). Only a handful of GFs have been detected. The intensity of a single event is suf-
 391 ficient to create ionospheric disturbances. KONUS has detected extragalactic GFs from
 392 the Andromeda and the M81 group (Mazets et al., 2008; D. D. Frederiks et al., 2007)
 393 and more recently identified a GF from the Sculptor galaxy (Roberts et al., 2021; D. Svin-
 394 kin et al., 2021).

395 Fast radio bursts (FRBs) are bright, millisecond-scale radio flashes whose origins
 396 are a subject of debate (e.g., see review by Petroff et al., 2019). Magnetars have been
 397 suggested as the most promising candidates for fast radio burst progenitors owing to their
 398 energetics and high X-ray flaring activity, but proof of this association has been elusive.
 399 KONUS detected a burst of X- and gamma-rays on April 28, 2020 (Bochenek et al., 2020;
 400 CHIME/FRB Collaboration et al., 2020; Ridnaia et al., 2020) which was temporally co-
 401 incident with a bright, two-peak fast radio burst; the light curves of the radio and X-
 402 ray bursts were remarkably similar. The source was the Galactic magnetar SGR 1935+2154,
 403 which had recently entered an active state. This was the first simultaneous detection of
 404 a fast radio burst from a Galactic magnetar and its high-energy counterpart, and it pro-
 405 vides the long-sought evidence of a magnetar origin for at least some FRBs.

406 **3.1.3 Solar Flares**

407 During its more than 25 year-long history, the KONUS instrument onboard *Wind*
 408 has accumulated an unique volume of solar flare observations in the hard X-ray and gamma
 409 ray range. Data on solar flares recorded by KONUS in the triggered mode are published
 410 online (<http://www.ioffe.ru/LEA/kwsun/>) from 1994 to the present along with their
 411 GOES classification (Pal'shin et al., 2014). This database (see Table C1 in Appendix C)

⁷ KONUS is the most prolific detector in the Interplanetary Network (IPN, <http://ssl.berkeley.edu/ipn3/index.html>), which contains gamma-ray detectors from a variety of telescopes, including *Swift* and *Fermi* (Cline et al., 2001; Hurley, Cline, et al., 2003; Hurley, Atteia, et al., 2003; Hurley et al., 2011), maintained by Dr. Kevin Hurley at UC Berkeley.

⁸ KONUS is also a member of the Gamma-ray Burst Coordinates Network or GCN (<https://gcn.gsfc.nasa.gov>), maintained by Dr. Scott Barthelmy at NASA's Goddard Space Flight Center

⁹ The authors also cite *Wind* data from the Interplanetary Network in their study.

412 provides light curves with high temporal resolution (up to 16 ms) and energy spectra over
 413 a wide energy range (now ~ 20 keV to ~ 15 MeV). The high time resolution of KONUS
 414 allows for the study of fine temporal structure in solar flares (e.g., Lysenko et al., 2018).
 415 The KONUS energy band covers the region of nonthermal emission due to accelerated
 416 electrons and ions in solar flares, which allows probing the source of their acceleration
 417 (e.g., Glesener & Fleishman, 2018). Thus, the *Wind* KONUS solar flare database offers
 418 a new, unique set of data for solar researchers.

419 3.2 Interstellar and Interplanetary Dust

420 The interplanetary and interstellar media are full of small debris ranging in size
 421 from millimeters to nanometers called dust. Dust is important as it can readily trans-
 422 port mass, momentum, and energy throughout the heliosphere but the sources, sinks,
 423 and transport are not well understood. Most of this dust is moving at large speeds re-
 424 lative to spacecraft, resulting in hypervelocity impacts when dust grains collide with space-
 425 craft. Such collisions convert enough kinetic energy to ablate and ionize small portions
 426 of the spacecraft causing a plasma plume to form. This abrupt ionization may be de-
 427 tected with high time resolution electric field instruments, as the plasma plume and ejected
 428 material affects the electric fields near the spacecraft (e.g., see review by Sterken et al.,
 429 2019). Although the original *Wind* mission objectives did not include the detection of
 430 dust, the *Wind*/WAVES TDS receiver has accumulated $>100,000$ identified dust impacts
 431 (Malaspina & Wilson III, 2016).

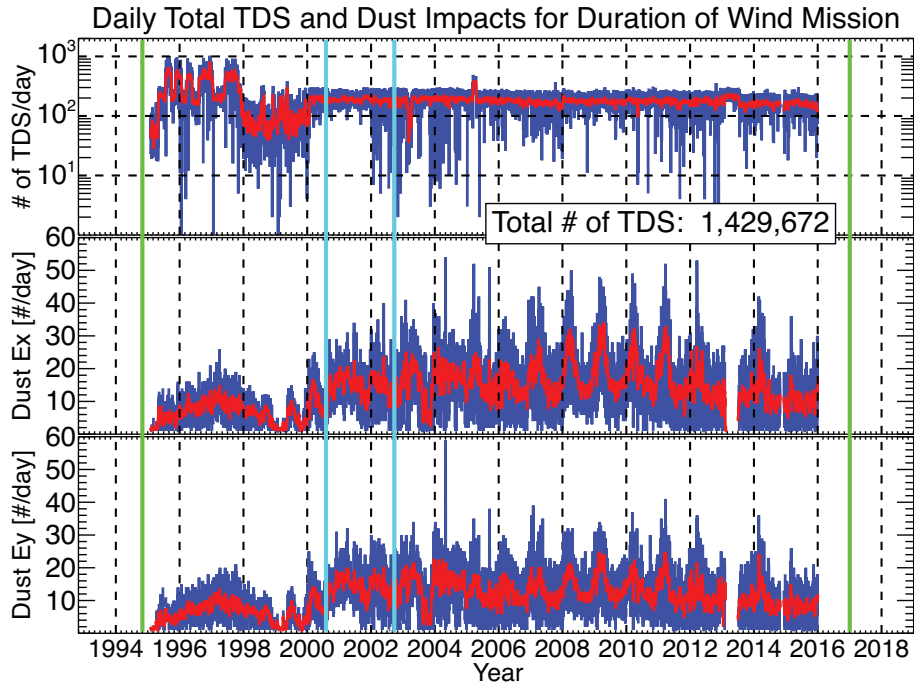


Figure 5: Plot of the entire *Wind* mission showing the daily totals. In each panel the dark blue and red lines represent the actual and 10-day smoothed counts, respectively. The panels shown are the following (in order from top-to-bottom): daily total number of TDS events; number of dust impacts observed on the x-antenna; and number of dust impacts observed on the y-antenna. The two vertical green lines define the duration of the *Wind* mission at the time of creation of this figure (i.e., Jan. 2017). The two vertical cyan lines define the times when the x-antenna was cut apparently by dust impacts (Adapted from Figures 5 and 6 in Malaspina & Wilson III, 2016).

432 Researchers determined that the signals corresponded to micron-sized (i.e., dust
 433 grains approximately $\sim 1 \mu\text{m}$ in size) interplanetary dust (IPD) and interstellar dust (ISD)
 434 (Malaspina et al., 2014; Sterken et al., 2019). S. R. Wood et al. (2015) then determined
 435 the longitudinal direction of ISD using spectroscopic measurements from *Ulysses*, which
 436 was orbiting the solar poles. Although dust had been detected previously using the same
 437 method on other spacecraft (Malaspina et al., 2015; Sterken et al., 2019; I. Mann et al.,
 438 2019), S. R. Wood et al. (2015) presented the first antenna triangulations of ISD with
 439 the *Wind* and *Ulysses* spacecraft across an entire solar cycle. They utilized the yearly
 440 modulation of dust count rates to separate ISD from IPD. The authors show an unex-
 441 plained source of variability in 2005 on a timescale of less than a year. This temporal
 442 variability is interesting because it deviates from the expected temporal variability of the
 443 dust count rates and remains unexplained.

444 Subsequent work led to the creation of a *Wind* dust impact database (Malaspina
 445 & Wilson III, 2016), comprised of $>107,000$ impacts, which is publicly available through
 446 SPDF CDAWeb (see Table C1 in Appendix C). The large statistics allowed researchers
 447 to determine that *Wind* does not respond to dust grains with sizes $\ll 0.1 \mu\text{m}$, the so called
 448 nanodust (Kellogg et al., 2016; Kellogg, 2017; Kellogg et al., 2018; Malaspina et al., 2014;
 449 Malaspina & Wilson III, 2016; Sterken et al., 2019).

450 Figure 5 shows the counting statistics for TDS events and dust impacts observed
 451 by the *Wind* TDS receiver. The obvious annual variation in dust impacts seen in the bot-
 452 tom two panels is primarily due to ISD. The reason is that for half of the year, *Wind* is
 453 moving approximately anti-parallel to the flow of ISD through the solar system. The dif-
 454 ference in flow speed of the ISD in *Wind*'s reference frame varies from $\sim 4\text{--}56 \text{ km/s}$, thus
 455 leading to an annual variation in the counting rates (i.e., higher impact speeds produces
 456 larger electric field amplitudes and thus more dust observations). This annual variation
 457 has been reported in multiple studies (Kellogg et al., 2016; Malaspina et al., 2014; Malaspina
 458 & Wilson III, 2016; S. R. Wood et al., 2015).

459 The *Wind* dust impact database presents exciting opportunities for investigating
 460 heliospheric dust dynamics (Sterken et al., 2019) and statistical studies of the dependence
 461 on large-scale, transient magnetic phenomena (see Sections 3.8.2 and 3.8.3). The rele-
 462 vance of dust has increased in recent years with the recognition that it plays an impor-
 463 tant role in numerous ways from mass, momentum, and energy transport to physical dam-
 464 age to spacecraft (e.g., cutting of wire antenna). For instance, one of the wire antennas,
 465 that form the electric field probes for *Wind*/WAVES, was cut twice by what is suspected
 466 to be dust impacts. The first occurrence happened on August 3, 2000 and the second
 467 time on September 24, 2002.

468 Finally, a more recent development arose when researchers using an Earth-observing
 469 spacecraft, Aeronomy of Ice in the Mesosphere (AIM) (Russell et al., 2009), found some
 470 variations in meteoric smoke – the product of meteoroid ablation (at $\sim 75\text{--}110 \text{ km}$ al-
 471 titude) in Earth's mesosphere. These observations were made by the Solar Occultation
 472 For Ice Experiment (SOFIE) (Gordley et al., 2009). Although the mission is cloud-focused,
 473 cloud science overlaps with studies of dust, geomagnetic activity, and solar cycles (Hervig
 474 et al., 2017, 2019; X. Liu et al., 2018). Interestingly, the temporal variations in meteoric
 475 smoke are consistent with the dust count rates observed by *Wind*, providing a new av-
 476 enue of research and future collaborations.

477 3.3 Lunar Wake Studies

478 Because the moon is relatively nonconducting, the interplanetary magnetic field
 479 passes through the obstacle while solar wind ions and electrons only interact with the

480 lunar surface. *Wind* offered the first modern¹⁰ glimpses into the lunar wake in 1994 giv-
 481 ing inspiration to new simulation efforts focusing on kinetic phenomena (e.g., see histor-
 482 ical discussion in review by Halekas et al., 2015). *Wind* completed 10 wake crossings be-
 483 fore entering a Lissajous orbit at L1 in 2004. Table 5 lists all crossings of the lunar op-
 484 tical wake (Ogilvie & Desch, 1997).

Table 5: Optical Lunar Wake Transits by *Wind*

| Start time [UTC] | End time [UTC] |
|---------------------|---------------------|
| 1994-12-01/15:04:07 | 1994-12-01/15:29:10 |
| 1994-12-27/14:36:30 | 1994-12-27/15:22:36 |
| 1996-03-24/05:19:43 | 1996-03-24/06:24:50 |
| 1996-11-13/01:43:16 | 1996-11-13/03:07:25 |
| 1999-04-01/20:38:02 | 1999-04-01/20:53:04 |
| 1999-05-12/20:52:12 | 1999-05-12/21:04:14 |
| 2000-08-19/15:35:45 | 2000-08-19/16:51:53 |
| 2001-12-05/16:48:53 | 2001-12-05/17:54:00 |
| 2002-07-18/17:46:39 | 2002-07-18/18:42:45 |
| 2002-11-30/11:30:28 | 2002-11-30/12:16:33 |

485 The lunar environment is an exciting laboratory for plasma physics (Halekas, An-
 486 gelopoulos, et al., 2011; Halekas, Saito, et al., 2011; Halekas et al., 2015), comparative
 487 planetology, solar system formation, and astrochemistry. As a result, the near-moon plasma
 488 environment has a low-density downstream cavity called a wake. *Wind* contributed the
 489 first wake measurements more than 2 lunar radii or R_L from the surface (Bosqued et al.,
 490 1996; Farrell et al., 1998; Owen et al., 1996). Ogilvie et al. (1996) presented wake field
 491 and particle observations which contradicted the previously accepted theory of a mag-
 492 netohydrodynamic (MHD) wake flow. The spatial scale of magnetic field perturbations
 493 near the wake should be much larger than an electron orbit while the ions are on a bal-
 494 listic trajectory interacting with an unmagnetized body. Therefore, the ions and elec-
 495 trons could be treated like a fluid around such an obstacle. This is why some of the orig-
 496 inal work suggested an MHD model approach (Farrell et al., 1997; Ogilvie et al., 1996).

497 This MHD model predicted that the lunar wake would extend to no more than four
 498 lunar radii or $\sim 4 R_L$ (Bosqued et al., 1996; Farrell et al., 1998; Owen et al., 1996). How-
 499 ever, *Wind* still observed a wake at $\sim 6 R_L$ (Bosqued et al., 1996; Farrell et al., 1996; Kel-
 500 logg, Goetz, et al., 1996; Ogilvie et al., 1996; Owen et al., 1996). The alignment of the
 501 lunar wake with respect to the moon’s optical shadow helps us understand the complex
 502 ion and electron flow patterns which act to replenish the low-density cavity (Clack et al.,
 503 2004). In the lunar wake, *Wind* observed oppositely directed ion beam distributions (Farrell
 504 et al., 1997; Ogilvie et al., 1996). These beams are a response to asymmetric ambipol-
 505 ar diffusion. Thus, *Wind* provided paradigm shifting observations showing us that the
 506 plasma-moon interaction is kinetic, not fluid, in nature.

507 3.4 Reconnection in the Magnetotail

508 Magnetic reconnection has been known to be an important particle energization
 509 mechanism in astrophysical plasmas for decades (see Hesse & Cassak, 2020, for a detailed
 510 review). This section describes magnetic reconnection discoveries made using *Wind* data

¹⁰ the first lunar wake observations by the *Explorer 35* and *Apollo* missions occurred at around 2 lunar radii from the lunar surface (Ness, 1972)

511 in the magnetotail – the region anti-sunward of Earth where Earth’s magnetic dipole field
 512 lines are stretched and compressed due to the solar wind.

513 Although early observations associated with reconnection in space provided evi-
 514 dence of the reconnection process through downstream outflows identified as exhausts,
 515 the diffusion region was not observed directly (e.g., Paschmann et al., 1979). The ob-
 516 servational discovery of the magnetic reconnection (ion) diffusion region was made in Earth’s
 517 magnetotail at $\sim 60 R_E$ by *Wind* (Øieroset et al., 2001). The primary evidence of recon-
 518 nection presented in this study was the quadrupolar (Hall) magnetic field around an X-
 519 line crossing (see Figure 6), which caused the ions to become demagnetized as they en-
 520 ter the diffusion region. In the same reconnection event, *Wind* found direct evidence that
 521 reconnection can accelerate electrons to suprathermal energies, up to 300 keV (Øieroset
 522 et al., 2002). The *Wind* findings led to new ideas of particle energization in magnetic
 523 reconnection which were developed to explain the observed suprathermal electron en-
 524 ergization. In particular, Drake et al. (2006) suggested that electrons could gain kinetic
 525 energy by reflecting from the ends of the contracting ‘magnetic islands’ that form in the
 526 current sheet as reconnection proceeds. The mechanism is analogous to the increase of
 527 energy of a ball reflecting between two converging walls – the ball gains energy with each
 528 bounce. The repetitive interaction of electrons with many magnetic islands allows a large
 529 number of electrons to be efficiently accelerated to high energy.

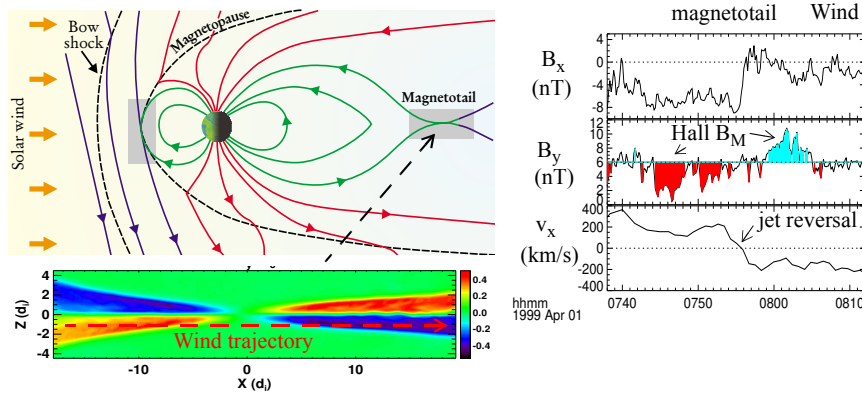


Figure 6: *Wind* encounter with the magnetic reconnection ion diffusion region in Earth’s magnetotail, showing (right) the out-of-plane Hall magnetic field B_y and the reversal of the reconnection outflow jets across the reconnection region. The simulation panel shows the normalized Hall B_y , with *Wind*’s trajectory overlaid (red dashed line). Note that the polarity in the simulation is different from the *Wind* data, which is a consequence of the coordinate basis (Modified from Figures 1 and 2 in Øieroset et al., 2001).

530 Raj et al. (2002) found a clear dawn-dusk asymmetry in the occurrence of mag-
 531 netic reconnection in *Wind* observations in Earth’s magnetotail. Reconnection occurred
 532 preferentially on the dusk side, which links tail reconnection to nightside auroral inten-
 533 sifications¹¹. The *Wind* discovery led to a number of studies trying to explain the source
 534 of the asymmetry, including ionospheric control of tail reconnection Lotko et al. (2014).

¹¹ Auroral intensifications are known to be strongly skewed toward the dusk/pre-midnight sector.

3.5 The Radiation Belts

Wind studies of large amplitude whistler waves in the terrestrial radiation belts (Kellogg et al., 2011; Kersten et al., 2011; Wilson III et al., 2011) have led to a series of new theoretical analyses based upon the new, much larger wave amplitude estimates (note these were originally discovered by C. Cattell et al., 2008, using STEREO observations). A comprehensive review of large amplitude whistler mode waves in the radiation belts can be found in the review by C. A. Cattell et al. (2012). Whistler mode waves are right-hand polarized (with respect to quasi-static magnetic field), electromagnetic emissions that are found in virtually all regions of space (e.g., see discussions in C. A. Cattell et al., 2012; Wilson III, Koval, Szabo, et al., 2013; Wilson III, 2016, and references therein). In the context of the radiation belts, the words *whistler mode wave* includes both chorus-like and hiss-like emissions. See the Glossary and Appendix B for more details.

The peak-to-peak electric and magnetic field amplitudes of whistler mode waves can exceed 200 mV/m and 8 nT, respectively (Kellogg et al., 2011; Wilson III et al., 2011). These values are >10 times the magnitude of previous observations and call into question the assumptions required in quasi-linear diffusion models that are based upon much smaller wave amplitudes (e.g., see review by C. A. Cattell et al., 2012). For each magnetospheric pass examined that traversed the radiation belts, Wilson III et al. (2011) found that large amplitude waves were present in the radiation belts. Kellogg et al. (2011) used *Wind* to provide some of the first evidence that these waves were being excited by electrons with energies below ~ 30 keV – previous work suggested that energies of at least 100 keV were necessary to excite whistler mode waves in the radiation belts. Kellogg et al. (2011) also showed evidence of electron beam-driven electrostatic solitary waves in conjunction with large amplitude whistler mode waves. This result suggested that the energy budget and particle dynamics of the radiation belts are not as well understood as previously thought.

Wilson III et al. (2011) showed that the whistler mode wave amplitudes had a weak positive correlation with the auroral electrojet index or AE-index¹². The large amplitude whistler mode waves in this study were concurrent with earthward injections of ~ 30 –300 keV electrons from the geomagnetic tail. Wilson III et al. (2011) also obtained a lower bound on the Poynting flux of one wave, which was $\gtrsim 300 \mu\text{W m}^{-2}$, or nearly four orders of magnitude larger than any previous measurement for radiation belt whistler mode waves. A previous statistical survey of whistler mode chorus Poynting flux found typical amplitudes of $\sim 0.05 \mu\text{W m}^{-2}$ (Santolík et al., 2010). The authors used this value to estimate the time scale for filling a $\sim 3 R_E$ long, field-aligned column flux tube in the radiation belt with ~ 1 MeV electrons energized from typical plasma sheet energies (i.e., ~ 200 – 10^4 eV). Assuming a 1% efficiency Santolík et al. (2010) estimated that chorus could fill the outer radiation belt in a matter of days, consistent with the then standard assumption of the radiation belt refilling time scale of ~ 1 day (Horne et al., 2005). For comparison, using the $\gtrsim 300 \mu\text{W m}^{-2}$ *Wind* observation and a 1% efficiency, the time scale decreases to ~ 33 seconds providing further evidence that the energy budget and particle dynamics of the radiation belts were not as well understood as previously thought.

These *Wind* studies also helped to define some of the primary science goals for the electromagnetic fields instruments (Wygant et al., 2013) on NASA’s *Van Allen Probes*, which were launched in 2012. The *Wind*-estimated timescale of sub-minute energization was considered much too short at the time of publication but later studies using *Van Allen Probes* (O. Agapitov et al., 2019) reduced the upper limit to less than ~ 3 hours from

¹² a set space weather numerical values designed to provide a global, quantitative measure of auroral zone magnetic activity produced by enhanced ionospheric currents

582 the previous ~ 12 -24 hour time scales¹³. *Wind* also serves as an upstream monitor for
 583 radiation belt studies by the *Van Allen Probes* and other magnetospheric missions (Borovsky
 584 & Denton, 2009; Halford et al., 2015; Jaynes et al., 2015; W. Li et al., 2015; I. R. Mann
 585 et al., 2016; Schiller et al., 2014; Turner et al., 2014).

586 In summary, *Wind* observations have led to paradigm shifting results in radiation
 587 belt studies specifically on particle energization and loss, modeling, and wave generation.

588 3.6 The Ion Foreshock

589 In this section, we discuss the advances made by *Wind* studies to our understand-
 590 ing of the terrestrial foreshock – the region magnetically connected to the quasi-parallel
 591 shock. Studies using *Wind* have shown the foreshock is far larger in spatial extent than
 592 previously thought, giving us insight into new transient, electromagnetic phenomena, and
 593 showed that foreshock transients can locally generate their own miniature foreshocks.
 594 Figure 7 shows a cartoon example of a possible foreshock scenario illustrating the multi-
 595 ple particle population regions and the presence of large amplitude electromagnetic fluc-
 596 tuations/disturbances (see Wilson III, 2016, for detailed review of the foreshock).

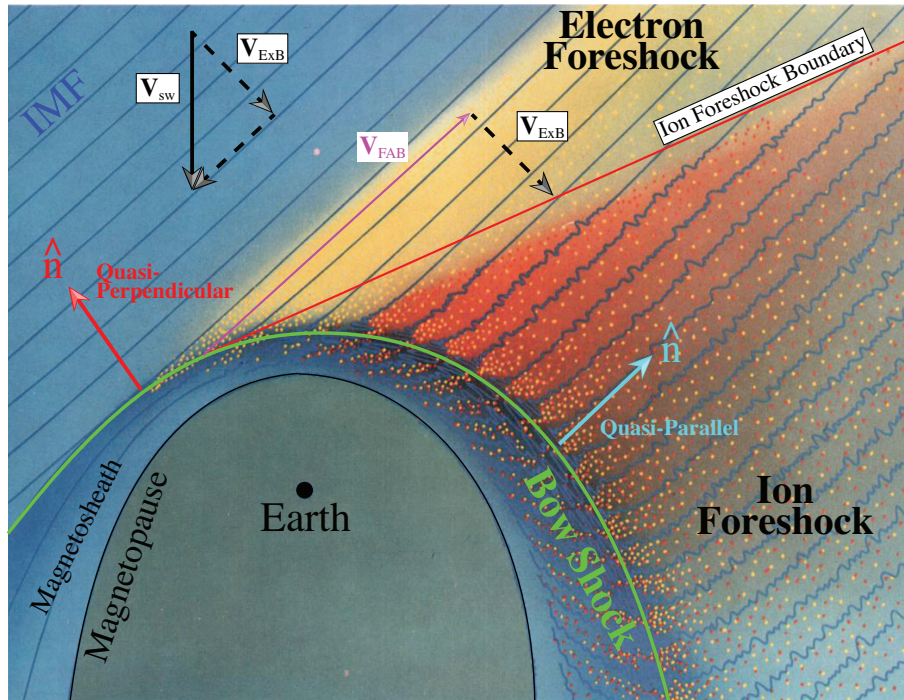


Figure 7: A cartoon example of a possible terrestrial foreshock configuration. The IMF is represented by the dark blue lines, \mathbf{V}_{sw} represents the bulk solar wind velocity, $\mathbf{V}_{E \times B}$ is the $(E \times B)$ -drift velocity due to the solar wind convection electric field, and \mathbf{V}_{FAB} is the reflected field-aligned ion beam velocity (Adapted from Figure 1 of Wilson III, 2016).

597 The spatial extent of shock-reflected ions defines the foreshock boundaries. Prior
 598 to *Wind*, the most distant foreshock measurement was made by ISEE-3 at $200 R_E$, *Wind*'s
 599 predecessor (Scholer et al., 1980). Using *Wind*, D. Berdichevsky et al. (1999) discovered

¹³ Note these time scales are for electrons below ~ 1 MeV. Changes in electrons at or above ~ 1 MeV are still in the ~ 12 hour time range.

600 that the ion foreshock could extend to $\sim 250 R_E$ from Earth. Using a combination of *Wind*
 601 and STEREO observations, Desai et al. (2008) subsequently found ion foreshock par-
 602 ticles $> 3000 R_E$ upstream.

603 In addition to redefining the extent of the foreshock, *Wind* observations also showed
 604 that the high energy cutoff for energetic ions is higher upstream of the quasi-perpendicular
 605 bow shock (Meziane et al., 1999, 2002, 2003) rather than the quasi-parallel bow shock,
 606 in contrast with theory (Caprioli & Spitkovsky, 2014; Park et al., 2015). Upstream of
 607 the quasi-parallel bow shock the highest energy ions only reach ~ 330 keV while upstream
 608 of the quasi-perpendicular bow shock the highest energy ions can reach ~ 2 MeV through
 609 shock drift and/or diffusive shock acceleration. These energetic ions were observed to
 610 be “gyrophase-bunched”¹⁴ due to their single, adiabatic reflection off of the bow shock.

611 At lower energies below ~ 30 keV, *Wind* observations revealed that magnetic field-
 612 aligned ion beams could become disrupted by waves (Meziane et al., 1997; Mazelle et
 613 al., 2000; Meziane et al., 2001). These three studies presented the first *in situ* evidence
 614 that ion-generated foreshock waves can modify foreshock ion velocity distributions by
 615 scattering and trapping the particles.

616 *Wind* has also played a pivotal role in our understanding of transient ion foreshock
 617 phenomena (TIFP) – large-scale (~ 1000 to $> 30,000$ km), solitary [~ 5 – 10 per day and
 618 transient] structures with durations of tens of seconds to several minutes (D. G. Sibeck
 619 et al., 2002; D. Sibeck et al., 2004; Wilson III, Koval, Sibeck, et al., 2013; Zesta & Sibeck,
 620 2004). For instance, D. G. Sibeck et al. (2002) used *Wind* to identify a new transient
 621 ion foreshock phenomenon, called a foreshock cavity¹⁵, which is driven by a diamagnetic
 622 effect due to shock-accelerated ions. More recently, Wilson III, Koval, Sibeck, et al. (2013)
 623 used *Wind* to show that transient ion foreshock phenomena can locally reflect ions, gen-
 624 erating their own miniature foreshocks. This discovery was completely unexpected be-
 625 cause it showed that a collisionless shock can self-consistently energize particles through
 626 a multi-step process: (1) the bow shock reflects incident ions; (2) the reflected ions stream
 627 against the incident solar wind; (3) the counter-streaming ion beams are unstable and
 628 generate TIFP; (4) the TIFP locally energize particles; and (5) these pre-energized par-
 629 ticles interact with bow shock and gain even more energy.

630 In an adjacent region of space called the electron foreshock (see Figure 7), *Wind*
 631 provided the some of the first determinations of the source of radio emissions near $2 f_{pe}$
 632 (Reiner et al., 1996, and see Section 3.10 for more discussion of radio measurements).
 633 The work showed the source region was within the electron foreshock and that the emis-
 634 sion lacked a distinct polarization, which helped advance our understanding of $2 f_{pe}$ emis-
 635 sions and reduced the number of possible sources. *Wind* measurements also allowed re-
 636 searchers to examine some of the first time series electric fields of Langmuir waves (Kellogg,
 637 Monson, et al., 1996). Electron and ion foreshock processes are relevant to a range of
 638 space plasma phenomena, including waves in the lunar wake (see Section 3.3), waves in
 639 the solar wind (see Section 3.7.2, magnetotail reconnection (see Section 3.4), and waves
 640 upstream interplanetary shocks (see Section 3.8.1).

641 In summary, *Wind* observations have led to paradigm shifting results in multiple
 642 areas of foreshock research and opened up new avenues for future studies.

¹⁴ a beam localized in velocity space and not symmetric about \mathbf{B}_0 .

¹⁵ Foreshock cavities are diamagnetic regions surrounded by density enhancements and filled with suprathermal particles. Unlike a somewhat similar phenomena, hot flow anomalies, foreshock cavities do not show significant bulk flow velocity deflections, no dramatic ion temperature increase, and they are not centered on an IMF discontinuity.

643 3.7 Solar Wind Studies

644 This section focuses on *Wind*'s contribution to several fields of solar wind physics.
 645 The section is broken up into four parts including large-scale magnetic phenomena (Sec-
 646 tion 3.7.1), kinetic instabilities and waves (Section 3.7.2), plasma turbulence (Section 3.7.3),
 647 and long-term statistical studies (Section 3.7.4).

648 3.7.1 Large-scale and Reconnection Investigations

649 *Wind*'s diverse orbits (Figure 1) combined with large spatial separation from mul-
 650 tiple other spacecraft provided unique opportunities to investigate large-scale magnetic
 651 phenomena from solar wind structures, large-scale turbulence, interplanetary (IP) shocks,
 652 and solar transients. This section reviews *Wind*'s contribution to advancing our under-
 653 standing of these phenomena on large spatial scales.

654 The prograde orbits extending tangentially in the east/west direction and separated
 655 from Earth by up to 1 degree in heliolongitude provided an opportunity for observations
 656 separated by much larger distances from Earth than is possible using spacecraft at L1.
 657 In fact, *Wind* holds the record for the most time spent at 65-500 R_E (2.5×10^{-3} - 0.02
 658 AU) tangentially from Earth (similar distances were reached by the STEREO spacecraft
 659 in March-April 2007). Investigations using observations from *Wind* and other spacecraft
 660 allowed researchers to test theories of very large scale turbulence (Ogilvie et al., 2007;
 661 Wicks et al., 2009, also see Section 3.7.3), solar energetic particles and energetic storm
 662 particles (Neugebauer & Giacalone, 2005; Neugebauer et al., 2006, see Section 3.9), the
 663 curvature/shape of IP shocks (Koval & Szabo, 2010), and the spatial coherence of in-
 664 terplanetary coronal mass ejections or ICMEs (Farrugia et al., 2005; Möstl et al., 2008;
 665 Lugaz et al., 2018, see Section 3.8.2).

666 Energetic storm particles (ESPs) are particles locally accelerated by an IP shock
 667 and have typical energies between 100 keV and 10 MeV. ESP events are typically clas-
 668 sified into the following types depending on their temporal profile: spike, rise, step, flat
 669 and complex (Lario et al., 2003; Tsurutani & Lin, 1985). There is no simple relation-
 670 ship between the presence/absence and type of ESP events and shock parameters, such
 671 as speed, Mach number, or shock normal angle (Cohen, 2006). To understand how the
 672 acceleration of particles varies along the shock front, ESP measurements made by *Wind*
 673 and ACE of the same events were compared, when *Wind* was in prograde or petal or-
 674 bits. The analyses of 86 ESP events measured for small longitudinal separations ($< 0.7^\circ$)
 675 revealed that the measurements become less correlated as the spacecraft separation in-
 676 creases (Neugebauer & Giacalone, 2005; Neugebauer et al., 2006).

677 The global radius of curvature of CME-driven shocks (Janvier et al., 2015) is thought
 678 to be 0.2-1 AU. This is one of the fundamental quantities that describes shocks since it
 679 characterizes the variation of the large-scale shock normal angle (the angle between the
 680 shock normal and the magnetic field) along the shock front. However, for smaller space-
 681 craft separations ($< 0.5^\circ$), Koval and Szabo (2010) examined 62 shocks measured by *Wind*
 682 and at least one other spacecraft (i.e., ACE, *Geotail*, IMP-8, *Interball-1*, and/or SoHO)
 683 to determine the shock radius of curvature. The largest shock curvature that could be
 684 determined was 0.04 AU, i.e. it reflects the “large-scale local” not global properties of
 685 the shock.

686 Taking advantage of *Wind*'s visit to Earth's magnetotail while ACE remained in
 687 an orbit at L1 in October-November 2003, Farrugia et al. (2005) calculated the radial
 688 correlation length inside ICMEs (see Section 3.8.2) using observations from the two space-
 689 craft radially separated by 0.02 AU, while Möstl et al. (2008) performed one of the first
 690 two-spacecraft reconstructions of a magnetic cloud. *Wind* underwent distant prograde
 691 orbits during the maximum phase of solar cycle 23 (2000 – 2002), i.e., *Wind* moved up
 692 to 0.01 AU tangentially (east-west in GSE coordinates) of the Sun-Earth line while mea-

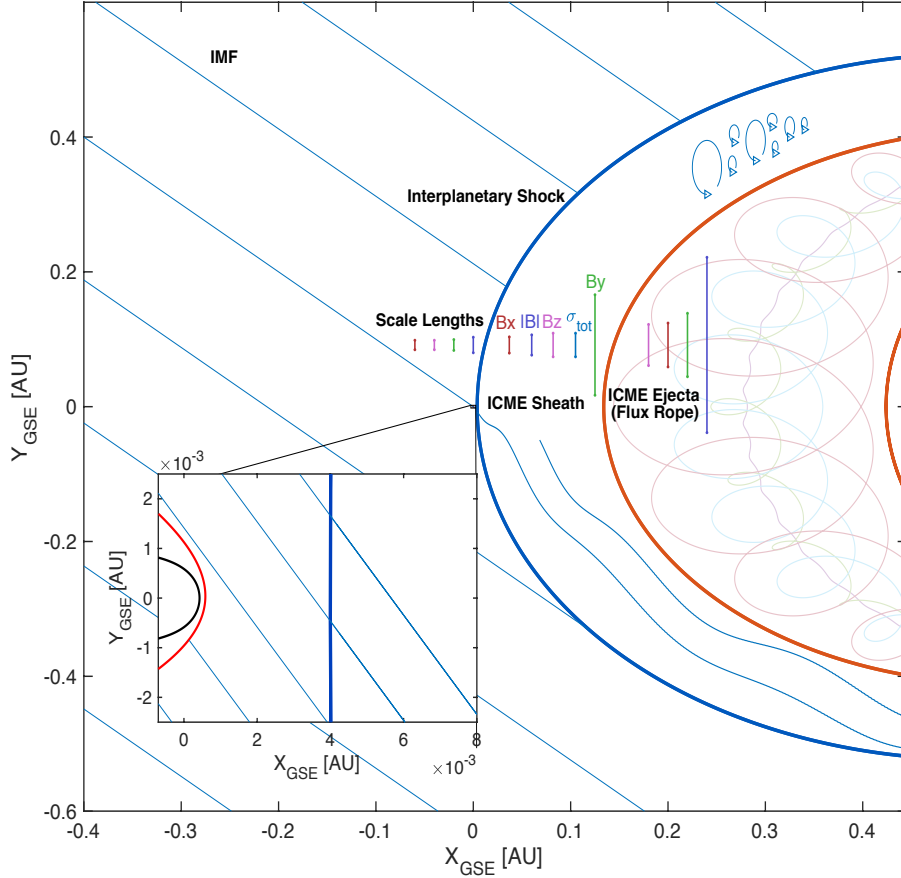


Figure 8: Sketch of an ICME in Earth-centered interplanetary space in the ecliptic plane with scale lengths. The ICME sheath is preceded by an interplanetary shock (dark blue curve) and driven by the ICME ejecta, bounded by orange curves. The ICME is modeled as arcs of a circle by taking the average angular width of the ICME ejecta given by (X. H. Zhao et al., 2017) and the average radial width reported by (E. Kilpua et al., 2017) for the sheath. Blue lines show IMF with a 45° Parker spiral angle at the Earth’s distance from the Sun. Scale lengths of the solar wind (J. D. Richardson & Paularena, 2001), ICME sheath (Ala-Mathi et al., 2020), and ICME ejecta (Lugaz et al., 2018) are illustrated in the y -direction with the color corresponding to the magnetic field component and magnitude as indicated for the sheath region. The correlation in light blue (σ_{tot}) illustrate the scale length associated with the overall Pearson correlation obtained by applying the averaging estimator of correlation coefficients for the Pearson correlation values of the magnitude and components (Adapted from Figure 6 in Ala-Mathi et al., 2020).

693 suring more than two dozen ICMEs. Lugaz et al. (2018) used these periods to calculate
 694 the non-radial correlation length inside ICMEs. Later Ala-Mathi et al. (2020) used the
 695 same observations to calculate the correlation length inside the sheath regions of ICMEs.
 696 Combined with measurements of the correlation lengths in the IP space, a picture of the
 697 coherence of ICMEs near 1 AU has emerged as shown in Figure 8. The correlation scale
 698 lengths of the magnetic field inside ICME ejecta were found to be larger than the scale
 699 lengths in ICME sheaths, themselves larger than the scale lengths in the solar wind, as
 700 expected. In addition, the correlation scale length of the magnetic field magnitude in-
 701 side ICME ejecta was very close to the average ejecta radial width of 0.21 AU (Lepping
 702 et al., 1990). However, the correlation scale lengths of the magnetic field components in-

side ICME ejecta were 2–4 times lower than this value, indicating that magnetic field components may not be correlated at two spacecraft separated by one quarter to one half of a ejecta width. The GSE B_y magnetic field in the sheath has a larger correlation length than any other components, in the solar wind, ICME ejecta or sheath. This may reveal processes associated with the deflection of the magnetic field away from the radial direction behind ICME-driven shocks.

Wind's high time resolution plasma and magnetic field measurements led to numerous studies of reconnection in solar wind current sheets (Gosling, Eriksson, Phan, et al., 2007; Gosling, Phan, et al., 2007; Gosling, 2007; Gosling & Szabo, 2008; Gosling, 2010, 2011). Widely-spaced multi-spacecraft in-situ observations revealed that the reconnection X-line in the solar wind can extend to millions of kilometers (or tens of thousands of ion inertial lengths) and persist for hours (or thousands of Alfvén transit times). An X-line extending at least 390 Earth radii was discovered using observations from *Wind*, ACE and *Cluster* (Phan et al., 2006). Later, even more extreme events, with X-lines extending 660–1800 Earth radii, were reported using in-situ data from *Wind*, ACE, *Geotail*, and both STEREO spacecraft (Gosling, Eriksson, Blush, et al., 2007; Lavraud et al., 2009). These observations indicate that reconnection is not intrinsically bursty and patchy. The process can operate in a large-scale and quasi-steady manner even when un-driven by external flows. These discoveries involving *Wind* could not have been made in Earth's spatially-limited magnetosphere, and have revealed the solar wind as a laboratory for studying the large-scale properties of reconnection.

3.7.2 Kinetic Instabilities and Waves

Perhaps the most unique advance that *Wind* provided to the field of space plasmas was its instrumentation designed to examine small-scale phenomena. For instance, *Wind* was one of the first spacecraft to fully resolve high frequency phenomena like Langmuir waves in time series electric field data (e.g., Kellogg, Monson, et al., 1996). This ability has been further leveraged by *Wind*'s longevity and redundant thermal particle measurement capabilities (i.e., 3DP, SWE, and WAVES), which have allowed researchers to examine one of the more elusive topics in plasma physics, plasma instabilities. Small-scale phenomena play a critical role in the evolution of the solar wind (e.g., see reviews by Marsch, 2006; Verscharen, Klein, & Maruca, 2019). In this section we discuss kinetic instabilities and waves.

Some of the more heavily examined instabilities are those involving temperature anisotropies in both electrons and ions. The long baseline of observations provided by *Wind* allowed researchers to perform a series of long-term statistical evaluations of the stability of particle VDFs in the solar wind (Adrian et al., 2016; Bale et al., 2009; C. H. K. Chen et al., 2016; Hellinger & Trávníček, 2006; Hellinger et al., 2006; Hellinger & Trávníček, 2014; Kasper et al., 2002, 2003, 2006, 2008, 2013; Maruca et al., 2011, 2012; Maruca & Kasper, 2013). *Wind*'s results showed that the firehose, mirror, and ion cyclotron modes (see Appendix B for details) are relevant to limiting the ion temperature anisotropy in the solar wind for protons and alpha-particles. Furthermore, theories of parallel and obliquely propagating firehose instabilities could be compared, which was only possible due to the large statistics and accuracy of the data. The critical takeaway is that some of these results help explain why the ion VDFs deviate from adiabatic approximations as they propagate away from the sun.

Another free energy source of great interest are secondary beams¹⁶ (secondary to the core population). Interestingly, the presence of a differential flow between the proton and alpha-particles was found to reduce the instability thresholds for the temper-

¹⁶ Note that the source of a second proton beam (in addition to the main solar wind proton beam) is still not well established.

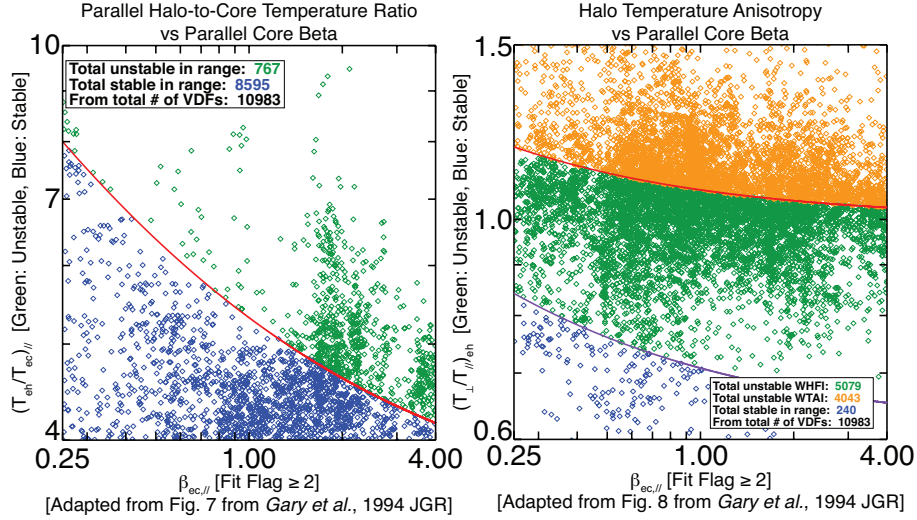


Figure 9: Adaptations of Figures 7 and 8 from Gary et al. (1994) showing the observed data from Wilson III et al. (2020a). The left panel shows the parallel halo-to-core electron temperature ratios, $(T_{eh}/T_{ec})_{||}$, versus parallel core electron beta, $\beta_{ec,||}$ (see Appendix A for symbol definitions) while the right panel shows halo temperature anisotropy, $(T_{\perp}/T_{||})_{eh}$, versus $\beta_{ec,||}$. The left panel is a proxy for heat flux instability while the right for temperature anisotropy instability. In each panel are curves indicating an instability thresholds (corresponding to maximum growth rates satisfying $\gamma_{max} > 10^{-1} \Omega_{cp}$), below(above) which the observed VDF is stable(unstable). Diamonds shown in green and orange are unstable while blue are stable. The green diamonds show data unstable to the whistler heat flux instability (WHFI) while the orange diamonds are unstable to the whistler temperature anisotropy instability (WTAI). This figure illustrates that most electron VDFs are unstable near IP shocks (Taken from Figure 6 in Wilson III et al., 2020a). Note these data are publicly available, e.g., see Table C1 in Appendix C.

751 ature anisotropy instabilities of the Alfvén ion cyclotron and fast/magnetosonic-whistler
 752 modes (Bourouaine et al., 2013; Verscharen et al., 2013; Wicks et al., 2016). Another study
 753 showed electromagnetic ion cyclotron waves were unstable to secondary proton beams
 754 in the solar wind (Wicks et al., 2016) suggesting ion cyclotron wave storms may be lo-
 755 cally generated. While the influence of this secondary proton beam reduces the thresh-
 756 olds for the temperature anisotropy instability, others have found it also introduces a new
 757 beam instability that radiates fast/magnetosonic-whistler modes (Alterman et al., 2018;
 758 C. H. K. Chen et al., 2016; Gary et al., 2016).

759 Electron-driven instabilities are also of great interest as they help regulate the parti-
 760 tion of energy among the multiple electron populations¹⁷ in the solar wind. Specifically,
 761 electron VDFs have been compared with electromagnetic wave observations to test the-
 762 oretical instability thresholds for the whistler mode (Moullard et al., 2001; Wilson III,
 763 Koval, Szabo, et al., 2013; Wilson III et al., 2020a), fast/magnetosonic modes (Kellogg
 764 et al., 2011; Verscharen, Chandran, et al., 2019; Wilson III et al., 2009; Wilson III, Ko-
 765 val, Szabo, et al., 2013), electrostatic solitary modes (Bale, Kellogg, Larson, et al., 1998;
 766 Bale et al., 2002; Kellogg et al., 2011), ion acoustic modes near interplanetary (IP) shocks
 767 (Wilson III et al., 2007; Wilson III, 2010; Wilson III et al., 2020a), Langmuir-like modes

¹⁷ Solar wind electrons are comprised of a cold, dense core, hot tenuous halo, and a warm, magnetic field-aligned beam streaming away from the sun called the strahl (Wilson III et al., 2019b, 2019a, 2020a).

(Ergun et al., 1998; Moullard et al., 2001; Pulupa & Bale, 2008), and electron cyclotron drift instability modes near IP shocks (Wilson III, 2010).

The studies mentioned above have focused on measurements of ions or electrons separately, however the stability of a plasma depends on all species simultaneously. In recent years, data from *Wind*'s multiple particle instruments have been combined to investigate the total plasma stability. C. H. K. Chen et al. (2016) combined data from SWE and 3DP, including all major solar wind species (protons, alphas, and electrons) to compare the stability of the solar wind to the long-wavelength firehose and mirror instabilities, for which analytical thresholds exist. For both instabilities, the dominant contribution ($\sim 2/3$) was found to be from the protons, but there were also significant contributions ($\sim 1/3$) from the other species. When a proton beam was present, drifts between species contributed 57% to the firehose instability. In this combined analysis, both instabilities were found to provide good constraints to the data with $< 1\%$ unstable, suggesting that these long-wavelength multi-species instabilities act to provide a robust limit the evolution of the solar wind.

K. G. Klein et al. (2018) then used a method involving Nyquist's instability criterion to search for the presence of unstable plasma using ion (proton and alpha) data from SWE and assuming isotropic electrons. They found the majority (53.7%) of solar wind intervals to be unstable, with the vast majority of these being kinetic (no long-wavelength counterpart), with growth rates satisfying $\sim 0-0.2 \Omega_{cp}$. However, the majority of growth rates were found to be slow compared to other dynamical timescales, such as the turbulence timescale, making it unclear whether these kinetic instabilities could be dynamically relevant or constrain the solar wind, and may explain why the majority of the plasma was found to be unstable.

Further, examination of ~ 10 years of data found that $(T_e/T_p)_{tot} \gtrsim 3$ was satisfied for $\sim 12.4\%$ of $\sim 446,000$ intervals (Wilson III et al., 2018). This temperature ratio is a threshold often used to determine the separation between strong and weak damping of ion acoustic waves. Wilson III et al. (2020a) examined electron VDFs near IP shocks finding only $\sim 3\%$ were stable to either the whistler heat flux or whistler temperature anisotropy instabilities, as shown in the right-hand panel of Figure 9. They also found $\sim 28.6\%$ of all VDFs examined satisfied $(T_e/T_p)_{tot} \gtrsim 3$ and $\sim 42.8\%$ of upstream-only VDFs satisfied the same criteria, i.e., conducive for ion acoustic wave growth. To compare with ambient solar wind studies, Wilson III et al. (2020a) examined the rate of instability of the firehose and mirror modes finding $\sim 1.3\%$ and $\sim 13.5\%$ were unstable, respectively. These rates are ~ 10 and ~ 20 times higher than those found by C. H. K. Chen et al. (2016) in the ambient solar wind for the same instability criteria.

These studies are just small sample of the overall contribution *Wind* has provided to advancing our understanding of instabilities. *Wind* data has revealed that solar wind VDFs are likely strongly shaped by plasma instabilities as they propagate away from the Sun and that the amplitudes of high frequency waves can be orders of magnitude larger than previous data would suggest. These advances were only possible with *Wind*'s unique suite of instruments and the major advance in resolution they provide.

3.7.3 Turbulence

Wind has enabled significant advances in our understanding of plasma turbulence. These were made possible due to the continuous 3 second resolution plasma moments from 3DP together with magnetic field vectors at up to 22 samples per second, allowing the full inertial range to be studied with all MHD variables for the first time, and the start of the kinetic range to begin being probed in detail. These high-resolution data are supported by measurements of the ion temperature anisotropy from SWE allowing a detailed examination of the interaction of electromagnetic fields and particles as a result of turbulence. The many years of data in the free solar wind also allow the study

819 of the dependence of the turbulence properties on important parameters, such as plasma
 820 beta and cross-helicity. In this section, we discuss *Wind*'s contribution to our understand-
 821 ing of plasma turbulence.

822 Turbulence can be described as fluctuations in properties of the plasma (e.g., den-
 823 sity) that are chaotic in nature (Bruno & Carbone, 2013; Verscharen, Klein, & Maruca,
 824 2019). Turbulence is an intrinsically multi-scale phenomenon where energy enters at large
 825 spatial scales and cascades to much smaller scales. Although the individual realizations
 826 cannot be predicted, the statistical properties of the energy cascade rate can be derived
 827 and in plasmas it changes at different temporal and spatial scales. Unlike in neutral fluid
 828 turbulence, turbulence in magnetized plasmas is generally anisotropic. That is, the dis-
 829 tribution of power in wave vector (\mathbf{k}) space is not equal in all directions relative to \mathbf{B}_0 ,
 830 i.e., $k_\perp \neq k_\parallel \neq k$. Often turbulence is examined by use of Fourier transforms in frequency
 831 or wavenumber space. In the solar wind, for instance, the magnetic fluctuation power
 832 spectrum has the form of multiple broken power-laws where each power-law corresponds
 833 to a different type of cascade. The range with the largest scales and lowest frequencies
 834 in the spacecraft frame is referred to as the injection range or outer scale. The next range
 835 is called the MHD inertial range and it extends up to slightly larger than the relevant
 836 ion scales (e.g., ion inertial length or ion thermal gyroradius). Beyond this is the kinetic
 837 range, also sometimes known as the dissipation range¹⁸ since this is where fluctuations
 838 can transfer energy to the medium through heat. For more details, see Appendix A and
 839 the Glossary for definitions.

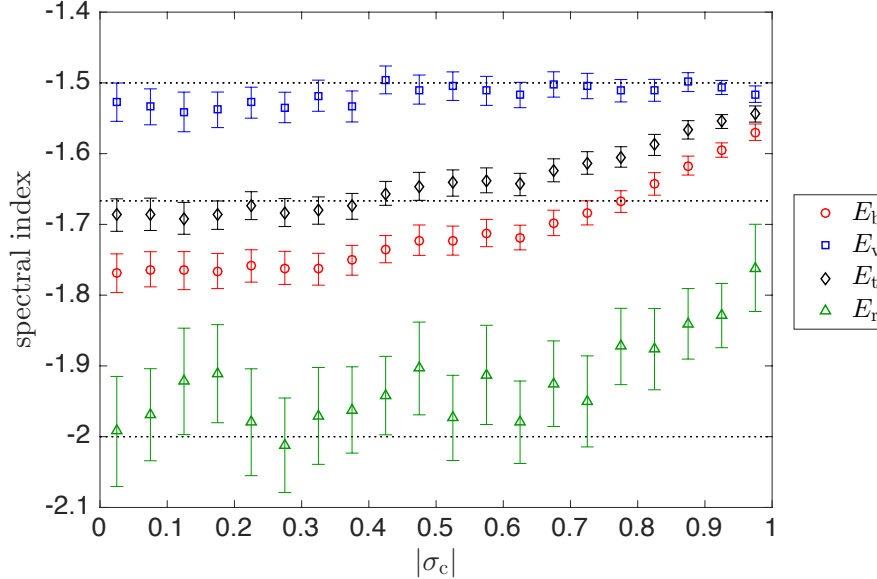


Figure 10: Variation of the wavenumber power spectral indices of magnetic field (E_b), velocity (E_v), total ($E_t = E_b + E_v$), and residual energy ($E_r = E_v - E_b$) with the level of imbalance $|\sigma_c|$. Note that $|\sigma_c| \approx 0$ corresponds to balanced turbulence and $|\sigma_c| \approx 1$ to highly imbalanced turbulence (Adapted from Figure 4 in C. H. K. Chen, 2016).

¹⁸ Note that this term has become less relevant and been replaced by “kinetic range.”

840 An important achievement of *Wind* has been to establish the MHD inertial range
 841 scaling properties. Mangeney (2001) investigated the scaling of the magnetic and veloc-
 842 ity fluctuations through conditioned structure functions, finding the velocity to have a
 843 shallower scaling, consistent with a wavenumber spectrum $k^{-3/2}$, compared to $k^{-5/3}$ for
 844 the magnetic field. This finding was confirmed by later studies (Podesta et al., 2006, 2007;
 845 Salem et al., 2009). Podesta and Borovsky (2010) showed that both Elsasser spectra¹⁹
 846 scale as $k^{-5/3}$, but that the magnetic field and total²⁰ energy spectra scale as $k^{-3/2}$ when
 847 the cross-helicity is large, which has since been confirmed by others (Boldyrev et al., 2011;
 848 C. H. K. Chen et al., 2013). These differences are significant since leading models of plasma
 849 turbulence predict these scalings, e.g., a total energy spectrum $k_{\perp}^{-5/3}$ by Goldreich and
 850 Sridhar (1995) and $k_{\perp}^{-3/2}$ by Boldyrev (2006). Boldyrev et al. (2011); Boldyrev and Perez
 851 (2012), based on previous work by Grappin et al. (1983), proposed that the difference
 852 between magnetic and velocity fluctuation spectra is due to turbulence-generated resid-
 853 ual energy, which is predicted to scale as k_{\perp}^{-2} and this steep scaling was confirmed by
 854 C. H. K. Chen et al. (2013). The large dataset provided by *Wind* allows conditional statis-
 855 tics to be used to separate solar wind with different properties and this has allowed the
 856 measurement of the impact of cross helicity and residual energy on the turbulent cas-
 857 cade to be measured simultaneously (Bowen et al. (2018), Bruno et al. (2007), and Wicks,
 858 Mallet, et al. (2013) following Bavassano et al. (1998)). The current state of knowledge
 859 is summarized in Figure 10 which shows the inertial range spectral indices of the MHD
 860 fields as functions of cross-helicity, $|\sigma_c|$, which is a quantitative measure of imbalance²¹.
 861 While not every aspect of this figure is explained (notably the cross-helicity dependence
 862 of the total energy spectrum), we are tantalizingly close to understand the physics that
 863 governs the spectral properties of the MHD turbulence cascade, and *Wind* has played
 864 a dominant role in enabling this.

865 *Wind* has also allowed us to measure the anisotropy of the turbulence to further
 866 determine the physics of the cascade. Wicks et al. (2011) used a wavelet technique (based
 867 on Horbury et al. (2008)) to measure the spectrum of the Alfvénic turbulence variables
 868 with respect to the local mean field direction. Deep in the inertial range, all fields were
 869 shown to be anisotropic, $k_{\perp} \gg k_{\parallel}$, with velocity, magnetic, and the dominant Elsasser
 870 field having k_{\parallel}^{-2} scaling parallel to the local mean field. This k_{\parallel}^{-2} spectrum is one the
 871 key predictions of critical balance, the conjecture at the heart of modern turbulence theo-
 872 ries, implying that the turbulence becomes increasingly anisotropic towards smaller scales.
 873 Verdini et al. (2018) took this further by using a structure function technique (based on
 874 C. H. K. Chen et al., 2012) to measure the 3D anisotropy of the turbulent eddies, con-
 875 cluding that under conditions of weak solar wind expansion the turbulence spectrum is
 876 different in all 3 directions resulting in “ribbon” rather than “tube” shaped eddies at small
 877 scales, consistent with the Boldyrev (2006) picture. Verdini et al. (2019) then showed
 878 that this is also true for the velocity fluctuations, although they maintain overall their
 879 shallower scaling compared to the magnetic fluctuations. Figure 11 shows an example
 880 of the 3D magnetic eddy shapes measured by *Wind*.

881 While the dominant fluctuation power in the solar wind is in the Alfvénic fluctu-
 882 ations, there is also a subdominant compressive component to the turbulence, which presents
 883 some interesting, but quite different physics. While it has long been known that the so-
 884 lar wind compressive components are broadly pressure-balanced, Howes et al. (2012) and
 885 K. G. Klein et al. (2012) performed a statistical analysis on the density and magnetic
 886 field strength correlation as a function of plasma β using 10 years of *Wind* data. They
 887 concluded a compressive component is consistent with being almost entirely in the ki-

¹⁹ spectra of the Elsasser variables \mathbf{z}^{\pm} defined in Appendix A

²⁰ i.e., magnetic plus velocity fluctuation energies

²¹ imbalance here refers to the different fluxes of turbulent fluctuations propagating toward or away from the sun

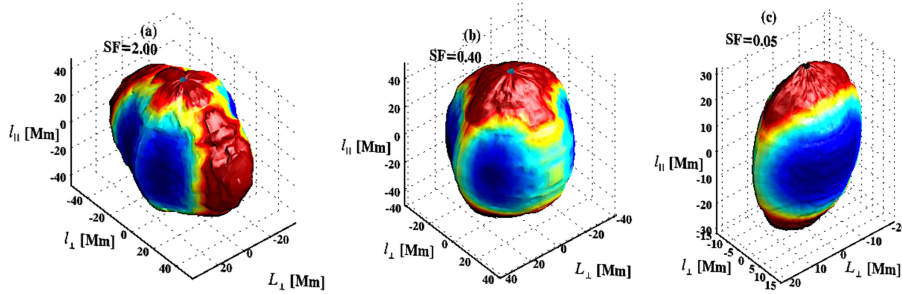


Figure 11: Statistical 3D eddy shapes of magnetic fluctuations at three different scales in the inertial range, from large scales (left) to small scales (right), for the case of weak expansion. Colors represent distance from the origin (Adapted from Figure 11 in Verdini et al., 2018).

888 netic slow mode, implying very little or no transfer of energy to whistler turbulence at
 889 smaller scales. Later, Verscharen et al. (2017) compared a larger variety of compressive
 890 quantities to linear predictions for both kinetic and MHD slow modes, finding the MHD
 891 polarizations to be a good match. This unexpected²² finding raises interesting possibil-
 892 ities about what may be causing such fluid-like behavior in the weakly-collisional solar
 893 wind, with possibilities including wave-particle scattering and anti-phase-mixing; both
 894 topics have much broader implications for weakly-collisional plasma physics in general.

895 It is well known that plasma turbulence is not a completely random process but
 896 generates correlated intermittent structures (e.g., Bruno & Carbone, 2013; Salem et al.,
 897 2009). However, an open question in solar wind physics is exactly how much of the struc-
 898 ture in the solar wind is generated in situ by turbulence vs remnant structure from pro-
 899 cesses at the Sun (Borovsky, 2008; M. J. Owens et al., 2010). One view is that large an-
 900 gles magnetic field rotations represent flux tubes or other structures from the Sun, while
 901 the turbulence is responsible for the small-amplitude fluctuations of these structures. How-
 902 ever, Zhdankin et al. (2012) presented an analysis to suggest that turbulence can account
 903 for the full distribution of angle rotations, large and small. They compared 5 years of
 904 *Wind* observations to an MHD turbulence simulation to show a very good match for this
 905 distribution, concluding that the majority of solar wind discontinuities arise as intermit-
 906 tent structures from the turbulent cascade. Osman et al. (2012) investigated these struc-
 907 tures further, finding the plasma near the discontinuities to be hotter and the temper-
 908 ature more anisotropic and often marginal to the mirror and firehose instabilities, sug-
 909 gesting a link between the structures, turbulent heating and kinetic instabilities. Although
 910 the debate on the nature of the structures continues, these results from *Wind* have changed
 911 the way we view solar wind structure.

912 At the large-scale end of the cascade, the correlation length of turbulence is linked
 913 to the energy containing scales that feed the cascade. When measuring such large-scale
 914 fluctuations in the solar wind, one significant problem is that plasma travels quickly over
 915 the spacecraft, meaning that at long timescales the stream structure dominates the sig-
 916 nature, rather than the low-frequency fluctuations that might be present within streams.
 917 The extensive *Wind* dataset allowed Bruno et al. (2019) to measure the low-frequency
 918 spectrum within extended intervals of slow solar wind, showing for the first time that
 919 slow solar wind, like the fast wind, is also able to support a “1/f” range, in addition to
 920 this well-known result in fast wind. Long time series of fast wind data from *Wind* were

²² It was not expected that MHD would do so well at predicting the polarizations since the solar wind is a weakly collisional plasma.

921 also used by Wicks, Roberts, et al. (2013) to show that the scale at which the 1/f range
 922 transitions to the inertial range of turbulence depends on the correlation properties of
 923 the fluctuations at the spectral break. Intervals with less aligned velocity and magnetic
 924 field fluctuations become turbulent at larger scales, even within a single stream. The re-
 925 realization of this property of turbulence is significant since it indicates that the turbu-
 926 lence spectrum may extend to larger scales than previously thought.

927 Data from *Wind* MFI and SWE have been used in combination with data from other
 928 spacecraft to achieve multi-point measurements of the turbulence in the solar wind. Such
 929 a multi-point analysis allows the study of the space-time structure of the turbulent fluc-
 930 tuations without having to rely on Taylor’s frozen-in hypothesis, which is usually em-
 931 ployed in single-point measurements (Verscharen, Klein, & Maruca, 2019). By combin-
 932 ing plasma and magnetic-field data from IMP-8 and *Wind*, J. D. Richardson and Paularena
 933 (2001) calculated multiple correlation coefficients for solar wind turbulence. The scale
 934 sizes for changes in the magnetic-field components perpendicular to the flow direction
 935 were found to be about 0.002 AU, while the plasma velocity and density scale lengths
 936 were found to be larger by a factor of more than two. The same study found a radial scale
 937 length of order 0.017 AU. These results were supported by a later study using the am-
 938 plitude ratio, coherence, and phase lag of field and plasma measurements from *Wind* and
 939 ACE (Matsui et al., 2002), although the radial scale was somewhat smaller than in the
 940 earlier estimate.

941 The combination of magnetic-field data from *Wind* with quasi-simultaneous mea-
 942 surements from ACE and *Cluster* facilitated the determination of the Eulerian correla-
 943 tion scale and the Taylor microscale in the solar-wind plasma frame near Earth (Matthaeus
 944 et al., 2005). This multi-spacecraft comparison gives an estimate for the omni-directional
 945 correlation length of 0.0082 AU. The combination of this result with *Cluster*’s simulta-
 946 neous measurement of the Taylor microscale of 1.6×10^{-5} AU provides an estimate for
 947 the effective Reynolds number of about 230,000 in the measured solar-wind interval. The
 948 same method also reveals a Eulerian decorrelation time of about 2.9 hours in the solar
 949 wind near 1 AU (Matthaeus et al., 2010). Later combinations of ACE, *Geotail*, and IMP-
 950 8 data with *Wind* data refined this picture, finding slightly smaller correlation lengths
 951 and different correlation lengths in fast and slow solar-wind streams (Matthaeus et al.,
 952 2016; Wicks et al., 2009, 2010). *Wind* also supported other turbulence studies through,
 953 for example, cross-calibrations with ACE measurements for the OMNI datasets (King
 954 & Papitashvili, 2005) or as a source of magnetic-field measurements for spacecraft with-
 955 out a working magnetometer (Pitña et al., 2019; Šafránková et al., 2019).

956 Leamon et al. (1998) attempted to distinguish between wave and turbulence paradigms
 957 at the dissipation scale using *Wind* MFI solar wind data. The authors observed steep-
 958 ening of the magnetic field spectrum at ~ 1 Hz with an associated increase in compress-
 959 ibility and non-zero magnetic helicity. Further, the turbulence was measured to be sig-
 960 nificantly oblique, interpreted as a combination of kinetic Alfvén waves and 2D ($k_{\parallel} =$
 961 0) modes. A reinterpretation of these results has contributed to our current understand-
 962 ing of a critically balanced dispersive cascade of kinetic Alfvén turbulence (with some
 963 damping at ion and electron scales).

964 Another way to understand the processes occurring in the kinetic range is to in-
 965 vestigate the scale at which the spectral break occurs. Leamon et al. (2000) compared
 966 the measured power spectral break point – the frequency or wavenumber where the power
 967 spectral density power-law profile changes exponent – to the cyclotron frequency, par-
 968 allel resonant wavenumber, and inertial scale, finding the latter to have the best corre-
 969 lation, and suggested this could be related to current sheets of the break point thickness.
 970 Bruno and Trenchi (2014) used *Wind* in combination with MESSENGER and *Ulysses*
 971 observations to show that the break point evolves linearly with distance from the Sun,
 972 similarly to the ion gyroscale, inertial length, and cyclotron resonance scale. The authors
 973 concluded that the scale of cyclotron resonance controls the linear evolution. The dif-

974 faculty, however, in distinguishing these scales (and therefore processes) is that at $\beta \sim$
 975 1 they are essentially the same, so C. H. K. Chen et al. (2014) examined intervals of very
 976 high and low β , showing the break point to be at the gyroscale at high β and inertial
 977 scale at low β . Woodham et al. (2018) came to a similar conclusion using the large *Wind*
 978 data archive and examining the full range of β . The high β result matches expectations
 979 for a transition to dispersive kinetic Alfvén turbulence, but a fully consistent explana-
 980 tion for the low β result has yet to be identified and remains an open question. Boldyrev
 981 et al. (2015) suggested that the result could be explained by a significant field-parallel
 982 wavenumber component at low β . Vech et al. (2018) used *Wind* data at low electron β
 983 to suggest the break to be related to the disruption scale at which reconnection could
 984 dominate the cascade dynamics. We still have much to learn about kinetic range tur-
 985 bulence, but *Wind*'s early pioneering results have certainly given key valuable insights.

986 The early Leamon et al. (1998) results were followed up by statistical studies of the
 987 high-frequency magnetic field data, identifying key features of coherent waves with dis-
 988 tinct left-handed and right-handed rotations (Markovskii et al., 2015). Woodham et al.
 989 (2019) linked these helical waves to the SWE proton temperature anisotropy data and
 990 showed that field-parallel propagating modes at the spectral break scale are dominated
 991 by ion cyclotron waves driven by temperature anisotropy and proton and alpha partic-
 992 le beams (Wicks et al., 2016) but the background of oblique modes are kinetic Alfvén
 993 waves with no particular dependence on proton temperature anisotropy. These statisti-
 994 cal studies, only possible with *Wind*, demonstrate the link between particle temper-
 995 ature and the inertial range energy cascade, and provide the current best knowledge of
 996 energy transfer in turbulent space plasmas.

997 These are just a selection of results that *Wind* has enabled in solar wind turbu-
 998 lence, but they illustrate the diverse aspects of the physics that have been revealed. Hope-
 999 fully *Wind* will continue contributing to our understanding of this important and widespread
 1000 plasma process over the coming years, in particular in combination with new missions
 1001 such as *Parker Solar Probe* and *Solar Orbiter*, where the multi-point measurements will
 1002 likely prove to be invaluable (e.g., Velli et al., 2020).

1003 **3.7.4 Long-term Solar Wind Studies**

1004 *Wind*'s longevity has been a major advantage for long-term statistical studies of
 1005 solar wind physics. Combined with the most accurate solar wind plasma measurements
 1006 of any near-Earth spacecraft, *Wind* observations have helped researchers uncover sub-
 1007 tle collisional effects, the first statistically significant estimate of the electron-to-ion tem-
 1008 perature ratio, $(T_e/T_s)_{tot}$ ($s = p$ for protons, α for alpha-particles), and novel relation-
 1009 ships between the alpha-to-proton abundance ratio and parameters such as the solar wind
 1010 speed and sunspot number. In this section, we highlight some of these results.

1011 Surprisingly, the first long-term statistical study of $(T_e/T_s)_{tot}$ was only recently
 1012 performed using *Wind* observations (Wilson III et al., 2018). The study used ~ 10 years
 1013 of solar wind data²³. A summary of the results for all solar wind conditions from Wilson
 1014 III et al. (2018) are shown in Table 6. See Appendix A for further symbol definitions.

1015 Wilson III et al. (2018) showed, however, that not only is the solar wind plasma
 1016 not in thermodynamic equilibrium, the plasma isn't in thermal equilibrium either²⁴. The
 1017 authors illustrated that because the particle-particle Coulomb collision rates are so low
 1018 in the IP medium, an interaction with just one small-amplitude wave packet can cause

²³ from January 1995 to December 2004, publicly available at SPDF CDAWeb

²⁴ Note that the work by Wilson III et al. (2018) was not the first to show the solar wind is out of equi-
 librium. It is referenced here as it's recent, it's a *Wind*-based study, and it shows the largest statistically
 significant dataset that includes electron velocity moments.

Table 6: Long-term Solar Wind Statistics

| Parameter | $X_{25\%}$ ^a | $X_{75\%}$ | \tilde{X} ^b |
|---------------------------------|-------------------------|------------|--------------------------|
| Densities | | | |
| n_e [cm^{-3}] | 5.71 | 13.0 | 8.57 |
| n_p [cm^{-3}] | 5.05 | 11.7 | 7.61 |
| n_α [cm^{-3}] | 0.13 | 0.32 | 0.21 |
| Temperatures and Thermal Speeds | | | |
| $T_{e,tot}$ [eV] | 9.41 | 13.1 | 11.1 |
| $T_{p,tot}$ [eV] | 4.80 | 15.1 | 8.45 |
| $T_{\alpha,tot}$ [eV] | 5.43 | 34.0 | 12.2 |
| $V_{T_{e,tot}}$ [km/s] | 1579 | 2411 | 1975 |
| $V_{T_{p,tot}}$ [km/s] | 21.9 | 76.9 | 40.2 |
| $(T_e/T_p)_{tot}$ | 0.78 | 2.14 | 1.28 |
| $(T_e/T_\alpha)_{tot}$ | 0.32 | 1.78 | 0.82 |
| $(T_\alpha/T_p)_{tot}$ | 1.39 | 3.62 | 2.01 |
| Plasma Betas | | | |
| $\beta_{e,tot}$ | 0.83 | 2.64 | 1.45 |
| $\beta_{p,tot}$ | 0.67 | 1.90 | 1.16 |
| $\beta_{\alpha,tot}$ | 0.02 | 0.19 | 0.07 |
| Frequencies and Lengths | | | |
| f_{cp} [Hz] | 0.04 | 0.22 | 0.09 |
| f_{ce} [Hz] | 80.2 | 409 | 162 |
| f_{pp} [Hz] | 371 | 944 | 578 |
| f_{pe} [kHz] | 17.2 | 42.5 | 26.3 |
| ρ_{ce} [km] | 1.03 | 4.62 | 2.28 |
| ρ_{cp} [km] | 32.5 | 186 | 88.8 |
| λ_e [km] | 1.12 | 2.77 | 1.82 |
| λ_p [km] | 50.5 | 129 | 82.5 |
| λ_{De} [m] | 4.74 | 13.8 | 8.58 |

^a $X_{y\%}$ is the y^{th} percentile ^b \tilde{X} is the median

1019 a greater effect than the cumulative effect of collisions between the sun and Earth. This
1020 begs the question of why we actually see any evidence of particle-particle collisions in
1021 the solar wind (e.g., see results in Adrian et al., 2016; Bale et al., 2013; Horaites et al.,
1022 2015, 2019; Kasper et al., 2017; Maruca et al., 2013; Salem et al., 2003; Wilson III et al.,
1023 2018, 2019a) since we consistently observe, directly or indirectly, numerous different types
1024 of electromagnetic fluctuations in the solar wind (O. V. Agapitov et al., 2020; Bale et
1025 al., 2009; He, Wang, et al., 2015; He, Pei, et al., 2015; He et al., 2019; Kasper et al., 2013;
1026 Malaspina et al., 2020; Maruca et al., 2012; Vasko et al., 2020; Wicks et al., 2016). That
1027 is, the ubiquitous electromagnetic waves should wash out any particle-particle collision
1028 signatures much faster than particle-particle collisions can relax the distributions²⁵. The
1029 observation of collisional effects despite their weak/slow influence on the particle distri-

²⁵ Note that the result of wave-particle interactions is not to reduce a particle distribution to an isotropic Maxwellian. Rather, wave-particle interactions tend to produce power-laws or plateaus and sometimes even introduce anisotropies (e.g., see discussion in Wilson III et al., 2020a, and references

1030 butions compared to other effects (e.g., waves and/or turbulence) remains an outstand-
 1031 ing question.

1032 In contrast researchers have found evidence of a preferential ion heating source in
 1033 the solar corona and even placed limits on the heliocentric distance below which this heat-
 1034 ing occurs (Kasper et al., 2017; Kasper & Klein, 2019), a result only found due to the
 1035 large statistics available from *Wind* data sets. That is, the ions appear to be heated be-
 1036 low some altitude near the sun and then negligible changes occur as the particles prop-
 1037 agate to Earth. The conflict between the preferential coronal ion heating observations
 1038 and the expected plasma evolution due to interactions with ubiquitous waves between
 1039 the Sun and Earth still remains an unanswered and fundamentally critical question in
 1040 studies of the solar wind.

1041 Finally, *Wind* studies of the relative abundance between protons and alpha-particles
 1042 have shown solar cycle and other effects (Alterman et al., 2018; Alterman & Kasper, 2019;
 1043 Kasper et al., 2007, 2012). The authors showed that the alpha-particle-to-proton abun-
 1044 dance varies with solar cycle and is a function of solar wind speed (Alterman & Kasper,
 1045 2019; Kasper et al., 2007, 2012). That is, higher speed solar wind has a higher alpha-
 1046 particle abundance than slower wind and the abundances peak near solar maximum. In
 1047 fact, when binned by solar wind speed, Kasper et al. (2007) showed a consistent six month
 1048 periodicity in the alpha-particle abundance, due to the heliographic latitudinal changes
 1049 as the spacecraft orbits the Sun. Later, Alterman and Kasper (2019) showed that there
 1050 is a phase delay between the rise in sunspot numbers and the rise in alpha-particle abun-
 1051 dance, which turns out to be a monotonic function of the solar wind speed. The authors
 1052 found that changes in the sunspot number precede changes in alpha-particle abundance
 1053 with the smallest lag time, ~ 150 days, corresponding to the lowest solar wind speed. The
 1054 alpha-particle abundance was assumed to be modified in the photosphere only but the
 1055 speed-dependent lag in the alpha-particle abundance in response to changes in SSN sug-
 1056 gests other processes at higher altitudes are important. This work has yielded new clues
 1057 about the source of the slow solar wind, a long-standing problem in solar wind physics.

1058 The above contributions to our understanding of the solar wind almost entirely rely
 1059 upon the longevity and accuracy of *Wind* measurements. That is, the use of data from
 1060 a single spacecraft removes the uncertainties introduced when cross-calibrating between
 1061 different sets of instrumentation from different spacecraft. Given that many of these nu-
 1062 anced results are relatively small in magnitude and/or difficult to measure, it is unlikely
 1063 many could have been obtained using multiple missions over similar periods of time.

1064 **3.8 Transient Large-scale Magnetic Phenomena**

1065 The *Wind* mission has provided numerous opportunities to identify, characterize,
 1066 and model IP transients such as corotating interaction regions (CIRs), stream interac-
 1067 tion regions (SIRs), IP shock waves, and ICMEs. This section summarizes the results
 1068 of investigations that have improved our understanding of these structures and their im-
 1069 portance for Sun-earth connections. This section is broken up into the following three
 1070 subsections: Section 3.8.1 highlights advances made on IP shocks, Section 3.8.2 discusses
 1071 *Wind*'s pivotal role in our understanding of ICMEs, and Section 3.8.3 discusses advances
 1072 in our understanding of SIRs/CIRs.

1073 **3.8.1 Interplanetary Shock Waves**

1074 One of the most important astrophysical phenomena for particle energization and
 1075 space weather impacts are collisionless shock waves. *Wind* has made several critical con-

therein for more details). So there are clear differences between the effect of waves versus particle-particle collisions on the particle distribution functions.

1076 tributions to our understanding of collisionless shock waves including, but not limited
 1077 to, improved understanding of energy dissipation mechanisms, particle energization pro-
 1078 cesses and sources, the structure of shocks, and remote sensing of shocks. In this section
 1079 we briefly highlight a few of these advances while pointing the reader to other sections
 1080 where the remaining topics are discussed. This section focuses on IP shocks but a few
 1081 important contributions from measurements at the terrestrial bow shock are discussed
 1082 as well.

1083 In the IPM, shocks are mainly caused by ICMEs (see Section 3.8.2) and planetary
 1084 bow shocks. When ICMEs reach a supersonic velocity as they propagate and expand through
 1085 the IPM (Lepping et al., 2007; Lepping, Wu, Berdichevsky, & Ferguson, 2008; Vandas
 1086 et al., 2009) a shock can form on their leading (anti-sunward) edge. IP shocks can also
 1087 be generated by interaction regions between slow and high speed solar streams (G. Mann
 1088 et al., 2002; Mason et al., 2009), often referred to as corotating interaction regions or CIRs,
 1089 or stream interaction regions or SIRs (see Section 3.8.3). Although we know what forms
 1090 collisionless shocks, the energy dissipation mechanism(s) that govern shock dynamics in
 1091 astrophysical plasmas are still not well understood.

1092 As previously discussed in Section 3.6 in relation to the terrestrial ion foreshock,
 1093 there are numerous unknowns on the topic of shock particle energization by collision-
 1094 less shocks. *Wind* studies led to some of the first pieces of evidence to illuminate how,
 1095 for example, field-aligned ion beams can be generated at the quasi-perpendicular bow
 1096 shock (e.g., Meziane et al., 1997, 1999, 2002, 2003, 2011). A tangential study discovered
 1097 that a type of TIFP could generate similar field-aligned ion beams, but the generation
 1098 was occurring locally in the ion foreshock not at the quasi-perpendicular bow shock (e.g.,
 1099 Wilson III, Koval, Sibeck, et al., 2013, and discussed in Section 3.6). This spawned a whole
 1100 new field of study and helped lead to the serendipitous discovery that the same types
 1101 of TIFP could also locally generate relativistic electrons (e.g., Wilson III et al., 2016, and
 1102 discussed in Section 3.6). Multispacecraft studies including *Wind* have even confirmed
 1103 the long-theorized concept of shock-shock acceleration between the terrestrial bow shock
 1104 and an IP shock (though this was not surprising) (e.g., Hietala et al., 2011, 2012). Thus,
 1105 *Wind's* unique compliment of instrumentation has led to several critical contributions
 1106 to our understanding of shock acceleration.

1107 Early *Wind* observations illustrated evidence of numerous kinetic instabilities lo-
 1108 cated in and around collisionless shocks (e.g., Bale et al., 1997; Bale, Kellogg, Larson,
 1109 et al., 1998; Bale, Kellogg, Goetz, & Monson, 1998; Kellogg, Monson, et al., 1996; Kel-
 1110 logg et al., 1999). The waves radiated by these instabilities have long been theorized to
 1111 dissipate energy in collisionless shock waves (e.g., see Sagdeev, 1966). Therefore, Wilson
 1112 III et al. (2007) examined electrostatic waves around 67 IP shocks finding that the wave
 1113 amplitudes increased with increasing Mach number and strength. The positive correla-
 1114 tion is evidence that as the shock gets stronger, it requires larger amplitude waves to dis-
 1115 sipate more energy. A follow-on case study examined a high Mach number shock pre-
 1116 senting the first observations of electron Bernstein-like modes identified as having been
 1117 radiated by the electron cyclotron drift instability or ECDI (Wilson III, 2010). The im-
 1118 portance of the identification is that the ECDI results from the free energy between in-
 1119 cident electrons and shock-reflected ions, i.e., the wave couples to both ions and electrons
 1120 and illustrates a connection between particle reflection and wave generation. Later work
 1121 (Wilson III et al., 2012) led to the observation of large amplitude magnetosonic-whistler
 1122 precursors (see Appendix B for definition and properties) upstream of shocks that could
 1123 not have generated said waves through dispersive radiation – waves emanating from a
 1124 time- and spatially-varying current structure with a frequency depending upon the wave
 1125 number (Tidman & Northrop, 1968). It was determined that the precursors were likely
 1126 radiated by a modified two-stream instability due to free energy similar to what drives
 1127 the ECDI. Further, the waves were shown to be stochastically accelerating the electrons
 1128 parallel and ions perpendicular to the quasi-static magnetic field. The same mechanism

1129 has since been proposed as a possible source mechanism for the relativistic electrons dis-
 1130 cussed above (e.g., see Roberg-Clark et al., 2018). Thus, *Wind*'s kinetic-physics-based
 1131 instrumentation has helped greatly advance our understanding of instability-based en-
 1132 ergy dissipation mechanisms in collisionless shocks.

1133 More recently a *Wind*-based study examined the structure of low Mach number,
 1134 low plasma beta, quasi-perpendicular shocks (Wilson III et al., 2017). The work was mo-
 1135 tivated by discussions in the literature that argued such shocks should be laminar in their
 1136 magnetic field profiles, thus the particle trajectories through the shock should be well
 1137 behaved (e.g., see review by Mellott, 1985). Interestingly, with the high cadence *Wind*
 1138 magnetometer data it was found that not only are these low Mach number, low plasma
 1139 beta, quasi-perpendicular shocks filled with magnetosonic-whistler precursors, the pre-
 1140 cursor amplitudes were, on average, $\sim 220\%$ of the change in magnetic field magnitude
 1141 across the shock. That is, the precursors contained the largest magnetic field gradients
 1142 in the shock transition, not the shock ramp. Note that unlike the Wilson III et al. (2012)
 1143 study, these shocks are too low in Mach number to reflect sufficient ions to generate the
 1144 modified two-stream instability or ECDI. Thus, the waves are likely generated through
 1145 dispersive radiation. The critical point is, however, that such large amplitude waves clearly
 1146 affect the incident ion and electron trajectories as recently illustrated using the Magne-
 1147 topheric Multiscale (MMS) spacecraft (e.g., L.-J. Chen et al., 2018; Hull et al., 2020;
 1148 Oka et al., 2019). Thus, *Wind* has also advanced our understanding of collisionless shock
 1149 structure.

1150 There are several other IP shock-related advances led by *Wind* studies that will
 1151 not be discussed here as they are discussed elsewhere in this review. Some of these in-
 1152 clude radio emissions such as type II solar radio bursts (e.g., Bale et al., 1999; Pulupa
 1153 & Bale, 2008, and discussed in Section 3.10), acceleration and transport of solar ener-
 1154 getic particles events (SEPs) (e.g., Reames, 2017, and discussed in Section 3.9), and the
 1155 nonplanar structure of IP shock fronts (e.g., Neugebauer & Giacalone, 2005, and discussed
 1156 in Section 3.7.1).

1157 Below we discuss *Wind*'s contribution to understanding the phenomena associated
 1158 with ICMEs and CIRs.

1159 **3.8.2 Interplanetary Coronal Mass Ejections**

1160 Interplanetary coronal mass ejections (ICMEs) are the manifestations in the so-
 1161 lar wind of CMEs at the Sun and are the major solar wind drivers of space weather. In
 1162 particular, around 90% of major geomagnetic storms ($Dst \leq -100$ nT) occur when ICMEs
 1163 encounter Earth (Zhang et al., 2007), and especially severe storms driven by ICMEs, such
 1164 as the March 1989 storm that caused a blackout of the Quebec power grid, and the 1859
 1165 “Carrington” event (Carrington, 1859; Siscoe et al., 2006), can lead to significant soci-
 1166 etal and economic impact (Oughton et al., 2017; Riley et al., 2018). On the other hand,
 1167 most ICMEs produce only modest geomagnetic effects (e.g., I. G. Richardson & Cane,
 1168 2010). A leading driver of enhanced geomagnetic activity is the presence of strong, sus-
 1169 tained southward-directed magnetic fields, and these are frequently found in a subset of
 1170 ICMEs termed “magnetic clouds” (MCs) (L. Burlaga et al., 1981) characterized by an
 1171 enhanced, slowly-rotating, flux-rope-like magnetic field; southward fields in the ICME
 1172 sheath can also contribute (E. K. J. Kilpua et al., 2017). Particles accelerated at ICME-
 1173 driven shocks also contribute to solar energetic particle events (e.g., Reames, 2012). Al-
 1174 though ICMEs and their characteristic signatures (e.g., Zurbuchen & Richardson, 2006)
 1175 were largely discovered in early in-situ observations (often being referred to as “shock
 1176 drivers”, “pistons,” and “ejecta”), *Wind* has made significant contributions to the study
 1177 of ICMEs and MCs (e.g., Hidalgo & Nieves-Chinchilla, 2012; Lepping, Wu, Berdichevsky,
 1178 & Szabo, 2018) and their space weather effects.

1179 *Wind* launched roughly two years before the SoHO spacecraft that carries the LASCO
 1180 coronagraphs, which makes near-continuous observations of the corona and CMEs. The
 1181 combination of *Wind* in situ measurements from MFI, SMS, 3DP, and SWE, SoHO LASCO
 1182 CME observations and extreme ultraviolet observations from EIT Yokohoh X-ray ob-
 1183 servations (e.g., D. B. Berdichevsky et al., 2002) resulted in the confirmation of the con-
 1184 nnection between CMEs in the corona and MCs subsequently observed near-Earth (e.g.,
 1185 see Webb et al., 1998; Webb, 1998; Webb et al., 2000). Previous studies had associated
 1186 the arrival of a magnetic cloud with the disappearance or eruption of a prominence at
 1187 the Sun a few days earlier (Webb, 1988; Wilson & Hildner, 1984), while the orientation
 1188 of the MC had been found to match well with the orientation of the prominence in many
 1189 cases (Bothmer & Schwenn, 1994). The discovery of cold prominence material in a small
 1190 fraction of a magnetic cloud at Earth (Larson et al., 2000) indicates that prominence and
 1191 magnetic cloud are not a one-to-one equivalent. Combining coronagraphic observations
 1192 with SoHO and statistical surveys showing that the typical radial size of a MC is 0.21
 1193 AU (e.g., Lepping et al., 2006) enabled the discovery that MCs are associated with the
 1194 dark cavity of the three-part CME structure (Illing & Hundhausen, 1985) observed re-
 1195 motely in the corona.

1196 Another important contribution to understanding the origin of ICMEs is the ob-
 1197 servation of enhanced solar wind $^3\text{He}^{2+}$ within ICMEs. Ho et al. (2000) identified six
 1198 enhanced $^3\text{He}^{2+}/^4\text{He}^{2+}$ periods from January 1995 to May 1998, using data from the
 1199 MASS high resolution solar wind spectrometer on *Wind*. The ratios observed in these
 1200 events were four to ten times higher than previously reported average solar wind values.
 1201 It was suggested that these enhancements originated in the prominence core embedded
 1202 within the CME. In a separate event, *Wind*/MASS high-mass resolution measurements
 1203 of helium ions, including their number density, velocity and temperature, revealed the
 1204 presence of $^4\text{He}^+$ ions, and SWICS observed unusually low charge states of O^{5+} and Fe^{5+} ,
 1205 during a short interval within an MC apparently composed of cold prominence material
 1206 (L. Burlaga et al., 1998).

1207 The 3DP instrument’s ability to measure thermal, suprathermal and energetic elec-
 1208 trons allowed *Wind* to provide some of the first measurements of extremely cold (tem-
 1209 perature down to below 1 eV) electrons inside MCs (Larson et al., 2000). Because *Wind*
 1210 is a spinning platform, careful analysis of the spacecraft potential with similar measure-
 1211 ments of proton temperatures allowed Larson et al. (2000) to presented the first exper-
 1212 imental observation of collisionally-coupled electrons and protons in interplanetary space.

1213 To probe the internal structure of MCs, Shodhan et al. (2000) used observations
 1214 of suprathermal electrons from *Wind* and several other spacecraft to assess the fraction
 1215 of time when bidirectional vs. unidirectional electron strahl flows were present during
 1216 the passage of MCs. This classification indicates the presence of looped field lines rooted
 1217 at the Sun at both ends vs. open field lines, respectively. The fraction of bidirectional
 1218 flows was found to vary widely from no bidirectional streaming to $\sim 100\%$, with the largest
 1219 MCs being the most closed. The different flows were also distributed randomly within
 1220 the MCs. These results suggest that although MCs are large-scale coherent structures,
 1221 reconnection, either near the Sun or with the IMF, sporadically alters the field topol-
 1222 ogy from closed to open. A separate analysis technique was also used to investigate the
 1223 open/closed field line nature of MCs. By measuring the arrival time and velocity dis-
 1224 persion of suprathermal and energetic electrons (100 eV – 100 keV) associated with a
 1225 series of impulsive solar flares that fortuitously were injected into the footpoints of a MC
 1226 as it passed over *Wind* in October 1995, Larson et al. (1997) estimated the path lengths
 1227 traveled by these electrons at different locations within the MC. These were overall found
 1228 to be consistent with a low-twist core and a more highly twisted outer shell, as expected
 1229 for a flux rope configuration as shown in Figure 12. On the other hand, Kahler et al. (2011)
 1230 applied a similar method to eight MCs and found a poor correlation between the inferred

1231
1232

electron path lengths and those expected from MC field models, with the exception of the event studied by Larson et al. (1997)²⁶.

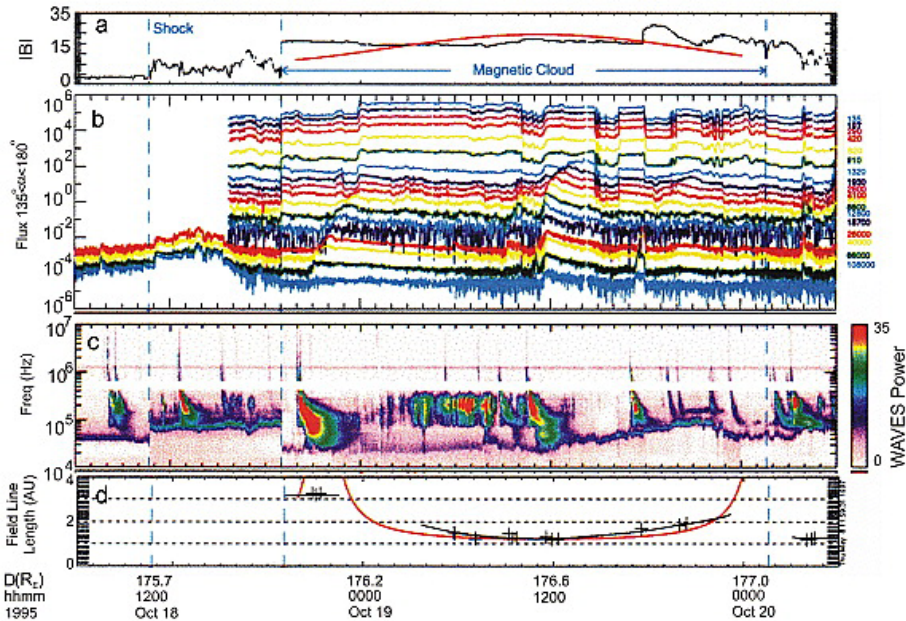


Figure 12: Analysis of the length of magnetic field lines inside an MC measured by Wind for the 1995 October 18-20 ICME (Larson et al., 1997). The figure is taken from Kahler et al. (2011), which was adapted from the Larson et al. (1997) study. The panels show from top to bottom, the magnetic field strength with results from the force-free model in red (a), the flux of suprathermal electrons for various energies between 135 eV and 100 keV propagating anti-parallel to the magnetic field from 3DP (b), the wave power of solar radio emissions observed by WAVES (c) including multiple type III bursts, some associated with the electron injections in (b), and the derived field line length in AU for each of these bursts with the modeled length from the force-free model of panel (a) in red (d).

1233
1234
1235
1236
1237
1238
1239
1240
1241
1242
1243
1244
1245

Fitting and reconstruction techniques are needed to determine the global structure of ICMEs and MCs from single-spacecraft crossings. In the best cases, MCs are well-ordered (single flux ropes) and they can be readily modeled by a variety of techniques. Although spheromak-like plasmoid models have been proposed for MCs (Vandas et al., 1993), work has focused on flux rope models of various levels of sophistication (Marubashi, 1986; L. F. Burlaga, 1988; Lepping et al., 1990; Farrugia et al., 1993; Hidalgo et al., 2002). Frequently, MC are reconstructed by neglecting expansion or cross-section distortion. In particular, Lepping et al. (1990) developed the most commonly used in situ reconstruction technique in which the magnetic structure is assumed to be a static, axially symmetric cylinder that can be approximated by a linear force-free magnetic configuration (L. F. Burlaga, 1988; Lundquist, 1951). Following the same geometrical assumptions, but relaxing the force-free requirement, Hidalgo et al. (2000) derived a family of models that attempt to reproduce the varying physical and geometrical characteristics of MCs found in in situ data (Hidalgo et al.,

²⁶ Note that the fitting discussed here refers to the model path length in panel d of Figure 12 and not to the magnetic field magnitude in panel a which is evidently a poorer fit to the observed field magnitude. We note that a critique of the magnetic field magnitude fit is not appropriate here as we are reporting the main findings of this work.

2002; Hidalgo & Nieves-Chinchilla, 2012; Nieves-Chinchilla et al., 2012, 2016). However, it is not yet clear whether any one of these models is sufficiently realistic to describe the observed variety of MC signatures. *Wind* measurements of the magnetic field and plasma pressure have resulted in the development of MC analysis techniques that go beyond force-free approximations to extend to magneto-hydrostatic equilibrium through the Grad-Shafranov technique (e.g., Hu & Sonnerup, 2001). This was first applied to *Wind* measurements of magnetic clouds by Hu and Sonnerup (2002) and has been used extensively since. However, recent comparisons of various fitting and reconstruction models, both for general (Al-Haddad et al., 2013) and simple ICMEs (Al-Haddad et al., 2018), have highlighted that different techniques do not return consistent results for the ICME orientation. While this result may appear pessimistic, we emphasize a couple of positive consequences: a) with the large number of reliable and complete measurements of MCs and ICMEs over 25 years by *Wind*, fitting and reconstruction models have been developed and improved to better integrate physics, i.e. moving away from a constant-alpha force-free circular cross-section model, b) comparative studies have highlighted that work using a single fitting or reconstruction technique may lead to unreliable results when comparing MC orientation with the orientation of the related prominence and flux rope at the Sun.

Gopalswamy, Yashiro, et al. (2015) and Nieves-Chinchilla et al. (2018) used *Wind* data to elucidate properties of MCs during solar cycles 23 and 24 (e.g., see Table C1 in Appendix C). Of particular importance is the relation between ICMEs or MCs measured at L1 and the solar activity, which was weaker in cycle 24 than cycle 23 with an extended deep minimum in 2007–2009. Although the average sunspot number declined by $\sim 40\%$ between solar cycles 23 and 24, there was no decline in the number of MCs in cycle 24 compared with cycle 23 (see Figure 13). However, of the intense geomagnetic storms ($Dst < -100$ nT), $\sim 80\%$ were associated with ICMEs and the majority associated with MCs was significantly lower in solar cycle 24 as compared to solar cycle 23 (Gopalswamy et al., 2020; L. K. Jian et al., 2018; Shen et al., 2017). Some of this reduction in geo-effectiveness in cycle 24 as compared to cycle 23 may be related to the 22-year cycle in bipolar MCs (Y. Li et al., 2018) and also associated with the weaker magnetic fields inside MCs, and the shorter MC duration, during solar cycle 24 (Lepping et al., 2011). B. E. Wood et al. (2017) used *Wind* in situ observations of MCs in conjunction with observations from the coronagraphs and Heliospheric Imagers on the STEREO spacecraft to track 31 MCs from the Sun to near 1 AU and compare the properties of the MCs with the associated erupting flux ropes at the Sun. They found that the flux rope orientations and sizes inferred from imaging near the Sun were not well correlated with those of the in situ MCs. This has significant implications for attempts to predict MC magnetic fields and their geo-effectiveness from observations of the solar source regions (e.g., Savani et al., 2015). However, the arrival times at 1 AU were well predicted.

Estimates in the literature of the fraction of ICMEs that include MCs vary from $\sim 15\%$ to 80% (Gosling et al., 1990; Bothmer & Schwenn, 1996; Marubashi, 2000; Mulligan et al., 1999; I. G. Richardson & Cane, 2004). Long-term statistical studies including observations during the *Wind* mission make it possible to reconcile these various studies by recognizing that the fraction of MCs varies with the solar cycle (I. G. Richardson & Cane, 2004; Lepping, Wu, Berdichevsky, & Kay, 2018; Lepping et al., 2020).

The several hundred ICMEs measured by *Wind* also allow the characteristics that distinguish MCs from those with more complex magnetic structures to be better defined (Nieves-Chinchilla et al., 2018). Non-MC-like configurations may arise in several circumstances: the ICME may result from the interaction of several individual ICMEs on their way to Earth (L. F. Burlaga et al., 2002; Lugaz et al., 2007), or if the magnetic field configuration of the original CME was more complex than a simple flux rope. For example, a MC may be a substructure of a more extended ICME region (I. G. Richardson & Cane, 2010) and not encounter the observing spacecraft. The absence of the flux rope signatures can be explained by the spacecraft encountering the MC far from the center

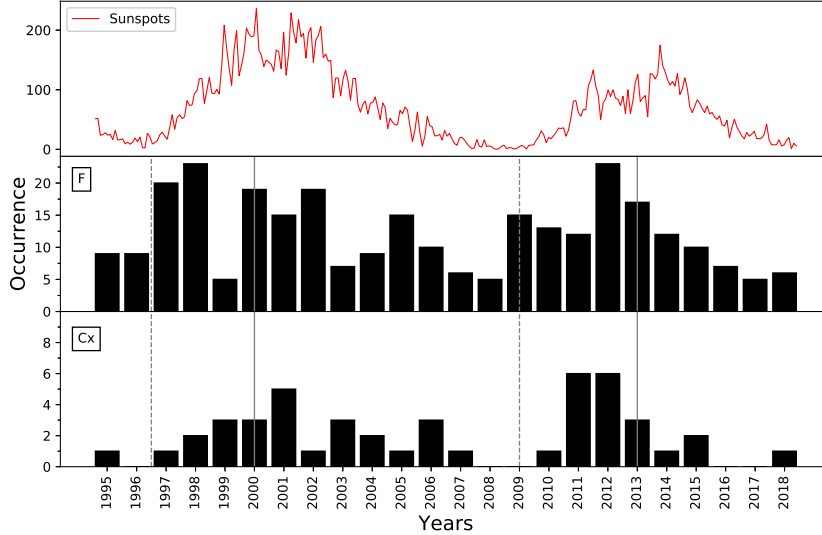


Figure 13: Occurrence of magnetic ejecta (e.g., MCs) per year near 1 AU as compared to sunspot number. Top panel: sunspot number showing the weaker solar maximum in 2012–2014 as compared to 2000–2002. Middle and bottom panels: number of flux-rope like ICME (F, middle) and complex ICMEs (Cx, bottom) from *Wind*.

1299 axis or in the flux rope leg. Magnetic flux erosion by reconnection at the front of the mag-
 1300 netic ejecta may also erase the clear flux rope signature (Dasso et al., 2007; E. K. J. Kilpua
 1301 et al., 2011; Ruffenach et al., 2012). Some studies classify a subset of ICMEs that meet
 1302 some but not all the magnetic and plasma signature of MCs as “MC-like” or “flux rope
 1303 like” (Gopalswamy, Yashiro, et al., 2015; Lepping et al., 2005; C.-C. Wu & Lepping, 2015).
 1304 One of the first detailed studies of an ICME with signatures of complexity was made by
 1305 Lepping et al. (1997). *Wind* instruments measured a coherent structure with an embed-
 1306 ded shock in the back half of the structure. This complex event triggered an intense ge-
 1307 omagnetic storm for which the joint measurements by *Wind* and *Polar* provided a new
 1308 coupling function between the solar wind and the magnetosphere (Farrugia et al., 1998;
 1309 Takeuchi et al., 2000).

1310 The Lepping et al. (2003) catalog of MCs has been central to numerous statisti-
 1311 cal studies (Démoulin et al., 2013, 2016; Janvier et al., 2019; Lepping, Wu, Gopalswamy,
 1312 & Berdichevsky, 2008; Lepping et al., 2017, among others) and is based on the approx-
 1313 imation of MCs as simple, circular flux rope in force-free equilibrium²⁷. Results from these
 1314 catalogs include data-driven models of typical MCs and shocks (Démoulin et al., 2016),
 1315 studies of the importance of expansion to understand MC measurements (Lepping, Wu,
 1316 Gopalswamy, & Berdichevsky, 2008) as well as investigations of the impact of the dis-
 1317 tance of closest approach on the spacecraft measurements (Démoulin et al., 2013; Lep-
 1318 ping et al., 2017). These studies revealed that the cross-section of MCs is in fact non-
 1319 circular (Démoulin et al., 2013, 2019) and the distribution of magnetic field line twist

²⁷ The results from the analyses have shaped two different MC catalogs, both included on the *Wind* webpage <https://wind.nasa.gov/ICMEindex.php>. These catalogs provide fitting parameters for most entries. These parameters include magnetic field strength, closest approach (or impact parameters), orientation as well as measures of the goodness of the fit for all *Wind* MC measurements.

1320 may be more complex than that derived from a force-free model (Lanabere et al., 2020).
 1321 These results have led to the development of several new models which incorporate more
 1322 complex magnetic field structures and cross-sections.

1323 The Nieves-Chinchilla et al. (2018) catalog also provides the internal flux-rope phys-
 1324 ical properties as well as the orientation and closest approach based on the model and
 1325 reconstruction technique described in Nieves-Chinchilla et al. (2016). The statistical study
 1326 published by Nieves-Chinchilla et al. (2019) revealed the remarkable spatial complex-
 1327 ity of ICMEs. Figure 13 displays the occurrence of ICMEs with complex topology (bot-
 1328 tom), with clear flux rope signatures (middle) and both populations compared with the
 1329 sunspot number over the *Wind* mission. It has been shown by Y. Li et al. (2018) that
 1330 the orientation of ICME flux ropes follow orientation of the heliospheric current sheet,
 1331 confirming the results of previous studies (e.g., Mulligan et al., 1998) based on visual in-
 1332 spection that found a Hale cycle dependence of the reversal in the flux rope poloidal field.

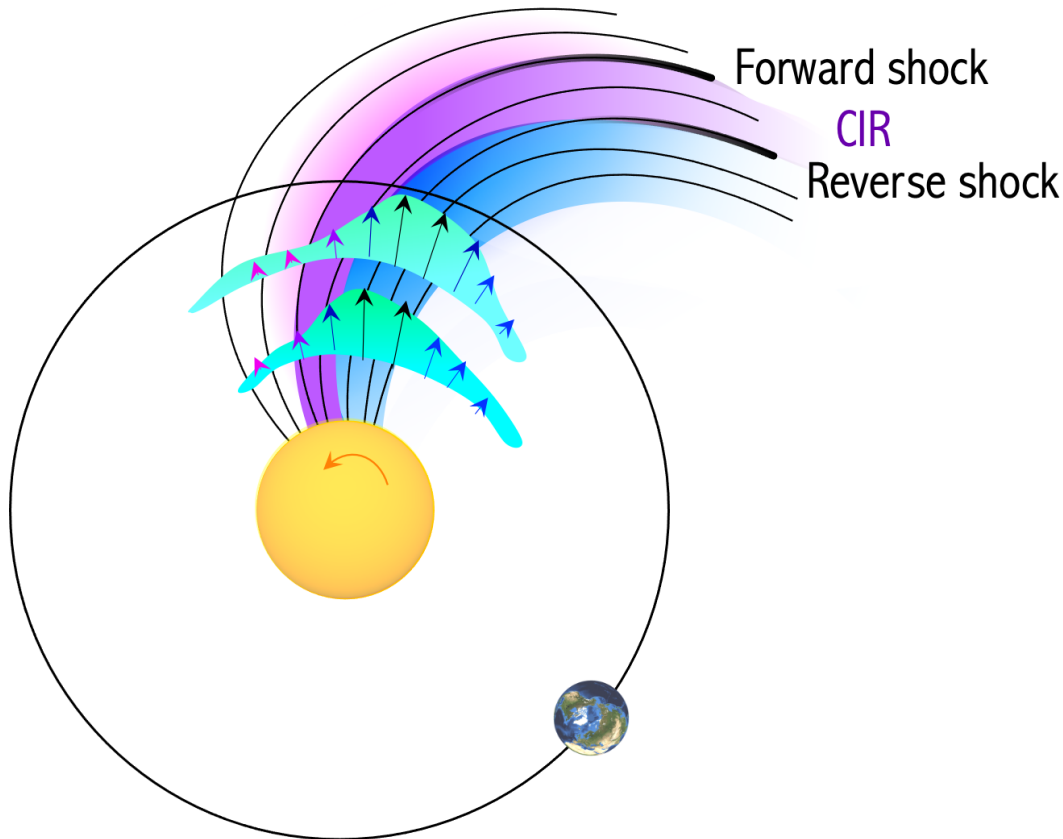


Figure 14: *Cartoon of stream interaction region (SIR) and/or corotating interaction region (CIR). The black arrows indicate velocity and the solid lines represent magnetic field lines. The thick magenta and blue arrows indicate the local, outward normals of the expanding compression region that can form a forward and reverse shock, respectively, as the SIR/CIR propagates further away from the sun.*

1333 In combination with measurements from *Wind*, in situ measurements from STEREO,
 1334 *Parker Solar Probe*, MESSENGER, *Venus Express*, and *Solar Orbiter* reveal the helio-
 1335 spheric dynamic evolution of the internal structure of MCs. The evolutionary signatures
 1336 of evolution include distortions, deformations, rotations, deflections, and deviations from
 1337 self-similar expansion or radial propagation (Good et al., 2019; Kubicka et al., 2016; Lugaz

1338 et al., 2020; Nakwacki et al., 2011; Nieves-Chinchilla et al., 2012; Salman et al., 2020;
 1339 Vršnak et al., 2019; Y. Wang et al., 2018; Winslow et al., 2016). These analyses use data
 1340 from spacecraft that are radially aligned or in quadrature, giving multi-point or multi-
 1341 view observations of the evolving MC, respectively.

1342 In summary, *Wind* has made important contributions to the study of ICMEs rang-
 1343 ing from confirming the fundamental association between CMEs and ICMEs and under-
 1344 standing the complexity of their structures and related space weather effects, through
 1345 the multi-spacecraft studies that are possible in conjunction with new missions in the
 1346 inner heliosphere and beyond.

1347 **3.8.3 Corotating Interaction Regions**

1348 *Wind* observations of corotating interaction regions (CIRs) and stream interaction
 1349 regions (SIRs) near 1 AU have helped researchers confirm that not only are particles ac-
 1350 celerated by these structures, the acceleration need not require a local shock. Further,
 1351 they have found that the structures evolve on much shorter time scales than the solar
 1352 rotation period. In this section we review some of these highlights of CIR and SIR re-
 1353 search using *Wind* observations.

1354 A CIR (e.g., see I. G. Richardson et al., 2018, for a recent review) is formed by the
 1355 interaction of a high-speed solar wind stream (HSS) originating in a coronal hole at the
 1356 Sun with the preceding slower solar wind (e.g., see Figure 14 for illustration). The term
 1357 SIR is often reserved for those interaction regions that do not recur on two or more so-
 1358 lar rotations, though SIR and CIR are also used interchangeably. This interaction forms
 1359 a region of compressed solar wind – the CIR – that lies along the leading edge of the high-
 1360 speed stream and has an approximately spiral configuration. CIRs/HSSs corotate with
 1361 the Sun and may recur for several solar rotations. Expansion of the CIR may lead to the
 1362 formation of a corotating forward (reverse) shock at the CIR leading (trailing) edge. These
 1363 shocks usually form beyond 1 AU (Smith & Wolfe, 1976) but occasionally are found at
 1364 1 AU (e.g., L. Jian et al., 2006). They are also important drivers of geomagnetic activ-
 1365 ity, accounting for around 10% of major geomagnetic storms (Alves et al., 2006; Zhang
 1366 et al., 2007). They can also generate extended (several day) periods of enhanced geo-
 1367 magnetic activity, driven by intermittent southward magnetic fields associated with Alfvénic
 1368 fluctuations propagating outward from the Sun, as they pass over Earth (Tsurutani et
 1369 al., 2006), which in turn may lead to the acceleration of MeV electrons in the outer ra-
 1370 diation belts (Baker & Kanekal, 2008; O’Brien et al., 2001). Such “killer electrons” are
 1371 often associated with spacecraft anomalies or failures (e.g., Wrenn et al., 2002).

1372 L. Jian et al. (2006) summarize the properties of 365 SIRs (some of which are CIRs)
 1373 at 1 AU during 1995 to 2004 using *Wind* and ACE data, and provide a catalog of these
 1374 events and their properties. They emphasize the use of the total (magnetic and plasma)
 1375 pressure perpendicular to the magnetic field direction as an aid to identifying interac-
 1376 tion regions, with a local pressure peak being a characteristic feature of the stream in-
 1377 terface (Forsyth & Marsch, 1999) separating slow and fast solar wind plasma. They found
 1378 that $\sim 17\%$ (5.75%) of interaction regions at 1 AU had only a forward (reverse) shock,
 1379 and 1.37% had a forward-reverse shock pair. An extended catalog of 588 CIR/HSS dur-
 1380 ing 1995–2017 has been compiled by Grandin et al. (2019) using a detection algorithm
 1381 applied to OMNI data which incorporates *Wind* observations. They also show superposed-
 1382 epoch analyses of the solar wind parameters and geomagnetic activity associated with
 1383 these structures for different phases of solar cycles 22–24, noting for example, cycle to
 1384 cycle variations in their occurrence and properties, such as the lower geoeffectiveness of
 1385 CIRs/HSS in cycle 24 due to lower magnetic field strengths and lower stream speeds (e.g.,
 1386 see Figure 15).

1387 Although CIRs and HSSs are long-lived structures corotating with the Sun, they
 1388 do evolve on shorter time-scales, for example due to changes in the configuration of the

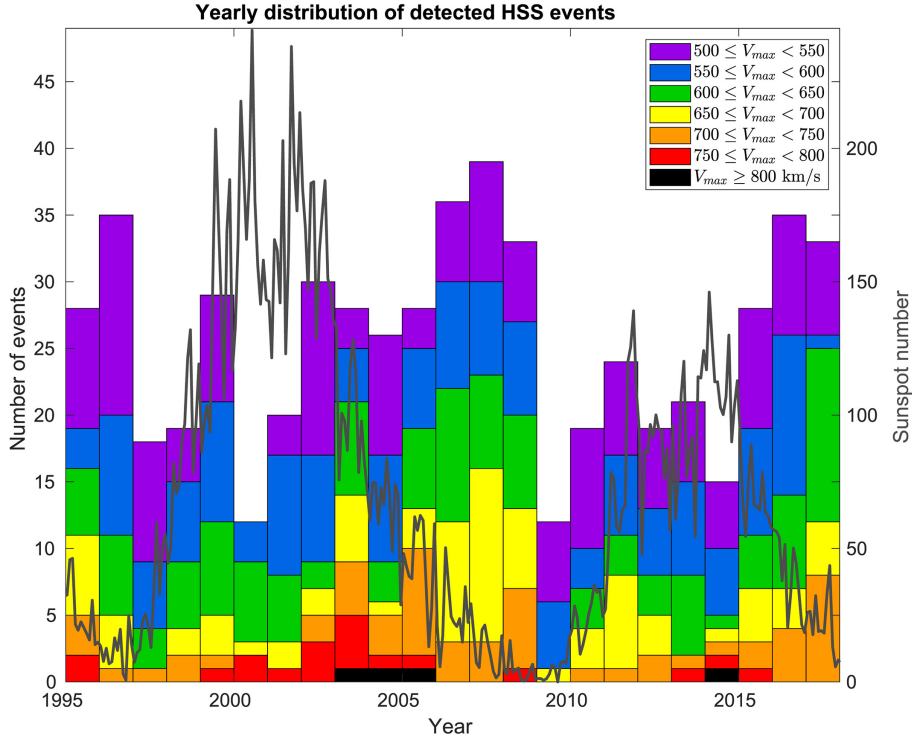


Figure 15: Yearly number of high speed streams in various peak speed ranges (minimum 500 km/s) with the sunspot number for solar cycles 23 and 24 superposed, showing the tendency for HSS to be most frequent during the declining phase of the cycle and the generally lower peak speeds in cycle 24 vs. 23 (Adapted from Grandin et al., 2019).

1389 source coronal holes and development of the stream interaction. Several studies have used
 1390 data from *Wind* and other spacecraft separated from Earth to study this evolution. For
 1391 example, L. K. Jian et al. (2009) examined a CIR in August 2007 that was observed in
 1392 succession by STEREO B, 10° east of *Wind*, then by *Wind*, and by STEREO A, 15° to
 1393 the west; the spacecraft were only separated by 2° in heliolatitude. Figure 16 shows the
 1394 differences in the profiles of various solar wind parameters at each spacecraft (the CIR
 1395 is indicated by enhanced magnetic fields and plasma densities on the leading edge of the
 1396 HSS) and the varying locations of a crossing of the heliospheric current sheet²⁸ (HCS)
 1397 ahead of the CIR, the stream interface (SI), and a forward shock forming at the CIR lead-
 1398 ing edge, which was only present at *Wind*, and a reverse shock forming at the CIR trail-
 1399 ing edge, only evident at STEREO B. Occasionally, a MC interacts with a CIR, as in
 1400 the example discussed by Farrugia et al. (2011). Observations from *Wind* and both STEREO
 1401 spacecraft, separated by ~40° in heliolongitude, illustrate the distortion and rotation of
 1402 the MC that resulted from this interaction.

1403 Such studies about CIRs and SIRs L. K. Jian et al. (2009) have highlighted a num-
 1404 ber of important aspects of the variability of corotating solar wind streams: a) their prop-
 1405 erties, including the presence/absence of shocks, can vary significantly close to the eclip-
 1406 tic even with small latitudinal separations as the slow and fast wind streams are tilted
 1407 and the interaction region can have a complex 3D shape, b) their properties can have
 1408 large variations on moderate timescales (~ 6-24 hours); some of this variability is likely

²⁸ the boundary that separates the two magnetic polarities or hemispheres of the heliosphere

1409 to be associated with the changing boundaries and magnetic field distribution of equa-
 1410 torial coronal holes at the Sun (the source of the fast solar wind streams), c) Earth (or
 1411 1 AU in general) is situated in a place where the interaction process between slow and
 1412 fast streams is still ongoing. As such, small variations in longitude, latitude or radial dis-
 1413 tance can result in significant differences in the SIR/CIR properties, in a way which is
 1414 not necessarily clearly understood yet. While *Wind* prograde orbits in 2000–2002 can
 1415 be used for such studies, there have not been any dedicated measurements of the solar
 1416 wind 0.5–5° from the Sun-Earth line since, except for a few months of STEREO mea-
 1417 surements after launch in 2007.

1418 Broiles et al. (2012) used observations from *Wind* and ACE to search for planar
 1419 magnetic structures in 153 CIRs and, from their orientation, inferred the tilt of the CIR,
 1420 which might be expected to reflect the orientation of the fast-slow stream interaction.
 1421 The mean azimuthal tilt was found to be consistent with the average Parker spiral direc-
 1422 tion. Average out-of-the-ecliptic tilts were $\sim 20^\circ$ both north or south, but these val-
 1423 ues often changed significantly between successive recurrences of the same stream. Such
 1424 studies for example raise questions about using observations from a spacecraft monitor-
 1425 ing the solar wind, and particularly CIRs/HSS, at a location east of Earth (e.g., L5) to
 1426 provide an advance forecast of near-Earth solar wind conditions. They also suggest the
 1427 presence of a complex, evolving, structured solar wind in the inner heliosphere that can
 1428 be studied by *Parker Solar Probe* and *Solar Orbiter* in conjunction with observations
 1429 by *Wind* and other spacecraft at 1 AU.

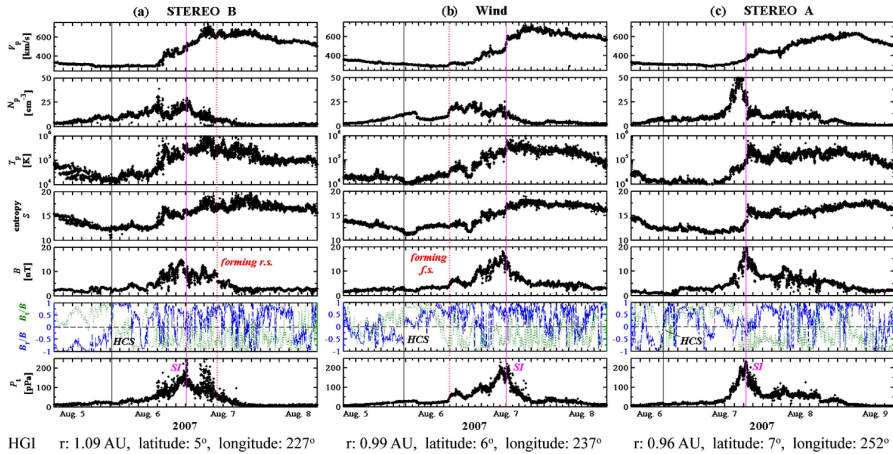


Figure 16: A CIR and HSS observed in turn by STEREO B (left), Wind (center) and STEREO A (right), illustrating the differences in various solar wind parameters observed over a heliolongitude range of only 25° . The parameters shown are (from top) the solar wind speed (V_p), proton density (n_p) and temperature (T_p), entropy ($S = \ln |T_p^{3/2} n_p|$), magnetic field intensity (B_o), the ratios of the radial and transverse components of the magnetic field to B_y , and the total perpendicular pressure (P_\perp) (Adapted from L. K. Jian et al., 2009).

1430 Several studies of energetic particles associated with CIRs have been made with
 1431 *Wind*/EPACT. For example, Mason et al. (1997) and Mason et al. (1999) used measure-
 1432 ments from *Wind*/EPACT to demonstrate that the spectra of energetic particles do not
 1433 show the depletion of low energy ions expected (Fisk & Lee, 1980) if the particles were
 1434 accelerated at CIR shocks at several AU (Barnes & Simpson, 1976). That is, the par-
 1435 ticles would lose energy due to adiabatic deceleration in the expanding solar wind whilst
 1436 propagating sunward to the spacecraft. Instead, observations suggest the particles are
 1437 accelerated closer to the spacecraft. Chottoo et al. (2000) found that the spectra of en-

ergetic particles in the vicinity of CIRs merged with the suprathermal tail of the solar wind ion distribution, also suggesting that the particles were accelerated relatively local to the spacecraft, possibly out of the solar wind distribution. Ebert et al. (2012) used EPACT/STEP observations of suprathermal He ions to show that acceleration occurred near the trailing edges of two well-developed CIRs. One of the CIRs was associated with a reverse shock, while the other was not. This surprising result suggests that particle acceleration at CIRs does not require the presence of a shock. Filwett et al. (2017) investigated suprathermal heavy ion abundances at 41 CIRs using STEP. The authors concluded that the upper limit on the distance traveled from the source to the spacecraft was 1 AU, which is consistent with a relatively local source. Filwett et al. (2017) also found evidence for enhanced Fe abundances in CIR-associated particles at higher solar activity levels. Their result suggests that Fe-rich particles from impulsive solar events contribute to the source of CIR particles. Interstellar pick up ions – interstellar neutrals that are ionized near the Sun – such as He⁺ (Chottoo et al., 2000), may also be accelerated at CIRs (J. H. Chen et al., 2015). Reames (2018), using EPACT/LEMT data, concluded that the element abundances of CIR-accelerated ions mirror the solar wind abundances with a modification depending on the mass to charge ratio of the ions.

3.9 Solar Energetic Particles

The *Wind* EPACT/LEMT instrument was the first to detect ultra-heavy ($34 \leq Z \leq 82$) ions in impulsive solar particle events accelerated by solar flares and jets. *Wind*'s longevity has given researchers a unique opportunity to examine SEP abundances at lower masses over extended time periods. In this section, we highlight some advances made by *Wind* on the topic of SEPs.

The *Wind* EPACT instrument has made observations of solar energetic particles or SEPs throughout the mission lifetime (e.g., see Reames, 2017, and references therein). First, we highlight one result that illustrates the ability of the EPACT/LEMT instrument to detect, for the first time, ultra-heavy ($34 \leq Z \leq 82$) ions in impulsive solar particle events accelerated by solar flares and jets. With a large collecting geometry, a large dynamic range above ~ 2 MeV amu⁻¹, and a pulse-height analysis scheme that prioritizes $Z > 33$ particles, LEMT is ideal for heavy element detection. It was well-established by previous missions that smaller and shorter duration “impulsive” SEP events accelerated by solar flares exhibit remarkable enhancements in the abundances of ³He and heavy ions compared to coronal abundances. LEMT observations (Reames, 2000; Reames & Ng, 2004) demonstrate that these abundance enhancements extend to ultra-heavy ions.

Figure 17, from Reames and Ng (2004) shows the increase in the ion abundance enhancement relative to coronal abundances with increasing Z . Clearly, the ultra-heavy ions continue the trend evident for ions lighter than iron (filled circles are LEMT data, open circles are from previous missions). Figure 17 (right) shows that the abundance enhancements decrease with increasing Q/A , where a coronal temperature of 3 MK is assumed to estimate the charge states. Note that the enhanced but low charge state ³He does not fit these trends, suggesting that the ³He enhancement arises from a separate process. Remarkably, the strongest heavy ion enhancements are associated with the smallest impulsive events associated with the weakest solar flares and softest particle spectra (Reames & Ng, 2004).

The reason for these heavy and ultra-heavy ion abundance enhancements is still under discussion, but they may occur if the ions interact with a turbulent region where there is more power at larger length scales, which favors the acceleration of heavier ions with larger gyroradii. A promising candidate is the formation of islands by reconnection (Drake et al., 2009; Drake & Swisdak, 2012), where the island size distribution may lead to a strong Q/A -dependence in the particle abundances. However, such a process could not account for the enhancement of ³He over ⁴He. This may result instead from accel-

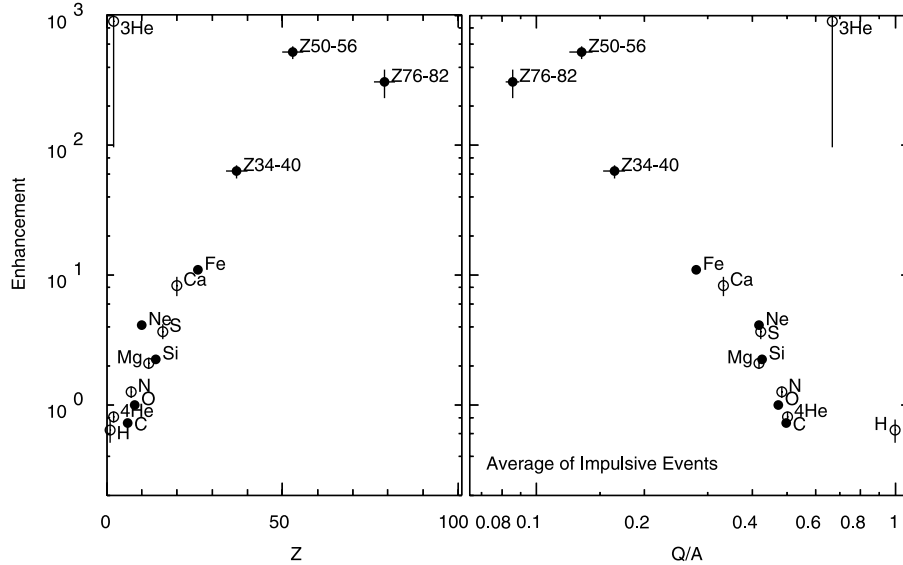


Figure 17: Abundance enhancements in average large impulsive events relative to coronal abundances, shown as a function of atomic number, Z , and charge-to-mass ratio, Q/A , at ~ 3 MK. The solid circles are from the study by Reames and Ng (2004) and open circles are from previous studies (Adapted from Figure 4 in Reames & Ng, 2004).

1489 eration through a resonance with ion cyclotron waves generated by streaming electrons
 1490 (Roth & Temerin, 1997; Temerin & Roth, 1992).

1491 The *Wind* mission has also allowed SEP abundances at lower masses to be com-
 1492 pared over an extended time period. For example, Reames et al. (2014) show, for 8 hour
 1493 intervals during a 19 year period, a range of values of Ne/O and Fe/O (both normalized
 1494 to typical values in large SEP events) at ~ 3 MeV/nucleon. The observations show ev-
 1495 idence for a bimodal distribution, with a group of periods with enhanced Fe and Ne abun-
 1496 dances likely to be associated with impulsive SEP events and another, larger, group with
 1497 abundances similar to those in large SEP events, associated with gradual events. How-
 1498 ever, intervals with intermediate values are also present.

1499 Considering particles accelerated by interplanetary shocks, Reames (2012) stud-
 1500 ied the spectra of ~ 1 -10 MeV/nucleon ^4He at 258 shocks in the CfA Wind shock database²⁹
 1501 with the aim of determining which shock parameters are more important to produce par-
 1502 ticle acceleration. Only 39 ($\sim 15\%$) of these shocks had significant particle acceleration
 1503 to these energies, and the shock speed was found to be the strongest determinant of the
 1504 particle intensity at the shock followed by the shock compression ratio; quasi-perpendicular
 1505 shocks were also favored.

1506 3.10 Solar Radio Bursts

1507 Before the launch of *Wind*, type II bursts were known in only two domains: met-
 1508 ric (> 15 MHz) from ground-based observations, and hectometric-kilometric (< 2 MHz)
 1509 from space-based observations (e.g., see discussion in Maroulis et al., 1993, and references
 1510 therein). These frequencies correspond to spatial domains of $< 2 R_s$ and $> 10 R_s$ from
 1511 the Sun center. The *Wind*/WAVES experiment is capable of observing radio emission

²⁹ https://www.cfa.harvard.edu/shocks/wi_data/

1512 in ~ 2 –14 MHz range and determining the direction to the emission source region. Thus,
 1513 *Wind*/WAVES filled a previous observational frequency gap and narrowed down the source
 1514 regions of these emissions, resulting in a number of new discoveries that will be highlighted
 1515 in this section. The coronal domain sampled by *Wind*/WAVES overlaps with that im-
 1516 aged by space-borne coronagraphs. A quarter century of *Wind*/WAVES observations and
 1517 white-light observations from the Solar and Heliospheric Observatory (SOHO) mission
 1518 have contributed enormously to our understanding of solar eruptions and their heliospheric
 1519 consequences. The combined radio and coronal imagery were enhanced with the addi-
 1520 tion of STEREO in 2006, which greatly advanced our understanding of inner heliospheric
 1521 nonthermal processes associated with solar magnetic active regions. All radio emissions
 1522 are due to nonthermal electrons of various energies, so the radio bursts provide key in-
 1523 formation not only on the particle energization process but also on the ambient medium
 1524 in which the electrons propagate and produce the radio signatures. Note that in this sec-
 1525 tion, we intentionally refer to both coronal mass ejections (CMEs) and interplanetary
 1526 coronal mass ejections (ICMEs). The former refers to CMEs observed using coronal im-
 1527 agers and the later to those observed with in situ plasma measurements (see Section 3.8.1).

1528 Nonthermal radio signatures in the interplanetary medium (IPM) are simple com-
 1529 pared to those in the corona ($< 2 R_s$). Most of the IP radio emissions arise from the plasma
 1530 emission mechanism³⁰, whereas near the Sun additional mechanisms such as cyclotron
 1531 emission, gyrosynchrotron emission, and bremsstrahlung emission operate. Early *Wind*
 1532 studies showed that nearly all the known radio burst types (e.g., type II, type III, and
 1533 type IV; see review by Wild et al., 1963) were observed³¹ by the WAVES radio receivers
 1534 (Bale et al., 1999; Gopalswamy et al., 1998, 2001; Gopalswamy, 2004a, 2004b; Gopalswamy
 1535 & Mäkelä, 2010; Kaiser, 2003; Reiner et al., 1998, 2001).

1536 Type III bursts occur as regular, frequency-drifting radio emissions and as type III
 1537 storms. Type III storms typically start in the metric domain (around 80 MHz) in asso-
 1538 ciation with type I storms at higher frequencies but extend down to sub-MHz frequen-
 1539 cies. Type III storms are characterized by broadband ($>$ few MHz), very short duration
 1540 (i.e., $\lesssim 1$ –2 minutes) emissions that occur in rapid succession (typically > 10 per hour).
 1541 Type III bursts are characterized by their fast frequency drift (i.e., MHz per minute) ver-
 1542 sus time, which is a tracer of the gradient in the IP electron number density. Type III
 1543 storms are caused by nonthermal processes taking place in active regions outside of erup-
 1544 tions. Both type III storm bursts and regular type III bursts result from emissions due
 1545 to nonthermal electrons propagating along open magnetic field lines. Type II bursts are
 1546 caused by nonthermal electrons accelerated by CME-driven shocks. Type II bursts are
 1547 characterized by their slow frequency drift (i.e., few 100s of kHz per hour) versus time,
 1548 which is a tracer of the shock speed and electron number density upstream of the shock.
 1549 Type IV bursts are thought to be due to nonthermal electrons trapped in post-eruption
 1550 arcades (i.e., half-loop-like arches of intense magnetic field connecting to active regions
 1551 on the solar surface) in the eruption site. Type IV bursts are characterized by a broad-
 1552 band frequency emission in the several to > 10 MHz range, sometimes showing a U-shaped
 1553 profile.

1554 Figure 18 shows a solar eruption that exhibits all the IP burst types: type III storm,
 1555 type III burst, type IV burst, and type II burst. All the burst types are associated with
 1556 complex magnetic regions on the Sun. All but the type III storm are associated with so-
 1557 lar eruptions involving CMEs and solar flares.

³⁰ i.e., nonthermal electron beams excite Langmuir-like waves which nonlinearly mode convert to free electromagnetic radio emissions at frequencies near the plasma frequency of their source region

³¹ Type I radio bursts occur at higher frequencies than can be resolved by *Wind*/WAVES, so they will not be discussed herein.

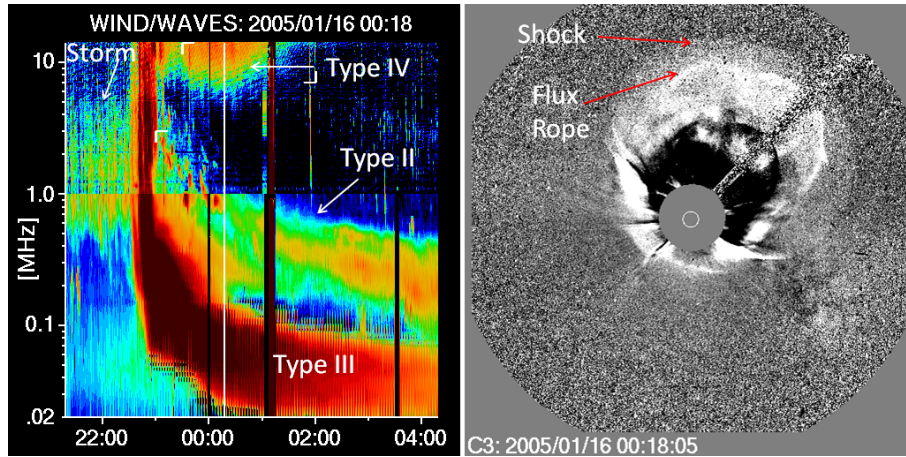


Figure 18: Four types of radio bursts observed by Wind/WAVES on 2005 January 15 toward the end of the day: type III storm was in progress when the eruption occurred. The eruption is marked by the regular type III burst, followed by a type II burst and a type IV burst. (right) The associated CME observed by SOHO/LASCO. The CME has a flux rope driving a shock as indicated. The shock is at a heliocentric distance of $\sim 25 R_s$ in sky-plane projection (Adapted from Gopalswamy, 2016).

3.10.1 Type II Bursts

1558

1559

1560

1561

1562

1563

1564

1565

As previously stated, type II bursts result from nonthermal electrons accelerated by CME-driven shock waves. Thus, they are a tracer of the shock speed/position versus time and of the electron number density immediately upstream of the shock front. Remotely tracking shocks using radio waves is an important element of our space weather forecasting infrastructure. It also provides information on the radial gradient of the IP electron number density, critical for heliospheric models. Therefore, it is important to understand the origin and evolution of the frequency drifts of type II bursts.

1566

1567

1568

1569

1570

1571

1572

1573

1574

Type II bursts can exist in the decametric-hectometric (DH), metric (m), and km wavelength range. Interestingly, there are type II bursts that start in the m range and evolve to the DH range (i.e., meter to DH or m-DH range) while other DH type II bursts are not continuations of m type II bursts. Some type II bursts start in the DH range and end there as well, called pure DH type II bursts. Some type II bursts occur in the m and DH ranges simultaneously while others start in the m range and evolve to the DH and onto the km range. Finally, there can be purely km type II radio bursts (Gopalswamy et al., 2000; Gopalswamy, 2004a; Kaiser et al., 1998; Reiner & Kaiser, 1999). Thus, initially there was a mystery as to the source of the diversity in type II radio bursts.

1575

1576

1577

1578

1579

1580

1581

1582

1583

The mystery was resolved in a subsequent investigation by Gopalswamy et al. (2005) who found that the wavelength extent of type II bursts depends on CME kinematics, i.e., their speed and acceleration/deceleration. The authors showed that the frequency/wavelength of the radio emissions depends upon the CME speeds where the emission ranges and speeds (averages from multiple events) were: ~ 610 km/s (m), 1068 km/s (m-DH, DH, and DH-km combined), 1490 km/s (m-to-km), and 540 km/s (purely km). When examining coronal images using the SOHO coronagraphs, Gopalswamy et al. (2005) observed all CMEs decelerated in the coronagraph FOV except those associated purely km type II bursts. These accelerated to super Alfvénic speeds at tens of R_s from the Sun.

1584

Simultaneous type II bursts at different frequencies

Further investigation after the accumulation of numerous type II bursts showed the simultaneous occurrence of two type II bursts: one in the DH domain that evolved from the m domain and one starting in the DH domain and continuing to the km domain. Gopalswamy (2011) reported on one such CME-associated event on 2003 June 17 where the inferred source height of the m-DH component (from the Sun center) was $\sim 2.4 R_s$ and the DH-km type II was at $\sim 7 R_s$. A possible explanation proposed was a curved shock front where the nose was at $\sim 7 R_s$ and the flanks at $\sim 2.4 R_s$ (e.g., see the shock surrounding the flux rope in Figure 18). The CME was very fast (~ 1800 km/s), so the flanks are also fast enough to drive shocks and accelerate electrons. The flanks are at lower altitudes (where the higher electron density corresponds to higher emission frequency), while the nose is at higher altitudes (lower electron density corresponds to lower emission frequency). The Gopalswamy (2011) study is supported by an earlier study by Raymond et al. (2000) of a slower CME (only ~ 1300 km/s, thus without flank shocks), only showing type II bursts in the m domain.

Wind/WAVES is also capable of determining the direction from which a radio emission propagated to the spacecraft (Hoang et al., 1998). This analysis has been applied to another fast CME (~ 1900 km/s) on 2012 July 6 with both m-DH and DH-km domain type II bursts (Mäkelä et al., 2018). The authors also used the same technique using STEREO to confirm the source regions to be near the nose of the CME shock. Thus, these studies support the nose-flank emission source regions, in contrast to another model that invokes a second shock – the flare blast wave – to explain the metric emission.

Type II burst dependence on ICME properties

Another curiosity is that not all CMEs have an associated type II burst. By the end of 2019, *Wind*/WAVES has observed more than 500 bursts at frequencies below 14 MHz. Even so, early work of ~ 100 events revealed that type II bursts are associated with fast (>900 km/s) and wide ($>60^\circ$) CMEs (Gopalswamy et al., 2000, 2001). Later work noted that the average CME speed in the sky plane of coronagraphs has increased to ~ 1164 km/s due to the energetic CMEs during the maxima of cycles 23 and 24 (Gopalswamy, Mäkelä, & Yashiro, 2019).

An interesting correlation was observed between the initial deceleration and initial speed of CMEs associated with type II bursts. The CMEs were found to decelerate in the coronagraph FOV at $\sim 0\text{--}100$ m s $^{-2}$, where the deceleration is correlated with initial speed (Gopalswamy et al., 2001). Later work confirmed the correlation between initial deceleration and initial speed using the frequency drift rate of the observed type II bursts (Reiner, Kaiser, & Bougeret, 2007; X. Zhao et al., 2019).

Given that CMEs are strongly coupled to the solar cycle, examinations of DH type II bursts showed a solar cycle variation with maximum rates of ~ 10 bursts per Carrington rotation (~ 27.3 days) – the approximate rotation period of low solar latitudes – during solar maximum. However, no DH type II bursts were observed in the lowest part of solar minimum (Gopalswamy et al., 2020). Interestingly, the occurrence rate of type II bursts depends upon the CME properties (i.e., fast and wide CMEs produce type II bursts) rather than the sunspot number (SSN). Gopalswamy et al. (2020) showed that the decrease in SSN between solar cycles 23 and 24 was $\sim 39\%$ while the decrease in type II bursts was $\sim 48\%$. The authors argued the decrease in fast and wide CMEs was also $\sim 48\%$, illustrating the connection between the CMEs and type II bursts.

Shock arrival prediction using type II bursts

Recall that type II bursts are a tracer of the shock speed/position versus time and of the electron number density immediately upstream of the shock front. Thus, researchers can use the frequency drift rate, $\frac{df}{dt}$, as a function of time to examine the evolution of the associated ICMEs and the density gradients in the interplanetary medium (IPM). Aguilar-Rodriguez et al. (2005) showed that the drift rate followed a power law of the form $|\frac{df}{dt}| \sim f^{-\varepsilon}$, where the exponent $\varepsilon \sim 1.8$ for the entire wavelength domain (m to km)

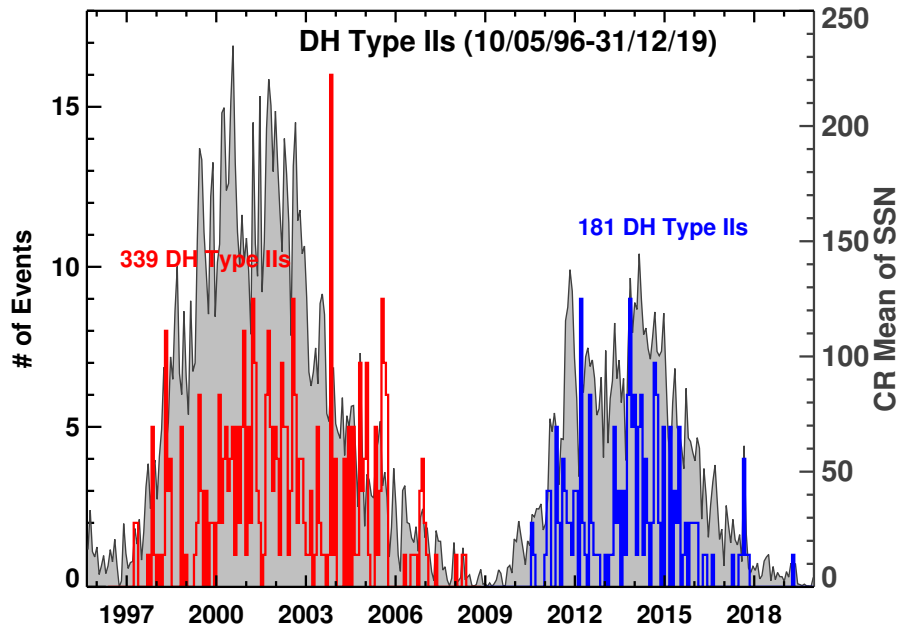


Figure 19: Occurrence rate of DH type II bursts 1996 May 10 to 2019 December 31 (red: cycle 23; blue: cycle 24) summed over Carrington rotation periods. The sunspot number is shown for comparison. Gopalswamy, Mäkelä, and Yashiro (2019) found that the drop in the number of events in cycle 24 is similar to the drop in the number of fast and wide CMEs (figure updated from Gopalswamy, Mäkelä, & Yashiro, 2019).

1637 and was higher in the km domain (2.7 at $f < 1$ MHz), and lower at m-DH domain (1.5
 1638 at $f > 1$ MHz). The different exponents in the different spectral domains reflect the CME/ICME
 1639 evolution at different distances from the Sun (Gopalswamy & Mäkelä, 2011; Vršnak et
 1640 al., 2001). Initially ICMEs accelerate into a more and more tenuous region which results
 1641 in a smaller ε . Further from the Sun, ICMEs decelerate which increases ε . The evolu-
 1642 tion of the ICME shocks and influence on ε have been supported by case studies (e.g.,
 1643 Gopalswamy, Mäkelä, Akiyama, et al., 2018; Y. D. Liu et al., 2013).

1644 After type II bursts reach the km range their evolution is more consistent with a
 1645 constant IP shock speed, thus allowing researchers to predict the shock arrival time at
 1646 Earth. Cremades et al. (2015) combined coronagraph images of CMEs, type II radio emis-
 1647 sions in the km range, and in situ information on shocks to investigate the height-time
 1648 history of 71 IP shocks. The authors were able to predict the shock arrival time within
 1649 ~ 6 hr for 85% of the events. Other studies (Corona-Romero et al., 2013) attempted to
 1650 approximate the shock evolution as that of a blast wave. However, the speeds of mag-
 1651 netic clouds (MCs) and the associated shocks have been shown to be highly correlated
 1652 (95%) (Gopalswamy, 2006). Thus, ICMEs and their shocks remain coupled at 1 AU, even
 1653 though both have undergone significant decelerations, which is inconsistent with a blast
 1654 wave scenario.

1655 Type II bursts and SEPs

1656 Type II bursts are the earliest indicators of CME-driven shocks, and can also serve
 1657 as an indicator of solar energetic particle (SEP) events because the same shock accel-
 1658 erates electrons and ions (see Section 3.9 for more discussion of SEPs). Recall that the
 1659 observed frequency of type II bursts is strongly related to the CME speed. For instance,
 1660 purely m type II bursts are associated with average speed CMEs satisfying ~ 600 km/s

1661 while m-DH type II bursts are associated with >1000 km/s CMEs. Faster CMEs tend
 1662 to result in stronger (higher Mach number) IP shocks, which are known to be more ef-
 1663 ficient accelerators of particles (e.g., see discussion in Caprioli & Spitkovsky, 2014, and
 1664 references therein). Therefore, investigating the relationship between type II bursts and
 1665 SEPs was an obvious avenue for improving space weather forecasting.

1666 Cliver et al. (2004) found that only $\sim 25\%$ of purely m type II bursts are associ-
 1667 ated with >20 MeV SEP events but the rate almost quadrupled to 90% when a m type
 1668 II had a DH counterpart. Gopalswamy et al. (2005) found that CMEs producing type
 1669 II bursts in the m-to-km range also had high energy SEPs. Further, all SEPs strong enough
 1670 to generate a ground level enhancement (GLE) – solar particles observed by ground-based
 1671 instruments – are associated with m-to-km type II bursts (Gopalswamy et al., 2012).

1672 Later work (Cliver et al., 2019; Gopalswamy, Mäkelä, et al., 2015; Gopalswamy, Yashiro,
 1673 et al., 2016) found that the initial frequency of type II bursts correlated with the spec-
 1674 tral slope of the SEP number flux versus energy power-law relationship. Shocks form-
 1675 ing closer to the solar surface (i.e., with a higher initial type II burst frequency) had harder
 1676 spectra³² than those forming at higher altitudes. The harder spectra SEP events are of-
 1677 ten also GLE events. The reason for the shock formation altitude dependence on spec-
 1678 tral slope relates to the background plasma parameters in which the shock formed. At
 1679 lower altitudes, the magnetic field magnitude is much larger and the geometry is more
 1680 complicated, both of which make for more efficient particle scattering and acceleration
 1681 (Cliver et al., 2019; Gopalswamy et al., 2017).

1682 Finally, the examination of type II bursts have helped us understand the source
 1683 of the >300 MeV protons required for producing the pion-decay continuum observed as
 1684 sustained gamma-ray emission (SGRE) from the Sun (Gopalswamy, Mäkelä, Yashiro,
 1685 et al., 2018; Share et al., 2018). Gopalswamy, Mäkelä, Yashiro, et al. (2018) and Gopalswamy,
 1686 Mäkelä, Yashiro, Lara, et al. (2019) demonstrated a close linear relationship between the
 1687 SGRE and type II burst durations, in every SGRE event with duration >3 hr, support-
 1688 ing the hypothesis that the >300 MeV protons continue to be accelerated at the shock
 1689 as it moves away from the Sun, and then propagate back to the Sun, generating the SGRE.
 1690 However, other studies (de Nolfo et al., 2019; K.-L. Klein et al., 2018; Malandraki & Crosby,
 1691 2018) may not support this hypothesis for the origin of SGRE.

1692 **3.10.2 Type III Bursts**

1693 Type III bursts result from nonthermal electrons accelerated in solar magnetic ac-
 1694 tive regions exciting plasma waves as they stream along the magnetic field away from
 1695 the Sun. Early work using triangulation between *Ulysses* and *Wind* identified the elec-
 1696 tron beam source of type III bursts, finding that the electrons were traveling at a speed
 1697 of ~ 0.3 c (Reiner et al., 1998). When the radio emission of a type III burst reaches the
 1698 local plasma frequency of the observing spacecraft, the emission is occurring locally. Reiner
 1699 and MacDowall (2015) analyzed five in-situ type III radio bursts observed by *Wind* and
 1700 STEREO, finding that the electron beam speed ranged from 0.2 c to 0.38 c near the Sun
 1701 but was only ~ 0.2 c near 1 AU. The reduction in beam speed corresponded to a decel-
 1702 eration of ~ 30 km s⁻². That is, the primary electrons exciting type III bursts near the
 1703 sun correspond to energies of 20–30 keV while they drop to ≤ 10 keV near 1 AU. The
 1704 reduction in energy is consistent with the beam losing energy as it converts kinetic en-
 1705 ergy to electromagnetic energy to generate the initial Langmuir waves.

1706 Type III bursts generally accompany SEP events (e.g., Cane et al., 2002; MacDowall
 1707 et al., 2003, 2009; Miteva et al., 2017; I. G. Richardson et al., 2018; Winter & Ledbet-
 1708 ter, 2015, and see Section 3.9). In particular, large SEP events are usually associated with

³² i.e., indicates a flatter or less-steep drop in number flux with increasing energy

bright, long duration, complex type IIIs such as that shown in Figure 19. These long-duration emissions were originally thought to result from electrons accelerated at or associated with CME-driven shocks (Bougeret et al., 1998; Cane et al., 1981). Based on *Wind*/WAVES observations, which as discussed above, closed a frequency gap between ground and previous space-based instruments, these complex type III emissions can appear to extend from the associated type II bursts (Gopalswamy et al., 2000), but they are now thought to result from electron acceleration in magnetic reconnection below CMEs (Cairns et al., 2018; Cane et al., 2002; Reiner et al., 2000). Characteristics such as correlations between the burst duration or intensity and SEP peak intensity, and their rapid onset and frequency drift following solar flares, have led to the inclusion of type IIIs in proposed SEP prediction schemes (e.g., Laurenza et al., 2009; I. G. Richardson et al., 2018; Winter & Ledbetter, 2015). However, these require real-time radio observations that are not available from *Wind*. The largest SEP events are usually associated with type III burst durations of $\gtrsim 15$ min at ~ 1 MHz (Cane et al., 2002; MacDowall et al., 2003, 2009; I. G. Richardson et al., 2018; Winter & Ledbetter, 2015). Krucker et al. (1999) examined the relationship between type III bursts and energetic electrons observed in situ using *Wind* 3DP electron and WAVES observations. They found that while some near-relativistic electron events are released at the Sun at the time of the type III burst, others are apparently released up to half an hour later, suggesting that they originate from a different population than the type III-producing electrons. Similar conclusions were reached by Haggerty and Roelof (2002), Klassen et al. (2002), and L. Wang et al. (2006, 2016). An alternative interpretation is that the energetic electrons may be delayed during propagation through the interplanetary medium (Cane, 2003; Cane & Erickson, 2003; L. Wang et al., 2011).

3.10.3 Type III Storms

Solar noise storms are nonthermal radio emission due to electrons accelerated in a non-eruptive energy release in active regions. At metric wavelengths, noise storms manifest as type I bursts, which transition into type III storms in the outer corona. Thus, type III storms are the low-frequency extensions of type I storms (Fainberg & Stone, 1970). Type III storms can last for several days and can be observed at heliocentric distances of up to $170 R_s$ (Bougeret et al., 1984). Interestingly the rate of type III storms and their intensity increase as the source active region crosses the central meridian (Gopalswamy, 2004b; Morioka et al., 2007, 2015; Reiner et al., 2001; Reiner, Fainberg, et al., 2007). Further work has indicated that type III bursts and storms have different energization processes based upon differences in occurrence frequency and emitted power flux (Morioka et al., 2007).

The source regions of type III storms were later identified to be solar active regions accompanied by coronal holes. These are regions in which the magnetic field lines do not connect back to the solar surface but rather are directed outward into the IPM. The suggested mechanism (Del Zanna et al., 2011) is a type of magnetic reconnection called interchange reconnection – magnetic reconnection between coronal hole and adjacent, closed magnetic field lines that leads to the energization of low energy electrons (see Section 3.4 for details on magnetic reconnection). These sustain the type III storm on closed magnetic field loops and give rise to weak type III emission on open field lines.

Type III storms can be disrupted by CMEs for upwards of ~ 10 hr (see Figure 18). Gopalswamy (2016) reported on a type III storm starting on 2005 January 14 that was disrupted by five CMEs (including that in Figure 18), with the last one being an extreme event that occurred on 2005 January 20. Following the final CME the type III storm did not reappear suggesting a possible reconfiguration of the active region or a change in the directivity of the storm or the active region complexity.

1759 Type III storms also exhibit an interesting change in degree of polarization with
 1760 radial distance. In the metric range, type III storms have a degree of circular polariza-
 1761 tion of up to $\sim 25\%$. In the IPM, type III storms have much smaller degrees of circular
 1762 polarization ($< 5\%$) at frequencies near 1 MHz (Reiner, Fainberg, et al., 2007). Reiner,
 1763 Fainberg, et al. (2007) used the change in the degree of circular polarization to deter-
 1764 mine the magnitude and radial projection of the magnetic fields above solar active re-
 1765 gions. Typical magnetic field strengths of ~ 50 mG (or ~ 5000 nT) at a heliocentric dis-
 1766 tance of $25 R_s$ were calculated and the field strength decreased faster than the inverse-
 1767 square of the radial distance. Thus, type III storms can be used to remotely probe the
 1768 magnetic structure and strength of solar active regions.

1769 **3.10.4 Type IV Bursts**

1770 Type IV bursts are another phenomenon that has been better understood through
 1771 observations of their lower frequency range by WAVES in the DH frequency range. The
 1772 type IV burst on 1998 May 2 studied by Leblanc et al. (2000) was one of the first ob-
 1773 served down to 7.5 MHz (e.g., similar to the one shown in Figure 18). Gopalswamy (2004b)
 1774 studied a dozen DH type IV bursts finding they are extensions of the emissions in the
 1775 metric range. The type IV bursts lasted typically for ~ 2 hours at 14 MHz with a typ-
 1776 ical ending frequency of ~ 7.7 MHz. The type IV bursts in the DH frequency range are
 1777 associated with very energetic CMEs (average speed ~ 1200 km/s). Further, the aver-
 1778 age speed of CMEs (~ 1500 km/s) associated with DH type IV bursts is similar to that
 1779 in large SEP events (Gopalswamy, 2011, 2016; Hillaris et al., 2016). The most likely source
 1780 of type IV bursts is electrons accelerated in a solar flare site that become trapped in the
 1781 closed magnetic fields of the post eruption arcades.

1782 More recent studies discovered that DH type IV bursts have a relatively narrow
 1783 emission cone (e.g., Gopalswamy, Akiyama, et al., 2016). That is, DH type IV bursts as-
 1784 sociated with eruptions in the middle of the solar disk show a symmetric time profile about
 1785 their lowest frequency (i.e., the lowest frequency boundary of the emission is U shaped).
 1786 In contrast, DH type IV bursts associated with eruptions on the limb of the solar disk
 1787 show an asymmetric time profile. Gopalswamy, Akiyama, et al. (2016) concluded that
 1788 the type IV emission cone is less than $\sim 60^\circ$ in full width and that this narrow cone re-
 1789 sults from the small angular extent of the source region, the post eruption solar arcades.
 1790 Another proposed explanation is that the shock-compressed, high-density plasmas in the
 1791 foreground of the emission attenuate the intensity of the type IV bursts more on the shock
 1792 flanks than the center (i.e., due to larger line of sight integration) (Pohjolainen & Talebpour
 1793 Sheshvan, 2020; Talebpour Sheshvan & Pohjolainen, 2018). The reason for the narrow
 1794 type IV emission cone continues to be an active area of research.

1795 **3.11 Wind’s Relevance to the HSO and Future Research**

1796 *Wind* is the “standard candle” against which numerous other missions have and
 1797 continue to calibrate their instruments (e.g., McFadden, Carlson, et al., 2008). *Wind* is
 1798 a primary collaborator with NASA’s *Parker Solar Probe* (PSP) (Fox et al., 2015) and
 1799 ESA’s *Solar Orbiter* (SolO) missions (Müller et al., 2020). The short ~ 88 day orbit of
 1800 PSP and the ~ 0.3 – 0.76 AU orbit of SolO will provide frequent radial and magnetic field
 1801 alignments with *Wind* allowing for multi-spacecraft studies that will significantly enhance
 1802 the science return of both PSP and SolO. *Wind* is also expected to play a major role in
 1803 NASA’s upcoming Interstellar MAPPING Probe (IMAP) mission (McComas et al., 2018).
 1804 Below we highlight some exciting new results that arose from the combined use of *Wind*
 1805 and PSP.

1806 *Wind*’s broad contributions to solar and heliospheric physics can be viewed through
 1807 the lens of PSP’s mission objectives. PSP was launched in August, 2018 to study the
 1808 origin and acceleration of the solar wind in the upper solar corona. PSP will not reach

1809 its minimum perihelion of ~ 10 solar radii (R_s) until 2026, but PSP is already significantly
 1810 closer to the sun than any previous mission. One method of understanding the evolu-
 1811 tion of the solar wind in the inner heliosphere is to compare the near-sun PSP in situ
 1812 observations with *Wind* observations at 1 AU. Although these studies may require spe-
 1813 cific spacecraft alignments and are still in their early phase, PSP and *Wind* have already
 1814 provided insight into the heliospheric current sheet, stream interaction regions, and ra-
 1815 dio remote sensing as detailed in the following.

1816 The Heliospheric Current Sheet (HCS) varies significantly from its formation in the
 1817 solar corona to its interaction with Earth at 1 AU. PSP observations of HCS crossings
 1818 during the first solar orbit were successfully mapped to *Wind* observations at 1 AU (Szabo
 1819 et al., 2020). The authors found that during this period at solar minimum, the HCS showed
 1820 remarkable stability and could be successfully traced over full solar rotations. However,
 1821 earlier work showed that the internal structure of the HCS exhibits a marked difference
 1822 between solar minimum and solar maximum. Although magnetic reconnection-induced
 1823 magnetic structures appear to have been present near PSP as well as near 1 AU, Szabo
 1824 et al. (2020) found that the characteristics of individual structures differed. Magnetic
 1825 signatures were stronger and more pronounced at PSP, while density enhancements were
 1826 more pronounced at 1 AU. SIRs can also be traced from PSP to *Wind* (Allen et al., 2020).
 1827 This study demonstrated that during the first PSP orbit, SIRs formed well within 0.5
 1828 AU, and also determined that the associated locally-accelerated Allen et al. (2020) suprather-
 1829 mal particles penetrate deeper into the fast stream further away from the sun.

1830 Supplemented with data from STEREO and *Wind*, PSP radio observations of Type
 1831 III radio bursts confirmed they are associated with energetic electron beams (Krupar et
 1832 al., 2020). The radio beams showed significant scattering due to solar wind density fluc-
 1833 tuations in the inner heliosphere. The predicted density fluctuation levels from the ra-
 1834 dio data were compared to the in-situ PSP observations and yielded the same 6–7% level.
 1835 There are additional efforts involving *Solo* and *Wind* that are currently in preparation
 1836 as of time of the submission of this review.

1837 Thus, *Wind* continues to produce significant and relevant data that contribute to
 1838 studies helping to improve the science output of other solar wind missions. As evidenced
 1839 by the numerous recent, novel scientific studies referenced herein, *Wind* also continues
 1840 to be a valuable independent mission for studies of topics ranging from solar wind physics,
 1841 kinetic physics, remote solar and astrophysics to large-scale structures such as ICMEs
 1842 and SIRs/CIRs. Its diverse compliment of instruments combined with their longevity
 1843 and accuracy have made *Wind* a truly special resource for studies of space plasma physics.

1844 4 Summary

1845 *Wind* launched on November 1, 1994 and has journeyed through nearly every part
 1846 of the terrestrial magnetosphere, several hundred R_E prograde and retrograde of Earth,
 1847 to L2 and is now stationed at L1. Over its 26+ year lifetime of observations and discov-
 1848 eries, *Wind* has illustrated its importance and relevance by the >5380 refereed publi-
 1849 cations, numerous discoveries and firsts, and its continued collaboration with multiple
 1850 other missions in the HSO. *Wind* has made paradigm altering advances in multiple fields
 1851 of study from gamma ray astrophysics to magnetospheric, solar wind, and solar radio
 1852 physics. *Wind*'s longevity and diverse and redundant instrumentation has led to it be-
 1853 coming the so called “standard candle” for near-Earth solar wind measurements.

1854 *Wind* was launched with the first Russian instrument to fly on a US spacecraft,
 1855 called KONUS. It was the first such collaboration and has been extremely fruitful lead-
 1856 ing to the identification of thousands of GRBs, nearly 30 magnetars or SGRs, several
 1857 magnetar GFs, and the first evidence of the source of FRBs originating from magnetars.

1858 *Wind*/KONUS continues to play an active role in the gamma ray astrophysics commu-
 1859 nity as part of the IPN and GCN.

1860 Although *Wind* was not designed explicitly to detect IPD or ISD, it has accumu-
 1861 lated >100,000 dust impact detections through the end of 2015, publicly available through
 1862 SPDF CDAWeb. The large statistics, directional information determined from *Wind*, when
 1863 combined with observations from the dedicated dust instrument on *Ulysses* helped re-
 1864 searchers calculate the flow of ISD, thus the interstellar flow. The dust impact database
 1865 has also been used in collaboration with the AIM SOFIE experiment revealing a corre-
 1866 lation between the rate of dust impacts on *Wind* and AIM observations of meteoric smoke.
 1867 *Wind*'s vital contributions to dust detection are expected to continue for the foreseeable
 1868 future.

1869 *Wind* has passed through the lunar wake on ten separate occasions at varying dis-
 1870 tances from the surface of the moon. *Wind*'s modern instrumentation (compared to the
 1871 pioneering missions that passed through the lunar wake) helped researchers to show that
 1872 the moon, an unmagnetized body, produced a wake and that the plasma-body interac-
 1873 tion was kinetic, not fluid-like. Although more recent experiments have improved our
 1874 understanding of the lunar-plasma environment, *Wind*'s contributions were groundbreak-
 1875 ing at the time.

1876 *Wind* observations showed evidence of locally energized electrons to 100s of keV
 1877 associated with magnetic reconnection in the geomagnetic tail. These observations led
 1878 to entirely new ideas of particle energization in reconnection events and altered our un-
 1879 derstanding of magnetic reconnection. *Wind* also helped advance our understanding of
 1880 reconnection in the solar wind showing that the exhaust regions can extend to >1800
 1881 R_E from the diffusion region. Again, these results were only obtained by leveraging *Wind*'s
 1882 unique orbits and highly accurate instrumentation.

1883 *Wind* also played a pivotal role in radiation belt physics, specifically on the top-
 1884 ics of waves and particle lifetimes. *Wind*'s ability to accurately measure high cadence
 1885 time series electric and magnetic fields allowed for some of the first statistical studies of
 1886 large amplitude whistler waves in the radiation belts. These modes are thought to be
 1887 critical for particle energization and loss from these regions. The waves were found to
 1888 be orders of magnitude larger in amplitude than previously thought and caused a dra-
 1889 matic shift in our understanding of particle lifetimes in the radiation belts that was used
 1890 to justify several primary science objectives for NASA's *Van Allen Probes* mission.

1891 *Wind* made major advances in the study of foreshocks as well. First *Wind* showed
 1892 the spatial extent of the terrestrial foreshock was much larger than previously thought,
 1893 i.e., increased from $\sim 200 R_E$ to $>3000 R_E$. *Wind* observations also led to the discov-
 1894 ery of a new TIFP called a foreshock cavity. *Wind* was also the first to show that TIFPs
 1895 can locally generate their own mini-foreshocks, which led to a whole new field of study
 1896 and the later discovery that TIFPs can locally generate relativistic electrons. Given that
 1897 TIFPs are thought to play a critical role in particle dynamics and global dynamics of
 1898 both the bow shock and magnetosphere, understanding them is critical for space weather
 1899 predictions and magnetospheric dynamics.

1900 The diverse, redundant, and accurate array of instruments on *Wind* have led to
 1901 major advances in our understanding of kinetic-scale instabilities and waves. This com-
 1902 bined with the longevity of continuous measurements has even allowed researchers to tease
 1903 out otherwise impossibly subtle features to reveal the importance of both Coulomb col-
 1904 lisions and instabilities in the evolution of the solar wind. The longevity also helped re-
 1905 searchers reduce the signal-to-noise ratio enough to test numerous previously inacces-
 1906 sible theories to find that, for instance, predictions that most solar wind VDFs are un-
 1907 stable. In short, *Wind*'s instrumentation and longevity have been critical to advancing
 1908 our understanding of kinetic-scale instabilities and waves affecting multiple fields of study.

1909 Not only has *Wind* greatly advanced our understanding of the comparatively co-
 1910 herent phenomena of instabilities, but also our understanding of plasma turbulence. Long-
 1911 term measurements in the solar wind provided the first opportunity to perform statis-
 1912 tics across multiple solar cycles. *Wind* has revealed that the scale at which bulk motions
 1913 of the plasma convert and mix into random thermal motions of the constituent parti-
 1914 cles depends on the magnetization of the plasma and the ability of the slow solar wind
 1915 to support a “1/f” range. *Wind* has also shown that solar wind turbulence is anisotropic,
 1916 consistent with critical balance theory, and has improved our understanding of the lo-
 1917 cation of the so called spectral break. Given the importance of turbulence to the evo-
 1918 lution of the solar wind and inaccessible astrophysical plasmas, the advancements made
 1919 by *Wind* observations should not be understated.

1920 As previously mentioned, the long-term baseline of solar wind observations makes
 1921 *Wind* a perfect platform for statistical studies. As such, *Wind* played a pivotal role in
 1922 our understanding of the importance of collisional effects on the evolution of the solar
 1923 wind plasma. This is surprising given that the plasma is, at best, weakly collisional near
 1924 Earth. *Wind* also performed the first statistically significant, long-term study of the $(T_e/T_s)_{tot}$
 1925 ratio, a parameter critical for testing numerous theories from instabilities to turbulence
 1926 to spectral inversion in astrophysics. *Wind* showed novel relationships between the re-
 1927 lative abundance between protons and alpha-particles and the solar wind speed and sunspot
 1928 number.

1929 *Wind* has made critical contributions to our understanding of IP collisionless shock
 1930 waves. Studies using *Wind* have improved our understanding of energy dissipation mech-
 1931 anisms, particle energization mechanisms, energetic particle sources, and shock evolu-
 1932 tion through remote detection. *Wind* studies have also shown that the structure of low
 1933 Mach number, low plasma beta, quasi-perpendicular shocks are not laminar as originally
 1934 theorized. In fact, the electromagnetic magnetosonic-whistler precursor waves have am-
 1935 plitudes exceeding the shock ramp amplitude, thus containing the largest magnetic field
 1936 gradients in the shock. As previously discussed, *Wind* also showed that TIFP can gen-
 1937 erate their own mini-foreshock within the larger terrestrial ion foreshock. All of these
 1938 advances have reignited interest in collisionless shock waves and improved our understand-
 1939 ing of their dynamics and the importance of kinetic phenomena within.

1940 Studies of ICMEs have made major strides in the decades since *Wind*’s launch. We
 1941 now know that most IP shocks near Earth are caused by ICMEs, and have a better un-
 1942 derstanding of the magnetic structure of ICMEs and their space weather impacts because
 1943 of *Wind*. *Wind* also made the first measurements of extremely cold (~ 1 eV), collision-
 1944 ally mediated electrons within an ICME, something that is not possible with any other
 1945 current space mission. *Wind* has also made advances in the study of CIRs/SIRs confirm-
 1946 ing that they are efficient at particle energization even when they do not yet exhibit a
 1947 collisionless shock near Earth.

1948 *Wind* made the first in situ measurements of ultra-heavy ions in SEP events with
 1949 atomic numbers between 34–82. *Wind* also discovered, through long-term statistical anal-
 1950 ysis, that the weakest solar flares are associated with the strongest SEP enhancements.
 1951 These measurements were made by instrumentation that are currently unique to *Wind*
 1952 for near Earth missions.

1953 Remote radio measurements from *Wind* have also led to numerous advances in un-
 1954 derstanding solar phenomena. Prior to the launch of *Wind*, there were virtually no ob-
 1955 servations of solar radio emissions between ~ 2 –15 MHz, i.e., ~ 2 –10 R_s from the Sun cen-
 1956 ter. *Wind* found that the occurrence of Type II bursts depends on the rate of the fast
 1957 and wide CMEs that generate Type II bursts, not on typical solar activity indices like
 1958 the sunspot number. Type II bursts are important because they can be used to help pre-
 1959 dict SEP events and the arrival times of ICME shocks, both critical space weather phe-
 1960 nomena. *Wind* made some of the first in situ measurements of the electron beams gen-

1961 erating Type III bursts and was the first to measure Type VI bursts down to ~ 7.5 MHz.
 1962 No other near-Earth mission has the accuracy, sensitivity, and capabilities of *Wind* for
 1963 radio measurements.

1964 The *Wind* mission is perhaps best known as a solar wind monitor but it also has
 1965 one of the most diverse arrays of instrument suites. For a majority of the mission, *Wind*
 1966 provided the only observations of kinetic phenomena in the solar wind, and *Wind* is still
 1967 the only mission to provide comprehensive, high-cadence plasma measurements across
 1968 multiple solar cycles. *Wind* continues to provide continuous low-frequency solar radio
 1969 observations, which are a critical part of space weather monitoring. In summary, the list
 1970 of accomplishments and advances made by the *Wind* mission are extensive. Its contri-
 1971 bution to multiple areas of research cannot be over stated and it continues to operate
 1972 nominally even after 26+ years of service. With the launch of PSP and SolO and future
 1973 missions, the importance of *Wind* is only expected to grow, not diminish. For this rea-
 1974 son and the numerous listed and unlisted above, *Wind* is a very special and critical space-
 1975 craft.

1976 Appendix A Definitions and Notation

1977 This appendix lists the symbols/notation used throughout.

1978 *one-variable statistics*

- 1979 – $X_{min} \equiv$ minimum
- 1980 – $X_{max} \equiv$ maximum
- 1981 – $\bar{X} \equiv$ mean
- 1982 – $\tilde{X} \equiv$ median
- 1983 – $X_{5\%} \equiv$ 5th percentile
- 1984 – $X_{25\%} \equiv$ 25th percentile
- 1985 – $X_{75\%} \equiv$ 75th percentile
- 1986 – $X_{95\%} \equiv$ 95th percentile
- 1987 – $\sigma \equiv$ standard deviation
- 1988 – $\sigma^2 \equiv$ variance

1989 *fundamental parameters*

- 1990 – $\varepsilon_o \equiv$ permittivity of free space
- 1991 – $\mu_o \equiv$ permeability of free space
- 1992 – $c \equiv$ speed of light in vacuum [$km\ s^{-1}$] = $(\varepsilon_o \mu_o)^{-1/2}$
- 1993 – $k_B \equiv$ the Boltzmann constant [$J\ K^{-1}$]
- 1994 – $e \equiv$ the fundamental charge [C]

1995 *plasma parameters*

- 1996 – $\mathbf{B}_o \equiv$ quasi-static magnetic field vector [nT] with magnitude B_o
- 1997 – $n_s \equiv$ the number density [cm^{-3}] of species s
- 1998 – $m_s \equiv$ the mass [kg] of species s
- 1999 – $Z_s \equiv$ the charge state of species s
- 2000 – $q_s = Z_s e \equiv$ the charge [C] of species s
- 2001 – $\rho_m = \sum_s m_s n_s \equiv$ total mass density [$kg\ cm^{-3}$]
- 2002 – $\gamma_s \equiv$ polytropic index or ratio of specific heats [N/A] of species s
- 2003 – $T_{s,j} \equiv$ the scalar temperature [eV] of the j^{th} component of species s , $j = \parallel, \perp$,
 2004 or tot where $\parallel(\perp)$ is parallel(perpendicular) with respect to \mathbf{B}_o (see Equation
 2005 A1a)
- 2006 – $P_{s,j} = n_s k_B T_{s,j} \equiv$ the partial thermal pressure [$eV\ cm^{-3}$] of the j^{th} compo-
 2007 nent of species s
- 2008 – $P_{t,j} = \sum_s P_{s,j} \equiv$ the total pressure [$eV\ cm^{-3}$] of the j^{th} component, summed
 2009 over all species
- 2010 – $V_{T_{s,j}} \equiv$ the most probable thermal speed [$km\ s^{-1}$] of a one-dimensional veloc-
 2011 ity distribution (see Equation A1b)
- 2012 – $\Omega_{cs} = 2 \pi f_{cs} \equiv$ the angular cyclotron frequency [$rad\ s^{-1}$] (see Equation A1c)

- 2013 – $\omega_{ps} = 2 \pi f_{ps} \equiv$ the angular plasma frequency [$rad\ s^{-1}$] (see Equation A1d)
 2014 – $\Omega_{lh} = 2 \pi \sqrt{f_{ce} f_{ci}} \equiv$ the angular lower hybrid resonance frequency [$rad\ s^{-1}$]
 2015 – $\Omega_{uh} = 2 \pi \sqrt{f_{ce}^2 + f_{pe}^2} \equiv$ the angular upper hybrid resonance frequency [$rad\ s^{-1}$]
 2016 – $\lambda_{De} \equiv$ the electron Debye length [m] (see Equation A1e)
 2017 – $\rho_{cs} \equiv$ the thermal gyroradius [km] (see Equation A1f)
 2018 – $\lambda_s \equiv$ the inertial length [km] (see Equation A1g)
 2019 – $\beta_{s,j} \equiv$ the plasma beta [N/A] of the j^{th} component of species s (see Equation
 2020 A1h)
 2021 – $V_A \equiv$ the Alfvén speed [$km\ s^{-1}$] (see Equation A1i)
 2022 – $C_s \equiv$ the sound or ion-acoustic sound speed [$km\ s^{-1}$] (see Equation A1j)
 2023 – $V_f \equiv$ the fast mode speed [$km\ s^{-1}$] (see Equation A1l)
 2024 – $\theta_{Bn} \equiv$ the shock normal angle, i.e., the acute reference angle between $\langle \mathbf{B}_o \rangle_{up}$
 2025 and the shock normal unit vector [deg]
 2026 – $\langle |U_{shn}| \rangle_j \equiv$ the j^{th} region average shock normal speed [$km\ s^{-1}$] in the shock
 2027 rest frame (i.e., the speed of the flow relative to the shock)
 2028 – $\langle M_A \rangle_j = \langle |U_{shn}| \rangle_j / \langle V_A \rangle_j \equiv$ the j^{th} region average Alfvénic Mach number [N/A]
 2029 – $\langle M_f \rangle_j = \langle |U_{shn}| \rangle_j / \langle V_f \rangle_j \equiv$ the j^{th} region average fast mode Mach number [N/A]
 2030 – $R_E \equiv$ mean equatorial radius of Earth (~ 6378 km)
 2031 – $R_L \equiv$ mean equatorial radius of Earth’s moon (~ 1737 km)
 2032 – $R_s \equiv$ mean solar radius ($\sim 695,700$ km)
 2033 – $\sigma_c \equiv$ normalized cross-helicity, a quantified measure of the imbalance in plasma
 2034 turbulence (see Equation A1m)
 2035 – $\mathbf{z}^\pm = \delta \mathbf{v} \pm \delta \mathbf{b} \equiv$ Elsasser variables [$km\ s^{-1}$], where $\delta \mathbf{v}$ and $\delta \mathbf{b}$ are the veloc-
 2036 ity and magnetic field fluctuations, the latter being normalized by $\sqrt{\mu_o n_i M_i}$ to
 2037 make it akin to an Alfvénic fluctuation speed

2038 where multiple parameters are given in the following equations:

$$T_{s,tot} = \frac{1}{3} (T_{s,\parallel} + 2 T_{s,\perp}) \quad (\text{A1a})$$

$$V_{Ts,j} = \sqrt{\frac{2 k_B T_{s,j}}{m_s}} \quad (\text{A1b})$$

$$\Omega_{cs} = \frac{q_s B_o}{m_s} \quad (\text{A1c})$$

$$\omega_{ps} = \sqrt{\frac{n_s q_s^2}{\epsilon_o m_s}} \quad (\text{A1d})$$

$$\lambda_{De} = \frac{V_{Te,tot}}{\sqrt{2} \omega_{pe}} = \sqrt{\frac{\epsilon_o k_B T_{e,tot}}{n_e e^2}} \quad (\text{A1e})$$

$$\rho_{cs} = \frac{V_{Ts,tot}}{\Omega_{cs}} \quad (\text{A1f})$$

$$\lambda_s = \frac{c}{\omega_{ps}} \quad (\text{A1g})$$

$$\beta_{s,j} = \frac{2 \mu_o n_s k_B T_{s,j}}{B_o^2} \quad (\text{A1h})$$

$$V_A = \frac{B_o}{\sqrt{\mu_o n_i M_i}} \quad (\text{A1i})$$

$$C_s^2 = \frac{\partial P}{\partial \rho_m} = \frac{\sum_s \gamma_s P_s}{\rho_m} \quad (\text{A1j})$$

$$2V_f^2 = (C_s^2 + V_A^2) \quad (\text{A1k})$$

$$+ \sqrt{(C_s^2 - V_A^2)^2 + 4C_s^2 V_A^2 \sin^2 \theta_{Bn}} \quad (\text{A1l})$$

$$\sigma_c = 2 \frac{\langle \delta \mathbf{v} \cdot \delta \mathbf{b} \rangle}{\langle \delta \mathbf{v}^2 + \delta \mathbf{b}^2 \rangle} \quad (\text{A1m})$$

Appendix B Instability and Wave Definitions and Summary

In this appendix we briefly summarize some of the most commonly investigated kinetic plasma instabilities and waves in the interplanetary medium to provide context and reference for the reader. Although not all of these are discussed in Section 3.7.2, *Wind* data has been used to examine each of these instabilities in multiple different regions of space. Therefore, we provide the comprehensive list for reference. We use the phrase “driven unstable” to mean the free energy was sufficiently above the growth threshold for the electric or magnetic fluctuations to grow in amplitude. The instabilities and/or waves are as follows in no particular order:

- **Firehose Instability:** The firehose mode can be driven unstable by temperature anisotropies (i.e., $T_{s,\perp} < T_{s,\parallel}$) in both electrons (Gary & Nishimura, 2003) and ions (Bale et al., 2009; Gary et al., 1976; Hellinger et al., 2006; Maruca et al., 2012). These are not typically observed with in situ time series data but more so inferred by statistical trends limiting $T_{s,\perp}/T_{s,\parallel}$.
 - **Electron Firehose Instability:** The electron firehose mode can be both resonant and non-resonant with the electrons (Gary & Nishimura, 2003). It either propagates along \mathbf{B}_o and is left-hand polarized (with respect to \mathbf{B}_o), or it is non-propagating³³ with \mathbf{k} oblique to \mathbf{B}_o and nearly linearly polarized.
 - **Ion Firehose Instability:** The ion firehose mode can be both resonant and non-resonant with the ions but can only experience a non-resonant, cyclotron-like interaction with the electrons (Gary et al., 1998). The mode is right-hand polarized (with respect to \mathbf{B}_o) and the wave vector is oriented nearly along \mathbf{B}_o in the linear regime but can become oblique when nonlinear.
- **Mirror Modes:** The mirror mode can be driven unstable by temperature anisotropies (i.e., $T_{s,\perp} > T_{s,\parallel}$) in both electrons (Gary & Karimabadi, 2006) and ions (C. H. K. Chen et al., 2016; Gary et al., 1976; Hellinger et al., 2006). In the linear stage mirror modes are purely growing modes, i.e., the real part of their frequency is zero so they do not propagate. They also show an anti-correlation between δB and δB . In the nonlinear regime, the mirror mode can propagate and \mathbf{k} can be obliquely³⁴ oriented with respect to \mathbf{B}_o . In time series they are usually seen as local decreases in the magnitude of \mathbf{B}_o and less commonly as enhancements.
 - **Electron Mirror Mode:** The electron mirror mode is a non-propagating mode with wave vector oriented obliquely to \mathbf{B}_o and has $k c/\omega_{pe} < 1$.
 - **Ion Mirror Mode:** The ion mirror mode is a non-propagating mode with wave vector oriented obliquely to \mathbf{B}_o and has $k \rho_{cp} < 1$.
- **ICWs:** Electromagnetic ion cyclotron waves (EMIC), ion cyclotron waves (ICWs), proton cyclotron waves (PCWs), or Alfvén/ion cyclotron (AIC) waves are linear or left-hand polarized (with respect to \mathbf{B}_o) modes that propagate small angles to \mathbf{B}_o . They have rest frame frequencies below the local f_{cp} in the solar wind and typically satisfy $k c/\omega_{pp} \sim 0.2\text{--}0.6$ (He, Wang, et al., 2015; He, Pei, et al., 2015; Wicks et al., 2016). They can be driven unstable by temperature anisotropies (Gary et al., 1976) or ion beams (Gary et al., 1981; Wicks et al., 2016). These waves can reach amplitudes in excess of >10 mV/m and >2 nT in the solar wind.
- **LHWs:** Electrostatic (or electromagnetic) lower hybrid waves (or lower hybrid drift or lower hybrid drift instability) are typically linearly polarized electrostatic (i.e., $\mathbf{k}\times\mathbf{B}_o = 0$) waves propagating perpendicular to \mathbf{B}_o . When obliquely propagating, they become a right-hand circularly polarized electromagnetic mode and lie on the same branch of the dispersion relation as fast/magnetosonic-whistler mode waves (Davidson & Gladd, 1975; Huba & Wu, 1976; Lemons & Gary, 1978; Marsch

³³ i.e., the real part of its frequency is zero

³⁴ In linear kinetic theory, mirror modes are always oblique and only in fluid theories is \mathbf{k} exactly orthogonal to \mathbf{B}_o .

- 2088 & Chang, 1983; C. S. Wu et al., 1983, 1984). The typical free energy sources in-
 2089 clude but are not limited to electric currents (Lemons & Gary, 1978), gradient drifts
 2090 (Davidson & Gladd, 1975; Huba & Wu, 1976; Lemons & Gary, 1978), the mod-
 2091 ified two-stream instability (C. S. Wu et al., 1983, 1984), and/or heat flux carry-
 2092 ing electrons (Marsch & Chang, 1983). In time series in situ data these waves look
 2093 like modulated sine waves in the perpendicular electric field for the electrostatic
 2094 version and much less well defined electric and magnetic fluctuations when elec-
 2095 tromagnetic (Walker et al., 2008; Wilson III, Koval, Szabo, et al., 2013). The elec-
 2096 trostatic fluctuations tend to remain below the local lower hybrid resonance fre-
 2097 quency, $f_{lh} = \sqrt{f_{ce} f_{ci}}$, while the electromagnetic fluctuations can extend to well
 2098 above f_{lh} (Walker et al., 2008; Wilson III, Koval, Szabo, et al., 2013). These waves
 2099 can reach amplitudes in excess of >30 mV/m and >20 nT in space plasmas.
- 2100 • **Magnetosonic-whistler Waves:** These are the electromagnetic version of elec-
 2101 trostatic LHWs discussed above and are sometimes called electromagnetic lower
 2102 hybrid waves, whistler precursors, “1 Hz waves” and/or ULF waves in the terres-
 2103 trial foreshock. They are part of the MHD fast mode branch of the dispersion re-
 2104 lation. They are right-hand polarized (with respect to \mathbf{B}_o), obliquely propagat-
 2105 ing modes with wave normal angles satisfying $10^\circ \lesssim \theta_{kB} \lesssim 60^\circ$, wavenumbers sat-
 2106 isfying $0.02 \lesssim k \rho_{ce} \lesssim 3.0$, spacecraft frame frequencies near 1 AU satisfying 0.01
 2107 $\text{Hz} \lesssim f_{sc} \lesssim 7.0$ Hz, and rest frame frequencies near 1 AU satisfying $0.01 \lesssim \frac{f_{rest}}{f_{cp}}$
 2108 $\lesssim 38$ (Wilson III, Koval, Szabo, et al., 2013; Wilson III, 2016; Wilson III et al.,
 2109 2017). The instabilities responsible for radiating these modes can be driven un-
 2110 stable by shock-reflected ions (Wilson III et al., 2012; C. S. Wu et al., 1983) and/or
 2111 heat heat flux carrying electrons (Verscharen, Chandran, et al., 2019; Marsch &
 2112 Chang, 1983). These modes can also be directly radiated through a process called
 2113 dispersive radiation (Tidman & Northrop, 1968; Krasnoselskikh et al., 2002; Wil-
 2114 son III et al., 2009, 2017), whereby the temporally and spatially varying magnetic
 2115 fields and currents in the nonlinearly steepening collisionless shock ramp radiate
 2116 electromagnetic fluctuations on the fast/magnetosonic-whistler branch of the dis-
 2117 persion relation. They are observed with in situ time series data as modulated sine
 2118 waves at low amplitudes and can exhibit soliton-like pulsations at large amplitudes
 2119 (Wilson III et al., 2012; Wilson III, Koval, Szabo, et al., 2013; Wilson III, Koval,
 2120 Sibeck, et al., 2013; Wilson III et al., 2017). These waves can reach amplitudes
 2121 in excess of >30 mV/m and >20 nT in space plasmas.
 - 2122 • **Whistler Waves:** Electromagnetic whistler mode waves (or whistler waves or whistlers
 2123 or lion roars or chorus or hiss) are right-hand polarized with respect to \mathbf{B}_o and
 2124 dispersive (i.e., phase speed depends upon the wavenumber) (Hull et al., 2012; San-
 2125 toľk et al., 2003, 2014). They are radiated by instabilities driven unstable by the
 2126 temperature anisotropy of hot electrons or heat flux carrying electrons (Tong et
 2127 al., 2019; Vasko et al., 2019; Verscharen, Chandran, et al., 2019; Wilson III et al.,
 2128 2009; Wilson III, Koval, Szabo, et al., 2013; Wilson III et al., 2020a). They tend
 2129 to have rest frame frequencies satisfying $\omega_{lh} \ll \omega < \omega_{ce}$ and wavenumbers satis-
 2130 fying $k c/\omega_{pe} \sim 0.2\text{--}1.0$ or $k \rho_{ce} \sim 0.2\text{--}0.8$ (Stansby et al., 2016; Wilson III, Ko-
 2131 val, Szabo, et al., 2013). These waves can reach amplitudes in excess of >300 mV/m
 2132 and >8 nT in space plasmas.
 - 2133 • **ESWs:** Electrostatic solitary waves (or BGK phase space holes or electron/ion
 2134 holes or solitary waves) are linearly polarized electrostatic structures that exhibit
 2135 a bipolar(unipolar) electric field pulse parallel(perpendicular) to \mathbf{B}_o with $\lambda \gtrsim 2 \pi \lambda_{De}$
 2136 (Bale, Kellogg, Larson, et al., 1998; C. Cattell et al., 2003, 2005; Breneman et al.,
 2137 2013; J. R. Franz et al., 2005; Malaspina et al., 2013; Vasko et al., 2018; Wilson
 2138 III et al., 2007, 2010). They can propagate along the quasi-static magnetic field
 2139 at fractions of V_{Te} (C. Cattell et al., 2005; J. R. Franz et al., 2005) or obliquely
 2140 to the field and at much lower speeds (Vasko et al., 2018). These waves can reach
 2141 amplitudes in excess of >1000 mV/m in space plasmas.

- 2142 • **IAWs:** Electrostatic ion acoustic waves (or ion sound waves) are linearly polar-
 2143 ized (parallel to \mathbf{B}_o) electrostatic (i.e., $\mathbf{k} \times \mathbf{B}_o = 0$) waves with $\lambda \gtrsim 2 \pi \lambda_{De}$ (Breneman
 2144 et al., 2013; Fuselier & Gurnett, 1984; Gurnett, Neubauer, & Schwenn, 1979; Gur-
 2145 nettt, Marsch, et al., 1979; Wilson III et al., 2007, 2010). The time series present
 2146 as symmetric (about zero) electric field oscillations in the form of modulated sine
 2147 waves with spacecraft frame frequencies near 1 AU satisfying $f_{sc} \lesssim 100 \text{ Hz} \lesssim f_{sc}$
 2148 $\lesssim 10 \text{ kHz}$. Near collisionless shock waves in space plasmas, these waves can reach
 2149 amplitudes in excess of $>300 \text{ mV/m}$.
- 2150 • **ECDI:** The electron cyclotron drift instability (D. W. Forslund et al., 1970; D. Forslund
 2151 et al., 1972) or beam cyclotron instability (Lampe, Manheimer, et al., 1971; Lampe,
 2152 McBride, et al., 1971) or electrostatic electron-ion streaming instability (Wong,
 2153 1970) occurs upstream of collisionless shocks due to the relative drift between in-
 2154 cident electrons and shock-reflected ions (D. W. Forslund et al., 1970; Muschietti
 2155 & Lembège, 2013, 2017). They are observed as electrostatic fluctuations with mix-
 2156 tures of IAW and electron cyclotron harmonics. That is, the power spectrum shows
 2157 a broad acoustic spectrum expected for IAWs and superposed are integer and/or
 2158 half-integer harmonics of f_{ce} . The polarizations shown in hodogram plots can look
 2159 like “tadpoles” or “tear drops.” The time series present as asymmetric (about zero)
 2160 electric field oscillations in both the parallel and perpendicular (with respect to
 2161 \mathbf{B}_o) components (Breneman et al., 2013; Wilson III et al., 2010). These waves can
 2162 reach amplitudes in excess of $>300 \text{ mV/m}$ in space plasmas.
- 2163 • **Langmuir Waves:** Langmuir waves can be both linearly (electrostatic) and el-
 2164 liptically (electromagnetic) polarized and are driven unstable by electron beams
 2165 (e.g., “bump-on-tail” instability). The time series signature is a modulated sine
 2166 wave with spacecraft frame frequencies near f_{pe} (Bale et al., 1996, 1997; Bale, Kel-
 2167 logg, Goetz, & Monson, 1998; Kellogg, Monson, et al., 1996; Malaspina & Ergun,
 2168 2008; Malaspina et al., 2011). In space plasmas, they are often large amplitude
 2169 with some in excess of $>500 \text{ mV/m}$.

2170 Appendix C Wind Databases

2171 This appendix provides a single reference table listing the databases relying upon
 2172 *Wind* databases created between 2013 to 2020. The limited scope of Table C1 is partly
 2173 for brevity’s sake and partly due to the difficulty in documenting/referencing older databases
 2174 (e.g., non-functional URLs and/or a lack of a working DOI).

Table C1: A selection of *Wind* databases first published between 2013 and 2020

| Year | Title | Citation & URL |
|------|---|---|
| 2020 | <i>Wind</i> WAVES TDSF Dataset | Wilson III (2020) https://doi.org/10.5281/zenodo.3911205 |
| 2020 | Supplement to: Electron energy partition across interplanetary shocks: III. Analysis | Wilson III et al. (2020b) https://doi.org/10.5281/zenodo.3627284 |
| 2020 | Radial Evolution of Coronal Mass Ejections Between MESSENGER, & Venus Express, STEREO, and L1: Catalog and Analysis | Salman et al. (2020) https://doi.org/10.1029/2019JA027084 |
| 2019 | Supplement to: Electron energy partition across interplanetary shocks | Wilson III et al. (2019c) https://doi.org/10.5281/zenodo.2875806 |
| 2019 | A Catalog of Type II radio bursts observed by <i>Wind</i> /WAVES and their Statistical Properties | Gopalswamy, Mäkelä, and Yashiro (2019) https://cdaw.gsfc.nasa.gov/CME_list/radio/waves_type2.html |
| 2018 | A database of small-scale magnetic flux ropes in the solar wind from <i>Wind</i> spacecraft measurements | Hu et al. (2018) https://doi.org/10.1088/1742-6596/1100/1/012012 |
| 2018 | <i>Wind</i> ICME Catalogue | Nieves-Chinchilla et al. (2018) https://wind.nasa.gov/ICMEindex.php |
| 2018 | The <i>Wind</i> /EPACT Proton Event Catalogue | Miteva et al. (2018) http://www.stil.bas.bg/SEFcatalog/ |
| 2017 | The KONUS- <i>Wind</i> GRB Catalogue with known Redshifts | Tsvetkova et al. (2017) http://www.ioffe.ru/LEA/zGRBs/triggered/ |
| 2017 | Interactive Multi-instrument Database of Solar Flares | Sadykov et al. (2017) https://solarflare.njit.edu |
| 2016 | The 2nd KONUS- <i>Wind</i> Catalogue of sGRBs | D. S. Svinin et al. (2016) http://www.ioffe.ru/LEA/shortGRBs/Catalog/ |
| 2016 | <i>Wind</i> Dust Impact Database | Malaspina and Wilson III (2016) https://cdaweb.gsfc.nasa.gov/index.html/ |
| 2014 | Catalogue of High-Speed Solar Wind Streams during Solar Cycle 23 | Xystouris et al. (2014) https://doi.org/10.1007/s11207-013-0355-z |
| 2014 | KONUS- <i>Wind</i> Solar Flares | Pal'shim et al. (2014) http://www.ioffe.ru/LEA/Solar/ |
| 2013 | Interplanetary Network Localizations of sGRBs | Pal'shim et al. (2013) https://doi.org/10.1088/0067-0049/207/2/38 |

2175 **Glossary**

- 2176 **AE-Index** An index designed to provide a global, quantitative measure of auroral zone
2177 magnetic activity produced by enhanced ionospheric currents.
- 2178 **Alpha-particle** A doubly-charged ion that is the nucleus of a ^4He atom.
- 2179 **Astronomical Unit** Roughly the distance between the Earth and sun called 1 AU. Orig-
2180 inally it was defined as the average distance between the two bodies but was de-
2181 fined as exactly 149,597,870,700 meters (or ~ 149.6 million kilometers or ~ 92.96
2182 million miles) in 2012.
- 2183 **Bow Shock** Shock wave standing upstream of an obstacle/piston in an incident, super-
2184 sonic flow. In a plasma, this only occurs upstream of magnetized planetary bod-
2185 ies.
- 2186 **Carrington rotation** An approximate time scale over which the photosphere (i.e., op-
2187 tical surface of the Sun) at low latitudes rotates through 2π radians. Richard C.
2188 Carrington determined this rate watching sun spots in the 1850s and arrived at
2189 a sidereal rotation period of ~ 23.38 days (1 day = 86400 seconds). Since sidereal
2190 rotation is relative to fixed stars and Earth orbits the sun, a Carrington rotation
2191 observed from Earth is ~ 27.2753 days.
- 2192 **Collisionless Shock** A shock wave where the ramp region, or region of sharpest pa-
2193 rameter gradients, spatial scale is orders of magnitude smaller than the mean free
2194 Coulomb collisional path. Anecdotally, the mean free path of a thermal proton
2195 near Earth is roughly 1 AU while the typical shock ramp thickness only several
2196 kilometers to a few tens of kilometers.
- 2197 **Coronal Hole** Regions in which the magnetic field lines do not connect back to the so-
2198 lar surface but rather are directed outward into the interplanetary medium.
- 2199 **Coronal Mass Ejection** Eruptions of plasma from the solar corona that are some of
2200 the largest (energetically) phenomena in the solar system. When moving out though
2201 the interplanetary medium, they are called interplanetary coronal mass ejections
2202 or ICMEs.
- 2203 **Corotating Interaction Region** The compressed plasma region that corotates with
2204 the Sun formed along the leading edge of a fast solar wind stream from a coro-
2205 nal hole as it interacts with preceding slower solar wind. Some reseachers require
2206 that the CIR is observed at least twice to distinguish it from a “stream interac-
2207 tion region” (SIR). Shock waves can develop along the CIR boundaries, usually
2208 beyond 1 AU, mostly due to the expansion speed of the CIR relative to the am-
2209 bient plasma. This becomes more favorable at larger heliocentric distances.
- 2210 **Cyclotron Frequency** The rate at which a charged particle orbits a magnetic field.
2211 It is also called the gyrofrequency.
- 2212 **Cyclotron Resonance** Condition where an electric field oscillates at the same rate as
2213 the particle gyrofrequency in the particle guiding center rest frame resulting in en-
2214 ergy gain/loss, depending upon whether the oscillations are damping/growing.
- 2215 **Critical Balance** A conjecture of turbulence models in which the linear and nonlin-
2216 ear timescales of the system remain comparable at all scales in the inertial range.
- 2217 **Debye Length** The maximum distance any single charged particle’s electric field can
2218 influence other charged particles in a plasma. This is often referred to in terms
2219 of the electrostatic screening or shielding because for scales larger than the De-
2220 bye length, only wave and convective electric fields tend to persist.
- 2221 **Dispersion Relation** The function that defines the relationship between the frequency
2222 and wavenumber, i.e., $\omega = \omega(\mathbf{k})$.
- 2223 **Dispersive Radiation** The process through which an electromagnetic emission is gener-
2224 ated due to temporally and spatially varying currents with the fluctuation fre-
2225 quencies having an explicit dependence upon the wavenumber. This phenomena
2226 typically occurs in the magnetic ramp of collisionless shocks, which are nonlinearly
2227 steepened fast/magnetosonic-whistler waves. Thus, the radiated waves are on the
2228 fast/magnetosonic-whistler branch of the dispersion relation.

- 2229 **Dispersive Wave** Any fluctuation that has an explicit wavenumber dependence in its
2230 frequency, i.e., $\omega = \omega(\mathbf{k})$.
- 2231 **Disruption Scale** The spatial scale at which the reconnection timescale becomes faster
2232 than the turbulent eddy timescale resulting in a reconnection dominated cascade
2233 range.
- 2234 **Dissipation Range** The range of scales in a turbulent medium where dissipation dom-
2235 inates over the energy cascade, usually at the smallest scales. Note that this term
2236 has become less relevant and been replaced by just kinetic range.
- 2237 **Dust** Dust here refers to particles ranging in size from nanometers to several microm-
2238 eters (microns) originating either with the interplanetary medium (IPD) or from
2239 the interstellar medium (ISD).
- 2240 **Dst Index** The Disturbance Storm-Time (Dst) index is a measure of space weather,
2241 specifically measuring the strength of the ring current of ions around the Earth's
2242 equatorial region in the magnetosphere.
- 2243 **Eddy Turnover Time** Approximate time scale necessary for a fluid vortex, or eddy,
2244 to rotate about its axis of symmetry.
- 2245 **Energetic Storm Particles** An enhancement in the energetic particle intensity, typ-
2246 ically at energies of tens of keV to ~ 10 MeV, in the vicinity of an interplanetary
2247 shock, usually attributed to local particle acceleration by the shock.
- 2248 **Eulerian Decorrelation Time** Timescale over which turbulent fluctuations remain
2249 correlated in the Eulerian frame of reference.
- 2250 **Fast Radio Burst** These are bright, millisecond-scale radio flashes of currently uncon-
2251 firmed origin. Some recent observations suggest that magnetars may be the most
2252 likely source candidates. They are likely associated with or caused by some cat-
2253 aclysmic astrophysical event as the estimated power associated with them can ex-
2254 ceed 10^{35} J s^{-1} or $10^{42} \text{ erg s}^{-1}$, i.e., the total solar output for ~ 3 days.
- 2255 **Foreshock** Region upstream of a shock wave in communication with the shock wave
2256 through electromagnetic waves and/or backstreaming particles.
- 2257 **Gamma Rays** These are photons with energies > 100 keV. There is no distinct cutoff
2258 between gamma rays and x-rays, but they are typically distinguished by their source.
2259 X-rays tend to be emitted by accelerating electrons and gamma rays from nuclear
2260 processes.
- 2261 **Gamma Ray Burst** The brightest electromagnetic events known to occur in the uni-
2262 verse, occurring transiently from the collapse of massive stars or coalescence of com-
2263 pact objects (e.g., two neutron stars or a neutron star-black hole merger). They
2264 consist of an initial flash of gamma-rays lasting from tens of milliseconds to min-
2265 utes followed by a longer duration “afterglow” at radio and optical wavelengths.
- 2266 **Giant Flare** These are of greater apparent intensity than gamma ray bursts and are
2267 very rare, averaging once per decade.
- 2268 **Ground Level Enhancement** Solar particle events that extend to sufficiently high
2269 ($\sim \text{GeV}$) energies that they produce secondary particles in the atmosphere that
2270 are detected by ground-based neutron monitors.
- 2271 **Gyrophase** The angular description of a particle's gyro orbit about the magnetic field.
- 2272 **Gyroradius** The orbital distance of a charged particle's motion about a magnetic field.
2273 It is also called the Larmor radius.
- 2274 **Halo Orbit** A periodic trajectory around a gravitational Lagrange point that consists
2275 of a subset of Lissajous orbits where all three components share the same peri-
2276 odicity.
- 2277 **Heliosphere** Region of space dominated by the sun's solar wind bounded by its inter-
2278 action with the interstellar medium.
- 2279 **Heliospheric Current Sheet** The surface that separates the two solar magnetic po-
2280 larities or hemispheres of the heliosphere.
- 2281 **Inertial Length** The distance covered by the speed of light in vacuum during one plasma
2282 oscillation. This is also called the skin depth.

- 2283 **Inertial Range** The range of scales in a turbulent medium in which the inertial forces
2284 dominate resulting in the proposed cascade of energy from larger to smaller scales.
- 2285 **Interplanetary Coronal Mass Ejection** A structure in the solar wind observed re-
2286 motely or in situ formed of material associated with a coronal mass ejection.
- 2287 **Interplanetary Magnetic Field** The magnetic field permeating the interplanetary
2288 medium.
- 2289 **Interplanetary Shock** Shock wave propagating in the interplanetary medium are gen-
2290 erated by either corotating/stream interaction regions or interplanetary coronal
2291 mass ejections.
- 2292 **Kinetic Instability** Similar to plasma instability defined below, it is a mechanism through
2293 which a plasma converts some free energy source into electromagnetic fluctuations.
2294 The difference between kinetic and plasma instabilities is that the former specif-
2295 ically refers to features in the VDFs while the latter also encompasses fluid-like
2296 instabilities.
- 2297 **Kinetic Range** The range of scales in a turbulent plasma comparable to or smaller than
2298 the plasma kinetic scales, e.g. particle gyroradii, inertial lengths, etc.
- 2299 **Lagrange Point** Region of space with a local minimum in the gravitational potential
2300 caused between at least two large masses (e.g., Earth and sun).
- 2301 **Landau Resonance** Condition where a longitudinal electric field oscillates along the
2302 same direction as a particle's velocity at such a rate as to allow the particle to gain/lose
2303 energy by effectively "surfing" on the electric potential gradients of the oscillat-
2304 ing field. The gain/loss depends upon whether the oscillations are damping/growing
2305 much like cyclotron resonance.
- 2306 **Lissajous Orbit** A quasi-periodic trajectory around a gravitational Lagrange point.
2307 Often, two of the three spatial coordinates of the orbit are stable and coupled to
2308 each other while the third is periodically independent.
- 2309 **Magnetar** These are rare, young, and isolated neutron stars with extremely strong mag-
2310 netic fields that can reach up to 10^{11} T or 10^{15} G. These have been confirmed to
2311 be the source of soft gamma repeaters and are a possible candidate source for fast
2312 radio bursts.
- 2313 **Magnetic Cloud** A structure in an interplanetary coronal mass ejection characterized
2314 by an enhanced magnetic field that rotates through a large angle, usually inter-
2315 preted as evidence for a magnetic flux rope, and low plasma beta.
- 2316 **Magnetic Island** Region of space wherein all magnetic field lines are closed either in
2317 two- or three-dimensions.
- 2318 **Magnetic Reconnection** The process of a change in the topology of a magnetic field
2319 through the destruction of magnetic flux and subsequent conversion to particle
2320 kinetic energy.
- 2321 **Magnetohydrodynamics** The approximation that the plasma can be represented as
2322 a single species fluid model which is scale-invariant. It is often abbreviated as MHD.
- 2323 **Magnetosheath** Region between the bow shock and magnetosphere where plasma flow
2324 is decelerated and deflected around the magnetosphere of the planetary body.
- 2325 **Magnetosphere** Region of space surrounding a magnetized planetary body separated/protected
2326 from the incident solar wind by the body's magnetic field.
- 2327 **Magnetotail** Region of magnetosphere on opposite side of solar wind incident flow, where
2328 the field has been stretched due to the asymmetric pressure (i.e., ram pressure)
2329 exerted on the planetary body's magnetic field combined with dayside reconnect-
2330 ing field lines being dragged into the nightside region.
- 2331 **Normal Mode** The natural or preferred frequency and wavelength of fluctuations/oscillations
2332 of a medium/system.
- 2333 **Phase Space** The region in which all possible states of a system can be expressed. In
2334 plasma physics and/or kinetic theory, this is usually limited to position and mo-
2335 mentum coordinates.

- 2336 **Plasma** An ionized gas that exhibits a collective behavior similar to a fluid and is gov-
 2337 erned by long-range interactions/forces.
- 2338 **Plasma Frequency** The fastest rate at which a collection of charged particles can os-
 2339 cillate in the absence of an external driving force. The oscillation is typically con-
 2340 sidered in the absence of a magnetic field because the frequency only depends upon
 2341 the charged species density and charge state.
- 2342 **Plasma Instability** The mechanism through which a plasma converts some free en-
 2343 ergy source into electromagnetic fluctuations.
- 2344 **Quasi-perpendicular(parallel) Shock** Denoting collisionless shock waves with shock
 2345 normal angles often considered to be $\geq 45^\circ$ ($< 45^\circ$).
- 2346 **Radiation Belts** A region of space surrounding magnetized planetary bodies that con-
 2347 tains particles that are much more energetic than in the surrounding medium. The
 2348 particles are trapped and perform three types of orbital motions: gyration about
 2349 the magnetic field, bouncing between the two magnetic poles, and drifting around
 2350 the magnetized planetary body. At Earth, these regions are sometimes called the
 2351 Van Allen radiation belts or Van Allen belts after their discoverer James Van Allen.
- 2352 **Ring Current** An electric current carried by particles on trapped, longitudinal orbits
 2353 about the Earth near the geomagnetic equator at altitudes of $\sim 3\text{--}8 R_E$. The par-
 2354 ticles involved are primarily ions (mostly protons and singly ionized oxygen) with
 2355 energies $\sim 10\text{--}200$ keV.
- 2356 **Shock Normal Angle** The angle between the upstream magnetic field vector and the
 2357 outward shock normal unit vector.
- 2358 **Shock Wave** A stable discontinuity arising from a nonlinearly steepened compressional
 2359 wave that has reached a balance between steepening and energy dissipation.
- 2360 **Solar Energetic Particles** Temporary enhancements of suprathermal ($\gtrsim 10$ keV) to
 2361 relativistic (\sim few GeV) particles following energetic solar events (e.g., flares and
 2362 coronal mass ejections) that last from hours to several days and include protons,
 2363 electrons and heavy ions.
- 2364 **Soft Gamma Repeater** These are strongly magnetized Galactic neutron stars that
 2365 emit large bursts of X-rays and gamma-rays at irregular intervals.
- 2366 **Solar Exclusion Zone** Region of sky about solar disk where solar radio emissions cause
 2367 sufficient interference with spacecraft communications to prevent telemetry sig-
 2368 nal locks.
- 2369 **Solar Flare** An abrupt and intense enhancement in ultraviolet to gamma ray electro-
 2370 magnetic radiation from a localized region on the sun. On rare occasions for strong
 2371 flares, the enhanced, localized emission can occur in the visible frequency range
 2372 too.
- 2373 **Solar Wind** A stream of plasma propagating away from the Sun. It is primarily com-
 2374 prised of electrons, protons, and alpha-particles (and heavier ions), is not in ther-
 2375 mal or thermodynamic equilibrium, and flows supersonically.
- 2376 **Stream Interaction Region** A corotating interaction region (CIR) that need not be
 2377 observed on two solar rotations. Also used interchangeably with CIR.
- 2378 **Structure Function** A statistical measure to describe the typical fluctuation ampli-
 2379 tudes as a function of scale in a turbulent medium; a conditioned structure func-
 2380 tion is a structure function constructed from a selected subset of the turbulent fluc-
 2381 tuations.
- 2382 **Suprathermal** Particles with kinetic energies above the thermal energy of the medium.
- 2383 **Sustained Gamma Ray Emission** A continuum at gamma ray frequencies caused
 2384 by pion-decay due to interaction with > 300 MeV protons.
- 2385 **Taylor's Hypothesis** The assumption that any variation in a moving flow is propa-
 2386 gating at a speed much slower than the bulk flow of the fluid, thus allowing one
 2387 to convert time series data into spatial scales.
- 2388 **Taylor Microscale** A fundamental scale in a turbulent medium characterizing the spa-
 2389 tial size of fluctuation gradients.

- 2390 **Thermal Equilibrium** Condition where the particle constituents of a medium are in
 2391 equipartition of energy (i.e., all have the same temperature) but there can be fi-
 2392 nite heat fluxes present.
- 2393 **Thermodynamic Equilibrium** Condition where the particle constituents of a medium
 2394 are in equipartition of energy (i.e., all have the same temperature) and there are
 2395 no heat fluxes present.
- 2396 **Transient Ion Foreshock Phenomena** These are large-scale (~ 1000 to $>30,000$ km),
 2397 solitary [~ 5 – 10 per day and transient] structures with durations of tens of seconds
 2398 to several minutes. They are driven by instabilities caused by the backstreaming
 2399 particles forming the foreshock.
- 2400 **Trans-iron Elements** These are elements on the periodic table at higher proton num-
 2401 ber than iron, i.e., more than 26 protons.
- 2402 **Turbulence** A process in fluids or plasmas characterized by chaotic broadband fluc-
 2403 tuations which is modelled by a cascade of energy, usually from large injection scales
 2404 to small dissipation scales.
- 2405 **Type II Burst** A class of solar radio emissions caused by nonthermal electrons accel-
 2406 erated by CME-driven shock waves. They are characterized by their slow frequency
 2407 drift (i.e., few 100s of kHz per hour) versus time, which is a tracer of the shock
 2408 speed and the electron number density upstream of the shock.
- 2409 **Type III Burst** A class of solar radio emissions caused by nonthermal electrons ac-
 2410 celerated during a solar eruption streaming out along the IMF. They are charac-
 2411 terized by their fast frequency drift (i.e., MHz per minute) versus time, which is
 2412 a tracer of the gradient in the interplanetary electron number density.
- 2413 **Type III Storm** A class of solar radio emissions caused by nonthermal electrons stream-
 2414 ing along local magnetic fields in active regions, but outside of flare or CME erup-
 2415 tion sites. They are characterized by broadband ($>$ few MHz), very short dura-
 2416 tion (i.e., $\lesssim 1$ – 2 minutes) emissions that occur in rapid succession (typically >10
 2417 per hour).
- 2418 **Type IV Burst** A class of solar radio emissions caused by nonthermal electrons trapped
 2419 in the post-eruption arcades (i.e., half-loop-like arches of intense magnetic field
 2420 connecting to active regions on the solar surface) in/around a solar flare or CME
 2421 eruption site. They are characterized by a broadband frequency emission in the
 2422 several to >10 MHz range, sometimes showing a U-shaped frequency-time pro-
 2423 file.
- 2424 **Velocity Distribution Function** A function that defines the probability density of
 2425 particles in phase space. An example is the Maxwell-Boltzmann velocity distri-
 2426 bution function.
- 2427 **X-line** The region within a magnetic reconnection site of an intense current sheet where
 2428 magnetic flux is being destroyed, changing the field topology.
- 2429 **X-rays** Photons with energies in the range ~ 124 eV to ~ 124 keV. These are split into
 2430 hard and soft ranges, with hard being photons with energies $\gtrsim 5$ – 10 keV.

2431 Acronyms

- 2432 **ACE** Advanced Composition Explorer
 2433 **ADS** Astrophysics Data System
 2434 **AE-Index** Auroral Electrojet Index
 2435 **AIM** Aeronomy of Ice in the Mesosphere
 2436 **APE** Alpha-Proton-Electron telescope, part of *Wind* EPACT/ELITE
 2437 **ARTEMIS** Acceleration, Reconnection, Turbulence, and Electrodynamics of the Moon's
 2438 Interaction with the Sun
 2439 **AU** Astronomical Unit
 2440 **CAP** Command and Attitude Processor

| | |
|------|--|
| 2441 | CDAWeb Coordinated Data Analysis Web |
| 2442 | CIR Corotating Interaction Region |
| 2443 | CME Coronal Mass Ejection |
| 2444 | DH Decametric-hectometer |
| 2445 | DSCOVR Deep Space Climate Observatory |
| 2446 | DTR Digital Tape Recorder |
| 2447 | EESA Electron Electrostatic Analyzer, part of <i>Wind</i> 3DP |
| 2448 | ECDI Electron Cyclotron Drift Instability |
| 2449 | ELITE Electron-Isotope Telescope system, part of <i>Wind</i> EPACT |
| 2450 | EPACT Energetic Particles: Acceleration, Composition, and Transport, the APE-ELITE- |
| 2451 | IT-LEMT-STEP instrument suite on <i>Wind</i> known as EPACT |
| 2452 | ESA ElectroStatic Analyzer |
| 2453 | ESA European Space Agency |
| 2454 | ESP Energetic Storm Particle |
| 2455 | ESW Electrostatic Solitary Wave |
| 2456 | eV electron volt |
| 2457 | FC Faraday Cup, e.g., <i>Wind</i> /SWE |
| 2458 | FOT Flight Operations Team |
| 2459 | FRB Fast Radio Burst |
| 2460 | GCN Gamma-ray Coordinates Network |
| 2461 | GeV Giga-electron volt |
| 2462 | GF SGR Giant Flare |
| 2463 | GGS Global Geospace Science |
| 2464 | GLE Ground Level Enhancement |
| 2465 | GRB Gamma Ray Burst |
| 2466 | GSE Geocentric Solar Ecliptic |
| 2467 | GSFC Goddard Space Flight Center |
| 2468 | HCS Heliospheric Current Sheet |
| 2469 | HK House Keeping, i.e., type of engineering data for spacecraft and instruments |
| 2470 | HSO Heliophysics System Observatory |
| 2471 | IAW electrostatic Ion Acoustic Wave |
| 2472 | ICME Interplanetary Coronal Mass Ejection |
| 2473 | ICW Ion Cyclotron Wave |
| 2474 | IMAP Interstellar MApping Probe |
| 2475 | IMF Interplanetary Magnetic Field |
| 2476 | INTEGRAL INTErnational Gamma-Ray Astrophysics Laboratory |
| 2477 | IP Interplanetary |
| 2478 | IPD Interplanetary Dust |
| 2479 | IPM Interplanetary Medium |
| 2480 | IPN Interplanetary GRB Network |
| 2481 | ISD Interstellar Dust |
| 2482 | ISTP International Solar-Terrestrial Physics |
| 2483 | IT Isotope Telescope, part of <i>Wind</i> EPACT/ELITE |
| 2484 | keV kilo-electron volt |
| 2485 | KONUS Gamma-Ray Spectrometer, i.e., the <i>Wind</i> KONUS instrument |
| 2486 | LEMT Low Energy Matrix Telescopes, part of <i>Wind</i> EPACT |
| 2487 | LHW Lower Hybrid Wave |
| 2488 | LIGO Laser Interferometer Gravitational-Wave Observatory |
| 2489 | MASS high-resolution MASS spectrometer, part of <i>Wind</i> SMS |
| 2490 | MeV Mega-electron volt |
| 2491 | MFI Magnetic Field Investigation, <i>Wind</i> MFI |

| | |
|------|--|
| 2492 | NASA National Aeronautics and Space Administration |
| 2493 | PESA Ion (Proton) ESA, part of <i>Wind</i> 3DP |
| 2494 | PSP <i>Parker Solar Probe</i> |
| 2495 | SEP Solar Energetic Particle |
| 2496 | SGR Soft Gamma Repeater |
| 2497 | SGRE Sustained Gamma-ray Emission |
| 2498 | SIR Stream Interaction Region |
| 2499 | SMS Solar Wind and Suprathermal Ion Composition Experiment, i.e., the SWICS-MASS- |
| 2500 | STICS instrument suite on <i>Wind</i> known as SMS |
| 2501 | SOFIE Solar Occultation For Ice Experiment |
| 2502 | SoHO Solar and Heliospheric Observatory mission |
| 2503 | Solo <i>Solar Orbiter</i> mission |
| 2504 | SPDF Space Physics Data Facility |
| 2505 | sps samples per second |
| 2506 | SSN Sunspot number |
| 2507 | SST Solid-State (semi-conductor detector) Telescope |
| 2508 | STEP SupraThermal Energetic Particle Telescope, part of <i>Wind</i> EPACT |
| 2509 | STICS SupraThermal Ion Composition Spectrometer, part of <i>Wind</i> SMS |
| 2510 | Strahl (detector) electron strahl sensor in <i>Wind</i> SWE instrument suite |
| 2511 | SWE Solar Wind Experiment, i.e., the VEIS-Strahl-FC instrument suite on <i>Wind</i> known |
| 2512 | as SWE |
| 2513 | SWICS Solar Wind Ion Composition Spectrometer, part of <i>Wind</i> SMS |
| 2514 | STEREO Solar Terrestrial Relations Observatory |
| 2515 | THEMIS Time History of Events and Macroscale Interactions during Substorms |
| 2516 | TDS Time Domain Sampler, part of <i>Wind</i> WAVES |
| 2517 | TGRS Transient Gamma-Ray Spectrometer, i.e., the <i>Wind</i> TGRS experiment |
| 2518 | TIFP Transient Ion Foreshock Phenomena |
| 2519 | TNR Thermal Noise Receiver, part of <i>Wind</i> WAVES |
| 2520 | TUA Tape Unit A |
| 2521 | TUB Tape Unit B |
| 2522 | VDF Velocity Distribution Function |
| 2523 | VEIS Vector Ion-Electron Spectrometers, part of <i>Wind</i> SWE |

2524 **Acknowledgments**

2525 L.B.W. is partially supported by *Wind* MO&DA grants and a Heliophysics Innovation
2526 Fund (HIF) grant. A.L.B. is supported by NASA grant 80NSSC20M0189. C.H.K.C. is
2527 supported by STFC Ernest Rutherford Fellowship ST/N003748/2 and STFC Consoli-
2528 dated Grant ST/T00018X/1. D.V. is supported by STFC Ernest Rutherford Fellowship
2529 ST/P003826/1 and STFC Consolidated Grant ST/S000240/1. I.G.R. is partially sup-
2530 ported by NASA programs NNH19ZDA001N-HSR and NNH19ZDA001N-LWS. N.L. is
2531 partially supported by NASA grant 80NSSC19K0831. The authors thank D.L. Turner,
2532 M. Henderson, and G. Reeves for useful discussions of the radiation belts. A.L.B. is grate-
2533 ful to Robert Candey for insightful discussions about the OPEN program and the GSFC
2534 Laboratory for Extraterrestrial Physics. The authors thank the Harvard Smithsonian
2535 Center for Astrophysics and the NASA SPDF/CDAWeb team for the interplanetary shock
2536 analysis and the *Wind* plasma and magnetic field data, respectively. The authors thank
2537 Carlos A. Perez Alanis for providing Figure 13. The authors thank Andrea Verdini for
2538 providing Figure 11. The authors thank Don V. Reames for providing Figure 17. The
2539 *Wind* shock database can be found at:
2540 https://www.cfa.harvard.edu/shocks/wi_data/.
2541 Analysis software for *Wind* data (Wilson III, 2021) can be found at:

2542 https://github.com/lynnwilsoniii/wind_3dp_pros, and open-sourced calibration
 2543 software (Wilson III & Others, 2021) at:
 2544 <https://github.com/lynnwilsoniii/Wind-Decom-Code>.
 2545 Nearly all *Wind* data is publicly available at:
 2546 <https://cdaweb.gsfc.nasa.gov>.
 2547 If not directly available through SPDF/CDAWeb, then data can be accessed indirectly
 2548 from the *Wind* webpage at:
 2549 <https://wind.nasa.gov>.

2550 References

- 2551 Abbott, B. P., Abbott, R., Abbott, T. D., Abraham, S., Acernese, F., Ackley,
 2552 K., ... others (2019, November). Search for Gravitational-wave Signals
 2553 Associated with Gamma-Ray Bursts during the Second Observing Run
 2554 of Advanced LIGO and Advanced Virgo. *Astrophys. J.*, *886*(1), 75. doi:
 2555 10.3847/1538-4357/ab4b48
- 2556 Acuña, M. H., Ogilvie, K. W., Baker, D. N., Curtis, S. A., Fairfield, D. H., & Mish,
 2557 W. H. (1995, February). The Global Geospace Science Program and Its
 2558 Investigations. *Space Sci. Rev.*, *71*, 5–21. doi: 10.1007/BF00751323
- 2559 Adrian, M. L., Viñas, A. F., Moya, P. S., & Wendel, D. E. (2016, December).
 2560 Solar Wind Magnetic Fluctuations and Electron Non-thermal Temperature
 2561 Anisotropy: Survey of Wind-SWE-VEIS Observations. *Astrophys. J.*, *833*, 49.
 2562 doi: 10.3847/1538-4357/833/1/49
- 2563 Agapitov, O., Mourenas, D., Artemyev, A., Hospodarsky, G., & Bonnell, J. W.
 2564 (2019, June). Time Scales for Electron Quasi-linear Diffusion by Lower-Band
 2565 Chorus Waves: The Effects of ω_{pe}/Ω_{ce} Dependence on Geomagnetic Activity.
 2566 *Geophys. Res. Lett.*, *46*(12), 6178–6187. doi: 10.1029/2019GL083446
- 2567 Agapitov, O. V., Dudok de Wit, T., Mozer, F. S., Bonnell, J. W., Drake, J. F.,
 2568 Malaspina, D., ... Wygant, J. R. (2020, March). Sunward-propagating
 2569 Whistler Waves Collocated with Localized Magnetic Field Holes in the Solar
 2570 Wind: Parker Solar Probe Observations at 35.7 R_s Radii. *Astrophys. J. Lett.*,
 2571 *891*(1), L20. doi: 10.3847/2041-8213/ab799c
- 2572 Aguilar-Rodriguez, E., Gopalswamy, N., MacDowall, R., Yashiro, S., & Kaiser, M. I.
 2573 (2005, September). A Study of the Drift Rate of Type II Radio Bursts at Dif-
 2574 ferent Wavelengths. In B. Fleck, T. H. Zurbuchen, & H. Lacoste (Ed.), *Solar*
 2575 *wind 11/soho 16, connecting sun and heliosphere* (Vol. 592, p. 393+).
- 2576 Al-Haddad, N., Nieves-Chinchilla, T., Savani, N. P., Lugaz, N., & Roussev, I. I.
 2577 (2018, May). Fitting and Reconstruction of Thirteen Simple Coronal Mass
 2578 Ejections. *Solar Phys.*, *293*, 73. doi: 10.1007/s11207-018-1288-3
- 2579 Al-Haddad, N., Nieves-Chinchilla, T., Savani, N. P., Möstl, C., Marubashi, K., Hi-
 2580 dalgo, M. A., ... Farrugia, C. J. (2013, May). Magnetic Field Configuration
 2581 Models and Reconstruction Methods for Interplanetary Coronal Mass Ejec-
 2582 tions. *Solar Phys.*, *284*, 129–149. doi: 10.1007/s11207-013-0244-5
- 2583 Ala-Mathi, M., Ruohotie, J., Good, S. W., Kilpua, E. K. J., & Lugaz, N. (2020).
 2584 Spatial coherence of interplanetary coronal mass ejection sheaths at 1 AU. *J.*
 2585 *Geophys. Res.*, *125*. doi: 10.1029/2020JA28002
- 2586 Allen, R. C., Lario, D., Odstrcil, D., Ho, G. C., Jian, L. K., Cohen, C. M. S., ...
 2587 Wiedenbeck, M. (2020, February). Solar Wind Streams and Stream Interaction
 2588 Regions Observed by the Parker Solar Probe with Corresponding Observations
 2589 at 1 au. *Astrophys. J. Suppl.*, *246*(2), 36. doi: 10.3847/1538-4365/ab578f
- 2590 Alterman, B. L., & Kasper, J. C. (2019, July). Helium Variation across Two Solar
 2591 Cycles Reveals a Speed-dependent Phase Lag. *Astrophys. J. Lett.*, *879*(1), L6.
 2592 doi: 10.3847/2041-8213/ab2391
- 2593 Alterman, B. L., Kasper, J. C., Stevens, M. L., & Koval, A. (2018, Septem-
 2594 ber). A Comparison of Alpha Particle and Proton Beam Differential

- 2595 Flows in Collisionally Young Solar Wind. *Astrophys. J.*, *864*, 112. doi:
2596 10.3847/1538-4357/aad23f
- 2597 Alves, M. V., Echer, E., & Gonzalez, W. D. (2006, July). Geoeffectiveness of corotating interaction regions as measured by Dst index. *J. Geophys. Res.*, *111*, 7.
2598 doi: 10.1029/2005JA011379
- 2599 Aptekar, R. L., Butterworth, P. S., Cline, T. L., Frederiks, D. D., Golenetskii, S. V.,
2600 Il'Inskii, V. N., ... Pal'Shin, V. D. (2002). General properties of recurrent
2601 bursts from SGRs. *Mem. Soc. Astron. It.*, *73*, 485–490.
- 2602 Aptekar, R. L., Frederiks, D. D., Golenetskii, S. V., Ilynskii, V. N., Mazets, E. P.,
2603 Panov, V. N., ... Stilwell, D. E. (1995, February). Konus-W Gamma-Ray
2604 Burst Experiment for the GGS Wind Spacecraft. *Space Sci. Rev.*, *71*, 265–272.
2605 doi: 10.1007/BF00751332
- 2606 Baker, D. N., & Kanekal, S. G. (2008, February). Solar cycle changes, geomagnetic
2607 variations, and energetic particle properties in the inner magnetosphere. *J. At-*
2608 *mos. Solar-Terr. Phys.*, *70*(2-4), 195–206. doi: 10.1016/j.jastp.2007.08.031
- 2609 Bale, S. D., Burgess, D., Kellogg, P. J., Goetz, K., Howard, R. L., & Monson, S. J.
2610 (1996). Phase coupling in Langmuir wave packets: Possible evidence of three-
2611 wave interactions in the upstream solar wind. *Geophys. Res. Lett.*, *23*, 109–
2612 112. doi: 10.1029/95GL03595
- 2613 Bale, S. D., Burgess, D., Kellogg, P. J., Goetz, K., & Monson, S. J. (1997, June).
2614 On the amplitude of intense Langmuir waves in the terrestrial electron fore-
2615 shock. *J. Geophys. Res.*, *102*, 11281–11286. doi: 10.1029/97JA00938
- 2616 Bale, S. D., Hull, A., Larson, D. E., Lin, R. P., Muschietti, L., Kellogg, P. J., ...
2617 Monson, S. J. (2002, August). Electrostatic Turbulence and Debye-Scale
2618 Structures Associated with Electron Thermalization at Collisionless Shocks.
2619 *Astrophys. J.*, *575*, L25-L28. doi: 10.1086/342609
- 2620 Bale, S. D., Kasper, J. C., Howes, G. G., Quataert, E., Salem, C., & Sundkvist, D.
2621 (2009, November). Magnetic Fluctuation Power Near Proton Temperature
2622 Anisotropy Instability Thresholds in the Solar Wind. *Phys. Rev. Lett.*, *103*,
2623 211101+. doi: 10.1103/PhysRevLett.103.211101
- 2624 Bale, S. D., Kellogg, P. J., Goetz, K., & Monson, S. J. (1998). Transverse z-mode
2625 waves in the terrestrial electron foreshock. *Geophys. Res. Lett.*, *25*, 9–12. doi:
2626 10.1029/97GL03493
- 2627 Bale, S. D., Kellogg, P. J., Larson, D. E., Lin, R. P., Goetz, K., & Lepping, R. P.
2628 (1998). Bipolar electrostatic structures in the shock transition region: Evi-
2629 dence of electron phase space holes. *Geophys. Res. Lett.*, *25*, 2929–2932. doi:
2630 10.1029/98GL02111
- 2631 Bale, S. D., Pulupa, M., Salem, C., Chen, C. H. K., & Quataert, E. (2013,
2632 June). Electron Heat Conduction in the Solar Wind: Transition from
2633 Spitzer-Härm to the Collisionless Limit. *Astrophys. J. Lett.*, *769*, L22. doi:
2634 10.1088/2041-8205/769/2/L22
- 2635 Bale, S. D., Reiner, M. J., Bougeret, J.-L., Kaiser, M. L., Krucker, S., Larson, D. E.,
2636 & Lin, R. P. (1999, June). The source region of an interplanetary type II radio
2637 burst. *Geophys. Res. Lett.*, *26*, 1573–1576. doi: 10.1029/1999GL900293
- 2638 Barnes, C. W., & Simpson, J. A. (1976, December). Evidence for interplanetary
2639 acceleration of nucleons in corotating interaction regions. *Astrophys. J. Lett.*,
2640 *210*, L91–L96. doi: 10.1086/182311
- 2641 Bavassano, B., Pietropaolo, E., & Bruno, R. (1998, April). Cross-helicity and
2642 residual energy in solar wind turbulence: Radial evolution and latitudinal de-
2643 pendence in the region from 1 to 5 AU. *J. Geophys. Res.*, *103*(A4), 6521–6530.
2644 doi: 10.1029/97JA03029
- 2645 Berdichevsky, D., Thejappa, G., Fitzenreiter, R. J., Lepping, R. L., Yamamoto, T.,
2646 Kokubun, S., ... Lin, R. P. (1999, January). Widely spaced wave-particle
2647 observations during GEOTAIL and wind magnetic conjunctions in the Earth's
2648 ion foreshock with near-radial interplanetary magnetic field. *J. Geophys. Res.*,
2649

- 2650 104(1), 463–482. doi: 10.1029/1998JA900018
- 2651 Berdichevsky, D. B., Farrugia, C. J., Thompson, B. J., Lepping, R. P., Reames,
2652 D. V., Kaiser, M. L., . . . Michels, D. J. (2002, July). Halo-coronal mass ejections
2653 near the 23rd solar minimum: lift-off, inner heliosphere, and in situ (1
2654 AU) signatures. *Ann. Geophys.*, 20, 891–916. doi: 10.5194/angeo-20-891-2002
- 2655 Bochenek, C. D., Ravi, V., Belov, K. V., Hallinan, G., Kocz, J., Kulkarni, S. R., &
2656 McKenna, D. L. (2020, November). A fast radio burst associated with a Galactic
2657 magnetar. *Nature*, 587(7832), 59–62. doi: 10.1038/s41586-020-2872-x
- 2658 Boldyrev, S. (2006, March). Spectrum of Magnetohydrodynamic Turbulence. *Phys.*
2659 *Rev. Lett.*, 96(11), 115002. doi: 10.1103/PhysRevLett.96.115002
- 2660 Boldyrev, S., Chen, C. H. K., Xia, Q., & Zhdankin, V. (2015, June). Spectral Breaks
2661 of Alfvénic Turbulence in a Collisionless Plasma. *Astrophys. J.*, 806, 238. doi:
2662 10.1088/0004-637X/806/2/238
- 2663 Boldyrev, S., & Perez, J. C. (2012, October). Spectrum of Kinetic-Alfvén Turbu-
2664 lence. *Astrophys. J. Lett.*, 758(2), L44. doi: 10.1088/2041-8205/758/2/L44
- 2665 Boldyrev, S., Perez, J. C., Borovsky, J. E., & Podesta, J. J. (2011, Novem-
2666 ber). Spectral Scaling Laws in Magnetohydrodynamic Turbulence Sim-
2667 ulations and in the Solar Wind. *Astrophys. J. Lett.*, 741, L19. doi:
2668 10.1088/2041-8205/741/1/L19
- 2669 Borovsky, J. E. (2008, August). Flux tube texture of the solar wind: Strands of the
2670 magnetic carpet at 1 AU? *J. Geophys. Res.*, 113(A8), A08110. doi: 10.1029/
2671 2007JA012684
- 2672 Borovsky, J. E., Delzanno, J. L., Valdivia, J. A., Moya, P. S., Stepanova, M., Birn,
2673 J., . . . Hesse, M. (2020, July). Outstanding questions in magnetospheric
2674 plasma physics: The pollenzo view. *J. Atmos. Solar-Terr. Phys.*, 208, 105377.
2675 Retrieved from <https://www.sciencedirect.com/science/article/pii/S1364682620301887> doi: 10.1016/j.jastp.2020.105377
- 2676 Borovsky, J. E., & Denton, M. H. (2009, February). Relativistic-electron dropouts
2677 and recovery: A superposed epoch study of the magnetosphere and the solar
2678 wind. *J. Geophys. Res.*, 114, 2201. doi: 10.1029/2008JA013128
- 2679 Bosqued, J. M., Lormant, N., Rème, H., d’Uston, C., Lin, R. P., Anderson, K. A.,
2680 . . . Wenzel, K.-P. (1996). Moon-solar wind interaction: First results from
2681 the WIND/3DP experiment. *Geophys. Res. Lett.*, 23, 1259–1262. doi:
2682 10.1029/96GL00303
- 2683 Bothmer, V., & Schwenn, R. (1994, October). Eruptive prominences as sources of
2684 magnetic clouds in the solar wind. *Space Sci. Rev.*, 70(1-2), 215–220. doi: 10
2685 .1007/BF00777872
- 2686 Bothmer, V., & Schwenn, R. (1996, January). Signatures of fast CMEs in interplan-
2687 etary space. *Adv. Space Res.*, 17(4-5), 319–322. doi: 10.1016/0273-1177(95)
2688 00593-4
- 2689 Bougeret, J. L., Fainberg, J., & Stone, R. G. (1984, July). Interplanetary ra-
2690 dio storms. I - Extension of solar active regions through the interplanetary
2691 medium. *Astron. & Astrophys.*, 136(2), 255–262.
- 2692 Bougeret, J.-L., Kaiser, M. L., Kellogg, P. J., Manning, R., Goetz, K., Monson,
2693 S. J., . . . Hoang, S. (1995, February). Waves: The Radio and Plasma Wave
2694 Investigation on the Wind Spacecraft. *Space Sci. Rev.*, 71, 231–263. doi:
2695 10.1007/BF00751331
- 2696 Bougeret, J.-L., Zarka, P., Caroubalos, C., Karlický, M., Leblanc, Y., Maroulis, D.,
2697 . . . Perche, C. (1998). A shock associated (SA) radio event and related phe-
2698 nomena observed from the base of the solar corona to 1 AU. *Geophys. Res.*
2699 *Lett.*, 25, 2513–2516. doi: 10.1029/98GL50563
- 2700 Bourouaine, S., Verscharen, D., Chandran, B. D. G., Maruca, B. A., & Kasper, J. C.
2701 (2013, November). Limits on Alpha Particle Temperature Anisotropy and Dif-
2702 ferential Flow from Kinetic Instabilities: Solar Wind Observations. *Astrophys.*
2703 *J. Lett.*, 777, L3. doi: 10.1088/2041-8205/777/1/L3
- 2704

- 2705 Bowen, T. A., Badman, S., Hellinger, P., & Bale, S. D. (2018, February). Density
2706 Fluctuations in the Solar Wind Driven by Alfvén Wave Parametric Decay. *As-*
2707 *trophys. J. Lett.*, *854*, L33. doi: 10.3847/2041-8213/aaabbe
- 2708 Breneman, A. W., Cattell, C. A., Kersten, K., Paradise, A., Schreiner, S., Kel-
2709 logg, P. J., . . . Wilson, L. B. (2013, December). STEREO and Wind ob-
2710 servations of intense cyclotron harmonic waves at the Earth’s bow shock
2711 and inside the magnetosheath. *J. Geophys. Res.*, *118*, 7654–7664. doi:
2712 10.1002/2013JA019372
- 2713 Broiles, T. W., Desai, M. I., & McComas, D. J. (2012, March). Formation, shape,
2714 and evolution of magnetic structures in CIRs at 1 AU. *J. Geophys. Res.*, *117*,
2715 3102. doi: 10.1029/2011JA017288
- 2716 Bruno, R., & Carbone, V. (2013, May). The Solar Wind as a Turbulence Labora-
2717 tory. *Living Rev. Solar Phys.*, *10*, 2. doi: 10.12942/lrsp-2013-2
- 2718 Bruno, R., D’Amicis, R., Bavassano, B., Carbone, V., & Sorriso-Valvo, L. (2007, Au-
2719 gust). Magnetically dominated structures as an important component of the
2720 solar wind turbulence. *Ann. Geophys.*, *25*, 1913–1927. doi: 10.5194/angeo-25
2721 -1913-2007
- 2722 Bruno, R., Telloni, D., Sorriso-Valvo, L., Marino, R., De Marco, R., & D’Amicis,
2723 R. (2019, July). The low-frequency break observed in the slow solar wind
2724 magnetic spectra. *Astron. & Astrophys.*, *627*, A96. doi: 10.1051/0004-6361/
2725 201935841
- 2726 Bruno, R., & Trenchi, L. (2014, June). Radial Dependence of the Frequency Break
2727 between Fluid and Kinetic Scales in the Solar Wind Fluctuations. *Astrophys.*
2728 *J. Lett.*, *787*(2), L24. doi: 10.1088/2041-8205/787/2/L24
- 2729 Burlaga, L., Fitzenreiter, R., Lepping, R., Ogilvie, K., Szabo, A., Lazarus, A., . . .
2730 Larson, D. E. (1998, January). A magnetic cloud containing prominence mate-
2731 rial - January 1997. *J. Geophys. Res.*, *103*, 277-+. doi: 10.1029/97JA02768
- 2732 Burlaga, L., Sittler, E., Mariani, F., & Schwenn, R. (1981, August). Magnetic loop
2733 behind an interplanetary shock: Voyager, Helios, and IMP 8 observations. *J.*
2734 *Geophys. Res.*, *86*(8), 6673–6684. doi: 10.1029/JA086iA08p06673
- 2735 Burlaga, L. F. (1988, July). Magnetic clouds and force-free fields with constant al-
2736 pha. *J. Geophys. Res.*, *93*(7), 7217–7224. doi: 10.1029/JA093iA07p07217
- 2737 Burlaga, L. F., Plunkett, S. P., & St. Cyr, O. C. (2002, October). Succes-
2738 sive CMEs and complex ejecta. *J. Geophys. Res.*, *107*(A10), 1266. doi:
2739 10.1029/2001JA000255
- 2740 Cairns, I. H., Lobzin, V. V., Donea, A., Tingay, S. J., McCauley, P. I., Oberoi, D.,
2741 . . . Williams, C. L. (2018, January). Low Altitude Solar Magnetic Recon-
2742 nection, Type III Solar Radio Bursts, and X-ray Emissions. *Sci. Rep.*, *8*, 1676.
2743 doi: 10.1038/s41598-018-19195-3
- 2744 Cane, H. V. (2003, December). Near-Relativistic Solar Electrons and Type III Radio
2745 Bursts. *Astrophys. J.*, *598*, 1403–1408. doi: 10.1086/379007
- 2746 Cane, H. V., & Erickson, W. C. (2003, May). Energetic particle propagation
2747 in the inner heliosphere as deduced from low-frequency (≤ 100 kHz) obser-
2748 vations of type III radio bursts. *J. Geophys. Res.*, *108*(A5), 1203. doi:
2749 10.1029/2002JA009488
- 2750 Cane, H. V., Erickson, W. C., & Prestage, N. P. (2002, October). Solar flares, type
2751 III radio bursts, coronal mass ejections, and energetic particles. *J. Geophys.*
2752 *Res.*, *107*(A10), 1315. doi: 10.1029/2001JA000320
- 2753 Cane, H. V., Stone, R. G., Fainberg, J., Stewart, R. T., Steinberg, J. L., & Hoang,
2754 S. (1981, December). Radio evidence for shock acceleration of elec-
2755 trons in the solar corona. *Geophys. Res. Lett.*, *8*(12), 1285–1288. doi:
2756 10.1029/GL008i012p01285
- 2757 Caprioli, D., & Spitkovsky, A. (2014, March). Simulations of Ion Acceleration at
2758 Non-relativistic Shocks. I. Acceleration Efficiency. *Astrophys. J.*, *783*, 91. doi:
2759 10.1088/0004-637X/783/2/91

- 2760 Carrington, R. C. (1859, November). Description of a Singular Appearance seen in
2761 the Sun on September 1, 1859. *Mon. Not. Roy. Astron. Soc.*, *20*, 13–15. doi:
2762 10.1093/mnras/20.1.13
- 2763 Cattell, C., Dombeck, J., Wygant, J., Drake, J. F., Swisdak, M., Goldstein, M. L.,
2764 ... Balogh, A. (2005, January). Cluster observations of electron holes in as-
2765 sociation with magnetotail reconnection and comparison to simulations. *J.*
2766 *Geophys. Res.*, *110*, 1211. doi: 10.1029/2004JA010519
- 2767 Cattell, C., Neiman, C., Dombeck, J., Crumley, J., Wygant, J., Kletzing, C. A., ...
2768 André, M. (2003). Large amplitude solitary waves in and near the Earth's
2769 magnetosphere, magnetopause and bow shock: Polar and Cluster observations.
2770 *Nonlin. Proc. Geophys.*, *10*, 13–26.
- 2771 Cattell, C., Wygant, J. R., Goetz, K., Kersten, K., Kellogg, P. J., von Rosenvinge,
2772 T., ... Russell, C. T. (2008, January). Discovery of very large amplitude
2773 whistler-mode waves in Earth's radiation belts. *Geophys. Res. Lett.*, *35*, 1105.
2774 doi: 10.1029/2007GL032009
- 2775 Cattell, C. A., Breneman, A., Goetz, K., Kellogg, P. J., Kersten, K., Wygant, J. R.,
2776 ... Roth, I. (2012, December). Large-Amplitude Whistler Waves and Elec-
2777 tron Acceleration in the Earth's Radiation Belts: A Review of STEREO and
2778 Wind Observations. In D. Summers, I. R. Mann, D. N. Baker, & M. Schulz
2779 (Eds.), *Dynamics of the Earth's Radiation Belts and Inner Magnetosphere*
2780 (Vol. 199, pp. 41–51). Washington, D.C.: American Geophysical Union. doi:
2781 10.1029/2012GM001322
- 2782 Chen, C. H. K. (2016, December). Recent progress in astrophysical plasma turbu-
2783 lence from solar wind observations. *J. Plasma Phys.*, *82*(6), 535820602. doi: 10
2784 .1017/S0022377816001124
- 2785 Chen, C. H. K., Bale, S. D., Salem, C. S., & Maruca, B. A. (2013, June). Residual
2786 Energy Spectrum of Solar Wind Turbulence. *Astrophys. J.*, *770*, 125. doi: 10
2787 .1088/0004-637X/770/2/125
- 2788 Chen, C. H. K., Leung, L., Boldyrev, S., Maruca, B. A., & Bale, S. D. (2014,
2789 November). Ion-scale spectral break of solar wind turbulence at high and
2790 low beta. *Geophys. Res. Lett.*, *41*, 8081–8088. doi: 10.1002/2014GL062009
- 2791 Chen, C. H. K., Mallet, A., Schekochihin, A. A., Horbury, T. S., Wicks, R. T., &
2792 Bale, S. D. (2012, October). Three-dimensional Structure of Solar Wind
2793 Turbulence. *Astrophys. J.*, *758*(2), 120. doi: 10.1088/0004-637X/758/2/120
- 2794 Chen, C. H. K., Matteini, L., Schekochihin, A. A., Stevens, M. L., Salem, C. S.,
2795 Maruca, B. A., ... Bale, S. D. (2016, July). Multi-species Measurements of the
2796 Firehose and Mirror Instability Thresholds in the Solar Wind. *Astrophys. J.*
2797 *Lett.*, *825*, L26. doi: 10.3847/2041-8205/825/2/L26
- 2798 Chen, J. H., Schwadron, N. A., Möbius, E., & Gorby, M. (2015, November). Model-
2799 ing interstellar pickup ion distributions in corotating interaction regions inside
2800 1 AU. *J. Geophys. Res.*, *120*(11), 9269–9280. doi: 10.1002/2014JA020939
- 2801 Chen, L.-J., Wang, S., Wilson, L. B., Schwartz, S., Bessho, N., Moore, T., ...
2802 Avanov, L. (2018, June). Electron Bulk Acceleration and Thermalization
2803 at Earth's Quasiperpendicular Bow Shock. *Phys. Rev. Lett.*, *120*(22), 225101.
2804 doi: 10.1103/PhysRevLett.120.225101
- 2805 CHIME/FRB Collaboration, B. C., Andersen, Bandura, K. M., Bhardwaj, M., Bij,
2806 A., Boyce, M. M., Boyle, P. J., ... Zwaniga, A. V. (2020, November). A bright
2807 millisecond-duration radio burst from a Galactic magnetar. *Nature*, *587*(7832),
2808 54–58. doi: 10.1038/s41586-020-2863-y
- 2809 Chotoo, K., Schwadron, N. A., Mason, G. M., Zurbuchen, T. H., Gloeckler, G., Pos-
2810 ner, A., ... Collier, M. R. (2000, October). The suprathermal seed population
2811 for corotating interaction region ions at 1 AU deduced from composition and
2812 spectra of H⁺, He⁺⁺, and He⁺ observed on Wind. *J. Geophys. Res.*, *105*,
2813 23107–23122. doi: 10.1029/1998JA000015
- 2814 Clack, D., Kasper, J. C., Lazarus, A. J., Steinberg, J. T., & Farrell, W. M. (2004,

- 2815 March). Wind observations of extreme ion temperature anisotropies in the
 2816 lunar wake. *Geophys. Res. Lett.*, *310*, L06812. doi: 10.1029/2003GL018298
- 2817 Cline, T. L., Hurley, K. C., Barthelmy, S., Butterworth, P., Feroci, M., Frontera,
 2818 F., . . . Trombka, J. (2001). The IPN I: From the Past to the Future. In
 2819 E. Costa, F. Frontera, & J. Hjorth (Ed.), *Gamma-ray bursts in the afterglow*
 2820 *era* (p. 375-+). doi: 10.1007/10853853_102
- 2821 Cliver, E. W., Kahler, S. W., Kazachenko, M., & Shimojo, M. (2019, May). The
 2822 Disappearing Solar Filament of 2013 September 29 and Its Large Associated
 2823 Proton Event: Implications for Particle Acceleration at the Sun. *Astrophys. J.*,
 2824 *877*(1), 11. doi: 10.3847/1538-4357/ab0e03
- 2825 Cliver, E. W., Nitta, N. V., Thompson, B. J., & Zhang, J. (2004, November). Coronal
 2826 Shocks of November 1997 Revisited: The Cme Type II Timing Problem.
 2827 *Solar Phys.*, *225*, 105–139. doi: 10.1007/s11207-004-3258-1
- 2828 Cohen, C. M. S. (2006, October). Observations of Energetic Storm Particles: An
 2829 Overview. *Washington DC American Geophysical Union Geophysical Mono-*
 2830 *graph Series*, *165*, 275–282. doi: 10.1029/165GM26
- 2831 Corona-Romero, P., Gonzalez-Esparza, J. A., & Aguilar-Rodriguez, E. (2013, July).
 2832 Propagation of Fast Coronal Mass Ejections and Shock Waves Associated with
 2833 Type II Radio-Burst Emission: An Analytic Study. *Solar Phys.*, *285*, 391–410.
 2834 doi: 10.1007/s11207-012-0103-9
- 2835 Cremades, H., Iglesias, F. A., St. Cyr, O. C., Xie, H., Kaiser, M. L., & Gopalswamy,
 2836 N. (2015, September). Low-Frequency Type-II Radio Detections and Coro-
 2837 nagraph Data Employed to Describe and Forecast the Propagation of 71
 2838 CMEs/Shocks. *Solar Phys.*, *290*, 2455–2478. doi: 10.1007/s11207-015-0776-y
- 2839 Dasso, S., Nakwacki, M. S., Démoulin, P., & Mandrini, C. H. (2007, August). Pro-
 2840 gressive Transformation of a Flux Rope to an ICME. Comparative Analysis
 2841 Using the Direct and Fitted Expansion Methods. *Solar Phys.*, *244*, 115–137.
 2842 doi: 10.1007/s11207-007-9034-2
- 2843 Davidson, R. C., & Gladd, N. T. (1975, October). Anomalous transport properties
 2844 associated with the lower-hybrid-drift instability. *Phys. Fluids*, *18*, 1327–1335.
 2845 doi: 10.1063/1.861021
- 2846 de Nolfo, G. A., Bruno, A., Ryan, J. M., Dalla, S., Giacalone, J., Richardson, I. G.,
 2847 . . . Munini, R. (2019, July). Comparing Long-duration Gamma-Ray Flares
 2848 and High-energy Solar Energetic Particles. *Astrophys. J.*, *879*(2), 90. doi:
 2849 10.3847/1538-4357/ab258f
- 2850 Del Zanna, G., Aulanier, G., Klein, K. L., & Török, T. (2011, February). A sin-
 2851 gle picture for solar coronal outflows and radio noise storms. *Astron. & Astro-*
 2852 *phys.*, *526*, A137. doi: 10.1051/0004-6361/201015231
- 2853 Démoulin, P., Dasso, S., & Janvier, M. (2013, February). Does spacecraft trajec-
 2854 tory strongly affect detection of magnetic clouds? *Astron. & Astrophys.*, *550*,
 2855 A3. doi: 10.1051/0004-6361/201220535
- 2856 Démoulin, P., Dasso, S., Janvier, M., & Lanabere, V. (2019, December). Re-analysis
 2857 of Lepping’s Fitting Method for Magnetic Clouds: Lundquist Fit Reloaded.
 2858 *Solar Phys.*, *294*(12), 172. doi: 10.1007/s11207-019-1564-x
- 2859 Démoulin, P., Janvier, M., & Dasso, S. (2016, February). Magnetic Flux and Helic-
 2860 ity of Magnetic Clouds. *Solar Phys.*, *291*, 531–557. doi: 10.1007/s11207-015
 2861 -0836-3
- 2862 Desai, M. I., Mason, G. M., Müller-Mellin, R., Korth, A., Mall, U., Dwyer, J. R.,
 2863 & von Rosenvinge, T. T. (2008, August). The spatial distribution of up-
 2864 stream ion events from the Earth’s bow shock measured by ACE, Wind, and
 2865 STEREO. *J. Geophys. Res.*, *113*(8), A08103. doi: 10.1029/2007JA012909
- 2866 Domingo, V., Fleck, B., & Poland, A. I. (1995, December). The SOHO Mission: an
 2867 Overview. *Solar Phys.*, *162*(1-2), 1–37. doi: 10.1007/BF00733425
- 2868 Drake, J. F., Cassak, P. A., Shay, M. A., Swisdak, M., & Quataert, E. (2009, July).
 2869 A Magnetic Reconnection Mechanism for Ion Acceleration and Abundance

- 2870 Enhancements in Impulsive Flares. *Astrophys. J. Lett.*, *700*, L16–L20. doi:
2871 10.1088/0004-637X/700/1/L16
- 2872 Drake, J. F., & Swisdak, M. (2012, November). Ion Heating and Acceleration Dur-
2873 ing Magnetic Reconnection Relevant to the Corona. *Space Sci. Rev.*, *172*(1-4),
2874 227–240. doi: 10.1007/s11214-012-9903-3
- 2875 Drake, J. F., Swisdak, M., Che, H., & Shay, M. A. (2006, October). Electron ac-
2876 celeration from contracting magnetic islands during reconnection. *Nature*, *443*,
2877 553–556. doi: 10.1038/nature05116
- 2878 Ebert, R. W., Desai, M. I., Dayeh, M. A., & Mason, G. M. (2012, August). He-
2879 lium Ion Anisotropies in Corotating Interaction Regions at 1 AU. *Astrophys. J.*
2880 *Lett.*, *754*, L30. doi: 10.1088/2041-8205/754/2/L30
- 2881 Ergun, R. E., Larson, D., Lin, R. P., McFadden, J. P., Carlson, C. W., Anderson,
2882 K. A., ... Bougeret, J.-L. (1998, August). Wind Spacecraft Observations of
2883 Solar Impulsive Electron Events Associated with Solar Type III Radio Bursts.
2884 *Astrophys. J.*, *503*, 435–+. doi: 10.1086/305954
- 2885 Escoubet, C. P., Schmidt, R., & Goldstein, M. L. (1997, January). Clus-
2886 ter - Science and Mission Overview. *Space Sci. Rev.*, *79*, 11–32. doi:
2887 10.1023/A:1004923124586
- 2888 Fainberg, J., & Stone, R. G. (1970, November). Type III Solar Radio Burst Storms
2889 Observed at Low Frequencies. *Solar Phys.*, *15*(1), 222–233. doi: 10.1007/
2890 BF00149487
- 2891 Farrell, W. M., Fitzenreiter, R. J., Owen, C. J., Byrnes, J. B., Lepping, R. P.,
2892 Ogilvie, K. W., & Neubauer, F. (1996). Upstream ULF waves and ener-
2893 getic electrons associated with the lunar wake: Detection of precursor activity.
2894 *Geophys. Res. Lett.*, *23*, 1271–1274. doi: 10.1029/96GL01355
- 2895 Farrell, W. M., Kaiser, M. L., & Steinberg, J. T. (1997, May). Electrostatic instabil-
2896 ity in the central lunar wake: A process for replenishing the plasma void? *Geo-*
2897 *phys. Res. Lett.*, *24*, 1135–1138. doi: 10.1029/97GL00878
- 2898 Farrell, W. M., Kaiser, M. L., Steinberg, J. T., & Bale, S. D. (1998, October). A
2899 simple simulation of a plasma void: Applications to Wind observations of the
2900 lunar wake. *J. Geophys. Res.*, *1032*, 23653–23660. doi: 10.1029/97JA03717
- 2901 Farrugia, C. J., Berdichevsky, D. B., Möstl, C., Galvin, A. B., Leitner, M., Popecki,
2902 M. A., ... Sauvaud, J. A. (2011, June). Multiple, distant (40°) in situ obser-
2903 vations of a magnetic cloud and a corotating interaction region complex. *J.*
2904 *Atmos. Solar-Terr. Phys.*, *73*, 1254–1269. doi: 10.1016/j.jastp.2010.09.011
- 2905 Farrugia, C. J., Burlaga, L. F., Osherovich, V. A., Richardson, I. G., Freeman,
2906 M. P., Lepping, R. P., & Lazarus, A. J. (1993, May). A study of an expanding
2907 interplanetary magnetic cloud and its interaction with the Earth's magneto-
2908 sphere: The interplanetary aspect. *J. Geophys. Res.*, *98*(A5), 7621–7632. doi:
2909 10.1029/92JA02349
- 2910 Farrugia, C. J., Matsui, H., Kucharek, H., Torbert, R. B., Smith, C. W., Jordanova,
2911 V. K., ... Skoug, R. (2005, September). Interplanetary coronal mass ejection
2912 and ambient interplanetary magnetic field correlations during the Sun-Earth
2913 connection events of October-November 2003. *J. Geophys. Res.*, *110*, A09S13.
2914 doi: 10.1029/2004JA010968
- 2915 Farrugia, C. J., Sandholt, P. E., Moen, J., & Arnoldy, R. L. (1998). Unusual
2916 features of the January 1997 magnetic cloud and their effect on optical
2917 dayside auroral signatures. *Geophys. Res. Lett.*, *25*, 3051–3054. doi:
2918 10.1029/98GL01226
- 2919 Filwett, R. J., Desai, M. I., Dayeh, M. A., & Broiles, T. W. (2017, March). Source
2920 Population and Acceleration Location of Suprathermal Heavy Ions in Coro-
2921 tating Interaction Regions. *Astrophys. J.*, *838*, 23. doi: 10.3847/1538-4357/
2922 aa5ca9
- 2923 Fishman, G. J. (1995, December). Gamma-Ray Bursts: an Overview. *Publ. Astron.*
2924 *Soc. Pacific*, *107*, 1145–+. doi: 10.1086/133672

- 2925 Fishman, G. J., & Meegan, C. A. (1995). Gamma-Ray Bursts. *Ann. Rev. Astron.*
 2926 *Astrophys.*, *33*, 415–458. doi: 10.1146/annurev.aa.33.090195.002215
- 2927 Fisk, L. A., & Lee, M. A. (1980, April). Shock acceleration of energetic particles in
 2928 corotating interaction regions in the solar wind. *Astrophys. J.*, *237*, 620–626.
 2929 doi: 10.1086/157907
- 2930 Forslund, D., Morse, R., Nielson, C., & Fu, J. (1972, July). Electron Cyclotron
 2931 Drift Instability and Turbulence. *Phys. Fluids*, *15*, 1303–1318. doi: 10.1063/
 2932 1.1694082
- 2933 Forslund, D. W., Morse, R. L., & Nielson, C. W. (1970, November). Elec-
 2934 tron Cyclotron Drift Instability. *Phys. Rev. Lett.*, *25*, 1266–1270. doi:
 2935 10.1103/PhysRevLett.25.1266
- 2936 Forsyth, R. J., & Marsch, E. (1999, July). Solar Origin and Interplanetary Evo-
 2937 lution of Stream Interfaces. *Space Sci. Rev.*, *89*, 7–20. doi: 10.1023/A:
 2938 1005235626013
- 2939 Fox, N. J., Velli, M. C., Bale, S. D., Decker, R., Driesman, A., Howard, R. A., ...
 2940 Szabo, A. (2015, November). The Solar Probe Plus Mission: Humanity’s First
 2941 Visit to Our Star. *Space Sci. Rev.* doi: 10.1007/s11214-015-0211-6
- 2942 Franz, H., Sharer, P., Ogilvie, K., & Desch, M. (1998). Wind nominal mission per-
 2943 formance and extended mission design. In *Aiaa/aas astrodynamics specialist*
 2944 *conference and exhibit*. Retrieved from [https://arc.aiaa.org/doi/abs/10](https://arc.aiaa.org/doi/abs/10.2514/6.1998-4467)
 2945 [.2514/6.1998-4467](https://arc.aiaa.org/doi/abs/10.2514/6.1998-4467) doi: 10.2514/6.1998-4467
- 2946 Franz, J. R., Kintner, P. M., Pickett, J. S., & Chen, L.-J. (2005, September). Prop-
 2947 erties of small-amplitude electron phase-space holes observed by Polar. *J. Geo-*
 2948 *phys. Res.*, *110*, 9212. doi: 10.1029/2005JA011095
- 2949 Fränz, M., & Harper, D. (2002, February). Heliospheric coordinate systems. *Planet.*
 2950 *Space Sci.*, *50*(2), 217–233. doi: 10.1016/S0032-0633(01)00119-2
- 2951 Frederiks, D., Svinkin, D., Tsvetkova, A., Aptekar, R., Golenetskii, S., Kozlova, A.,
 2952 ... Ulanov, M. (2019, February). GRB observations with Konus-WIND
 2953 experiment. *Mem. Soc. Astron. Ital.*, *90*(1–2), 67–70. Retrieved from
 2954 <http://sait.oat.ts.astro.it/MSAIt9001-0219/>
- 2955 Frederiks, D. D., Golenetskii, S. V., Palshin, V. D., Aptekar, R. L., Ilyinskii, V. N.,
 2956 Oleinik, F. P., ... Cline, T. L. (2007, January). Giant flare in SGR 1806-
 2957 20 and its Compton reflection from the Moon. *Astron. Lett.*, *33*, 1–18. doi:
 2958 10.1134/S106377370701001X
- 2959 Fuselier, S. A., & Gurnett, D. A. (1984, January). Short wavelength ion waves up-
 2960 stream of the earth’s bow shock. *J. Geophys. Res.*, *89*, 91–103. doi: 10.1029/
 2961 JA089iA01p00091
- 2962 Gary, S. P. (1993). *Theory of Space Plasma Microinstabilities*. Cambridge University
 2963 Press.
- 2964 Gary, S. P., Gosling, J. T., & Forslund, D. W. (1981, August). The electromagnetic
 2965 ion beam instability upstream of the earth’s bow shock. *J. Geophys. Res.*, *86*,
 2966 6691–6696. doi: 10.1029/JA086iA08p06691
- 2967 Gary, S. P., Jian, L. K., Broiles, T. W., Stevens, M. L., Podesta, J. J., & Kasper,
 2968 J. C. (2016, January). Ion-driven instabilities in the solar wind: Wind
 2969 observations of 19 March 2005. *J. Geophys. Res.*, *121*, 30–41. doi:
 2970 10.1002/2015JA021935
- 2971 Gary, S. P., & Karimabadi, H. (2006, November). Linear theory of electron temper-
 2972 ature anisotropy instabilities: Whistler, mirror, and Weibel. *J. Geophys. Res.*,
 2973 *111*, 11224. doi: 10.1029/2006JA011764
- 2974 Gary, S. P., Li, H., O’Rourke, S., & Winske, D. (1998, July). Proton resonant fire-
 2975 hose instability: Temperature anisotropy and fluctuating field constraints. *J.*
 2976 *Geophys. Res.*, *103*, 14567–14574. doi: 10.1029/98JA01174
- 2977 Gary, S. P., Montgomery, M. D., Feldman, W. C., & Forslund, D. W. (1976, March).
 2978 Proton temperature anisotropy instabilities in the solar wind. *J. Geophys.*
 2979 *Res.*, *81*, 1241–1246. doi: 10.1029/JA081i007p01241

- 2980 Gary, S. P., & Nishimura, K. (2003, September). Resonant electron firehose instability: Particle-in-cell simulations. *Phys. Plasmas*, *10*, 3571–3576. doi: 10.1063/
2981 1.1590982
- 2982
- 2983 Gary, S. P., Scime, E. E., Phillips, J. L., & Feldman, W. C. (1994, December). The
2984 whistler heat flux instability: Threshold conditions in the solar wind. *J. Geophys. Res.*, *99*(12), 23391–23399. doi: 10.1029/94JA02067
- 2985
- 2986 Glesener, L., & Fleishman, G. D. (2018, November). Electron Acceleration and Jet-
2987 facilitated Escape in an M-class Solar Flare on 2002 August 19. *Astrophys. J.*,
2988 *867*, 84. doi: 10.3847/1538-4357/aacefe
- 2989 Gloeckler, G., Balsiger, H., Bürgi, A., Bochsler, P., Fisk, L. A., Galvin, A. B., ...
2990 Wilken, B. (1995, February). The Solar Wind and Suprathermal Ion Compo-
2991 sition Investigation on the Wind Spacecraft. *Space Sci. Rev.*, *71*, 79–124. doi:
2992 10.1007/BF00751327
- 2993 Goldreich, P., & Sridhar, S. (1995, January). Toward a Theory of Interstellar Tur-
2994 bulence. II. Strong Alfvénic Turbulence. *Astrophys. J.*, *438*, 763. doi: 10.1086/
2995 175121
- 2996 Good, S. W., Kilpua, E. K. J., LaMoury, A. T., Forsyth, R. J., Eastwood, J. P., &
2997 Möstl, C. (2019, July). Self-Similarity of ICME Flux Ropes: Observations
2998 by Radially Aligned Spacecraft in the Inner Heliosphere. *J. Geophys. Res.*,
2999 *124*(7), 4960–4982. doi: 10.1029/2019JA026475
- 3000 Gopalswamy, N. (2004a, September). Interplanetary Radio Bursts. In D. E. Gary &
3001 C. U. Keller (Ed.), *Astrophysics and space science library* (Vol. 314, p. 305-+).
3002 doi: 10.1007/1-4020-2814-8\15
- 3003 Gopalswamy, N. (2004b, December). Recent advances in the long-wavelength radio
3004 physics of the Sun. *Planet. Space Sci.*, *52*, 1399–1413. doi: 10.1016/j.pss.2004
3005 .09.016
- 3006 Gopalswamy, N. (2006, June). Properties of Interplanetary Coronal Mass Ejections.
3007 *Space Sci. Rev.*, *124*(1-4), 145–168. doi: 10.1007/s11214-006-9102-1
- 3008 Gopalswamy, N. (2011, January). Coronal Mass Ejections and Solar Radio Emis-
3009 sions. In H. O. Rucker, W. S. Kurth, P. Louarn, & G. Fischer (Eds.), *Planetary, solar and heliospheric radio emissions (pre vii)* (pp. 325–342).
3010
- 3011 Gopalswamy, N. (2016, May). Low-Frequency Radio Bursts and Space Weather.
3012 *arXiv e-prints*, arXiv:1605.02218.
- 3013 Gopalswamy, N., Aguilar-Rodriguez, E., Yashiro, S., Nunes, S., Kaiser, M. L., &
3014 Howard, R. A. (2005, October). Type II radio bursts and energetic solar
3015 eruptions. *J. Geophys. Res.*, *110*, A12S07. doi: 10.1029/2005JA011158
- 3016 Gopalswamy, N., Akiyama, S., Mäkelä, P., Yashiro, S., & Cairns, I. H. (2016, May).
3017 On the Directivity of Low-Frequency Type IV Radio Bursts. *arXiv e-prints*,
3018 arXiv:1605.02223.
- 3019 Gopalswamy, N., Akiyama, S., Yashiro, S., Michalek, G., Xie, H., & Mäkelä, P.
3020 (2020, July). Effect of the Weakened Heliosphere in Solar Cycle 24 on the
3021 Properties of Coronal Mass Ejections. *arXiv e-prints*, arXiv:2007.08291.
- 3022 Gopalswamy, N., Kaiser, M. L., Lepping, R. P., Kahler, S. W., Ogilvie, K.,
3023 Berdichevsky, D., ... Akioka, M. (1998, January). Origin of coronal and
3024 interplanetary shocks - A new look with WIND spacecraft data. *J. Geophys. Res.*, *103*, 307-+. doi: 10.1029/97JA02634
- 3025
- 3026 Gopalswamy, N., Kaiser, M. L., Thompson, B. J., Burlaga, L. F., Szabo, A., Vourli-
3027 idas, A., ... Bougeret, J.-L. (2000, May). Radio-rich Solar Eruptive Events.
3028 *Geophys. Res. Lett.*, *27*, 1427-+. doi: 10.1029/1999GL003665
- 3029 Gopalswamy, N., & Mäkelä, P. (2010, September). Long-duration Low-frequency
3030 Type III Bursts and Solar Energetic Particle Events. *Astrophys. J.*, *721*, L62-
3031 L66. doi: 10.1088/2041-8205/721/1/L62
- 3032 Gopalswamy, N., & Mäkelä, P. (2011). Low-frequency type III radio bursts and solar
3033 energetic particle events. *Central European Astrophys. Bull.*, *35*, 71–82.
- 3034 Gopalswamy, N., Mäkelä, P., Akiyama, S., Yashiro, S., Xie, H., & Thakur, N. (2018,

- 3035 November). Sun-to-earth propagation of the 2015 June 21 coronal mass ejection
 3036 revealed by optical, EUV, and radio observations. *J. Atmos. Solar-Terr.*
 3037 *Phys.*, *179*, 225–238. doi: 10.1016/j.jastp.2018.07.013
- 3038 Gopalswamy, N., Mäkelä, P., Akiyama, S., Yashiro, S., Xie, H., Thakur, N., &
 3039 Kahler, S. W. (2015, June). Large Solar Energetic Particle Events Associated
 3040 with Filament Eruptions Outside of Active Regions. *Astrophys. J.*, *806*,
 3041 8. doi: 10.1088/0004-637X/806/1/8
- 3042 Gopalswamy, N., Mäkelä, P., & Yashiro, S. (2019, January). A Catalog of Type II
 3043 radio bursts observed by Wind/WAVES and their Statistical Properties. *Sun*
 3044 *and Geosphere*, *14*, 111–121. doi: 10.31401/SunGeo.2019.02.03
- 3045 Gopalswamy, N., Mäkelä, P., Yashiro, S., Lara, A., Akiyama, S., & Xie, H.
 3046 (2019, November). On the Shock Source of Sustained Gamma-Ray Emis-
 3047 sion from the Sun. In *J. phys. conf. ser.* (Vol. 1332, p. 012004). doi:
 3048 10.1088/1742-6596/1332/1/012004
- 3049 Gopalswamy, N., Mäkelä, P., Yashiro, S., Lara, A., Xie, H., Akiyama, S., & Mac-
 3050 Dowall, R. J. (2018, December). Interplanetary Type II Radio Bursts from
 3051 Wind/WAVES and Sustained Gamma-Ray Emission from Fermi/LAT: Evi-
 3052 dence for Shock Source. *Astrophys. J. Lett.*, *868*, L19. doi: 10.3847/2041-8213/
 3053 aaf36
- 3054 Gopalswamy, N., Mäkelä, P., Yashiro, S., Thakur, N., Akiyama, S., & Xie, H. (2017,
 3055 September). A Hierarchical Relationship between the Fluence Spectra and
 3056 CME Kinematics in Large Solar Energetic Particle Events: A Radio Per-
 3057 spective. In *Journal of physics conference series* (Vol. 900, p. 012009). doi:
 3058 10.1088/1742-6596/900/1/012009
- 3059 Gopalswamy, N., Xie, H., Yashiro, S., Akiyama, S., Mäkelä, P., & Usoskin, I. G.
 3060 (2012, October). Properties of Ground Level Enhancement Events and the As-
 3061 sociated Solar Eruptions During Solar Cycle 23. *Space Sci. Rev.*, *171*, 23–60.
 3062 doi: 10.1007/s11214-012-9890-4
- 3063 Gopalswamy, N., Yashiro, S., Kaiser, M. L., Howard, R. A., & Bougeret, J. L. (2001,
 3064 December). Characteristics of coronal mass ejections associated with long-
 3065 wavelength type II radio bursts. *J. Geophys. Res.*, *106*(A12), 29219–29230.
 3066 doi: 10.1029/2001JA000234
- 3067 Gopalswamy, N., Yashiro, S., Thakur, N., Mäkelä, P., Xie, H., & Akiyama, S. (2016,
 3068 December). The 2012 July 23 Backside Eruption: An Extreme Energetic Parti-
 3069 cle Event? *Astrophys. J.*, *833*, 216. doi: 10.3847/1538-4357/833/2/216
- 3070 Gopalswamy, N., Yashiro, S., Xie, H., Akiyama, S., & Mäkelä, P. (2015, November).
 3071 Properties and geoeffectiveness of magnetic clouds during solar cycles 23 and
 3072 24. *J. Geophys. Res.*, *120*, 9221–9245. doi: 10.1002/2015JA021446
- 3073 Gordley, L. L., Hervig, M. E., Fish, C., Russell, I., James M., Bailey, S., Cook, J.,
 3074 ... Kemp, J. (2009, March). The solar occultation for ice experiment. *J.*
 3075 *Atmos. Solar-Terr. Phys.*, *71*(3-4), 300–315. doi: 10.1016/j.jastp.2008.07.012
- 3076 Gosling, J. T. (2007, December). Observations of Magnetic Reconnection in the Tur-
 3077 bulent High-Speed Solar Wind. *Astrophys. J.*, *671*, L73-L76. doi: 10.1086/
 3078 524842
- 3079 Gosling, J. T. (2010, March). Magnetic Reconnection in the Solar Wind: An Up-
 3080 date. *Twelfth International Solar Wind Conference*, *1216*, 188–193. doi: 10
 3081 .1063/1.3395833
- 3082 Gosling, J. T. (2011, February). Magnetic Reconnection in the Solar Wind. *Space*
 3083 *Sci. Rev.*, *104*. doi: 10.1007/s11214-011-9747-2
- 3084 Gosling, J. T., Bame, S. J., McComas, D. J., & Phillips, J. L. (1990, June). Coronal
 3085 mass ejections and large geomagnetic storms. *Geophys. Res. Lett.*, *17*(7), 901–
 3086 904. doi: 10.1029/GL017i007p00901
- 3087 Gosling, J. T., Eriksson, S., Blush, L. M., Phan, T. D., Luhmann, J. G., McComas,
 3088 D. J., ... Simunac, K. D. (2007, October). Five spacecraft observations of
 3089 oppositely directed exhaust jets from a magnetic reconnection X-line extending

- 3090 $>4.26 \times 10^6$ km in the solar wind at 1 AU. *Geophys. Res. Lett.*, *34*(2), L20108.
 3091 doi: 10.1029/2007GL031492
- 3092 Gosling, J. T., Eriksson, S., Phan, T. D., Larson, D. E., Skoug, R. M., & McComas,
 3093 D. J. (2007, March). Direct evidence for prolonged magnetic reconnection at
 3094 a continuous x-line within the heliospheric current sheet. *Geophys. Res. Lett.*,
 3095 *34*(0), 6102. doi: 10.1029/2006GL029033
- 3096 Gosling, J. T., Phan, T. D., Lin, R. P., & Szabo, A. (2007, August). Prevalence of
 3097 magnetic reconnection at small field shear angles in the solar wind. *Geophys.*
 3098 *Res. Lett.*, *34*(1), 15110. doi: 10.1029/2007GL030706
- 3099 Gosling, J. T., & Szabo, A. (2008, October). Bifurcated current sheets produced by
 3100 magnetic reconnection in the solar wind. *J. Geophys. Res.*, *113*, A10103. doi:
 3101 10.1029/2008JA013473
- 3102 Grandin, M., Aikio, A. T., & Kozlovsky, A. (2019, June). Properties and Geoeffec-
 3103 tiveness of Solar Wind High-Speed Streams and Stream Interaction Regions
 3104 During Solar Cycles 23 and 24. *J. Geophys. Res.*, *124*(6), 3871–3892. doi:
 3105 10.1029/2018JA026396
- 3106 Grappin, R., Leorat, J., & Pouquet, A. (1983, September). Dependence of MHD tur-
 3107 bulence spectra on the velocity field-magnetic field correlation. *Astron. & As-*
 3108 *trophys.*, *126*(1), 51–58.
- 3109 Guiriec, S., Gehrels, N., McEnery, J., Kouveliotou, C., & Hartmann, D. H. (2017,
 3110 September). Photospheric Emission in the Joint GBM and Konus Prompt
 3111 Spectra of GRB 120323A. *Astrophys. J.*, *846*, 138. doi: 10.3847/1538-4357/
 3112 aa81c2
- 3113 Gurnett, D. A., Marsch, E., Pilipp, W., Schwenn, R., & Rosenbauer, H. (1979,
 3114 May). Ion acoustic waves and related plasma observations in the solar wind. *J.*
 3115 *Geophys. Res.*, *84*, 2029–2038. doi: 10.1029/JA084iA05p02029
- 3116 Gurnett, D. A., Neubauer, F. M., & Schwenn, R. (1979, February). Plasma wave
 3117 turbulence associated with an interplanetary shock. *J. Geophys. Res.*, *84*, 541–
 3118 552. doi: 10.1029/JA084iA02p00541
- 3119 Haggerty, D. K., & Roelof, E. C. (2002, November). Impulsive Near-relativistic So-
 3120 lar Electron Events: Delayed Injection with Respect to Solar Electromagnetic
 3121 Emission. *Astrophys. J.*, *579*, 841–853. doi: 10.1086/342870
- 3122 Halekas, J. S., Angelopoulos, V., Sibeck, D. G., Khurana, K. K., Russell, C. T.,
 3123 Delory, G. T., . . . Glassmeier, K. H. (2011, January). First Results from
 3124 ARTEMIS, a New Two-Spacecraft Lunar Mission: Counter-Streaming
 3125 Plasma Populations in the Lunar Wake. *Space Sci. Rev.*, *95*. doi: 10.1007/
 3126 s11214-010-9738-8
- 3127 Halekas, J. S., Brain, D. A., & Holmström, M. (2015, January). Moon’s Plasma
 3128 Wake. In *Magnetotails in the solar system* (Vol. 207, pp. 149–167). doi: 10
 3129 .1002/9781118842324.ch9
- 3130 Halekas, J. S., Saito, Y., Delory, G. T., & Farrell, W. M. (2011, November). New
 3131 views of the lunar plasma environment. *Planet. Space Sci.*, *59*(14), 1681–1694.
 3132 doi: 10.1016/j.pss.2010.08.011
- 3133 Halford, A. J., McGregor, S. L., Murphy, K. R., Millan, R. M., Hudson, M. K.,
 3134 Woodger, L. A., . . . Fennell, J. F. (2015, April). BARREL observations of an
 3135 ICME-shock impact with the magnetosphere and the resultant radiation belt
 3136 electron loss. *J. Geophys. Res.*, *120*, 2557–2570. doi: 10.1002/2014JA020873
- 3137 Harten, R., & Clark, K. (1995, February). The Design Features of the GGS Wind
 3138 and Polar Spacecraft. *Space Sci. Rev.*, *71*, 23–40. doi: 10.1007/BF00751324
- 3139 He, J., Pei, Z., Wang, L., Tu, C., Marsch, E., Zhang, L., & Salem, C. (2015,
 3140 June). Sunward Propagating Alfvén Waves in Association with Sunward
 3141 Drifting Proton Beams in the Solar Wind. *Astrophys. J.*, *805*, 176. doi:
 3142 10.1088/0004-637X/805/2/176
- 3143 He, J., Wang, L., Tu, C., Marsch, E., & Zong, Q. (2015, February). Evi-
 3144 dence of Landau and Cyclotron Resonance between Protons and Kinetic

- 3145 Waves in Solar Wind Turbulence. *Astrophys. J. Lett.*, 800, L31. doi:
3146 10.1088/2041-8205/800/2/L31
- 3147 He, J., Wang, Y., & Sorriso-Valvo, L. (2019, March). Unified Quantitative De-
3148 scription of Solar Wind Turbulence Intermittency in Both Inertial and Kinetic
3149 Ranges. *Astrophys. J.*, 873(1), 80. doi: 10.3847/1538-4357/ab03d0
- 3150 Hellinger, P., & Trávníček, P. (2006, January). Parallel and oblique proton fire hose
3151 instabilities in the presence of alpha/proton drift: Hybrid simulations. *J. Geo-
3152ophys. Res.*, 111, A01107. doi: 10.1029/2005JA011318
- 3153 Hellinger, P., Trávníček, P., Kasper, J. C., & Lazarus, A. J. (2006, May). Solar wind
3154 proton temperature anisotropy: Linear theory and WIND/SWE observations.
3155 *Geophys. Res. Lett.*, 330, L09101. doi: 10.1029/2006GL025925
- 3156 Hellinger, P., & Trávníček, P. M. (2014, March). Solar Wind Protons at 1 AU:
3157 Trends and Bounds, Constraints and Correlations. *Astrophys. J. Lett.*, 784,
3158 L15. doi: 10.1088/2041-8205/784/1/L15
- 3159 Hervig, M. E., Brooke, J. S. A., Feng, W., Bardeen, C. G., & Plane, J. M. C. (2017,
3160 December). Constraints on Meteoric Smoke Composition and Meteoric Influx
3161 Using SOFIE Observations With Models. *J. Geophys. Res.*, 122(24), 13495–
3162 13505. doi: 10.1002/2017JD027657
- 3163 Hervig, M. E., Siskind, D. E., Bailey, S. M., Merkel, A. W., DeLand, M. T., &
3164 Russell, J. M. (2019, August). The Missing Solar Cycle Response of the
3165 Polar Summer Mesosphere. *Geophys. Res. Lett.*, 46(16), 10132–10139. doi:
3166 10.1029/2019GL083485
- 3167 Hesse, M., & Cassak, P. A. (2020, January). Magnetic Reconnection in the Space
3168 Sciences: Past, Present, and Future. *J. Geophys. Res.*, 125(2), e2018JA025935.
3169 doi: 10.1029/2018JA025935
- 3170 Hidalgo, M. A., Cid, C., Medina, J., & Viñas, A. F. (2000, May). A new model for
3171 the topology of magnetic clouds in the solar wind. *Solar Phys.*, 194, 165–174.
- 3172 Hidalgo, M. A., & Nieves-Chinchilla, T. (2012, April). A Global Magnetic Topol-
3173 ogy Model for Magnetic Clouds. I. *Astrophys. J.*, 748, 109. doi: 10.1088/0004
3174 -637X/748/2/109
- 3175 Hidalgo, M. A., Nieves-Chinchilla, T., & Cid, C. (2002, July). Elliptical cross-section
3176 model for the magnetic topology of magnetic clouds. *Geophys. Res. Lett.*,
3177 29(13), 1637. doi: 10.1029/2001GL013875
- 3178 Hietala, H., Agueda, N., Andréová, K., Vainio, R., Nylund, S., Kilpua, E. K. J.,
3179 & Koskinen, H. E. J. (2011, October). In situ observations of particle ac-
3180 celeration in shock-shock interaction. *J. Geophys. Res.*, 116, 10105. doi:
3181 10.1029/2011JA016669
- 3182 Hietala, H., Sandroos, A., & Vainio, R. (2012, May). Particle Acceleration in Shock-
3183 Shock Interaction: Model to Data Comparison. *Astrophys. J. Lett.*, 751, L14.
3184 doi: 10.1088/2041-8205/751/1/L14
- 3185 Hillaris, A., Bouratzis, C., & Nindos, A. (2016, August). Interplanetary Type IV
3186 Bursts. *Solar Phys.*, 291, 2049–2069. doi: 10.1007/s11207-016-0946-6
- 3187 Ho, G. C., Hamilton, D. C., Gloeckler, G., & Bochsler, P. (2000). Enhanced solar
3188 wind $^3\text{He}^{2+}$ associated with coronal mass ejections. *Geophys. Res. Lett.*, 27,
3189 309–312. doi: 10.1029/1999GL003660
- 3190 Hoang, S., Maksimovic, M., Bougeret, J.-L., Reiner, M. J., & Kaiser, M. L. (1998).
3191 Wind-Ulysses source location of radio emissions associated with the Jan-
3192 uary 1997 Coronal Mass Ejection. *Geophys. Res. Lett.*, 25, 2497–2500. doi:
3193 10.1029/98GL00571
- 3194 Horaites, K., Boldyrev, S., Krasheninnikov, S. I., Salem, C., Bale, S. D., & Pulupa,
3195 M. (2015, June). Self-Similar Theory of Thermal Conduction and Appli-
3196 cation to the Solar Wind. *Physical Review Letters*, 114(24), 245003. doi:
3197 10.1103/PhysRevLett.114.245003
- 3198 Horaites, K., Boldyrev, S., & Medvedev, M. V. (2019, April). Electron strahl and
3199 halo formation in the solar wind. *Mon. Not. Roy. Astron. Soc.*, 484, 2474–

2481. doi: 10.1093/mnras/sty3504
- 3200 Horbury, T. S., Forman, M., & Oughton, S. (2008, October). Anisotropic Scaling of
3201 Magnetohydrodynamic Turbulence. *Phys. Rev. Lett.*, *101*(17), 175005. doi: 10
3202 .1103/PhysRevLett.101.175005
- 3203
- 3204 Horne, R. B., Thorne, R. M., Glauert, S. A., Albert, J. M., Meredith, N. P., & An-
3205 derson, R. R. (2005, March). Timescale for radiation belt electron acceleration
3206 by whistler mode chorus waves. *J. Geophys. Res.*, *110*(A3), A03225. doi:
3207 10.1029/2004JA010811
- 3208 Howes, G. G., Bale, S. D., Klein, K. G., Chen, C. H. K., Salem, C. S., & Ten-
3209 Barge, J. M. (2012, July). The Slow-mode Nature of Compressible Wave
3210 Power in Solar Wind Turbulence. *Astrophys. J. Lett.*, *753*, L19. doi:
3211 10.1088/2041-8205/753/1/L19
- 3212 Hu, Q., & Sonnerup, B. U. Ö. (2001, February). Reconstruction of mag-
3213 netic flux ropes in the solar wind. *Geophys. Res. Lett.*, *28*, 467–470. doi:
3214 10.1029/2000GL012232
- 3215 Hu, Q., & Sonnerup, B. U. Ö. (2002, July). Reconstruction of magnetic clouds in
3216 the solar wind: Orientations and configurations. *J. Geophys. Res.*, *107*, 1142.
3217 doi: 10.1029/2001JA000293
- 3218 Hu, Q., Zheng, J., & Chen, Y. (2018, October). A database of small-scale magnetic
3219 flux ropes in the solar wind from Wind spacecraft measurements. In *Journal of*
3220 *physics conference series* (Vol. 1100, p. 012012). doi: 10.1088/1742-6596/1100/
3221 1/012012
- 3222 Huba, J. D., & Wu, C. S. (1976, July). Effects of a magnetic field gradient
3223 on the lower hybrid drift instability. *Phys. Fluids*, *19*, 988–994. doi:
3224 10.1063/1.861594
- 3225 Hull, A. J., Muschietti, L., Le Contel, O., Dorelli, J. C., & Lindqvist, P. A. (2020,
3226 July). MMS Observations of Intense Whistler Waves Within Earth’s Su-
3227 percritical Bow Shock: Source Mechanism and Impact on Shock Struc-
3228 ture and Plasma Transport. *J. Geophys. Res.*, *125*(7), e27290. doi:
3229 10.1029/2019JA027290
- 3230 Hull, A. J., Muschietti, L., Oka, M., Larson, D. E., Mozer, F. S., Chaston, C. C.,
3231 ... Hospodarsky, G. B. (2012, December). Multiscale whistler waves
3232 within Earth’s perpendicular bow shock. *J. Geophys. Res.*, *117*, 12104. doi:
3233 10.1029/2012JA017870
- 3234 Hurley, K., Atteia, J.-L., Crew, G., Ricker, G., Doty, J., Monnelly, G., ... Cline, T.
3235 (2003, April). HETE-II and the Interplanetary Network. In G. R. Ricker &
3236 R. K. Vanderspek (Ed.), *Gamma-ray burst and afterglow astronomy 2001: A*
3237 *workshop celebrating the first year of the hete mission* (Vol. 662, pp. 42–44).
3238 doi: 10.1063/1.1579296
- 3239 Hurley, K., Cline, T., Mitrofanov, I., Mazets, E., Golenetskii, S., Frontera, F., ...
3240 Feroci, M. (2003, April). The Current Performance of the Third Interplanetary
3241 Network. In G. R. Ricker & R. K. Vanderspek (Eds.), *Gamma-ray burst and*
3242 *afterglow astronomy 2001: A workshop celebrating the first year of the hete*
3243 *mission* (Vol. 662, pp. 473–476). doi: 10.1063/1.1579405
- 3244 Hurley, K., Golenetskii, S., Aptekar, R., Mazets, E., Pal’Shin, V., Frederiks, D.,
3245 ... Hajdas, W. (2011, August). The Third Interplanetary Network. In
3246 J. E. McEnery, J. L. Racusin, & N. Gehrels (Eds.), *American institute of*
3247 *physics conference series* (Vol. 1358, pp. 385–388). doi: 10.1063/1.3621810
- 3248 Hurley, K., Rowlinson, A., Bellm, E., Perley, D., Mitrofanov, I. G., Golovin,
3249 D. V., ... von Kienlin, A. (2010, March). A new analysis of the short-
3250 duration, hard-spectrum GRB 051103, a possible extragalactic soft gamma
3251 repeater giant flare. *Mon. Not. Roy. Astron. Soc.*, *403*, 342–352. doi:
3252 10.1111/j.1365-2966.2009.16118.x
- 3253 Illing, R. M. E., & Hundhausen, A. J. (1985, January). Observation of a coronal
3254 transient from 1.2 to 6 solar radii. *J. Geophys. Res.*, *90*(1), 275–282. doi: 10

- 3255 .1029/JA090iA01p00275
 3256 Janvier, M., Dasso, S., Démoulin, P., Masías-Meza, J. J., & Lugaz, N. (2015, May).
 3257 Comparing generic models for interplanetary shocks and magnetic clouds
 3258 axis configurations at 1 AU. *J. Geophys. Res.*, *120*(5), 3328–3349. doi:
 3259 10.1002/2014JA020836
- 3260 Janvier, M., Winslow, R. M., Good, S., Bonhomme, E., Démoulin, P., Dasso, S.,
 3261 ... Boakes, P. D. (2019, February). Generic Magnetic Field Intensity Pro-
 3262 files of Interplanetary Coronal Mass Ejections at Mercury, Venus, and Earth
 3263 From Superposed Epoch Analyses. *J. Geophys. Res.*, *124*(2), 812–836. doi:
 3264 10.1029/2018JA025949
- 3265 Jaynes, A. N., Baker, D. N., Singer, H. J., Rodriguez, J. V., Loto'aniu, T. M., Ali,
 3266 A. F., ... Reeves, G. D. (2015, September). Source and seed populations for
 3267 relativistic electrons: Their roles in radiation belt changes. *J. Geophys. Res.*,
 3268 *120*, 7240–7254. doi: 10.1002/2015JA021234
- 3269 Jian, L., Russell, C. T., Luhmann, J. G., & Skoug, R. M. (2006, December). Prop-
 3270 erties of Stream Interactions at One AU During 1995–2004. *Solar Phys.*, *239*,
 3271 337–392. doi: 10.1007/s11207-006-0132-3
- 3272 Jian, L. K., Russell, C. T., Luhmann, J. G., & Galvin, A. B. (2018, March).
 3273 STEREO Observations of Interplanetary Coronal Mass Ejections in 2007–2016.
 3274 *Astrophys. J.*, *855*, 114. doi: 10.3847/1538-4357/aab189
- 3275 Jian, L. K., Russell, C. T., Luhmann, J. G., Galvin, A. B., & MacNeice, P. J. (2009,
 3276 October). Multi-Spacecraft Observations: Stream Interactions and Associated
 3277 Structures. *Solar Phys.*, *259*, 345–360. doi: 10.1007/s11207-009-9445-3
- 3278 Kahler, S. W., Krucker, S., & Szabo, A. (2011, January). Solar energetic electron
 3279 probes of magnetic cloud field line lengths. *J. Geophys. Res.*, *116*, 1104. doi:
 3280 10.1029/2010JA015328
- 3281 Kaiser, M. L. (2003, August). Solar radio emissions at solar maximum: Interplane-
 3282 tary perspective. *Adv. Space Res.*, *32*, 461–465. doi: 10.1016/S0273-1177(03)
 3283 00330-2
- 3284 Kaiser, M. L., Reiner, M. J., Gopalswamy, N., Howard, R. A., St. Cyr, O. C.,
 3285 Thompson, B. J., & Bougeret, J.-L. (1998). Type II radio emissions in the
 3286 frequency range from 1–14 MHz associated with the April 7, 1997 solar event.
 3287 *Geophys. Res. Lett.*, *25*, 2501–2504. doi: 10.1029/98GL00706
- 3288 Kasper, J. C., & Klein, K. G. (2019, June). Strong Preferential Ion Heating is Lim-
 3289 ited to within the Solar Alfvén Surface. *Astrophys. J. Lett.*, *877*(2), L35. doi:
 3290 10.3847/2041-8213/ab1de5
- 3291 Kasper, J. C., Klein, K. G., Weber, T., Maksimovic, M., Zaslavsky, A., Bale, S. D.,
 3292 ... Case, A. W. (2017, November). A Zone of Preferential Ion Heating
 3293 Extends Tens of Solar Radii from the Sun. *Astrophys. J.*, *849*, 126. doi:
 3294 10.3847/1538-4357/aa84b1
- 3295 Kasper, J. C., Lazarus, A. J., & Gary, S. P. (2002, September). Wind/SWE observa-
 3296 tions of firehose constraint on solar wind proton temperature anisotropy. *Geo-
 3297 phys. Res. Lett.*, *29*, 1839. doi: 10.1029/2002GL015128
- 3298 Kasper, J. C., Lazarus, A. J., & Gary, S. P. (2008, December). Hot Solar-Wind
 3299 Helium: Direct Evidence for Local Heating by Alfvén-Cyclotron Dissipation.
 3300 *Phys. Rev. Lett.*, *101*, 261103–+. doi: 10.1103/PhysRevLett.101.261103
- 3301 Kasper, J. C., Lazarus, A. J., Gary, S. P., & Szabo, A. (2003, September). Solar
 3302 Wind Temperature Anisotropies. In M. Velli, R. Bruno, F. Malara, & B. Bucci
 3303 (Ed.), *Solar wind ten* (Vol. 679, pp. 538–541). doi: 10.1063/1.1618653
- 3304 Kasper, J. C., Lazarus, A. J., Steinberg, J. T., Ogilvie, K. W., & Szabo, A. (2006,
 3305 March). Physics-based tests to identify the accuracy of solar wind ion mea-
 3306 surements: A case study with the Wind Faraday Cups. *J. Geophys. Res.*, *111*,
 3307 A03105. doi: 10.1029/2005JA011442
- 3308 Kasper, J. C., Maruca, B. A., Stevens, M. L., & Zaslavsky, A. (2013, March). Sen-
 3309 sitive Test for Ion-Cyclotron Resonant Heating in the Solar Wind. *Phys. Rev.*

- 3310 *Lett.*, 110(9), 091102. doi: 10.1103/PhysRevLett.110.091102
- 3311 Kasper, J. C., Stevens, M. L., Korreck, K. E., Maruca, B. A., Kiefer, K. K.,
3312 Schwadron, N. A., & Lepri, S. T. (2012, February). Evolution of the
3313 Relationships between Helium Abundance, Minor Ion Charge State, and
3314 Solar Wind Speed over the Solar Cycle. *Astrophys. J.*, 745, 162. doi:
3315 10.1088/0004-637X/745/2/162
- 3316 Kasper, J. C., Stevens, M. L., Lazarus, A. J., Steinberg, J. T., & Ogilvie, K. W.
3317 (2007, May). Solar Wind Helium Abundance as a Function of Speed and
3318 Heliographic Latitude: Variation through a Solar Cycle. *Astrophys. J.*, 660,
3319 901–910. doi: 10.1086/510842
- 3320 Kellogg, P. J. (2017, January). Note on the Pantellini et al. process for
3321 dust impact signals on spacecraft. *J. Geophys. Res.*, 122, 63–70. doi:
3322 10.1002/2016JA023073
- 3323 Kellogg, P. J., Cattell, C. A., Goetz, K., Monson, S. J., & Wilson, L. B., III. (2011,
3324 September). Large amplitude whistlers in the magnetosphere observed with
3325 Wind-Waves. *J. Geophys. Res.*, 116, 9224. doi: 10.1029/2010JA015919
- 3326 Kellogg, P. J., Goetz, K., & Monson, S. J. (2016, February). Dust impact
3327 signals on the wind spacecraft. *J. Geophys. Res.*, 121, 966–991. doi:
3328 10.1002/2015JA021124
- 3329 Kellogg, P. J., Goetz, K., & Monson, S. J. (2018, May). Sign of the Dust Impact-
3330 Antenna Coupling Cloud. *J. Geophys. Res.*, 123(5), 3273–3276. doi: 10.1029/
3331 2017JA025173
- 3332 Kellogg, P. J., Goetz, K., Monson, S. J., & Bale, S. D. (1999, April). A search for
3333 Langmuir solitons in the Earth’s foreshock. *J. Geophys. Res.*, 104, 6751–6758.
3334 doi: 10.1029/1999JA900021
- 3335 Kellogg, P. J., Goetz, K., Monson, S. J., Bougeret, J.-L., Manning, R., & Kaiser,
3336 M. L. (1996). Observations of plasma waves during a traversal of the moon’s
3337 wake. *Geophys. Res. Lett.*, 23, 1267–1270. doi: 10.1029/96GL00376
- 3338 Kellogg, P. J., Monson, S. J., Goetz, K., Howard, R. L., Bougeret, J.-L., & Kaiser,
3339 M. L. (1996). Early wind observations of bow shock and foreshock waves.
3340 *Geophys. Res. Lett.*, 23, 1243–1246. doi: 10.1029/96GL01067
- 3341 Kersten, K., Cattell, C. A., Breneman, A., Goetz, K., Kellogg, P. J., Wygant, J. R.,
3342 ... Roth, I. (2011, April). Observation of relativistic electron microbursts in
3343 conjunction with intense radiation belt whistler-mode waves. *Geophys. Res.*
3344 *Lett.*, 38, 8107.
- 3345 Kilpua, E., Koskinen, H. E. J., & Pulkkinen, T. I. (2017, November). Coronal mass
3346 ejections and their sheath regions in interplanetary space. *Living Reviews in*
3347 *Solar Physics*, 14, 5. doi: 10.1007/s41116-017-0009-6
- 3348 Kilpua, E. K. J., Balogh, A., von Steiger, R., & Liu, Y. D. (2017, November). Geo-
3349 effective Properties of Solar Transients and Stream Interaction Regions. *Space*
3350 *Sci. Rev.*, 212, 1271–1314. doi: 10.1007/s11214-017-0411-3
- 3351 Kilpua, E. K. J., Lee, C. O., Luhmann, J. G., & Li, Y. (2011, August). Interplane-
3352 tary coronal mass ejections in the near-Earth solar wind during the minimum
3353 periods following solar cycles 22 and 23. *Ann. Geophys.*, 29, 1455–1467. doi:
3354 10.5194/angeo-29-1455-2011
- 3355 King, J. H., & Papitashvili, N. E. (2005, February). Solar wind spatial scales in and
3356 comparisons of hourly Wind and ACE plasma and magnetic field data. *J. Geo-*
3357 *phys. Res.*, 110, A02104. doi: 10.1029/2004JA010649
- 3358 Klassen, A., Bothmer, V., Mann, G., Reiner, M. J., Krucker, S., Vourlidas, A., &
3359 Kunow, H. (2002, April). Solar energetic electron events and coronal shocks.
3360 *Astron. & Astrophys.*, 385, 1078–1088. doi: 10.1051/0004-6361:20020205
- 3361 Klebesadel, R. W., Strong, I. B., & Olson, R. A. (1973, June). Observations of
3362 Gamma-Ray Bursts of Cosmic Origin. *Astrophys. J. Lett.*, 182, L85. doi: 10
3363 .1086/181225
- 3364 Klein, K. G., Alterman, B. L., Stevens, M. L., Vech, D., & Kasper, J. C. (2018,

- 3365 May). Majority of Solar Wind Intervals Support Ion-Driven Instabilities. *Phys.*
3366 *Rev. Lett.*, *120*(20), 205102. doi: 10.1103/PhysRevLett.120.205102
- 3367 Klein, K. G., Howes, G. G., TenBarge, J. M., Bale, S. D., Chen, C. H. K., & Salem,
3368 C. S. (2012, August). Using Synthetic Spacecraft Data to Interpret Com-
3369 pressible Fluctuations in Solar Wind Turbulence. *Astrophys. J.*, *755*, 159. doi:
3370 10.1088/0004-637X/755/2/159
- 3371 Klein, K.-L., Tziotziou, K., Zucca, P., Valtonen, E., Vilmer, N., Malandraki, O. E.,
3372 ... Kiener, J. (2018). X-Ray, Radio and SEP Observations of Relativistic
3373 Gamma-Ray Events. In O. E. Malandraki & N. B. Crosby (Eds.), *Solar par-*
3374 *ticle radiation storms forecasting and analysis* (Vol. 444, pp. 133–155). doi:
3375 10.1007/978-3-319-60051-2_8
- 3376 Kouveliotou, C., Strohmayer, T., Hurley, K., van Paradijs, J., Finger, M. H., Dieters,
3377 S., ... Duncan, R. C. (1999, January). Discovery of a Magnetar Associated
3378 with the Soft Gamma Repeater SGR 1900+14. *Astrophys. J.*, *510*, L115-L118.
3379 doi: 10.1086/311813
- 3380 Koval, A., & Szabo, A. (2010, December). Multispacecraft observations of interplan-
3381 etary shock shapes on the scales of the Earth’s magnetosphere. *J. Geophys.*
3382 *Res.*, *115*, 12105. doi: 10.1029/2010JA015373
- 3383 Krasnoselskikh, V. V., Lembège, B., Savoini, P., & Lobzin, V. V. (2002, April).
3384 Nonstationarity of strong collisionless quasiperpendicular shocks: Theory
3385 and full particle numerical simulations. *Phys. Plasmas*, *9*, 1192–1209. doi:
3386 10.1063/1.1457465
- 3387 Krucker, S., Larson, D. E., Lin, R. P., & Thompson, B. J. (1999, July). On the Ori-
3388 gin of Impulsive Electron Events Observed at 1 AU. *Astrophys. J.*, *519*, 864–
3389 875. doi: 10.1086/307415
- 3390 Krupar, V., Szabo, A., Maksimovic, M., Kruparova, O., Kontar, E. P., Balmaceda,
3391 L. A., ... Hegedus, A. M. (2020, February). Density Fluctuations in the So-
3392 lar Wind Based on Type III Radio Bursts Observed by Parker Solar Probe.
3393 *Astrophys. J. Suppl.*, *246*(2), 57. doi: 10.3847/1538-4365/ab65bd
- 3394 Kubicka, M., Möstl, C., Amerstorfer, T., Boakes, P. D., Feng, L., Eastwood, J. P., &
3395 Törmänen, O. (2016, December). Prediction of Geomagnetic Storm Strength
3396 from Inner Heliospheric In Situ Observations. *Astrophys. J.*, *833*(2), 255. doi:
3397 10.3847/1538-4357/833/2/255
- 3398 Lampe, M., Manheimer, W. M., McBride, J. B., Orens, J. H., Shanny, R., & Sudan,
3399 R. N. (1971, May). Nonlinear Development of the Beam-Cyclotron Instability.
3400 *Phys. Rev. Lett.*, *26*, 1221–1225. doi: 10.1103/PhysRevLett.26.1221
- 3401 Lampe, M., McBride, J. B., Orens, J. H., & Sudan, R. N. (1971, May). On the the-
3402 ory of the beam cyclotron instability in plasmas. *Phys. Lett. A*, *35*, 129–130.
3403 doi: 10.1016/0375-9601(71)90583-4
- 3404 Lanabere, V., Dasso, S., Démoulin, P., Janvier, M., Rodriguez, L., & Masías-Meza,
3405 J. J. (2020, March). Magnetic twist profile inside magnetic clouds derived
3406 with a superposed epoch analysis. *Astron. & Astrophys.*, *635*, A85. doi:
3407 10.1051/0004-6361/201937404
- 3408 Lario, D., Ho, G. C., Decker, R. B., Roelof, E. C., Desai, M. I., & Smith, C. W.
3409 (2003, September). ACE Observations of Energetic Particles Associated
3410 with Transient Interplanetary Shocks. In M. Velli, R. Bruno, F. Malara, &
3411 B. Bucci (Eds.), *Proc. 10th intl. solar wind conf.* (Vol. 679, pp. 640–643). doi:
3412 10.1063/1.1618676
- 3413 Larson, D. E., Lin, R. P., McTiernan, J. M., McFadden, J. P., Ergun, R. E., Mc-
3414 Carthy, M., ... Mazur, J. (1997). Tracing the topology of the October 18-20,
3415 1995, magnetic cloud with $\sim 0.1\text{-}10^2$ keV electrons. *Geophys. Res. Lett.*, *24*,
3416 1911–1914. doi: 10.1029/97GL01878
- 3417 Larson, D. E., Lin, R. P., & Steinberg, J. (2000). Extremely cold electrons in the
3418 January 1997 magnetic cloud. *Geophys. Res. Lett.*, *27*, 157–160. doi: 10.1029/
3419 1999GL003632

- 3420 Laurenza, M., Cliver, E. W., Hewitt, J., Storini, M., Ling, A. G., Balch, C. C., &
 3421 Kaiser, M. L. (2009, April). A technique for short-term warning of solar ener-
 3422 getic particle events based on flare location, flare size, and evidence of particle
 3423 escape. *Space Weather*, *70*, S04008. doi: 10.1029/2007SW000379
- 3424 Lavraud, B., Gosling, J. T., Rouillard, A. P., Fedorov, A., Opitz, A., Sauvaud, J.-A.,
 3425 ... Russell, C. T. (2009, May). Observation of a Complex Solar Wind Re-
 3426 connection Exhaust from Spacecraft Separated by over 1800 R_E . *Solar Phys.*,
 3427 *256*, 379–392. doi: 10.1007/s11207-009-9341-x
- 3428 Leamon, R. J., Matthaeus, W. H., Smith, C. W., Zank, G. P., Mullan, D. J., &
 3429 Oughton, S. (2000, July). MHD-driven Kinetic Dissipation in the Solar Wind
 3430 and Corona. *Astrophys. J.*, *537*(2), 1054–1062. doi: 10.1086/309059
- 3431 Leamon, R. J., Smith, C. W., Ness, N. F., Matthaeus, W. H., & Wong, H. K. (1998,
 3432 March). Observational constraints on the dynamics of the interplanetary mag-
 3433 netic field dissipation range. *J. Geophys. Res.*, *103*, 4775–+. doi: 10.1029/
 3434 97JA03394
- 3435 Leblanc, Y., Dulk, G. A., Cairns, I. H., & Bougeret, J.-L. (2000, August). Type
 3436 II fixed on boards flare continuum in the corona and solar wind. *J. Geophys.*
 3437 *Res.*, *105*, 18215–18224. doi: 10.1029/1999JA000429
- 3438 Lemons, D. S., & Gary, S. P. (1978, April). Current-driven instabilities in a lam-
 3439 inar perpendicular shock. *J. Geophys. Res.*, *83*, 1625–1632. doi: 10.1029/
 3440 JA083iA04p01625
- 3441 Lepping, R. P., Acuña, M. H., Burlaga, L. F., Farrell, W. M., Slavin, J. A., Schat-
 3442 ten, K. H., ... Worley, E. M. (1995, February). The Wind Magnetic Field
 3443 Investigation. *Space Sci. Rev.*, *71*, 207–229. doi: 10.1007/BF00751330
- 3444 Lepping, R. P., Berdichevsky, D. B., Szabo, A., Arqueros, C., & Lazarus, A. J.
 3445 (2003, February). Profile of an Average Magnetic Cloud at 1 au for the Quiet
 3446 Solar Phase: Wind Observations. *Solar Phys.*, *212*, 425–444.
- 3447 Lepping, R. P., Berdichevsky, D. B., & Wu, C.-C. (2017, February). Average Mag-
 3448 netic Field Magnitude Profiles of Wind Magnetic Clouds as a Function of
 3449 Closest Approach to the Clouds' Axes and Comparison to Model. *Solar Phys.*,
 3450 *292*, 27. doi: 10.1007/s11207-016-1040-9
- 3451 Lepping, R. P., Berdichevsky, D. B., Wu, C. C., Szabo, A., Narock, T., Mariani, F.,
 3452 ... Quivers, A. J. (2006, March). A summary of WIND magnetic clouds for
 3453 years 1995-2003: model-fitted parameters, associated errors and classifications.
 3454 *Ann. Geophys.*, *24*(1), 215–245. doi: 10.5194/angeo-24-215-2006
- 3455 Lepping, R. P., Burlaga, L. F., Szabo, A., Ogilvie, K. W., Mish, W. H., Vassiliadis,
 3456 D., ... Mariani, F. (1997, July). The Wind magnetic cloud and events of
 3457 October 18-20, 1995: Interplanetary properties and as triggers for geomagnetic
 3458 activity. *J. Geophys. Res.*, *102*, 14049–14064. doi: 10.1029/97JA00272
- 3459 Lepping, R. P., Jones, J. A., & Burlaga, L. F. (1990, August). Magnetic field struc-
 3460 ture of interplanetary magnetic clouds at 1 AU. *J. Geophys. Res.*, *95*(A8),
 3461 11957–11965. doi: 10.1029/JA095iA08p11957
- 3462 Lepping, R. P., Narock, T. W., & Chen, H. (2007, January). Comparison of mag-
 3463 netic field observations of an average magnetic cloud with a simple force free
 3464 model: the importance of field compression and expansion. *Ann. Geophys.*, *25*,
 3465 2641–2648.
- 3466 Lepping, R. P., Wu, C.-C., & Berdichevsky, D. B. (2005, October). Auto-
 3467 matic identification of magnetic clouds and cloud-like regions at 1 AU: oc-
 3468 currence rate and other properties. *Ann. Geophys.*, *23*, 2687–2704. doi:
 3469 10.5194/angeo-23-2687-2005
- 3470 Lepping, R. P., Wu, C.-C., Berdichevsky, D. B., & Ferguson, T. (2008, July). Es-
 3471 timates of magnetic cloud expansion at 1 AU. *Ann. Geophys.*, *26*, 1919–1933.
 3472 doi: 10.5194/angeo-26-1919-2008
- 3473 Lepping, R. P., Wu, C.-C., Berdichevsky, D. B., & Kay, C. (2018, December). Mag-
 3474 netic Field Magnitude Modification for a Force-free Magnetic Cloud Model.

- 3475 *Solar Phys.*, 293, 162. doi: 10.1007/s11207-018-1383-5
- 3476 Lepping, R. P., Wu, C. C., Berdichevsky, D. B., & Szabo, A. (2011, December).
 3477 Magnetic Clouds at/near the 2007 - 2009 Solar Minimum: Frequency of Oc-
 3478 currence and Some Unusual Properties. *Solar Phys.*, 274(1-2), 345–360. doi:
 3479 10.1007/s11207-010-9646-9
- 3480 Lepping, R. P., Wu, C.-C., Berdichevsky, D. B., & Szabo, A. (2018, April). Wind
 3481 Magnetic Clouds for the Period 2013 - 2015: Model Fitting, Types, Associated
 3482 Shock Waves, and Comparisons to Other Periods. *Solar Phys.*, 293, 65. doi:
 3483 10.1007/s11207-018-1273-x
- 3484 Lepping, R. P., Wu, C. C., Berdichevsky, D. B., & Szabo, A. (2020, June). Model
 3485 Fitting of Wind Magnetic Clouds for the Period 2004 - 2006. *Solar Phys.*,
 3486 295(6), 83. doi: 10.1007/s11207-020-01630-2
- 3487 Lepping, R. P., Wu, C.-C., Gopalswamy, N., & Berdichevsky, D. B. (2008, March).
 3488 Average Thickness of Magnetosheath Upstream of Magnetic Clouds at 1
 3489 AU versus Solar Longitude of Source. *Solar Phys.*, 248, 125–139. doi:
 3490 10.1007/s11207-007-9111-6
- 3491 Li, W., Thorne, R. M., Bortnik, J., Baker, D. N., Reeves, G. D., Kanekal, S. G., ...
 3492 Green, J. C. (2015, September). Solar wind conditions leading to efficient
 3493 radiation belt electron acceleration: A superposed epoch analysis. *Geophys.*
 3494 *Res. Lett.*, 42, 6906–6915. doi: 10.1002/2015GL065342
- 3495 Li, Y., Luhmann, J. G., & Lynch, B. J. (2018, October). Magnetic Clouds: Solar
 3496 Cycle Dependence, Sources, and Geomagnetic Impacts. *Solar Phys.*, 293, 135.
 3497 doi: 10.1007/s11207-018-1356-8
- 3498 Lin, R. P., Anderson, K. A., Ashford, S., Carlson, C., Curtis, D., Ergun, R., ...
 3499 Paschmann, G. (1995, February). A Three-Dimensional Plasma and Energetic
 3500 Particle Investigation for the Wind Spacecraft. *Space Sci. Rev.*, 71, 125–153.
 3501 doi: 10.1007/BF00751328
- 3502 Liu, X., Yue, J., Wang, W., Xu, J., Zhang, Y., Li, J., ... Nakamura, T. (2018,
 3503 May). Responses of Lower Thermospheric Temperature to the 2013 St.
 3504 Patrick’s Day Geomagnetic Storm. *Geophys. Res. Lett.*, 45(10), 4656–4664.
 3505 doi: 10.1029/2018GL078039
- 3506 Liu, Y. D., Luhmann, J. G., Lugaz, N., Möstl, C., Davies, J. A., Bale, S. D., & Lin,
 3507 R. P. (2013, May). On Sun-to-Earth Propagation of Coronal Mass Ejections.
 3508 *Astrophys. J.*, 769(1), 45. doi: 10.1088/0004-637X/769/1/45
- 3509 Lotko, W., Smith, R. H., Zhang, B., Ouellette, J. E., Brambles, O. J., & Lyon, J. G.
 3510 (2014, July). Ionospheric control of magnetotail reconnection. *Science*, 345,
 3511 184–187. doi: 10.1126/science.1252907
- 3512 Lugaz, N., Farrugia, C. J., Winslow, R. M., Al-Haddad, N., Galvin, A. B., Nieves-
 3513 Chinchilla, T., ... Janvier, M. (2018, September). On the Spatial Coherence of
 3514 Magnetic Ejecta: Measurements of Coronal Mass Ejections by Multiple Space-
 3515 craft Longitudinally Separated by 0.01 au. *Astrophys. J. Lett.*, 864, L7. doi:
 3516 10.3847/2041-8213/aad9f4
- 3517 Lugaz, N., Manchester, W. B., IV, Roussev, I. I., Tóth, G., & Gombosi, T. I. (2007,
 3518 April). Numerical Investigation of the Homologous Coronal Mass Ejec-
 3519 tion Events from Active Region 9236. *Astrophys. J.*, 659, 788–800. doi:
 3520 10.1086/512005
- 3521 Lugaz, N., Winslow, R. M., & Farrugia, C. J. (2020, January). Evolution of a
 3522 Long-Duration Coronal Mass Ejection and Its Sheath Region Between Mer-
 3523 cury and Earth on 9-14 July 2013. *J. Geophys. Res.*, 125(1), e27213. doi:
 3524 10.1029/2019JA027213
- 3525 Lundquist, S. (1951, July). On the Stability of Magneto-Hydrostatic Fields. *Phys.*
 3526 *Rev.*, 83(2), 307–311. doi: 10.1103/PhysRev.83.307
- 3527 Lysenko, A. L., Altyntsev, A. T., Meshalkina, N. S., Zhdanov, D., & Fleish-
 3528 man, G. D. (2018, April). Statistics of “Cold” Early Impulsive Solar
 3529 Flares in X-Ray and Microwave Domains. *Astrophys. J.*, 856, 111. doi:

- 10.3847/1538-4357/aab271
- 3530
3531 MacDowall, R. J., Lara, A., Manoharan, P. K., Nitta, N. V., Rosas, A. M., &
3532 Bougeret, J. L. (2003, May). Long-duration hectometric type III radio bursts
3533 and their association with solar energetic particle (SEP) events. *Geophys. Res.*
3534 *Lett.*, *30*, 8018. doi: 10.1029/2002GL016624
- 3535 MacDowall, R. J., Richardson, I. G., Hess, R. A., & Thejappa, G. (2009, March).
3536 Re-examining the correlation of complex solar type III radio bursts and solar
3537 energetic particles. In N. Gopalswamy & D. F. Webb (Ed.), *Iau symposium*
3538 (Vol. 257, pp. 335–340). doi: 10.1017/S1743921309029512
- 3539 Mäkelä, P., Gopalswamy, N., & Akiyama, S. (2018, November). Direction-finding
3540 Analysis of the 2012 July 6 Type II Solar Radio Burst at Low Frequencies. *As-*
3541 *trophys. J.*, *867*, 40. doi: 10.3847/1538-4357/aae2b6
- 3542 Malandraki, O. E., & Crosby, N. B. (2018). Solar Energetic Particles and Space
3543 Weather: Science and Applications. In O. E. Malandraki & N. B. Crosby
3544 (Eds.), *Solar particle radiation storms forecasting and analysis* (Vol. 444, p. 1-
3545 26). doi: 10.1007/978-3-319-60051-2_1
- 3546 Malaspina, D. M., Cairns, I. H., & Ergun, R. E. (2011, July). Dependence of Lang-
3547 muir wave polarization on electron beam speed in type III solar radio bursts.
3548 *Geophys. Res. Lett.*, *38*, L13101. doi: 10.1029/2011GL047642
- 3549 Malaspina, D. M., & Ergun, R. E. (2008, December). Observations of three-
3550 dimensional Langmuir wave structure. *J. Geophys. Res.*, *113*, 12108. doi:
3551 10.1029/2008JA013656
- 3552 Malaspina, D. M., Halekas, J., Berčić, L., Larson, D., Whittlesey, P., Bale, S. D., ...
3553 Stevens, M. L. (2020, February). Plasma Waves near the Electron Cyclotron
3554 Frequency in the Near-Sun Solar Wind. *Astrophys. J. Suppl.*, *246*(2), 21. doi:
3555 10.3847/1538-4365/ab4c3b
- 3556 Malaspina, D. M., Horányi, M., Zaslavsky, A., Goetz, K., Wilson, L. B., & Kersten,
3557 K. (2014, January). Interplanetary and interstellar dust observed by the
3558 Wind/WAVES electric field instrument. *Geophys. Res. Lett.*, *41*, 266–272. doi:
3559 10.1002/2013GL058786
- 3560 Malaspina, D. M., Newman, D. L., Wilson, L. B., III, Goetz, K., Kellogg, P. J., &
3561 Kersten, K. (2013, February). Electrostatic Solitary Waves in the Solar Wind:
3562 Evidence for Instability at Solar Wind Current Sheets. *J. Geophys. Res.*, *118*,
3563 591–599.
- 3564 Malaspina, D. M., O’Brien, L. E., Thayer, F., Sternovsky, Z., & Collette, A.
3565 (2015, August). Revisiting STEREO interplanetary and interstellar
3566 dust flux and mass estimates. *J. Geophys. Res.*, *120*, 6085–6100. doi:
3567 10.1002/2015JA021352
- 3568 Malaspina, D. M., & Wilson III, L. B. (2016, November). A database of interplan-
3569 etary and interstellar dust detected by the Wind spacecraft. *J. Geophys. Res.*,
3570 *121*, 9369–9377. doi: 10.1002/2016JA023209
- 3571 Mangeney, A. (2001, January). Intermittency in the Solar Wind Turbulence and the
3572 Haar Wavelet Transform. In B. Warmbein (Ed.), *Sheffield space plasma meet-*
3573 *ing: Multipoint measurements versus theory* (Vol. 492, p. 53-+).
- 3574 Mann, G., Classen, H. T., Keppler, E., & Roelof, E. C. (2002, August). On electron
3575 acceleration at CIR related shock waves. *Astron. & Astrophys.*, *391*, 749–756.
3576 doi: 10.1051/0004-6361:20020866
- 3577 Mann, I., Nouzák, L., Vaverka, J., Antonsen, T., Fredriksen, Å., Issautier, K., ...
3578 Zaslavsky, A. (2019, December). Dust observations with antenna measure-
3579 ments and its prospects for observations with Parker Solar Probe and Solar
3580 Orbiter. *Ann. Geophys.*, *37*(6), 1121–1140. doi: 10.5194/angeo-37-1121-2019
- 3581 Mann, I. R., Ozeke, L. G., Murphy, K. R., Claudepierre, S. G., Turner, D. L., Baker,
3582 D. N., ... Honary, F. (2016, October). Explaining the dynamics of the ultra-
3583 relativistic third Van Allen radiation belt. *Nature Phys.*, *12*, 978–983. doi:
3584 10.1038/nphys3799

- 3585 Markovskii, S. A., Vasquez, B. J., & Smith, C. W. (2015, June). Statistical Analysis
3586 of the Magnetic Helicity Signature of the Solar Wind Turbulence at 1 AU. *As-*
3587 *trophys. J.*, *806*, 78. doi: 10.1088/0004-637X/806/1/78
- 3588 Maroulis, D., Dumas, G., Bougeret, J. L., Caroubalos, C., & Poquérousse, M. (1993,
3589 October). The digital system ARTEMIS for real-time processing of radio tran-
3590 sient emissions in the solar corona. *Solar Phys.*, *147*(2), 359–375. doi: 10.1007/
3591 BF00690725
- 3592 Marsch, E. (2006, July). Kinetic Physics of the Solar Corona and Solar Wind. *Living*
3593 *Reviews in Solar Physics*, *3*, 1-+.
- 3594 Marsch, E., & Chang, T. (1983, September). Electromagnetic lower hy-
3595 brid waves in the solar wind. *J. Geophys. Res.*, *88*, 6869–6880. doi:
3596 10.1029/JA088iA09p06869
- 3597 Marubashi, K. (1986, January). Structure of the interplanetary magnetic clouds and
3598 their solar origins. *Adv. Space Res.*, *6*(6), 335–338. doi: 10.1016/0273-1177(86)
3599 90172-9
- 3600 Marubashi, K. (2000, January). Physics of Interplanetary Magnetic Flux Ropes: To-
3601 ward Prediction of Geomagnetic Storms. *Adv. Space Res.*, *26*(1), 55–66. doi:
3602 10.1016/S0273-1177(99)01026-1
- 3603 Maruca, B. A., Bale, S. D., Sorriso-Valvo, L., Kasper, J. C., & Stevens, M. L. (2013,
3604 December). Collisional Thermalization of Hydrogen and Helium in Solar-Wind
3605 Plasma. *Phys. Rev. Lett.*, *111*(24), 241101. doi: 10.1103/PhysRevLett.111
3606 .241101
- 3607 Maruca, B. A., & Kasper, J. C. (2013, August). Improved interpretation of so-
3608 lar wind ion measurements via high-resolution magnetic field data. *Adv. Space*
3609 *Res.*, *52*, 723–731. doi: 10.1016/j.asr.2013.04.006
- 3610 Maruca, B. A., Kasper, J. C., & Bale, S. D. (2011, November). What Are the
3611 Relative Roles of Heating and Cooling in Generating Solar Wind Tem-
3612 perature Anisotropies? *Phys. Rev. Lett.*, *107*, 201101. doi: 10.1103/
3613 PhysRevLett.107.201101
- 3614 Maruca, B. A., Kasper, J. C., & Gary, S. P. (2012, April). Instability-driven Limits
3615 on Helium Temperature Anisotropy in the Solar Wind: Observations and Lin-
3616 ear Vlasov Analysis. *Astrophys. J.*, *748*, 137. doi: 10.1088/0004-637X/748/2/
3617 137
- 3618 Mason, G. M., Desai, M. I., Mall, U., Korth, A., Bucik, R., von Rosenvinge, T. T.,
3619 & Simunac, K. D. (2009, May). In situ Observations of CIRs on STEREO,
3620 Wind, and ACE During 2007 - 2008. *Solar Phys.*, *256*, 393–408. doi:
3621 10.1007/s11207-009-9367-0
- 3622 Mason, G. M., Mazur, J. E., Dwyer, J. R., Reames, D. V., & von Rosenvinge, T. T.
3623 (1997, September). New Spectral and Abundance Features of Interplanetary
3624 Heavy Ions in Corotating Interaction Regions. *Astrophys. J.*, *486*, L149+. doi:
3625 10.1086/310845
- 3626 Mason, G. M., von Steiger, R., Decker, R. B., Desai, M. I., Dwyer, J. R., Fisk, L. A.,
3627 ... Mazur, J. E. (1999, July). Origin, Injection, and Acceleration of CIR Par-
3628 ticles: Observations Report of Working Group 6. *Space Sci. Rev.*, *89*, 327–367.
3629 doi: 10.1023/A:1005278214143
- 3630 Matsui, H., Farrugia, C. J., & Torbert, R. B. (2002, November). Wind-ACE solar
3631 wind correlations, 1999: An approach through spectral analysis. *J. Geophys.*
3632 *Res.*, *107*, 1355. doi: 10.1029/2002JA009251
- 3633 Matthaeus, W. H., Dasso, S., Weygand, J. M., Kivelson, M. G., & Osman, K. T.
3634 (2010, September). Eulerian Decorrelation of Fluctuations in the Interplane-
3635 tary Magnetic Field. *Astrophys. J.*, *721*, L10-L13. doi: 10.1088/2041-8205/
3636 721/1/L10
- 3637 Matthaeus, W. H., Dasso, S., Weygand, J. M., Milano, L. J., Smith, C. W., & Kivel-
3638 son, M. G. (2005, December). Spatial Correlation of Solar-Wind Turbul-
3639 ence from Two-Point Measurements. *Phys. Rev. Lett.*, *95*, 231101-+. doi:

- 10.1103/PhysRevLett.95.231101
- 3640 Matthaeus, W. H., Weygand, J. M., & Dasso, S. (2016, June). Ensemble Space-
3641 Time Correlation of Plasma Turbulence in the Solar Wind. *Phys. Rev. Lett.*,
3642 *116*(24), 245101. doi: 10.1103/PhysRevLett.116.245101
- 3643 Mazelle, C., Le Quéau, D., & Meziane, K. (2000). Nonlinear wave-particle inter-
3644 action upstream from the Earth's bow shock. *Nonlin. Proc. Geophys.*, *7*, 185–
3645 190.
- 3646 Mazets, E. P., Aptekar, R. L., Cline, T. L., Frederiks, D. D., Goldsten, J. O.,
3647 Golenetskii, S. V., . . . Pal'shin, V. D. (2008, June). A Giant Flare from a
3648 Soft Gamma Repeater in the Andromeda Galaxy (M31). *Astrophys. J.*, *680*,
3649 545–549. doi: 10.1086/587955
- 3650 McComas, D. J., Christian, E. R., Schwadron, N. A., Fox, N., Westlake, J., Alle-
3651 grini, F., . . . Zirnstein, E. J. (2018, December). Interstellar Mapping and
3652 Acceleration Probe (IMAP): A New NASA Mission. *Space Sci. Rev.*, *214*(8),
3653 116. doi: 10.1007/s11214-018-0550-1
- 3654 McFadden, J. P., Carlson, C. W., Larson, D., Ludlam, M., Abiad, R., Elliott, B.,
3655 . . . Angelopoulos, V. (2008, December). The THEMIS ESA Plasma In-
3656 strument and In-flight Calibration. *Space Sci. Rev.*, *141*, 277–302. doi:
3657 10.1007/s11214-008-9440-2
- 3658 McFadden, J. P., Phan, T. D., Carlson, C. W., Angelopoulos, V., Glassmeier, K.-H.,
3659 & Auster, U. (2008, May). Structure of the subsolar magnetopause regions
3660 during northward IMF: First results from THEMIS. *Geophys. Res. Lett.*, *35*,
3661 L17S09. doi: 10.1029/2008GL033630
- 3662 Mellott, M. M. (1985). Subcritical Collisionless Shock Waves. In B. T. Tsurutani &
3663 R. G. Stone (Eds.), *Collisionless Shocks in the Heliosphere: Reviews of Current*
3664 *Research* (Vol. 35, pp. 131–140). Washington, D.C.: AGU. Retrieved from
3665 <http://dx.doi.org/10.1029/GM035p0131> doi: 10.1029/GM035p0131
- 3666 Meziane, K., Hamza, A. M., Wilber, M., Lee, M. A., Mazelle, C., Lucek, E. A., &
3667 Hada, T. (2011, May). Specular refraction at a non-stationary shock: A simple
3668 model. *Planet. Space Sci.*, *59*, 495–501. doi: 10.1016/j.pss.2010.10.016
- 3669 Meziane, K., Hull, A. J., Hamza, A. M., & Lin, R. P. (2002, September). On the
3670 bow shock θ_{Bn} dependence of upstream 70 keV to 2 MeV ion fluxes. *J. Geo-*
3671 *phys. Res.*, *107*, 1243. doi: 10.1029/2001JA005012
- 3672 Meziane, K., Lin, R. P., Parks, G. K., Larson, D. E., Bale, S. D., Mason, G. M.,
3673 . . . Lepping, R. P. (1999, October). Evidence for acceleration of ions to ~ 1
3674 MeV by adiabatic-like reflection at the quasi-perpendicular Earth's bow shock.
3675 *Geophys. Res. Lett.*, *26*, 2925–2928. doi: 10.1029/1999GL900603
- 3676 Meziane, K., Mazelle, C., D'Uston, C., Rème, H., Lin, R. P., Carlson, C. W., . . .
3677 Lepping, R. P. (1997, September). Wind observation of gyrating-like ion dis-
3678 tributions and low frequency waves upstream from the earth's bow shock. *Adv.*
3679 *Space Res.*, *20*, 703–706. doi: 10.1016/S0273-1177(97)00459-6
- 3680 Meziane, K., Mazelle, C., Lin, R. P., Le Quéau, D., Larson, D. E., Parks, G. K.,
3681 & Lepping, R. P. (2001, April). Three-dimensional observations of gyrating
3682 ion distributions far upstream from the Earth's bow shock and their asso-
3683 ciation with low-frequency waves. *J. Geophys. Res.*, *106*, 5731–5742. doi:
3684 10.1029/2000JA900079
- 3685 Meziane, K., Wilber, M., Lin, R. P., & Parks, G. K. (2003, October). Gyrophase-
3686 restricted 100 keV-2 MeV ion beams near the foreshock boundary. *Geophys.*
3687 *Res. Lett.*, *30*, 20000–1. doi: 10.1029/2003GL017592
- 3688 Miteva, R., Samwel, S. W., & Costa-Duarte, M. V. (2018, February). The
3689 Wind/EPACT Proton Event Catalog (1996 - 2016). *Solar Phys.*, *293*, 27.
3690 doi: 10.1007/s11207-018-1241-5
- 3691 Miteva, R., Samwel, S. W., & Krupar, V. (2017, December). Solar energetic parti-
3692 cles and radio burst emission. *J. Space Weather Space Clim.*, *7*(27), A37. doi:
3693 10.1051/swsc/2017035
- 3694

- 3695 Morioka, A., Miyoshi, Y., Iwai, K., Kasaba, Y., Masuda, S., Misawa, H., & Obara,
3696 T. (2015, August). Solar Micro-Type III Burst Storms and Long Dipolar
3697 Magnetic Field in the Outer Corona. *Astrophys. J.*, *808*(2), 191. doi:
3698 10.1088/0004-637X/808/2/191
- 3699 Morioka, A., Miyoshi, Y., Masuda, S., Tsuchiya, F., Misawa, H., Matsumoto, H., ...
3700 Oya, H. (2007, March). Micro-Type III Radio Bursts. *Astrophys. J.*, *657*,
3701 567–576. doi: 10.1086/510507
- 3702 Möstl, C., Miklenic, C., Farrugia, C. J., Temmer, M., Veronig, A., Galvin, A. B., ...
3703 Biernat, H. K. (2008, October). Two-spacecraft reconstruction of a magnetic
3704 cloud and comparison to its solar source. *Ann. Geophys.*, *26*, 3139–3152. doi:
3705 10.5194/angeo-26-3139-2008
- 3706 Moullard, O., Burgess, D., Salem, C., Mangeney, A., Larson, D. E., & Bale, S. D.
3707 (2001, May). Whistler waves, Langmuir waves and single loss cone electron
3708 distributions inside a magnetic cloud: Observations. *J. Geophys. Res.*, *106*,
3709 8301–8314. doi: 10.1029/2000JA900144
- 3710 Müller, D., St. Cyr, O. C., Zouganelis, I., Gilbert, H. R., Marsden, R., Nieves-
3711 Chinchilla, T., ... Williams, D. (2020, October). The Solar Orbiter mission.
3712 Science overview. *Astron. & Astrophys.*, *642*, 31. doi: 10.1051/0004-6361/
3713 202038467
- 3714 Mulligan, T., Russell, C. T., Anderson, B. J., Lohr, D. A., Rust, D., Toth, B. A.,
3715 ... Gosling, J. T. (1999). Intercomparison of NEAR and Wind interplanetary
3716 coronal mass ejection observations. *J. Geophys. Res.*, *104*2, 28217–28224. doi:
3717 10.1029/1999JA900215
- 3718 Mulligan, T., Russell, C. T., & Luhmann, J. G. (1998, January). Solar cycle evolu-
3719 tion of the structure of magnetic clouds in the inner heliosphere. *Geophys. Res.*
3720 *Let.*, *25*(15), 2959–2962. doi: 10.1029/98GL01302
- 3721 Muschietti, L., & Lembège, B. (2013, May). Microturbulence in the electron cy-
3722 clotron frequency range at perpendicular supercritical shocks. *J. Geophys.*
3723 *Res.*, *118*, 2267–2285. doi: 10.1002/jgra.50224
- 3724 Muschietti, L., & Lembège, B. (2017, September). Two-stream instabilities from
3725 the lower-hybrid frequency to the electron cyclotron frequency: application to
3726 the front of quasi-perpendicular shocks. *Ann. Geophys.*, *35*, 1093–1112. doi:
3727 10.5194/angeo-35-1093-2017
- 3728 Nakwacki, M. S., Dasso, S., Démoulin, P., Mandrini, C. H., & Gulisano, A. M.
3729 (2011, November). Dynamical evolution of a magnetic cloud from the Sun to
3730 5.4 AU. *Astron. & Astrophys.*, *535*, A52. doi: 10.1051/0004-6361/201015853
- 3731 Ness, N. F. (1972, January). Interaction of the solar wind with the moon. In *The in-*
3732 *terplanetary medium: Part ii of solar-terrestrial physics/1970* (pp. 159–205).
- 3733 Neugebauer, M., & Giacalone, J. (2005, December). Multispacecraft observations of
3734 interplanetary shocks: Nonplanarity and energetic particles. *J. Geophys. Res.*,
3735 *110*, A12106. doi: 10.1029/2005JA011380
- 3736 Neugebauer, M., Giacalone, J., Chollet, E., & Lario, D. (2006, December). Variabil-
3737 ity of low-energy ion flux profiles on interplanetary shock fronts. *J. Geophys.*
3738 *Res.*, *111*, A12107. doi: 10.1029/2006JA011832
- 3739 Nieves-Chinchilla, T., Colaninno, R., Vourlidas, A., Szabo, A., Lepping, R. P.,
3740 Boardson, S. A., ... Korth, H. (2012, June). Remote and in situ observations
3741 of an unusual Earth-directed coronal mass ejection from multiple viewpoints.
3742 *J. Geophys. Res.*, *117*, 6106. doi: 10.1029/2011JA017243
- 3743 Nieves-Chinchilla, T., Jian, L. K., Balmaceda, L., Vourlidas, A., dos Santos,
3744 L. F. G., & Szabo, A. (2019, July). Unraveling the Internal Magnetic Field
3745 Structure of the Earth-directed Interplanetary Coronal Mass Ejections During
3746 1995 - 2015. *Solar Phys.*, *294*(7), 89. doi: 10.1007/s11207-019-1477-8
- 3747 Nieves-Chinchilla, T., Linton, M. G., Hidalgo, M. A., Vourlidas, A., Savani,
3748 N. P., Szabo, A., ... Yu, W. (2016, May). A Circular-cylindrical Flux-
3749 rope Analytical Model for Magnetic Clouds. *Astrophys. J.*, *823*, 27. doi:

- 10.3847/0004-637X/823/1/27
- 3750 Nieves-Chinchilla, T., Vourlidis, A., Raymond, J. C., Linton, M. G., Al-haddad, N.,
3751 Savani, N. P., . . . Hidalgo, M. A. (2018, February). Understanding the Internal
3752 Magnetic Field Configurations of ICMs Using More than 20 Years of Wind
3753 Observations. *Solar Phys.*, *293*, 25. doi: 10.1007/s11207-018-1247-z
3754
- 3755 Nishida, A. (1994, December). The Geotail mission. *Geophys. Res. Lett.*, *21*(25),
3756 2871–2873. doi: 10.1029/94GL01223
- 3757 O’Brien, T. P., McPherron, R. L., Sornette, D., Reeves, G. D., Friedel, R., & Singer,
3758 H. J. (2001, August). Which magnetic storms produce relativistic electrons
3759 at geosynchronous orbit? *J. Geophys. Res.*, *106*(A8), 15533–15544. doi:
3760 10.1029/2001JA000052
- 3761 Ogilvie, K. W., Chornay, D. J., Fritzenreiter, R. J., Hunsaker, F., Keller, J., Lo-
3762 bell, J., . . . Gergin, E. (1995, February). SWE, A Comprehensive Plasma
3763 Instrument for the Wind Spacecraft. *Space Sci. Rev.*, *71*, 55–77. doi:
3764 10.1007/BF00751326
- 3765 Ogilvie, K. W., Coplan, M. A., Roberts, D. A., & Ipavich, F. (2007, August). Solar
3766 wind structure suggested by bimodal correlations of solar wind speed and den-
3767 sity between the spacecraft SOHO and Wind. *J. Geophys. Res.*, *112*, A08104.
3768 doi: 10.1029/2007JA012248
- 3769 Ogilvie, K. W., & Desch, M. D. (1997). The wind spacecraft and its early scientific
3770 results. *Adv. Space Res.*, *20*, 559–568. doi: 10.1016/S0273-1177(97)00439-0
- 3771 Ogilvie, K. W., Steinberg, J. T., Fritzenreiter, R. J., Owen, C. J., Lazarus, A. J.,
3772 Farrell, W. M., & Torbert, R. B. (1996). Observations of the lunar plasma
3773 wake from the WIND spacecraft on December 27, 1994. *Geophys. Res. Lett.*,
3774 *23*, 1255–1258. doi: 10.1029/96GL01069
- 3775 Øieroset, M., Lin, R. P., Phan, T. D., Larson, D. E., & Bale, S. D. (2002, October).
3776 Evidence for Electron Acceleration up to ~ 300 keV in the Magnetic Reconnec-
3777 tion Diffusion Region of Earth’s Magnetotail. *Phys. Rev. Lett.*, *89*, 195001–+.
3778 doi: 10.1103/PhysRevLett.89.195001
- 3779 Øieroset, M., Phan, T. D., Fujimoto, M., Lin, R. P., & Lepping, R. P. (2001, July).
3780 In situ detection of collisionless reconnection in the Earth’s magnetotail. *Nature*,
3781 *412*, 414–417. doi: 10.1038/35086520
- 3782 Oka, M., Otsuka, F., Matsukiyo, S., Wilson III, L. B., Argall, M. R., Amano, T., . . .
3783 Lindqvist, P.-A. (2019, November). Electron Scattering by Low-Frequency
3784 Whistler Waves at Earth’s Bow Shock. *Astrophys. J.*, *886*(53), 11. Retrieved
3785 from <https://iopscience.iop.org/article/10.3847/1538-4357/ab4a81>
3786 doi: 10.3847/1538-4357/ab4a81
- 3787 Osman, K. T., Matthaeus, W. H., Hnat, B., & Chapman, S. C. (2012, June). Ki-
3788 netic Signatures and Intermittent Turbulence in the Solar Wind Plasma. *Phys.*
3789 *Rev. Lett.*, *108*(26), 261103. doi: 10.1103/PhysRevLett.108.261103
- 3790 Oughton, E. J., Skelton, A., Horne, R. B., Thomson, A. W. P., & Gaunt, C. T.
3791 (2017, January). Quantifying the daily economic impact of extreme space
3792 weather due to failure in electricity transmission infrastructure. *Space*
3793 *Weather*, *15*(1), 65–83. doi: 10.1002/2016SW001491
- 3794 Owen, C. J., Lepping, R. P., Ogilvie, K. W., Slavin, J. A., Farrell, W. M., & Byrnes,
3795 J. B. (1996). The lunar wake at 6.8 R_L : WIND magnetic field observations.
3796 *Geophys. Res. Lett.*, *23*, 1263–1266. doi: 10.1029/96GL01354
- 3797 Owens, A., Baker, R., Cline, T. L., Gehrels, N., Jermakian, J., Nolan, T., . . .
3798 Post, A. H., Jr. (1995, February). A High-Resolution GE Spectromer-
3799 ter for Gamma-Ray Burst Astronomy. *Space Sci. Rev.*, *71*, 273–296. doi:
3800 10.1007/BF00751333
- 3801 Owens, M. J., Horbury, T. S., & Arge, C. N. (2010, May). Probing the Large-scale
3802 Topology of the Heliospheric Magnetic Field using Jovian Electrons. *Astro-*
3803 *phys. J.*, *714*(2), 1617–1623. doi: 10.1088/0004-637X/714/2/1617
- 3804 Pal’shin, V. D., Charikov, Y. E., Aptekar, R. L., Golenetskii, S. V., Kokomov, A. A.,

- 3805 Svinkin, D. S., . . . Tsvetkova, A. E. (2014, December). Konus-Wind and
 3806 Helicon-Coronas-F observations of solar flares. *Geomagnetism and Aeronomy*,
 3807 *54*, 943–948. doi: 10.1134/S0016793214070093
- 3808 Pal'shin, V. D., Hurley, K., Svinkin, D. S., Aptekar, R. L., Golenetskii, S. V., Fred-
 3809 eriks, D. D., . . . Ricker, G. (2013, August). Interplanetary Network Localiza-
 3810 tions of Konus Short Gamma-Ray Bursts. *Astrophys. J. Suppl.*, *207*, 38. doi:
 3811 10.1088/0067-0049/207/2/38
- 3812 Park, J., Caprioli, D., & Spitkovsky, A. (2015, February). Simultaneous Acceleration
 3813 of Protons and Electrons at Nonrelativistic Quasiparallel Collisionless Shocks.
 3814 *Phys. Rev. Lett.*, *114*(8), 085003. doi: 10.1103/PhysRevLett.114.085003
- 3815 Paschmann, G., Papamastorakis, I., Sckopke, N., Haerendel, G., Sonnerup, B. U. O.,
 3816 Bame, S. J., . . . Elphic, R. C. (1979, November). Plasma acceleration at the
 3817 earth's magnetopause - Evidence for reconnection. *Nature*, *282*, 243–246. doi:
 3818 10.1038/282243a0
- 3819 Petroff, E., Hessels, J. W. T., & Lorimer, D. R. (2019, May). Fast radio bursts. *As-
 3820 tron. Astrophys. Rev.*, *27*(4), 75. doi: 10.1007/s00159-019-0116-6
- 3821 Phan, T. D., Gosling, J. T., Davis, M. S., Skoug, R. M., Øieroset, M., Lin, R. P.,
 3822 . . . Balogh, A. (2006, January). A magnetic reconnection X-line extending
 3823 more than 390 Earth radii in the solar wind. *Nature*, *439*, 175–178. doi:
 3824 10.1038/nature04393
- 3825 Pitňa, A., Šafránková, J., Němeček, Z., Franci, L., Pi, G., & Montagud Camps, V.
 3826 (2019, July). Characteristics of Solar Wind Fluctuations at and below Ion
 3827 Scales. *Astrophys. J.*, *879*(2), 82. doi: 10.3847/1538-4357/ab22b8
- 3828 Podesta, J. J., & Borovsky, J. E. (2010, November). Scale invariance of normal-
 3829 ized cross-helicity throughout the inertial range of solar wind turbulence. *Phys.
 3830 Plasmas*, *17*, 112905+. doi: 10.1063/1.3505092
- 3831 Podesta, J. J., Roberts, D. A., & Goldstein, M. L. (2006, October). Power spec-
 3832 trum of small-scale turbulent velocity fluctuations in the solar wind. *J. Geo-
 3833 phys. Res.*, *111*, A10109. doi: 10.1029/2006JA011834
- 3834 Podesta, J. J., Roberts, D. A., & Goldstein, M. L. (2007, July). Spectral Exponents
 3835 of Kinetic and Magnetic Energy Spectra in Solar Wind Turbulence. *Astrophys.
 3836 J.*, *664*, 543–548. doi: 10.1086/519211
- 3837 Pohjolainen, S., & Talebpour Sheshvan, N. (2020, March). Cut-off features in inter-
 3838 planetary solar radio type IV emission. *Adv. Space Res.*, *65*(6), 1663–1672. doi:
 3839 10.1016/j.asr.2019.05.034
- 3840 Pulupa, M., & Bale, S. D. (2008, April). Structure on Interplanetary Shock Fronts:
 3841 Type II Radio Burst Source Regions. *Astrophys. J.*, *676*, 1330–1337. doi: 10
 3842 .1086/526405
- 3843 Raj, A., Phan, T., Lin, R. P., & Angelopoulos, V. (2002, December). Wind survey of
 3844 high-speed bulk flows and field-aligned beams in the near-Earth plasma sheet.
 3845 *J. Geophys. Res.*, *107*, 1419. doi: 10.1029/2001JA007547
- 3846 Raymond, J. C., Thompson, B. J., St. Cyr, O. C., Gopalswamy, N., Kahler,
 3847 S., Kaiser, M., . . . O'Neal, R. (2000, May). SOHO and radio observa-
 3848 tions of a CME shock wave. *Geophys. Res. Lett.*, *27*, 1439–1442. doi:
 3849 10.1029/1999GL003669
- 3850 Reames, D. V. (2000, September). Abundances of Trans-Iron Elements in Solar En-
 3851 ergetic Particle Events. *Astrophys. J.*, *540*, L111–L114. doi: 10.1086/312886
- 3852 Reames, D. V. (2012, September). Particle Energy Spectra at Traveling Interplane-
 3853 tary Shock Waves. *Astrophys. J.*, *757*, 93. doi: 10.1088/0004-637X/757/1/93
- 3854 Reames, D. V. (2017). *Solar Energetic Particles* (Vol. 932). doi: 10.1007/978-3-319
 3855 -50871-9
- 3856 Reames, D. V. (2018, October). Corotating Shock Waves and the Solar-wind Source
 3857 of Energetic Ion Abundances: Power Laws in A/Q. *Solar Phys.*, *293*, 144. doi:
 3858 10.1007/s11207-018-1369-3
- 3859 Reames, D. V., Cliver, E. W., & Kahler, S. W. (2014, October). Abun-

- 3860 dance Enhancements in Impulsive Solar Energetic-Particle Events with
 3861 Associated Coronal Mass Ejections. *Solar Phys.*, 289, 3817–3841. doi:
 3862 10.1007/s11207-014-0547-1
- 3863 Reames, D. V., & Ng, C. K. (2004, July). Heavy-Element Abundances in Solar En-
 3864 ergetic Particle Events. *Astrophys. J.*, 610, 510–522. doi: 10.1086/421518
- 3865 Reiner, M. J., Fainberg, J., Kaiser, M. L., & Bougeret, J.-L. (2007, April). Circular
 3866 Polarization Observed in Interplanetary Type III Radio Storms. *Solar Phys.*,
 3867 241, 351–370. doi: 10.1007/s11207-007-0277-8
- 3868 Reiner, M. J., & Kaiser, M. L. (1999, August). High-frequency type II radio emis-
 3869 sions associated with shocks driven by coronal mass ejections. *J. Geophys.*
 3870 *Res.*, 1041, 16979–16992. doi: 10.1029/1999JA900143
- 3871 Reiner, M. J., Kaiser, M. L., & Bougeret, J.-L. (2007, July). Coronal and Inter-
 3872 planetary Propagation of CME/Shocks from Radio, In Situ and White-Light
 3873 Observations. *Astrophys. J.*, 663, 1369–1385. doi: 10.1086/518683
- 3874 Reiner, M. J., Kaiser, M. L., Fainberg, J., Desch, M. D., & Stone, R. G. (1996). $2f_p$
 3875 radio emission from the vicinity of the Earth’s foreshock: WIND observations.
 3876 *Geophys. Res. Lett.*, 23, 1247–+. doi: 10.1029/96GL00841
- 3877 Reiner, M. J., Kaiser, M. L., Fainberg, J., & Stone, R. G. (1998, December).
 3878 A new method for studying remote type II radio emissions from coronal
 3879 mass ejection-driven shocks. *J. Geophys. Res.*, 1032, 29651–29664. doi:
 3880 10.1029/98JA02614
- 3881 Reiner, M. J., Kaiser, M. L., Karlický, M., Jiříčka, K., & Bougeret, J.-L. (2001, De-
 3882 cember). Bastille Day Event: A Radio Perspective. *Solar Phys.*, 204, 121–137.
 3883 doi: 10.1023/A:1014225323289
- 3884 Reiner, M. J., Kaiser, M. L., Plunkett, S. P., Prestage, N. P., & Manning, R. (2000,
 3885 January). Radio Tracking of a White-Light Coronal Mass Ejection from Solar
 3886 Corona to Interplanetary Medium. *Astrophys. J.*, 529, L53–L56. doi: 10.1086/
 3887 312446
- 3888 Reiner, M. J., & MacDowall, R. J. (2015, October). Electron Exciter Speeds Associ-
 3889 ated with Interplanetary Type III Solar Radio Bursts. *Solar Phys.*, 290, 2975–
 3890 3004. doi: 10.1007/s11207-015-0779-8
- 3891 Richardson, I. G., & Cane, H. V. (2004, September). The fraction of interplanetary
 3892 coronal mass ejections that are magnetic clouds: Evidence for a solar cycle
 3893 variation. *Geophys. Res. Lett.*, 311, L18804. doi: 10.1029/2004GL020958
- 3894 Richardson, I. G., & Cane, H. V. (2010, June). Near-Earth Interplanetary Coronal
 3895 Mass Ejections During Solar Cycle 23 (1996 - 2009): Catalog and Summary of
 3896 Properties. *Solar Phys.*, 264, 189–237. doi: 10.1007/s11207-010-9568-6
- 3897 Richardson, I. G., Mays, M. L., & Thompson, B. J. (2018, November). Prediction
 3898 of Solar Energetic Particle Event Peak Proton Intensity Using a Simple Algo-
 3899 rithm Based on CME Speed and Direction and Observations of Associated Solar
 3900 Phenomena. *Space Weather*, 16, 1862–1881. doi: 10.1029/2018SW002032
- 3901 Richardson, J. D., & Paularena, K. I. (2001, January). Plasma and magnetic field
 3902 correlations in the solar wind. *J. Geophys. Res.*, 106(1), 239–252. doi: 10
 3903 .1029/2000JA000071
- 3904 Ridnaia, A., Svinkin, D., Frederiks, D., Bykov, A., Popov, S., Aptekar, R., . . .
 3905 Cline, T. (2020, May). A peculiar hard X-ray counterpart of a Galac-
 3906 tic fast radio burst. *Nature Astron.*, arXiv:2005.11178. (in press) doi:
 3907 10.1038/s41550-020-01265-0
- 3908 Riley, P., Baker, D., Liu, Y. D., Verronen, P., Singer, H., & Güdel, M. (2018, Febru-
 3909 ary). Extreme Space Weather Events: From Cradle to Grave. *Space Sci. Rev.*,
 3910 214(1), 21. doi: 10.1007/s11214-017-0456-3
- 3911 Roberg-Clark, G. T., Drake, J. F., Swisdak, M., & Reynolds, C. S. (2018, Novem-
 3912 ber). Wave Generation and Heat Flux Suppression in Astrophysical Plasma
 3913 Systems. *Astrophys. J.*, 867, 154. doi: 10.3847/1538-4357/aac393
- 3914 Roberts, O. J., Veres, P., Baring, M. G., & Others. (2021, January). Rapid

- 3915 spectral variability of a giant flare from a magnetar in NGC 253. *Nature*,
 3916 589(7841), 207–210. Retrieved from [https://www.nature.com/articles/](https://www.nature.com/articles/s41586-020-03077-8)
 3917 s41586-020-03077-8 doi: 10.1038/s41586-020-03077-8
- 3918 Roth, I., & Temerin, M. (1997, March). Enrichment of ^3He and Heavy Ions in Im-
 3919 pulsive Solar Flares. *Astrophys. J.*, 477(2), 940–957. doi: 10.1086/303731
- 3920 Ruffenach, A., Lavraud, B., Owens, M. J., Sauvaud, J.-A., Savani, N. P., Rouillard,
 3921 A. P., ... Galvin, A. B. (2012, September). Multispacecraft observation
 3922 of magnetic cloud erosion by magnetic reconnection during propagation. *J.*
 3923 *Geophys. Res.*, 117, 9101. doi: 10.1029/2012JA017624
- 3924 Russell, I., James M., Bailey, S. M., Gordley, L. L., Rusch, D. W., Horányi, M.,
 3925 Hervig, M. E., ... Merkel, A. W. (2009, March). The Aeronomy of Ice in
 3926 the Mesosphere (AIM) mission: Overview and early science results. *J. Atmos.*
 3927 *Solar-Terr. Phys.*, 71(3-4), 289–299. doi: 10.1016/j.jastp.2008.08.011
- 3928 Sadykov, V. M., Kosovichev, A. G., Oria, V., & Nita, G. M. (2017, July). An Inter-
 3929 active Multi-instrument Database of Solar Flares. *Astrophys. J. Suppl.*, 231, 6.
 3930 doi: 10.3847/1538-4365/aa79a9
- 3931 Sagdeev, R. Z. (1966). Cooperative Phenomena and Shock Waves in Collisionless
 3932 Plasmas. *Rev. Plasma Phys.*, 4, 23.
- 3933 Salem, C., Hubert, D., Lacombe, C., Bale, S. D., Mangeney, A., Larson, D. E., &
 3934 Lin, R. P. (2003, March). Electron Properties and Coulomb Collisions in the
 3935 Solar Wind at 1 AU: Wind Observations. *Astrophys. J.*, 585, 1147–1157. doi:
 3936 10.1086/346185
- 3937 Salem, C., Mangeney, A., Bale, S. D., & Veltri, P. (2009, September). Solar Wind
 3938 Magnetohydrodynamics Turbulence: Anomalous Scaling and Role of Intermit-
 3939 tency. *Astrophys. J.*, 702, 537–553. doi: 10.1088/0004-637X/702/1/537
- 3940 Salman, T. M., Winslow, R. M., & Lugaz, N. (2020, January). Radial Evolution of
 3941 Coronal Mass Ejections Between MESSENGER, Venus Express, STEREO,
 3942 and L1: Catalog and Analysis. *J. Geophys. Res.*, 125(1), e27084. doi:
 3943 10.1029/2019JA027084
- 3944 Santolík, O., Gurnett, D. A., Pickett, J. S., Parrot, M., & Cornilleau-Wehrin, N.
 3945 (2003, July). Spatio-temporal structure of storm-time chorus. *J. Geophys.*
 3946 *Res.*, 108, 1278. doi: 10.1029/2002JA009791
- 3947 Santolík, O., Kletzing, C. A., Kurth, W. S., Hospodarsky, G. B., & Bounds, S. R.
 3948 (2014, January). Fine structure of large-amplitude chorus wave packets. *Geo-*
 3949 *phys. Res. Lett.*, 41, 293–299. doi: 10.1002/2013GL058889
- 3950 Santolík, O., Pickett, J. S., Gurnett, D. A., Menietti, J. D., Tsurutani, B. T.,
 3951 & Verkhoglyadova, O. (2010, July). Survey of Poynting flux of whistler
 3952 mode chorus in the outer zone. *J. Geophys. Res.*, 115(15), A00F13. doi:
 3953 10.1029/2009JA014925
- 3954 Savani, N. P., Vourlidas, A., Szabo, A., Mays, M. L., Richardson, I. G., Thompson,
 3955 B. J., ... Nieves-Chinchilla, T. (2015, June). Predicting the magnetic vectors
 3956 within coronal mass ejections arriving at Earth: 1. Initial architecture. *Space*
 3957 *Weather*, 13, 374–385. doi: 10.1002/2015SW001171
- 3958 Schiller, Q., Li, X., Blum, L., Tu, W., Turner, D. L., & Blake, J. B. (2014, January).
 3959 A nonstorm time enhancement of relativistic electrons in the outer radiation
 3960 belt. *Geophys. Res. Lett.*, 41, 7–12. doi: 10.1002/2013GL058485
- 3961 Scholer, M., Ipavich, F. M., Gloeckler, G., Hovestadt, D., & Klecker, B. (1980, Janu-
 3962 ary). Upstream particle events close to the bow shock and 200 R_E upstream:
 3963 ISEE-1 and ISEE-3 observations. *Geophys. Res. Lett.*, 7(1), 73–76. doi: 10
 3964 .1029/GL007i001p00073
- 3965 Share, G. H., Murphy, R. J., White, S. M., Tolbert, A. K., Dennis, B. R., Schwartz,
 3966 R. A., ... Shea, M. A. (2018, December). Characteristics of Late-phase >100
 3967 MeV Gamma-Ray Emission in Solar Eruptive Events. *Astrophys. J.*, 869, 182.
 3968 doi: 10.3847/1538-4357/aebf7
- 3969 Shen, C., Chi, Y., Wang, Y., Xu, M., & Wang, S. (2017, June). Statistical com-

- 3970 comparison of the ICME's geoeffectiveness of different types and different so-
3971 lar phases from 1995 to 2014. *J. Geophys. Res.*, *122*, 5931–5948. doi:
3972 10.1002/2016JA023768
- 3973 Shodhan, S., Crooker, N. U., Kahler, S. W., Fitzenreiter, R. J., Larson, D. E.,
3974 Lepping, R. P., ... Gosling, J. T. (2000, December). Counterstreaming
3975 electrons in magnetic clouds. *J. Geophys. Res.*, *105*, 27261–27268. doi:
3976 10.1029/2000JA000060
- 3977 Shu, F. H. (1992). *Physics of Astrophysics, Vol. II*. University Science Books, ISBN
3978 0-935702-65-2.
- 3979 Sibeck, D., Kudela, K., Mukai, T., Nemecek, Z., & Safrankova, J. (2004, December).
3980 Radial dependence of foreshock cavities: a case study. *Ann. Geophys.*, *22*,
3981 4143–4151. doi: 10.5194/angeo-22-4143-2004
- 3982 Sibeck, D. G., Phan, T.-D., Lin, R., Lepping, R. P., & Szabo, A. (2002, October).
3983 Wind observations of foreshock cavities: A case study. *J. Geophys. Res.*, *107*,
3984 1271. doi: 10.1029/2001JA007539
- 3985 Siscoe, G., Crooker, N. U., & Clauer, C. R. (2006, January). Dst of the Carrington
3986 storm of 1859. *Adv. Space Res.*, *38*(2), 173–179. doi: 10.1016/j.asr.2005.02
3987 .102
- 3988 Smith, E. J., & Wolfe, J. H. (1976, March). Observations of interaction regions and
3989 corotating shocks between one and five AU: Pioneers 10 and 11. *Geophys. Res.*
3990 *Lett.*, *3*(3), 137–140. doi: 10.1029/GL003i003p00137
- 3991 Sonnerup, B. U. Ö. (1979). Magnetic field reconnection. In *Solar system plasma*
3992 *physics* (Vol. 3, pp. 45–108).
- 3993 Stansby, D., Horbury, T. S., Chen, C. H. K., & Matteini, L. (2016, September).
3994 Experimental Determination of Whistler Wave Dispersion Relation in the Solar
3995 Wind. *Astrophys. J. Lett.*, *829*, L16. doi: 10.3847/2041-8205/829/1/L16
- 3996 Sterken, V. J., Westphal, A. J., Altobelli, N., Malaspina, D., & Postberg, F. (2019,
3997 October). Interstellar Dust in the Solar System. *Space Sci. Rev.*, *215*(7), 32.
3998 doi: 10.1007/s11214-019-0607-9
- 3999 Stix, T. H. (1992). *Waves in plasmas*. Springer.
- 4000 Stone, E. C., Frandsen, A. M., Mewaldt, R. A., Christian, E. R., Margolies, D.,
4001 Ormes, J. F., & Snow, F. (1998, July). The Advanced Composition Explorer.
4002 *Space Sci. Rev.*, *86*, 1–22. doi: 10.1023/A:1005082526237
- 4003 Svinkin, D., Frederiks, D., Hurley, K., Aptekar, R., & Others. (2021, January). A
4004 bright γ -ray flare interpreted as a giant magnetar flare in NGC 253. *Nature*,
4005 *589*(7841), 211–213. Retrieved from [https://www.nature.com/articles/](https://www.nature.com/articles/s41586-020-03076-9)
4006 [s41586-020-03076-9](https://www.nature.com/articles/s41586-020-03076-9) doi: 10.1038/s41586-020-03076-9
- 4007 Svinkin, D. S., Frederiks, D. D., Aptekar, R. L., Golenetskii, S. V., Pal'shin, V. D.,
4008 Oleynik, P. P., ... Hurley, K. (2016, May). The Second Konus-Wind Cat-
4009 alog of Short Gamma-Ray Bursts. *Astrophys. J. Suppl.*, *224*, 10. doi:
4010 10.3847/0067-0049/224/1/10
- 4011 Szabo, A., Larson, D., Whittlesey, P., Stevens, M. L., Lavraud, B., Phan, T., ...
4012 Pulupa, M. (2020, February). The Heliospheric Current Sheet in the Inner
4013 Heliosphere Observed by the Parker Solar Probe. *Astrophys. J. Suppl.*, *246*(2),
4014 47. doi: 10.3847/1538-4365/ab5dac
- 4015 Takeuchi, T., Araki, T., Luehr, H., Rasmussen, O., Watermann, J., Milling, D. K.,
4016 ... Nagai, T. (2000, August). Geomagnetic negative sudden impulse due to
4017 a magnetic cloud observed on May 13, 1995. *J. Geophys. Res.*, *105*, 18835–
4018 18846. doi: 10.1029/2000JA900055
- 4019 Talebpour Sheshvan, N., & Pohjolainen, S. (2018, November). Visibility and Origin
4020 of Compact Interplanetary Radio Type IV Bursts. *Solar Phys.*, *293*, 148. doi:
4021 10.1007/s11207-018-1371-9
- 4022 Temerin, M., & Roth, I. (1992, June). The Production of ^3He and Heavy Ion En-
4023 richments in ^3He -rich Flares by Electromagnetic Hydrogen Cyclotron Waves.
4024 *Astrophys. J. Lett.*, *391*, L105. doi: 10.1086/186408

- 4025 Tidman, D. A., & Northrop, T. G. (1968, March). Emission of plasma waves
4026 by the Earth's bow shock. *J. Geophys. Res.*, *73*, 1543–1553. doi: 10.1029/
4027 JA073i005p01543
- 4028 Tong, Y., Vasko, I. Y., Pulupa, M., Mozer, F. S., Bale, S. D., Artemyev, A. V.,
4029 & Krasnoselskikh, V. (2019, January). Whistler Wave Generation by
4030 Halo Electrons in the Solar Wind. *Astrophys. J. Lett.*, *870*, L6. doi:
4031 10.3847/2041-8213/aaf734
- 4032 Tsurutani, B. T., Gonzalez, W. D., Gonzalez, A. L. C., Guarnieri, F. L., Gopal-
4033 swamy, N., Grande, M., . . . Vasyliunas, V. (2006, July). Corotating solar
4034 wind streams and recurrent geomagnetic activity: A review. *J. Geophys. Res.*,
4035 *111*(A7), A07S01. doi: 10.1029/2005JA011273
- 4036 Tsurutani, B. T., & Lin, R. P. (1985, January). Acceleration of ~ 47 keV ions and ~ 2
4037 keV electrons by interplanetary shocks at 1 AU. *J. Geophys. Res.*, *90*(A1), 1–
4038 11. doi: 10.1029/JA090iA01p00001
- 4039 Tsvetkova, A., Frederiks, D., Golenetskii, S., Lysenko, A., Oleynik, P., Pal'shin, V.,
4040 . . . Aptekar, R. (2017, December). The Konus-Wind Catalog of Gamma-
4041 Ray Bursts with Known Redshifts. I. Bursts Detected in the Triggered Mode.
4042 *Astrophys. J.*, *850*, 161. doi: 10.3847/1538-4357/aa96af
- 4043 Turner, D. L., Angelopoulos, V., Morley, S. K., Henderson, M. G., Reeves, G. D.,
4044 Li, W., . . . Rodriguez, J. V. (2014, March). On the cause and extent of outer
4045 radiation belt losses during the 30 September 2012 dropout event. *J. Geophys.*
4046 *Res.*, *119*, 1530–1540. doi: 10.1002/2013JA019446
- 4047 Vandas, M., Fischer, S., Pelant, P., & Geranios, A. (1993, December). Evidence for
4048 a spheroidal structure of magnetic clouds. *J. Geophys. Res.*, *98*(A12), 21061–
4049 21070. doi: 10.1029/93JA01749
- 4050 Vandas, M., Geranios, A., & Romashets, E. (2009, August). On expansion of mag-
4051 netic clouds in the solar wind. *Astrophys. Space Sci. Trans.*, *5*, 35–38. doi: 10
4052 .5194/astra-5-35-2009
- 4053 Vasko, I. Y., Krasnoselskikh, V., Tong, Y., Bale, S. D., Bonnell, J. W., & Mozer,
4054 F. S. (2019, February). Whistler Fan Instability Driven by Strahl Electrons
4055 in the Solar Wind. *Astrophys. J. Lett.*, *871*, L29. doi: 10.3847/2041-8213/
4056 ab01bd
- 4057 Vasko, I. Y., Kuzichev, I. V., Artemyev, A. V., Bale, S. D., Bonnell, J. W., & Mozer,
4058 F. S. (2020, August). On quasi-parallel whistler waves in the solar wind. *Phys.*
4059 *Plasmas*, *27*(8), 082902. doi: 10.1063/5.0003401
- 4060 Vasko, I. Y., Mozer, F. S., Krasnoselskikh, V. V., Artemyev, A. V., Agapitov, O. V.,
4061 Bale, S. D., . . . Torbert, R. (2018, June). Solitary Waves Across Supercritical
4062 Quasi-Perpendicular Shocks. *Geophys. Res. Lett.*, *45*(12), 5809–5817. doi:
4063 10.1029/2018GL077835
- 4064 Vech, D., Mallet, A., Klein, K. G., & Kasper, J. C. (2018, March). Magnetic Recon-
4065 nection May Control the Ion-scale Spectral Break of Solar Wind Turbulence.
4066 *Astrophys. J. Lett.*, *855*, L27. doi: 10.3847/2041-8213/aab351
- 4067 Velli, M., Harra, L. K., Vourlidis, A., Schwadron, N., Panasenco, O., Liewer, P. C.,
4068 . . . Maksimovic, M. (2020, September). Understanding the origins of the helio-
4069 sphere: Integrating observations and measurements from Parker Solar Probe,
4070 Solar Orbiter and Other space and ground based observatories. *Astron. &*
4071 *Astrophys.* (in press) doi: 10.1051/0004-6361/202038245
- 4072 Verdini, A., Grappin, R., Alexandrova, O., Franci, L., Landi, S., Matteini, L., &
4073 Papini, E. (2019, July). Three-dimensional local anisotropy of velocity fluctua-
4074 tions in the solar wind. *Mon. Not. Roy. Astron. Soc.*, *486*(3), 3006–3018. doi:
4075 10.1093/mnras/stz1041
- 4076 Verdini, A., Grappin, R., Alexandrova, O., & Lion, S. (2018, January). 3D
4077 Anisotropy of Solar Wind Turbulence, Tubes, or Ribbons? *Astrophys. J.*,
4078 *853*, 85. doi: 10.3847/1538-4357/aaa433
- 4079 Verscharen, D., Bourouaine, S., & Chandran, B. D. G. (2013, August). Instabilities

- 4080 Driven by the Drift and Temperature Anisotropy of Alpha Particles in the
4081 Solar Wind. *Astrophys. J.*, 773(2), 163. doi: 10.1088/0004-637X/773/2/163
- 4082 Verscharen, D., Chandran, B. D. G., Jeong, S.-Y., Salem, C. S., Pulupa, M. P., &
4083 Bale, S. D. (2019, December). Self-induced Scattering of Strahl Electrons in
4084 the Solar Wind. *Astrophys. J.*, 886(2), 136. doi: 10.3847/1538-4357/ab4c30
- 4085 Verscharen, D., Chen, C. H. K., & Wicks, R. T. (2017, May). On Kinetic Slow
4086 Modes, Fluid Slow Modes, and Pressure-balanced Structures in the Solar
4087 Wind. *Astrophys. J.*, 840, 106. doi: 10.3847/1538-4357/aa6a56
- 4088 Verscharen, D., Klein, K. G., & Maruca, B. A. (2019, December). The multi-scale
4089 nature of the solar wind. *Living Reviews in Solar Physics*, 16(1), 5. doi: 10
4090 .1007/s41116-019-0021-0
- 4091 von Rosenvinge, T. T., Barbier, L. M., Karsch, J., Liberman, R., Madden, M. P.,
4092 Nolan, T., ... Walpole, P. (1995, February). The Energetic Particles: Ac-
4093 celeration, Composition, and Transport (EPACT) investigation on the WIND
4094 spacecraft. *Space Sci. Rev.*, 71, 155–206. doi: 10.1007/BF00751329
- 4095 Vršnak, B., Amerstorfer, T., Dumbović, M., Leitner, M., Veronig, A. M., Temmer,
4096 M., ... Galvin, A. B. (2019, June). Heliospheric Evolution of Magnetic Clouds.
4097 *Astrophys. J.*, 877(2), 77. doi: 10.3847/1538-4357/ab190a
- 4098 Vršnak, B., Aurass, H., Magdalenic, J., & Gopalswamy, N. (2001, October). Band-
4099 splitting of coronal and interplanetary type II bursts. I. Basic properties. *As-
4100 tron. & Astrophys.*, 377, 321–329. doi: 10.1051/0004-6361:20011067
- 4101 Šafránková, J., Němeček, Z., Němec, F., Verscharen, D., Chen, C. H. K., Ďurovcová,
4102 T., & Riazantseva, M. O. (2019, January). Scale-dependent Polarization of
4103 Solar Wind Velocity Fluctuations at the Inertial and Kinetic Scales. *Astrophys.
4104 J.*, 870(1), 40. doi: 10.3847/1538-4357/aaf239
- 4105 Walker, S. N., Balikhin, M. A., Alleyne, H. S. C. K., Hobara, Y., André, M., &
4106 Dunlop, M. W. (2008, March). Lower hybrid waves at the shock front: a
4107 reassessment. *Ann. Geophys.*, 26, 699–707.
- 4108 Wang, L., Krucker, S., Mason, G. M., Lin, R. P., & Li, G. (2016, January). The in-
4109 jection of ten electron/³He-rich SEP events. *Astron. & Astrophys.*, 585, A119.
4110 doi: 10.1051/0004-6361/201527270
- 4111 Wang, L., Lin, R. P., & Krucker, S. (2011, February). Pitch-angle Distributions
4112 and Temporal Variations of 0.3–300 keV Solar Impulsive Electron Events. *As-
4113 trophys. J.*, 727, 121. doi: 10.1088/0004-637X/727/2/121
- 4114 Wang, L., Lin, R. P., Krucker, S., & Gosling, J. T. (2006, February). Evidence for
4115 double injections in scatter-free solar impulsive electron events. *Geophys. Res.
4116 Lett.*, 330, L03106. doi: 10.1029/2005GL024434
- 4117 Wang, Y., Shen, C., Liu, R., Liu, J., Guo, J., Li, X., ... Zhang, T. (2018, May).
4118 Understanding the Twist Distribution Inside Magnetic Flux Ropes by Anato-
4119 mizing an Interplanetary Magnetic Cloud. *J. Geophys. Res.*, 123, 3238–3261.
4120 doi: 10.1002/2017JA024971
- 4121 Webb, D. F. (1988, March). Erupting prominences and the geometry of cor-
4122 onal mass ejections. *J. Geophys. Res.*, 93(3), 1749–1758. doi: 10.1029/
4123 JA093iA03p01749
- 4124 Webb, D. F. (1998). CMEs and Prominences and Their Evolution over the Solar
4125 Cycle (Review). In D. F. Webb, B. Schmieder, & D. M. Rust (Ed.), *Iau colloq.
4126 167: New perspectives on solar prominences* (Vol. 150, p. 463–+).
- 4127 Webb, D. F., Cliver, E. W., Crooker, N. U., Cry, O. C. S., & Thompson, B. J.
4128 (2000, April). Relationship of halo coronal mass ejections, magnetic
4129 clouds, and magnetic storms. *J. Geophys. Res.*, 105(4), 7491–7508. doi:
4130 10.1029/1999JA000275
- 4131 Webb, D. F., Cliver, E. W., Gopalswamy, N., Hudson, H. S., & St. Cyr, O. C.
4132 (1998). The solar origin of the January 1997 coronal mass ejection, mag-
4133 netic cloud and geomagnetic storm. *Geophys. Res. Lett.*, 25, 2469–2472. doi:
4134 10.1029/98GL00493

- 4135 Whipple, E., & Lancaster, H. (1995, February). International Coordina-
 4136 tion of Solar Terrestrial Science. *Space Sci. Rev.*, *71*(1-4), 41–54. doi:
 4137 10.1007/BF00751325
- 4138 Wicks, R. T., Alexander, R. L., Stevens, M. L., Wilson III, L. B., Moya, P. S.,
 4139 Viñas, A. F., . . . Zurbuchen, T. H. (2016, March). A Proton-cyclotron Wave
 4140 Storm Generated by Unstable Proton Distribution Functions in the Solar
 4141 Wind. *Astrophys. J.*, *819*(1), 6. doi: 10.3847/0004-637X/819/1/6
- 4142 Wicks, R. T., Chapman, S. C., & Dendy, R. O. (2009, January). Spatial Correlation
 4143 of Solar Wind Fluctuations and Their Solar Cycle Dependence. *Astrophys. J.*,
 4144 *690*, 734–742. doi: 10.1088/0004-637X/690/1/734
- 4145 Wicks, R. T., Horbury, T. S., Chen, C. H. K., & Schekochihin, A. A. (2011, Janu-
 4146 ary). Anisotropy of Imbalanced Alfvénic Turbulence in Fast Solar Wind.
 4147 *Phys. Rev. Lett.*, *106*, 045001. doi: 10.1103/PhysRevLett.106.045001
- 4148 Wicks, R. T., Mallet, A., Horbury, T. S., Chen, C. H. K., Schekochihin, A. A.,
 4149 & Mitchell, J. J. (2013, January). Alignment and Scaling of Large-Scale
 4150 Fluctuations in the Solar Wind. *Phys. Rev. Lett.*, *110*(2), 025003. doi:
 4151 10.1103/PhysRevLett.110.025003
- 4152 Wicks, R. T., Owens, M. J., & Horbury, T. S. (2010, March). The Variation of So-
 4153 lar Wind Correlation Lengths Over Three Solar Cycles. *Solar Phys.*, *262*, 191–
 4154 198. doi: 10.1007/s11207-010-9509-4
- 4155 Wicks, R. T., Roberts, D. A., Mallet, A., Schekochihin, A. A., Horbury, T. S., &
 4156 Chen, C. H. K. (2013, December). Correlations at Large Scales and the On-
 4157 set of Turbulence in the Fast Solar Wind. *Astrophys. J.*, *778*(2), 177. doi:
 4158 10.1088/0004-637X/778/2/177
- 4159 Wild, J. P., Smerd, S. F., & Weiss, A. A. (1963, January). Solar Bursts. *Ann. Rev.*
 4160 *Astron. Astrophys.*, *1*, 291–366. doi: 10.1146/annurev.aa.01.090163.001451
- 4161 Wilson, R. M., & Hildner, E. (1984, March). Are Interplanetary Magnetic Clouds
 4162 Manifestations of Coronal Transients at 1A.U. *Solar Phys.*, *91*(1), 169–180.
 4163 doi: 10.1007/BF00213622
- 4164 Wilson III, L. B. (2010). *The microphysics of collisionless shocks* (Unpublished doc-
 4165 toral dissertation). University of Minnesota.
- 4166 Wilson III, L. B. (2016, February). Low frequency waves at and upstream of
 4167 collisionless shocks. In A. Keiling, D.-H. Lee, & V. Nakariakov (Eds.), *Low-*
 4168 *frequency Waves in Space Plasmas* (Vol. 216, pp. 269–291). Washington, D.C.:
 4169 American Geophysical Union. doi: 10.1002/9781119055006.ch16
- 4170 Wilson III, L. B. (2020, June). Wind WAVES TDSF Dataset. In *Zenodo wind waves*
 4171 *tdsf dataset* (Vol. 39, p. 11205). doi: 10.5281/zenodo.3911205
- 4172 Wilson III, L. B. (2021, January). *Space plasma missions idl software library*. Zen-
 4173 odo. Retrieved from <https://doi.org/10.5281/zenodo.4451331> doi: 10
 4174 .5281/zenodo.4451331
- 4175 Wilson III, L. B., Cattell, C., Kellogg, P. J., Goetz, K., Kersten, K., Hanson, L., . . .
 4176 Kasper, J. C. (2007, July). Waves in Interplanetary Shocks: A Wind/WAVES
 4177 Study. *Phys. Rev. Lett.*, *99*, 041101+. doi: 10.1103/PhysRevLett.99.041101
- 4178 Wilson III, L. B., Cattell, C. A., Kellogg, P. J., Goetz, K., Kersten, K., Kasper,
 4179 J. C., . . . Meziane, K. (2009, October). Low-frequency whistler waves and
 4180 shocklets observed at quasi-perpendicular interplanetary shocks. *J. Geophys.*
 4181 *Res.*, *114*, A10106. doi: 10.1029/2009JA014376
- 4182 Wilson III, L. B., Cattell, C. A., Kellogg, P. J., Goetz, K., Kersten, K., Kasper,
 4183 J. C., . . . Wilber, M. (2010, December). Large-amplitude electrostatic
 4184 waves observed at a supercritical interplanetary shock. *J. Geophys. Res.*,
 4185 *115*, A12104. doi: 10.1029/2010JA015332
- 4186 Wilson III, L. B., Cattell, C. A., Kellogg, P. J., Wygant, J. R., Goetz, K., Bren-
 4187 eman, A., & Kersten, K. (2011, September). The properties of large am-
 4188 plitude whistler mode waves in the magnetosphere: Propagation and rela-
 4189 tionship with geomagnetic activity. *Geophys. Res. Lett.*, *38*, 17107. doi:

- 4190 10.1029/2011GL048671
- 4191 Wilson III, L. B., Chen, L.-J., Wang, S., Schwartz, S. J., Turner, D. L., Stevens,
4192 M. L., ... Goodrich, K. A. (2019a, December). Electron Energy Partition
4193 across Interplanetary Shocks. II. Statistics. *Astrophys. J. Suppl.*, *245*(2), 24.
4194 doi: 10.3847/1538-4365/ab5445
- 4195 Wilson III, L. B., Chen, L.-J., Wang, S., Schwartz, S. J., Turner, D. L., Stevens,
4196 M. L., ... Goodrich, K. A. (2019b, July). Electron Energy Partition across In-
4197 terplanetary Shocks. I. Methodology and Data Product. *Astrophys. J. Suppl.*,
4198 *243*(1), 8. doi: 10.3847/1538-4365/ab22bd
- 4199 Wilson III, L. B., Chen, L.-J., Wang, S., Schwartz, S. J., Turner, D. L., Stevens,
4200 M. L., ... Goodrich, K. A. (2019c, May). Supplement to: Electron energy
4201 partition across interplanetary shocks. In *Zenodo supplementary pdf and two*
4202 *ascii files* (Vol. 28, p. 75806). doi: 10.5281/zenodo.2875806
- 4203 Wilson III, L. B., Chen, L.-J., Wang, S., Schwartz, S. J., Turner, D. L., Stevens,
4204 M. L., ... Goodrich, K. A. (2020a, April). Electron Energy Partition
4205 across Interplanetary Shocks. III. Analysis. *Astrophys. J.*, *893*(22), 21. doi:
4206 10.3847/1538-4357/ab7d39
- 4207 Wilson III, L. B., Chen, L.-J., Wang, S., Schwartz, S. J., Turner, D. L., Stevens,
4208 M. L., ... Goodrich, K. A. (2020b, January). Supplement to: Electron energy
4209 partition across interplanetary shocks: III. Analysis. In *Zenodo supplementary*
4210 *pdf* (Vol. 36, p. 27284). doi: 10.5281/zenodo.3627284
- 4211 Wilson III, L. B., Koval, A., Sibeck, D. G., Szabo, A., Cattell, C. A., Kasper, J. C.,
4212 ... Wilber, M. (2013, March). Shocklets, SLAMS, and field-aligned ion
4213 beams in the terrestrial foreshock. *J. Geophys. Res.*, *118*, 957–966. doi:
4214 10.1029/2012JA018186
- 4215 Wilson III, L. B., Koval, A., Szabo, A., Breneman, A., Cattell, C. A., Goetz, K., ...
4216 Pulupa, M. (2012, April). Observations of electromagnetic whistler precursors
4217 at supercritical interplanetary shocks. *Geophys. Res. Lett.*, *39*, 8109. doi:
4218 10.1029/2012GL051581
- 4219 Wilson III, L. B., Koval, A., Szabo, A., Breneman, A., Cattell, C. A., Goetz, K., ...
4220 Pulupa, M. (2013, January). Electromagnetic waves and electron anisotropies
4221 downstream of supercritical interplanetary shocks. *J. Geophys. Res.*, *118*,
4222 5–16. doi: 10.1029/2012JA018167
- 4223 Wilson III, L. B., Koval, A., Szabo, A., Stevens, M. L., Kasper, J. C., Cattell, C. A.,
4224 & Krasnoselskikh, V. V. (2017, October). Revisiting the structure of low
4225 Mach number, low beta, quasi-perpendicular shocks. *J. Geophys. Res.*, *122*(9),
4226 9115–9133. doi: 10.1002/2017JA024352
- 4227 Wilson III, L. B., & Others. (2021, January). Wind *lz calibration and decommuta-*
4228 *tion software*. Zenodo. Retrieved from [https://doi.org/10.5281/zenodo](https://doi.org/10.5281/zenodo.4451304)
4229 [.4451304](https://doi.org/10.5281/zenodo.4451304) doi: 10.5281/zenodo.4451304
- 4230 Wilson III, L. B., Sibeck, D. G., Turner, D. L., Osmane, A., Caprioli, D., & An-
4231 gelopoulos, V. (2016, November). Relativistic electrons produced by foreshock
4232 disturbances observed upstream of the Earth's bow shock. *Phys. Rev. Lett.*,
4233 *117*(21), 215101. (Editors' Suggestion) doi: 10.1103/PhysRevLett.117.215101
- 4234 Wilson III, L. B., Stevens, M. L., Kasper, J. C., Klein, K. G., Maruca, B. A., Bale,
4235 S. D., ... Salem, C. S. (2018, June). The Statistical Properties of Solar
4236 Wind Temperature Parameters Near 1 au. *Astrophys. J. Suppl.*, *236*, 41. doi:
4237 10.3847/1538-4365/aab71c
- 4238 Winslow, R. M., Lugaz, N., Schwadron, N. A., Farrugia, C. J., Yu, W., Raines,
4239 J. M., ... Zurbuchen, T. H. (2016, July). Longitudinal conjunction be-
4240 tween MESSENGER and STEREO A: Development of ICME complexity
4241 through stream interactions. *J. Geophys. Res.*, *121*(7), 6092–6106. doi:
4242 10.1002/2015JA022307
- 4243 Winter, L. M., & Ledbetter, K. (2015, August). Type II and Type III Radio Bursts
4244 and their Correlation with Solar Energetic Proton Events. *Astrophys. J.*, *809*,

- 4245 105. doi: 10.1088/0004-637X/809/1/105
- 4246 Wong, H. V. (1970, March). Electrostatic Electron-Ion Streaming Instability. *Phys.*
4247 *Fluids*, *13*, 757–760. doi: 10.1063/1.1692983
- 4248 Wood, B. E., Wu, C.-C., Lepping, R. P., Nieves-Chinchilla, T., Howard, R. A., Lin-
4249 ton, M. G., & Socker, D. G. (2017, April). A STEREO Survey of Magnetic
4250 Cloud Coronal Mass Ejections Observed at Earth in 2008–2012. *Astrophys. J.*
4251 *Suppl.*, *229*, 29. doi: 10.3847/1538-4365/229/2/29
- 4252 Wood, S. R., Malaspina, D. M., Andersson, L., & Horanyi, M. (2015, September).
4253 Hypervelocity dust impacts on the Wind spacecraft: Correlations between
4254 Ulysses and Wind interstellar dust detections. *J. Geophys. Res.*, *120*, 7121–
4255 7129. doi: 10.1002/2015JA021463
- 4256 Woodham, L. D., Wicks, R. T., Verscharen, D., & Owen, C. J. (2018, March). The
4257 Role of Proton Cyclotron Resonance as a Dissipation Mechanism in Solar
4258 Wind Turbulence: A Statistical Study at Ion-kinetic Scales. *Astrophys. J.*,
4259 *856*, 49. doi: 10.3847/1538-4357/aab03d
- 4260 Woodham, L. D., Wicks, R. T., Verscharen, D., Owen, C. J., Maruca, B. A., &
4261 Alterman, B. L. (2019, October). Parallel-propagating Fluctuations at Proton-
4262 kinetic Scales in the Solar Wind Are Dominated By Kinetic Instabilities.
4263 *Astrophys. J. Lett.*, *884*(2), L53. doi: 10.3847/2041-8213/ab4adc
- 4264 Wrenn, G. L., Rodgers, D. J., & Ryden, K. A. (2002, July). A solar cycle of space-
4265 craft anomalies due to internal charging. *Ann. Geophys.*, *20*(7), 953–956. doi:
4266 10.5194/angeo-20-953-2002
- 4267 Wu, C.-C., & Lepping, R. P. (2015, April). Comparisons of Characteristics of Mag-
4268 netic Clouds and Cloud-Like Structures During 1995 - 2012. *Solar Phys.*, *290*,
4269 1243–1269. doi: 10.1007/s11207-015-0656-5
- 4270 Wu, C. S., Winske, D., Papadopoulos, K., Zhou, Y. M., Tsai, S. T., & Guo, S. C.
4271 (1983, May). A kinetic cross-field streaming instability. *Phys. Fluids*, *26*,
4272 1259–1267. doi: 10.1063/1.864285
- 4273 Wu, C. S., Winske, D., Tanaka, M., Papadopoulos, K., Akimoto, K., Goodrich,
4274 C. C., ... Lin, C. S. (1984, January). Microinstabilities associated with a high
4275 Mach number, perpendicular bow shock. *Space Sci. Rev.*, *37*, 63–109. doi:
4276 10.1007/BF00213958
- 4277 Wygant, J. R., Bonnell, J. W., Goetz, K., Ergun, R. E., Mozer, F. S., Bale, S. D.,
4278 ... Tao, J. B. (2013, November). The Electric Field and Waves Instruments on
4279 the Radiation Belt Storm Probes Mission. *Space Sci. Rev.*, *179*(1-4), 183–220.
4280 doi: 10.1007/s11214-013-0013-7
- 4281 Xystouris, G., Sigala, E., & Mavromichalaki, H. (2014, March). A Complete Cat-
4282 alogue of High-Speed Solar Wind Streams during Solar Cycle 23. *Solar Phys.*,
4283 *289*, 995–1012. doi: 10.1007/s11207-013-0355-z
- 4284 Zesta, E., & Sibeck, D. G. (2004, January). A detailed description of the solar wind
4285 triggers of two dayside transients: Events of 25 July 1997. *J. Geophys. Res.*,
4286 *109*, 1201. doi: 10.1029/2003JA009864
- 4287 Zhang, J., Richardson, I. G., Webb, D. F., Gopalswamy, N., Huttunen, E., Kasper,
4288 J. C., ... Zhukov, A. N. (2007, October). Solar and interplanetary sources
4289 of major geomagnetic storms ($\text{Dst} \leq -100$ nT) during 1996-2005. *J. Geophys.*
4290 *Res.*, *112*, A10102. doi: 10.1029/2007JA012321
- 4291 Zhao, X., Liu, Y. D., Hu, H., & Wang, R. (2019, September). Quantifying the
4292 Propagation of Fast Coronal Mass Ejections from the Sun to Interplanetary
4293 Space by Combining Remote Sensing and Multi-point In Situ Observations.
4294 *Astrophys. J.*, *882*(2), 122. doi: 10.3847/1538-4357/ab379b
- 4295 Zhao, X. H., Feng, X. S., Feng, H. Q., & Li, Z. (2017, November). Correlation be-
4296 tween Angular Widths of CMEs and Characteristics of Their Source Regions.
4297 *Astrophys. J.*, *849*, 79. doi: 10.3847/1538-4357/aa8e49
- 4298 Zhdankin, V., Boldyrev, S., & Mason, J. (2012, December). Distribution of Magnetic
4299 Discontinuities in the Solar Wind and in Magnetohydrodynamic Turbulence.

4300 *Astrophys. J. Lett.*, 760, L22. doi: 10.1088/2041-8205/760/2/L22
4301 Zurbuchen, T. H., & Richardson, I. G. (2006, March). In-Situ Solar Wind and Mag-
4302 netic Field Signatures of Interplanetary Coronal Mass Ejections. *Space Sci.*
4303 *Rev.*, 123(1-3), 31–43. doi: 10.1007/s11214-006-9010-4